Ph.D. Program in Civil, Chemical and Environmental Engineering
Curriculum of Chemical, Material and Process Engineering

Department of Civil, Chemical and Environmental Engineering
Polytechnic School, University of Genoa, Italy.

Simulation of High Temperature Fuel Cells for Carbon Capture

Emilio Audasso

SIMULATION OF HIGH TEMPERATURE FUEL CELLS FOR CARBON CAPTURE

BY

EMILIO AUDASSO

Simulation of high temperature fuel cells

DOCTOR OF PHILOSOPHY

Civil, Chemical and Environmental Engineering
Curriculum of Chemical, Material and Process Engineering,
Department of Civil, Chemical and Environmental Engineering, University of Genoa, Italy

February 26, 2021

Advisers:
Prof. Barbara Bosio - University of Genoa
Timothy Barckholtz Ph.D. - ExxonMobil Research and Engineering
Jonathan Rosen Ph.D. - ExxonMobil Research and Engineering

External Reviewers:
Prof. Mariagiovanna Minutillo - Parthenope University of Naples
Prof. Federico Rossi - University of Perugia

Examination Committee:
Prof. Elisabetta Arato - University of Genoa
Prof. Marco Baratieri - Free University of Bozen-Bolzano
Prof. Stefano Consonni - Polytechnic University of Milan

Substitute members:
Prof. Antonio Barbucci - University of Genoa
Prof. Michel Cassir - École nationale supérieure de Chimie de Paris
Prof. Maria Chiara Ferrari - University of Edinburgh

Ph.D. program in Civil, Chemical and Environmental Engineering
Curriculum in Chemical, Materials and Process Engineering
Cycle XXXIII

ABSTRACT

The aim of this doctoral thesis is to develop and apply a kinetic model for the simulation of High Temperature Fuel Cells for energy conversion and Carbon Capture applications. In particular, the work will focus on the analysis and the modeling of a newly discovered mechanism in Molten Carbonate Fuel Cells that sees the net migration of H_2O from the cathode to the anode side in competition with the usually encountered migration of CO_2. This mechanism was never reported in the literature and was named "dual-anion mechanism" to underline the parallel migration of carbonate and hydroxide ions. It is important because it can greatly affect the cell's performance in terms of both energy conversion and CO_2 sequestration.

The work was performed in collaboration with ExxonMobil that first observed this phenomenon during a campaign to test the use of molten carbonate fuel cells as Carbon Capture devices. The work was also done in partnership with FuelCell Energy, who through an agreement with ExxonMobil obtained all of the experimental data of this phenomenon.

The analysis of the mechanism and the development of a model to simulate cells working at such conditions were conducted in a series of different steps. To start, based on experimental data, the mechanism was studied as a function of the reactant gases to understand the main dependences of the occurring phenomena. Consequently, as more data became available, additional dependences to improve the knowledge of the mechanism and the modeling were studied. In particular, the work was focused on the analysis of the effects that the diffusion resistance has on the extent on which one anionic path evolves over the other. Successively, the operating temperature and the carbonate/hydroxide equilibrium were studied and included in the model. The analysis of the experimental data also allowed to observe the effects that the gas atmosphere can have on the cell ohmic resistance as it was determined that the electrolyte melt can change based on equilibria between melt and gas phase. The developed kinetic formulation was implemented into the SIMFC code, a home-made Fortran program realized by the group PERT of the University of Genoa for the simulation of High Temperature Fuel Cells (Molten Carbonate and Solid Oxide). In this way, the model was successfully tested by simulating the experimental data.

Additionally, a formulation to consider the direct internal steam reforming of CH_4 on the performance of cells was also included into the SIMFC code. The formulation considers the reaction locally with dependence on catalyst loading. As such, it allows the study of the effect of catalyst distribution and degradation. This part of the thesis was developed on Solid Oxide Fuel Cells instead of Molten Carbonate. This choice was dictated by the fact that I spent a period of 8 months during the first year of the Ph.D. program at the Korea Institute of Science and Technology studying solid oxide fuel cells materials, specifically focused on the use of perovskite (a possible solid oxide fuel cells anode material) as catalysts for the CH_4 reforming reaction which will be presented.

The overall model developed and implemented into the SIMFC code was demonstrated to be very promising in simulating High Temperature Fuel Cells performance under a great range of operating conditions.

ACKNOWLEDGEMENTS

First and foremost I am extremely grateful to my supervisors: Prof. Barbara Bosio for her valuable advice, continuous support, and patience during my PhD study, and Dr. Timothy Barckholtz and Dr. Jonathan Rosen for sharing their knowledge and making possible for me to work together with ExxonMobil Research and Engineering.

I would also like to extend my gratitude to my lab mates Dr. Dario Bove, Dr. Bruno Conti and Fiammetta Bianchi for their support and fruitful collaboration.

Also, a great thank to the numerous people from ExxonMobil Research and Engineering I had the honor to work with: Dr. Heather Elsen, Dr. Rodrigo Blanco Gutierrez, Dr. Lu Han, Dr. Carla Pereira, Dr. Yesim Igci, and especially Dr. Gabor Kiss for the numerous and precious discussions that helped in the developing of the work.

I would also like to extend my gratitude to Dr. Suk Woo Nam, Dr. Sung Pil Yoon and Dr. Hyun Tae Sohn for the guide that I received during my time at the Korea Institute of Science and Technology supported by the Global Research Laboratory Program. Together, I would like to thanks my lab mates, in particular Dr. Grazia Accardo, Dr. Domenico Frattini and Yong Doo Kim.

For the precious collaborations, I would also like to thanks Prof. Linda Barelli from the University of Perugia, Prof. Gianfranco Dell'Agli and Dr. Luca Spiridigliozzi from the University of Cassino, Prof. Maria Chiara Ferrari from the University of Edinburgh and her exchange students Patrick Campell, Sotiris Papasotiriou and Ross Cooper.

INDEX

List of Figures

List of Tables

Introduction

In the last decades, the concentration of carbon dioxide (CO_2) in the atmosphere has drastically increased due to the emissions derived from stationary electricity and heat production and distributed transportation systems utilizing fossil fuel combustion as well as industrial plants. The scientific community agrees that the increase in atmospheric CO_2 stemming from these inputs is one of the main causes of climate changes.

To reduce the CO_2 emissions in the atmosphere the best solutions would be to increase the energy production efficiency, the usage of renewable sources, and the identification of different reactions that do not involve or reduce the formation of by-product CO_2. However, this implies a drastic change to the actual way of energy production and manufacturing that would require a huge amount of investment. A different solution that can be more easily applied is to rely on Carbon Capture and Storage (CCS). CCS is a broad term that includes a number of different technologies that can be used to capture CO_2 from point sources. One example is using High Temperature Fuel Cells and more specifically Molten Carbonate Fuel Cells. This kind of high temperature cell can concentrate a CO_2 poor stream using it as the oxidant (cathode inlet) to a more concentrated stream (anode outlet), thus making further separation process easier and less expensive.

Recently, the American based company ExxonMobil has started investigating the use of Molten Carbonate Fuel Cells as CCS devices to achieve CO_2 capture rates higher than 90%. Through an experimental campaign to test the cells capability, they observed the net migration of water from the cathode to the anode side in competition with the transfer of CO_2 that is normally observed. This newly discovered mechanism, once understood, can greatly affect the uses and the spread of this technology as it can influence cell performance in both their energy production and CO_2 capture capability.

Based on experimental observation provided by ExxonMobil and FuelCell Energy, in this thesis I will present a study of this newly observed phenomena together with the development of the first kinetic model to simulate Molten Carbonate Fuel Cells working at these conditions. The model equations will be integrated into the SIMFC code a homemade program developed by my research group at the University of Genoa for the simulation of high temperature fuel cells performance. Using SIMFC, I will test the quality of the model on the experimental data.

The work will be divided into nine chapters. The part of work that will be presented in the chapters from three to seven was funded by ExxonMobil and produced using experimental data provided by FuelCell Energy. The part of work that will be presented in chapters one, two, eight and nine was performed independently from ExxonMobil. In the first chapter a brief introduction on the Molten Carbonate Fuel Cells technology will be presented with particular focus on the modeling works realized until now. The basic equations used in the SIMFC code will also be introduced here. In the second chapter, I will present the simulation of two study cases that involve the use of Molten Carbonate Fuel Cells in integrated systems for Carbon Capture. For the simulation of these two cases I will use the SIMFC code integrated into Aspen plus, and a simplified SIMFC code rewritten in Aspen Modeler and integrated again into Aspen plus. In the third chapter, based on the experimental campaign conducted by ExxonMobil, I will present a basic formulation to model Molten Carbonate Fuel Cells with parallel migration of CO_2 and H_2O from cathode to anode. In the following fourth chapter, the model will be improved with the introduction of a diffusion term as it will be demonstrated that diffusion resistance is extremely relevant in favoring or hindering H_2O migration. In the fifth chapter, through sensitivity analysis on the parameters of the models, I will show how to simplify the model if needed and how such studies can be used to improve the cell performance. In the sixth chapter, the model will be redefined by rendering explicit the tempera-

ture dependence in the polarization resistance. This dependence was initially neglected to focus on the causes of the newly discovered mechanism. In the seventh chapter I will present additional experimental evidence on the carbonate/hydroxide equilibrium that control the newly observed mechanism to improve the polarization resistance expressions. High temperature fuel cells can work using CH_4 and light hydrocarbon as fuels exploiting reforming reactions. These reactions can occur either before or inside the fuel cell. In the eighth chapter I will integrate to the SIMFC code the formulation necessary to consider a cell working with direct internal steam reforming of CH_4. This work will be presented on Solid Oxide Fuel Cells since it was done in collaboration with a colleague focused on this typology of cell and since during the my Ph.D. experience I worked on Solid Oxide Fuel Cell materials in collaboration with the Korean Institute of Science and Technology. The model, using simple corrections to consider different materials, can be easily applied also to Molten Carbonate Fuel Cells. In the final chapter, I will present a study on a Rh-doped SYT catalyst for CH_4 reforming for application as SOFC anode. This final work was conducted at the Center for Hydrogen and Fuel Cell Research of the Korea Institute of Science and Technology.

Finally, I will present the conclusion of this work and present future steps that can be followed to improve the knowledge on high temperature fuel cells and further widen their use.

In the Appendixes at the end of the thesis, readers can find additional information on different aspect of the modeling and the collection of the experimental data used to study the phenomena and develop the model.

1
Molten Carbonate Fuel Cells

A fuel cell is an electrochemical device that directly converts the chemical energy of a fuel into electrical energy exploiting reduction and oxidation reactions in a manner that is similar to batteries [6, 7]. However, unlike batteries, fuel cells are open systems where the reactants are constantly fed to the cell and the products removed, and unable to store energy.

There is a large variety of fuel cells that differ by components and catalyst materials used, charge carriers, operating temperatures and range of applications [6]. Among these, Molten Carbonate Fuel Cells (MCFCs) are high-temperature, stationary operating systems characterized by the use of a liquid eutectic mixture of alkali metal carbonate as electrolyte. For this reason, MCFCs operate in a limited temperature range ($853\,K \sim 973\,K$) to ensure that the electrolyte is in its liquid state and to limit its losses due to high electrolyte volatility induced by high temperatures.

As with any other kind of fuel cell, the main structure of an MCFC is constituted of an electrolyte sandwiched between two electrodes: an anode for the oxidation and a cathode for the reduction. It is important to underline that, in contrast to battery nomenclature, in the field of fuel cells, the term "electrode" does not indicate the reactants that reduce (O_2) or oxidize (H_2), but instead refers to solid supports for the electrochemical reactions to occur. In the specific case of MCFCs, the anode material is a porous Ni-based alloy (typically with Al or Cr), the cathode material is a porous lithiated NiO, and the electrolyte consists of an eutectic mixture of alkali carbonates of which Li_2/K_2CO_3 and Li_2/Na_2CO_3 are the most common. Moreover, MCFCs need a ceramic matrix usually made of $LiAlO_2$ to support and keep the electrodes and electrolytes (using capillary forces) in place.

1.1. MCFC working principle

As in any other kind of fuel cell, in MCFCs the main reaction that provides energy is the formation of H_2O from reduction of O_2 and oxidation of H_2. However, in the specific case of MCFCs, CO_2 serves as an additional reactant with O_2 to form, at the cathode, the carbonate ion (CO_3^{2-}) that function as the anion carrier through the electrolyte and matrix. It is this very fact that makes MCFCs suitable for carbon capture whereas other fuel cells are not viable. The total MCFC reaction is the following[1]

$$H_2 + \frac{1}{2}\,O_2 + CO_{2,\text{cathode}} \longrightarrow H_2O + CO_{2,\text{anode}} \qquad \text{(R. 1.1)}$$

This is not a single step, but is composed of two main half-reactions that occur at the cathode and anode side respectively. The working principle is schematized in Figure 1.1.

[1] Unless differently specified, in the reactions all the reactants are in the gas phase, but the ions are dissolved in the liquid phase.

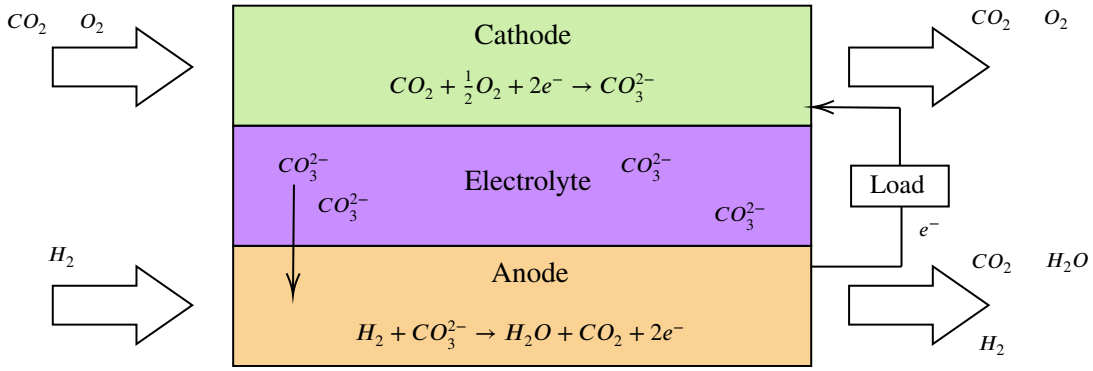

Figure 1.1: Schematization of the MCFC working principle.

1.1.1. Anode reactions

At the anode side, H_2 reacts with CO_3^{2-} from the electrolyte to form CO_2 and H_2O and release electrons (e^-) according to the following oxidation reaction:

$$H_2 + CO_3^{2-} \longrightarrow H_2O + CO_2 + 2\,e^- \qquad \text{(R. 1.2)}$$

A secondary fuel that can oxidize is carbon monoxide (CO) as shown in Rxn. 1.3.

$$CO + CO_3^{2-} \longrightarrow 2\,CO_2 + 2\,e^- \qquad \text{(R. 1.3)}$$

Although experiments were conducted to show the possibility of using CO as direct fuel in MCFCs [8], this does not usually happen. The reason can be found in the difference between the exchange current density at 923 K for the oxidation of CO (about 0.04 $mA\,cm^{-2}$) and H_2 (100 $mA\,cm^{-2}$) [8]. This substantial difference means that the oxidation rate of CO is three order of magnitude slower to that of H_2, thus resulting in CO-fed MCFCs having much lower performance than H_2-fed ones.

Nevertheless, CO is usually encountered in MCFCs anode feeds since it can be obtained as byproduct of the production of H_2 from reforming of hydrocarbons. Its consumption is mainly ascribed to the water-gas-shift (WGS, Rxn. 1.4) to replace the H_2 consumed in the electrochemical reaction.

$$H_2 + CO_2 \longleftrightarrow H_2O + CO \qquad \text{(R. 1.4)}$$

Thanks to the high temperatures, if specific catalysts are used, MCFCs can also operate directly using methane (CH_4) or other light hydrocarbons, exploiting reforming reactions for the internal production of H_2. An example of commonly exploited reforming reactions is the steam reforming of CH_4 (Rxn. 1.5).

$$CH_4 + H_2O \longleftrightarrow 3\,H_2 + CO \qquad \text{(R. 1.5)}$$

In addition to these reactions that are necessary for the correct cell operations, there could be other parasitic reactions that can reduce the performance and harm the cell. A major example is the carbon deposition in the form of the Boudouard reaction (Rxn. 1.6). This reaction is inhibited by CO_2 formation at the anode and it is usually limited by water vapor addition to the anode inlet.

$$2\,CO \longrightarrow CO_2 + C\,(s) \qquad \text{(R. 1.6)}$$

Other reactions that greatly affect MCFC performance are the ones that depend on the presence of pollutant compounds that can be usually traced to the fuel sources. Among these, sulfur is one of the

most commonly found and can be harmful for the cell even in low concentrations (e.g.: single digit parts per million) [6]. At the anode side, sulfur affects the cell in three main ways: (i) blocking the active electrochemical sites as it reacts with Ni, (ii) poisoning the catalysts site for the WGS reaction and the reforming catalyst, if present, and (iii) oxidization of SO_2 that can reacts with the electrolyte altering its composition and forming H_2S on the anode [9, 10].

1.1.2. Cathode reactions

At the cathode side, O_2 reduces thanks to the electrons coming from the anode and, by reaction with CO_2, forms CO_3^{2-} closing the circuit (Rxn. 1.7).

$$CO_2 + \frac{1}{2}O_2 + 2e^- \longrightarrow CO_3^{2-} \tag{R. 1.7}$$

In reality this is not a single reaction but a multi-step process that occurs through formation of intermediate activated species. In the literature, different mechanisms have been proposed, but the actual one has not been conclusively identified yet. The most widely accepted paths presented in the literature to describe the evolution of O_2 involve the intermediate formation of peroxide (O_2^{2-}) or superoxide (O_2^-).

Peroxide path (POP):

$$\frac{1}{2}O_2 + CO_3^{2-} \longrightarrow CO_2 + O_2^{2-} \tag{R. 1.8}$$

$$O_2^{2-} + 2e^- + 2CO_2 \longrightarrow 2CO_3^{2-} \tag{R. 1.9}$$

Superoxide path (SOP):

$$\frac{3}{4}O_2 + \frac{1}{2}CO_3^{2-} \longrightarrow \frac{1}{2}CO_2 + O_2^- \tag{R. 1.10}$$

$$O_2^- + 3e^- + 2CO_2 \longrightarrow 2CO_3^{2-} \tag{R. 1.11}$$

Different authors [11, 12] also suggested a path that involves the formation of the peroxycarbonate ions (CO_4^{2-}). The CO_4^{2-} driven reaction chain is the following:

$$CO_3^{2-} + \frac{1}{2}O_2 \longrightarrow CO_4^{2-} \tag{R. 1.12}$$

$$CO_4^{2-} + 2e^- \longrightarrow CO_3^{2-} + O^{2-} \tag{R. 1.13}$$

$$O^{2-} + CO_2 \longrightarrow CO_3^{2-} \tag{R. 1.14}$$

Even though, the presence of peroxycarbonate ions in the melt has been verified through Raman spectroscopy [13] together with other species such as pyrocarbonate ($C_2O_5^{2-}$) [14] and peroxidicarbonate ($C_2O_6^{2-}$) [15], many authors disregard this path as the one followed by O_2. Nevertheless, it is quite difficult to determine a specific path for the O_2 reduction and it is possible that a combination of all the paths

is followed, with different priority as a function of the operating conditions, also in terms of electrolyte composition [16]. This is evident if we consider the equilibria between ionic oxygen species [16, 17]:

$$2\,O^{2-} + O_2 \longleftrightarrow 2\,O_2^{2-} \tag{R. 1.15}$$

$$3\,O_2^{2-} \longleftrightarrow 2\,O^{2-} + 2\,O_2^{-} \tag{R. 1.16}$$

As discussed for the anode side, also at the cathode side several parasitic reactions can occur affecting the cell behavior. The NiO cathode material can dissolve in the carbonate according to the following reaction [6]:

$$NiO\,(s) + CO_2 \longrightarrow Ni^{2+}CO_3^{2-} \tag{R. 1.17}$$

The Ni ions can diffuse in the electrolyte and precipitate at the anode side after reduction by H_2. To reduce this issue the cathode is usually lithiated (mostly *in situ*) as a form of protection. The lithiation also serves to make NiO, an insulator, into a good electrical conductor which is required for the cathode reaction Rxn. 1.17 to occur.

Reactions due to pollutants are ascribable to the presence of SO_X and NO_X. SO_X reacts to form sulphate or sulphide that migrates to the anode side releasing H_2S that cause the anode poisoning previously discussed [18, 19]. NO_X in part reacts to form nitrate or nitrite and migrate to the anode side releasing N_2 or NH_3 which are not particularly harmful to the cell, in part react with the cathode current collector and manifold manifold corroding them and thus increasing the ohmic resistance [20].

1.2. MCFC current status

Until the last decades, the main industrial developers of MCFC technology were found in Europe (Italy: Ansaldo Fuel Cell, Germany: CFC Solutions, France: Franco Cell), America (US: FuelCell Energy (FCE) and GenCell Corporation), and Asia (Japan: Ishikawajima-Harima Heavy Industries, South Korea POSCO/KEPCO consortium and Doosan Heavy Industries) [21, 22]. In parallel, several universities and research facilities conducted different levels of studies [21]. Although this academic effort is still ongoing in the aforementioned and in other countries, the main industrial developers are now limited to FCE in the US and POSCO Energy in South Korea, with the latter using the former's technology [23].

Historically MCFCs have been mainly studied and developed for stationary energy production. Apart from the option to directly feed electricity to the grid, due to their dimension, operating temperature and manufacturing costs, MCFCs are suitable to function as direct or back-up power for big facilities such as hospitals, prisons, hotel and universities, but less indicated for small ones [21]. As of 2020, South Korea hosts the largest fuel cell park operated by Gyeonggi Green Energy. It consists of 59 MW of MCFCs and was develop by a joint agreement between FCE and POSCO [24, 23]. Others smaller installations developed by FCE can be found in the areas of California and New England in the US.

Naval applications have also been investigated, in particular the combination of MCFCs with batteries [25]. Although, currently there are no ongoing projects or studies for naval use, MCFCs can be suitable since their size and slow start-up time are not a real issue in marine applications [26] compared to other locomotion systems.

As discussed in the previous section, thanks to their particular *modus operandi*, MCFCs enable the transfer of CO_2 from a CO_2-poor (cathode feed) to a CO_2-rich stream (anode exhaust). This CO_2 transport and enrichment enables the recovery of pure CO_2 that then can be further utilized or sequestered. This

property allows MCFCs to be considered as a technology for Carbon Capture. For this reason, due to the continuous demand to reduce CO_2 emissions, MCFC related research has flourished with studies to apply this technology to capture CO_2 especially after combustion plants. In fact, compared to more traditional sorption-based carbon capture technologies, MCFCs not only allow CO_2 capture from flue gases, but also simultaneously production of electricity, surplus hydrogen, and heat (while consuming additional fuel).

In light of this application, the American based company ExxonMobil established in 2016 a joint development agreement with FCE [27]. The aim of this collaboration is to develop the use of MCFCs for large scale capture and concentration of CO_2 from industrial facilities. The MCFC modelling work that will be presented in this thesis is developed in this time frame.

Finally, MCFCs can be also applied for H_2 production if used in reverse way as electrolytic cell. This last application has currently gained interest from different research groups [28, 29, 30, 31] as an energy storage media.

1.3. Modeling of MCFC

The modeling of physical and chemical phenomena is of extreme importance to understand and visualize the mechanisms that are involved in manufacturing, energy production or any other kind of industrial processes. The use of modeling is not limited to the mere simulation of processes to gain information of the mass and energy balances, as it also allows for the improvement of process or plant design and control.

A substantial literature exists on the subject of the numerical simulation of MCFCs. In these works, the modeling effort spans from the study of electrochemical and mass transport processes of a single electrode to the simulation of stacks of MCFCs integrated in complex systems in what can be interpreted as an overall multi-scale approach. However, it is difficult to encounter a single research group that integrated multiple length scale in a unique model as most groups focus only on a single level of scale.

The lowest level usually encountered in MCFC modeling is at the electrode scale. As in similar systems that involves the diffusion of gas in porous media, one of the main issues is the lack of accurate information and thus understanding of how the gas diffuses and how the electrolyte is distributed in porous structure [32].

Wilemski [33] developed one of the first electrode scale models specifically for MCFCs. He based his work on the assumption of a thin film cylindrical pore model previously introduced by Srinivasan and Hurwitz [34] for gas diffusion in porous electrodes. In this type of approach, the electrolyte fills the micropores of the electrode porous structure making them electrochemically inert. However, it only covers the walls of the gas-filled macropores with a thin film as shown in Figure 1.2. The electrochemical reactions occur on the walls of the pores covered with the thin electrolyte film. As explained by Wilemski, this approach was chosen since it is easy to manage, despite the overly simplified porous structure and the lack of values for the film thickness and coverage. Nonetheless, the model was able to successfully evaluate the current density of both the cathode and anode over a wide range of operating conditions. Based on this electrode model, Wolf and Wilemski [35] developed a 2D cell model that was successfully tested on a small cell.

Due to the oversimplification of the thin film model, a different approach was developed for the description of porous electrodes: the agglomerate model. In this approach the electrode structure is assumed as an agglomerate of catalyst particles that under working conditions are flooded with the electrolyte. Gas diffuses through the macropores to dissolve in the electrolyte. After a certain distance from the surface of the aggregate, the reactants react on the catalyst particle active sites. The agglomerate is usually assumed to be cylindrical in shape, and may be coated with a thin electrolyte film that if present is assumed to have

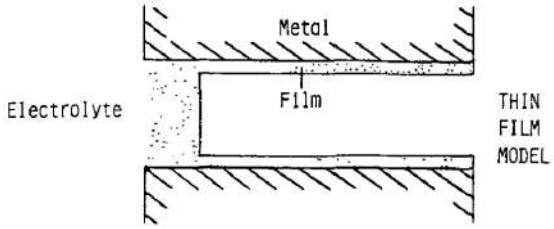

Figure 1.2: Schematic representation of a pore covered with an electrolyte thin film [1].

a constant thickness. Figure 1.3 shows a schematic representation of an agglomerate model to describe an electrode, with the left agglomerate being dry, i.e. no electrolyte thin film coverage, and the right one being wet.

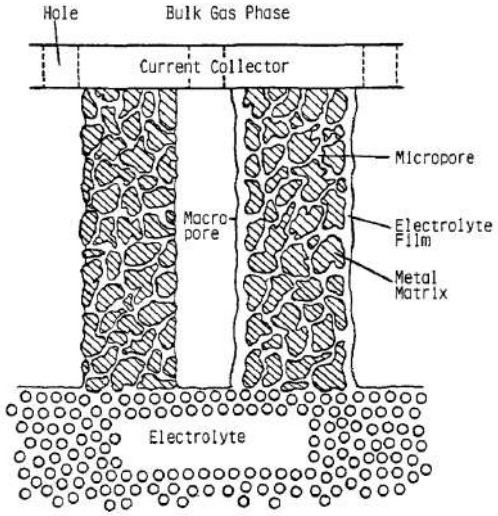

Figure 1.3: Schematic representation of a porous structured as agglomerate [1]. The right agglomerate is wetted with an electrolye film, while the left one is dry.

Yuh and Selman [36, 1] chose this approach to develop a model for the MCFC anode and cathode. Due to their different wetting characteristic, they considered a dry agglomerate for the anode and a wet agglomerate for the cathode. Coupling this structure with mass transport and electrode kinetics in the form of Butler-Volmer, they developed a cell model that showed good agreement with experimental data.

Based on the agglomerate approach, Kunz et al. [37] developed an electrode model for the cathode. They calculated the agglomerate diameter, porosity and tortuosity from a knowledge of the pore size distribution and electrolyte content. Following this initial work, they also developed a model to determine the cell overpotential as function of the electrolyte filling level of the cathode [38].

The main difference between the work of Yu and Selman and the work of Kunz et al. is that Yu and Selman [36] assumed the external agglomerate surface wetted with a thin electrolyte film and consequently with reactions happening both on the surface and inside the agglomerate, while Kunz et al. [37] assumed cathodic reactions only occurring inside the agglomerate with no film on the external surface.

Fontes et al. [39] argued with the validity of both models. Specifically, they demonstrate the importance of the film covering the agglomerate and criticized the assumption of a homogeneous agglomerate. In parallel Fontes et al. developed a spherical agglomerate model that appears physically more realis-

tic than the homogeneous one for the prediction of the effects of the electrolyte fill of the electrode on the electrochemical performance. A different three-phase homogeneous model of the MCFC cathode was developed by Subramanian et al. [40]. Using this model, they studied the contributions of different processes to the cell performance.

These last discussed electrode models have emphasized the importance of the electrolyte fill level on the cathode and have concluded that the electrolyte distribution plays an important role in the performance of the MCFCs. The electrolyte fill level is the percentage of the electrode pores occupied by the electrolyte. Further studies showed that the electrolyte may also redistribute due to the current flow and as a function of time. Hong and Selman [2] developed a stochastic model to describe the structure of the MCFC electrodes obtaining a representation closer to the reality than the ones assumed in the previous models. The schematic representation of the cross-section of a wet electrode is shown in Figure 1.4. Using this model, they studied the effects of the electrode filling and its distribution and concluded that the electrochemical reaction occurs close to the agglomerate surface.

Figure 1.4: Two-dimensional wet cathode structure obtained via stochastic approach. (■) electrocatalyst particle, (■) electrolyte, (□) pore [2].

Models at the electrode level are fundamental to support the understanding of the physico-chemical processes and basic electrode mechanisms. Researchers relied on these models for the study of electrode materials, structure and physical characteristic. However, they are not usually applied for the description of the cell mechanisms for higher simulation scale level.

The aim of cell level modeling is to provide the relationship between measured cell voltage and applied current density in small cells by considering all of the losses involved in the electrochemical processes that cause deviations from the Nernstian voltage. At this level ionic resistance, concentration polarization and gas mass transport are introduced, while the electrode related phenomena are usually simplified to reduce the model complexity. In addition, temperature acquires a fundamental role, and both temperature and current density profile along the cell plane are investigated. As such, cell level scale modeling functions as bridge between electrode processes and stack design.

Sampath et al. [41] developed one of the first 2D models for MCFC single cell working in cross-flow configuration and having an active surface area of $100\,cm^2$. The model was constructed based on the polarization resistances obtained with experiments on a button cell having an active surface area of $3\,cm^2$. They also demonstrated the importance of considering the effects of the WGS reaction, that, if neglected, greatly affects the results of the model.

A large contribution to cell level modeling was made by the work of different Japanese research groups

between 1990 and 2010, when Japan was one of the leading countries in MCFC development. Mugikura et al. [42] developed a 2D model that used semi-empirical correlations to express the polarization resistances of the cell. They defined the total cell polarization resistance (R_{TOT}) as sum of three contributions (internal R_{Ω}, anode R_{An}, and cathode R_{Cat}):

$$R_{TOT} = R_{\Omega} + R_{An} + R_{Cat} \tag{Eq. 1.1}$$

The internal resistance, R_{Ω} was defined with an Arrenhius temperature dependence with Arr and ΔE_{Ω} being empirical parameters:

$$R_{\Omega} = Arr\, e^{-\frac{\Delta E_{\Omega}}{RT}} \tag{Eq. 1.2}$$

For the electrode resistance, they distinguished between a first term dependent on the temperature that includes the activation energy required for the reactions to occur, and a second term that shows the concentration dependence (as local reactant partial pressure, p_i) of the reacts. ΔE_{An}, ΔE_{Cat}, R^0_{An}, R^0_{Cat}, A, B, C, D and E are empirical parameters.

$$R_{An} = e^{-\frac{\Delta E_{An}}{RT}} \ln\left(R^0_{An}\, p^A_{H_2,An}\, p^C_{CO_2,An}\, p^C_{H_2O,An}\right) \tag{Eq. 1.3}$$

$$R_{Cat} = e^{-\frac{\Delta E_{Cat}}{RT}} \ln\left(R^0_{Cat}\, p^D_{O_2,Cat}\, p^E_{CO_2,Cat}\right) \tag{Eq. 1.4}$$

The parameter values were fitted using data from an experimental campaign [43] opportunely designed to study MCFC behavior and the model was positively tested. In subsequent works, the model was improved with studies focus on both cathode [44] and anode [45], and then also for the use of a different electrolyte melt [46]. In this period, the work of Nishina et al. [47] was one of the few in which water effects at the cathode side were considered and a model to take these into account was introduced.

Other authors developed polarization resistances with similar structure based on either empirical observation or deriving them from more general electrochemical equations such as the Butler-Volmer equation. This group of equations represents the core of the kinetics modeling at the cell level.

In parallel with the construction of more complete 2D model, cell scale modeling saw also the development of 0D models. These models are usually simpler in structure, because they require the introduction of far less parameters, but yet useful for performance prediction of specific cells. An example is a model recently developed by Milewski et al. [48]. It is based on only three parameters: internal resistance, pre-exponential factor and activation energy for ionic conductivity expressed with an Arrhenius type function. Another example is a model developed by Au et al. [49] that requires the evaluation of only two parameters to identify the cell total polarization resistance.

Moreover, cell level modeling allows the study and description of dynamic modeling, of which the work of Brouwer et al. [50] is an example. Also, Heidebrecht et al. [51] realized a dynamic model to include the simulation of internal reforming of CH_4.

With the increasing length scale, stack level models are encountered. Their main objective is to offer a clear description of the fluid dynamics in the cell in order to simulate different flow configurations and study the distribution alongside the cell stack of the profiles of temperature, current and reactant composition. Consequently, stack models mainly focus on momentum, mass and energy balances, while simplifying the analysis of the electrochemical performances. Due to the large amount of equations involved, these models usually require the use of dedicated CFD software.

He and Chen [52] developed a stack model to study the 3-dimensional distribution of temperature, pressure, gas concentration and current across the stack in different flow configurations using the software package PHOENICS. Subsequently, they updated it to consider also transient operations [53]. Yoshiba et al. [54] developed a model to diagnose the internal conditions of a co-flow MCFC stack. In the work,

they focused on the voltage profile along the stack and its effects on the energy balances. In particular, the different values of internal resistance along the stack and the unequal gas supply were analyzed to understand the effects on the voltage. Lee et al. [55] developed a 3D MCFC stack model composed of 150 cells to study temperature, current and gas concentration distribution both on each cell surface and along the z-direction perpendicular to each cell. Recently, a dynamic model for a 1 kW MCFC stack was developed by Szczęśniak et al. [56].

In parallel to models exclusively based on physical laws, stochastic models can also be found. The electrolyte fill level is the percentage of the electrode pores occupied by the electrolyte. For example, Yang et al. [57] and Shen et al. [58] developed two different fuzzy models to facilitate valid control strategy design and analysis of system stability, and Shen et al. [59] also developed a Radial Basis Function neural network model to describe a stack operations.

Compared to the previous modeling scales, at plant level the object of interest is not the fuel cell itself, but the results of its interactions with all the other elements that compose the system under study. Plant models are based on global energy and mass balances whose aim is to provide information on the total energy produced and required by the system, and the amount products generated. In the case of MCFCs used as carbon capture devices, the focus will be specifically on the CO_2 capture rates achieved. For this reason, if the scope of the model is to provide only information on the overall system, local information is not important to the users. Consequently, to model the MCFC usually simple lumped 0D model are used. This simplification is not only for MCFCs but for all the unit operations included.

Most of these models are usually realized using the commercial software to describe the whole plant. The most commonly used in the Chemical Engineering sector is Aspen Plus.

Example of computational works at plant level include MCFCs implementation in natural gas combined cycles [60, 61, 62], cogeneration plants [63, 64], coal-fired plants [65, 66, 67], integrated gasification combined cycles [68, 69, 70], thermal in-situ oil sand facilities [71], cement production [72], steel production [73], wastewater biogas process [74], in novel pressurized MCFC hybrid systems [75], in combination with gas separation membranes [76], and in hybrid MCFC-SOFC systems [77].

1.3.1. UNIGE's modeling effort

The Process Engineering Research Team (PERT) of the Department of Civil, Chemical and Environmental Engineering of the University of Genoa to which I am affiliated has been developing MCFCs models for the past two decades. The result of PERT's studies is the development of a program for the simulation of the performance of fuel cells named SIMFC (SIMulation of Fuel Cells). Initially developed solely for MCFCs, recently it has been improved to offer the possibility to simulate also Solid Oxide Fuel Cells (SOFCs) [78, 5, 79].

SIMFC is a Fortran written code based on local mass, energy and momentum balances. However, the momentum balance included is simplified with the use of parameters to describe the fluid dynamics characteristics that have been previously determined using CFD software. The basic structure is of a cell-scale level modeling. However, it can also be applied for stack-level simulations also offering the possibility to adjust different parameters and other variables for each cell of the simulated stack. As such it can be considered either a 2D or a pseudo 3D deterministic model. The basic 2D structure can be used to gain not only overall cell information such as the cell voltage or the total current density, but also to evaluate local variables on the cell plane such as current density, gas concentrations or polarization resistances.

It also allows the simulation of cells working with different gas flow configurations, namely, cross-flow (the base case), co-flow and counter-flow. Moreover, SIMFC can be easily implemented in complex

system simulators such as Aspen Plus or other commercial process modeling software.

The balance equations used for the model are presented in Table 1.1 for a cross-flow configuration.

Mass balances	Anodic gas	$\frac{\partial n_x}{\partial x} = r_i$
	Cathodic gas	$\frac{\partial n_y}{\partial y} = r_i$
	Cross over	$q_{cross-over} = \xi \left\lvert p_{An} - p_{Cat} \right\rvert$
Energy balances	Anodic gas	
	$\sum_i n_i Cp_i \frac{\partial T_{An}}{\partial x} = \sum_i \frac{\partial n_i}{\partial x} \int_{T_{An}}^{T_s} Cp_i dT_{An} + A_{An} h_{An} \left(T_s - T_{An}\right) + Q_{cross-over}$	
	if $p_{An} < p_{Cat}$	$Q_{cross-over} = -\sum_j r_i \Delta H_j \frac{\partial T_{An}}{\partial x}$
	if $p_{An} > p_{Cat}$	$Q_{cross-over} = 0$
	Cathodic gas	
	$\sum_i n_i Cp_i \frac{\partial T_{Cat}}{\partial y} = \sum_i \frac{\partial n_i}{\partial y} \int_{T_{Cat}}^{T_s} Cp_i dT_{Cat} + A_{Cat} h_{Cat} \left(T_s - T_{Cat}\right) + Q_{cross-over}$	
	if $p_{An} > p_{Cat}$	$Q_{cross-over} = -\sum_j r_i \Delta H_j \frac{\partial T_{Cat}}{\partial y}$
	if $p_{An} < p_{Cat}$	$Q_{cross-over} = 0$
	Solid	
	$A_{An} h_{An} \left(T_s - T_{An}\right) + A_{Cat} h_{Cat} \left(T_s - T_{Cat}\right) = Q_{cond} - Q_{reac}$	
	$Q_{cond} = \sum_n \left(s_n \lambda_n\right) \left(\frac{\partial^2 T_s}{\partial x^2} + \frac{\partial^2 T_s}{\partial y^2}\right)$	
	$Q_{reac} = \sum_j r_j \Delta H_j - VJ$	
Momentum balances	Simplified fluid-dynamics	
	Anodic gas	$\frac{\partial p_{An}}{\partial x} = Z_{An} \frac{\mu_{An} v_{An}}{l^2}$
	Cathodic gas	$\frac{\partial p_{Cat}}{\partial y} = Z_{Cat} \frac{\mu_{Cat} v_{Cat}}{l^2}$
	Detailed fluid-dynamics	
	Anodic gas longitudinal flow	$\vartheta_{An,L} = M_L Re_{An,L}^{\gamma_L} - \frac{w^i}{w_{max}} N_{An,L} Re_{An,L}^{\sigma_{An,L}}$
	Anodic gas transversal flow	$\vartheta_{An,T} = M_T Re_{An,T}^{\gamma_T} - \frac{w^i}{w_{max}} N_{An,T} Re_{An,T}^{\sigma_{An,T}}$
	Cathodic gas longitudinal flow	$\vartheta_{Cat,L} = M_L Re_{Cat,L}^{\gamma_L} - \frac{w^i}{w_{max}} N_{Cat,L} Re_{Cat,L}^{\sigma_{Cat,L}}$
	Cathodic gas transversal flow	$\vartheta_{Cat,T} = M_T Re_{Cat,T}^{\gamma_L} - \frac{w^i}{w_{max}} N_{Cat,T} Re_{Cat,T}^{\sigma_{Cat,T}}$

Table 1.1: Mass, energy and momentum balance equations used in the SIMFC code for a cross-flow configuration.

The cell performance is expressed as:

$$V = E - R_{TOT} J \qquad \text{(Eq. 1.5)}$$

where V is the cell measured voltage $[V]$, E is the equilibrium potential given by the Nernst equation (Eq. 1.6) $[V]$, R_{TOT} is the cell total area specific polarization resistance $[\Omega\, cm^2]$, and J is the cell current density $[A\, cm^{-2}]$.

$$E = E^0 - \frac{RT}{z_e F} \ln\left(\frac{\prod |ox|_i^{\nu_{ox}}}{\prod |red|_i^{\nu_{red}}}\right) \qquad \text{(Eq. 1.6)}$$

The core of SIMFC is the kinetic equation of the total polarization resistances used to express the electrochemical performance of the simulated cell. Over the years, thanks to collaborations with other entities (both with a private company, Ansaldo Fuel Cell, and public institutions such as the University of Perugia, Enea, and the Korean Institute of Science and Technology) the PERT group obtained a large volume of experimental data. This allowed improving the equations for these resistances and expanded the model applicability range.

Prior to this Ph.D. work, the most updated kinetic core equations taking into account the effects of H_2O, as presented in [3], were the following:

$$R_{TOT} = R_{\Omega} + R_{Cat,CO_2} + R_{Cat,O_2} + R_{An,H_2} \tag{Eq. 1.7}$$

with:

$$R_{\Omega} = P_1 e^{\frac{P_2}{T}} \tag{Eq. 1.8}$$

$$R_{Cat,CO_2} = \frac{P_3 T e^{\frac{P_4}{T}}}{p \ln\left[1 - \frac{1.5}{1+\vartheta}\left(x_{CO_2} + \vartheta x_{H_2O}\right)\right]^{-1}} \tag{Eq. 1.9}$$

$$R_{Cat,O_2} = P_5 T e^{\frac{P_6}{T}} p^{0-.25} x_{CO_2}^{0.5} x_{O_2}^{0.75} \tag{Eq. 1.10}$$

$$R_{An,H_2} = \frac{P_7 T e^{\frac{P_8}{T}}}{p \ln\left(1 + x_{H_2}\right)} \tag{Eq. 1.11}$$

where $P_i s$ are empirical parameters whose values are reported in table 1.2.

P_i	Value	Unit
P_1	0.016461	$\Omega\, cm^2$
P_2	3054	K
P_3	$3.2\,10^{-6}$	$\Omega\, cm^2\, K^{-1*}\, atm$
P_4	2743	K
P_5	$4.5\,10^{-9}$	$\Omega\, cm^2\, K^{-1*}\, atm^{0.5}$
P_6	10036	K
P_7	$3.4\,10^{-9}$	$\Omega\, cm^2\, K^{-1*}$
P_8	9362	K
ϑ	0.16	–

Table 1.2: Last set before this Ph.D. work of kinetic parameters to simulate the performance of MCFCs as reported in [3].

2
Modeling of MCFC systems for Carbon Capture applications

As mentioned in Chapter 1, in most of the models of MCFCs at plant scale level the local effects of variables such as temperature, current density and reactant concentrations are usually neglected to focus on plant global balances, energy efficiency, and carbon capture rate. Indeed, users of such models are generally more interested in a global vision rather than in the behavior of each single element composing the plant. Consequently, many of such models have been developed using a 0D approach to simulate the behavior of MCFC. This simplification is also justified by the need to have a satisfactory calculation speed that can be penalized by extremely detailed local models. In fact, speed requirements are crucial when modeling is used for control purposes and not just for the studies of the outputs.

Although this approach is usually satisfactory to determine and study the global values the users need to know, it hinders the possibility to identify working conditions that can cause harm to the MCFC stacks. For example, by neglecting local analysis, users are not able to identify local values of temperature that may be too high or too low for proper operations. If these values are not properly controlled, they might induce premature cell failure. As such, local analysis is needed not only to simulate working conditions more accurately, but also for control as several local variables cannot be easily measured.

Generally, models at the plant level are not coded from scratch but are constructed using already existing plant simulation programs of which Aspen Plus is the leading one for Chemical Engineering. These programs allow the combination of different unit operations to construct the desired plant design. Each unit operation has been extensively coded and tested and can be characterized in terms of either operating conditions or desired output to reach the required solution. These programs also include extensive libraries about compounds properties, physical law and model, etc.

However, due to their complexity, non-trivial scale up, and mostly a small market, fuel cell units are not present as already built elements in such programs. If the model is developed using Aspen Plus, there are three possible solutions:

1. use of simple blocks such as separators and mixers to deal with the mass balances. Thermal balances are usually neglected or are particularly simplified to determine the heat required or in excess by considering the enthalpy difference between inlets and outlets. The electrochemical performance is evaluated as external parameters and the model does not allow local studies as the structure is overly simplified.

2. integration of an external Fortran written subroutine. This solution may cause issues, in particular for the thermal balances, if physical parameters used for calculation in the code do not match the one of the Aspen properties (e.g., the specific heats, etc.). It lacks the possibility to deal with non-stationary simulation.

3. integration of an external user made program written using Aspen Custom Modeler. Aspen Custom Modeler is an Aspen Plus package that allows to share the components data directly with Aspen Plus libraries and contains already pre-programmed numerical resolution methods [80]. It also permits non-stationary simulations.

In this chapter, I will present the integration of a 2D MCFC model into a plant simulation designed using the software Aspen Plus specifically for CO_2 capture.

In the first part, I will present the integration in Aspen Plus of the SIMFC code following the second of the solutions introduced above. This solution is extremely interesting because it allows the use of an already meticulously developed and tested code. The results of this part have been published with the title "*Molten Carbonate Fuel Cells in Integrated Systems for the Exploitation of Poor Fuels and the Segregation of CO_2*" in the *Bulgarian Chemical Communications* [81]. The work has been performed in collaboration with the University of Edinburgh and ENEA from which I received the information for the calcium looping process.

In the second part, I will present the integration in Aspen Plus of a newly developed code in Aspen Custom Modeler. The results of this part have been published with the title "*A feasibility assessment of a retrofit Molten Carbonate Fuel Cell coal-fired plant for flue gas CO_2 segregation* " in the *International Journal of Hydrogen Energy* [82]. The work has been performed in collaboration with the University of Edinburgh.

2.1. Integration of the SIMFC code in Aspen Plus

The first analyzed system consists in the integration of an MCFC with calcium looping process for the segregation of CO_2 and the exploitation of poor fuels. This integration was done using the software Aspen Plus integrated with the SIMFC code to simulate the MCFC stack.

Calcium looping is a technology for carbon capture that is based on the reversibility of lime carbonation. The process, schematized in Figure 2.1, can be divided into two main steps: carbonation and calcination. The carbonation consists in an exothermic step where a CO_2-containing flue gas enters a carbonator reactor where the CO_2 reacts with CaO to form $CaCO_3$ (usually at an operating temperature between 870 and 970 K), following reaction [83].

$$CO_2 + CaO\,(s) \longrightarrow CaCO_3\,(s) \qquad \text{(R. 2.1)}$$

The CO_2-depleted flue gas ("Rich fuel" in Fig. 2.1) has acquired a higher heating value than the initial flue gas ("Poor fuel" in Fig. 2.1) due to lower dilution in CO_2 and can be more proficiently used for combustion scopes. The formed carbonates are sent to a calciner where, at temperatures higher than 1170 K, they dissociate to CO_2 and CaO. The CO_2 can be captured, while the solid can be recycled to the carbonator reactor. This step is endothermic and the required heat is usually provided with combustion of fuel with pure O_2 to obtain a highly concentrated stream of CO_2 [83]. This represents one of the main disadvantages of this process due to the high cost of pure O_2 [84]. A possible solution foresees the use of air, but a subsequent separation of N_2 and CO_2 would be required for an effective for carbon sequestration. This separation can be performed exploiting MCFCs.

2.1.1. Case study

The studied system was based on the ZECOMIX high efficiency hydrogen power plant currently operating at the ENEA research center Cassaccia (Italy) [85], where the carbon looping is integrated downstream of a gasifier for the decarbonization of raw syngas.

After sulfur removal[1], a CO_2 rich fuel gas that cannot be directly used in MCFC due to low H_2

[1] This aspect has been neglected in this analysis.

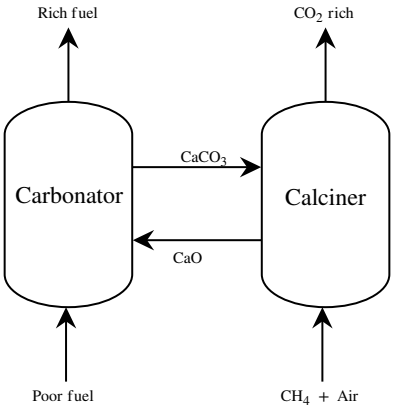

Figure 2.1: Calcium looping process scheme.

concentration is sent to the calcium looping system. In the carbonator reactor the fuel is depleted of CO_2 according to Rxn. 2.1 increasing its H_2 concentration and thus acquiring the possibility to be used as MCFC anode inlet. The obtained $CaCO_3$ is moved to the calciner where the thermal regeneration of the solid sorbent (CaO) occurs. Combustion of CH_4 in air is used to provide the adequate heat to sustain the regeneration process.

The integration of the MCFC downstream allows for CH_4 combustion in the presence of air instead of pure O_2, reducing the energy and cost penalty associated with producing pure O_2 in an air separation unit. The regenerated CaO is recycled back to the carbonator while the CO_2 rich gas is used as the cathode inlet to an MCFC stack, allowing for further CO_2 concentration and the generation of additional electrical power. The utilization of the decarbonized syngas for electricity generation in an MCFC is preferable due to the higher electrical efficiencies observed in MCFCs compared to commonly utilized gas turbines. At the end of the process the enriched CO_2 should undergo a further separation to remove steam or other impurities. Three different possibilities have been investigated: simple condensation, combustion and condensation to remove possible unreacted O_2, and membranes [86, 87]. A scheme of the proposed solution with the integration of the burner and condensation separation process as used in the simulation in Aspen Plus is presented in Figure 2.2.

2.1.2. System modeling

To simulate the process, the following assumptions have been made:

1. The carbonator operates at 973 K. The carbonation reaction is at the thermodynamic equilibrium, while the conversion of CH_4 is fixed at 80%. CH_4 and CaO feed flow rates are optimized as a function of the operating conditions.

2. In the calciner the regeneration occurs at 1173 K. The reaction is at the thermodynamic equilibrium, while the conversion of CH_4 is total. The amount of the "CH_4+O_2" stream has been calculated in order to ensure an adiabatic reaction.

3. The solid phases after the carbonator and the regenerator are completely separated from the gas phases in downstream cyclones.

4. A reformer is placed before the cell to convert all the CH_4 to H_2 for the anode inlet. Prior to this

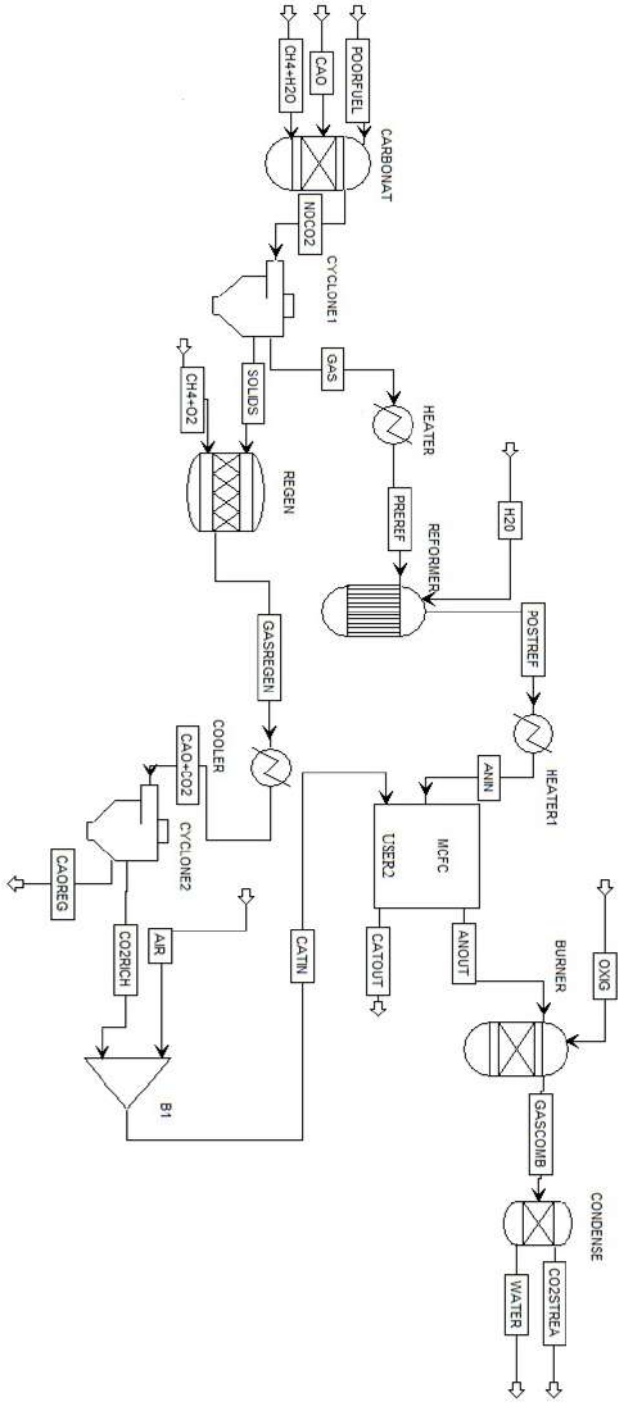

Figure 2.2: Aspen plus schematic representation of the calcium looping and MCFC integration.

reaction the stream is preheated up to 1123 K. Also, steam is added to increase the content up to 10 mol% since it is necessary to avoid carbon deposition.

5. The cathode inlet stream is mixed with air to ensure an amount of O_2 equal to 20% in v/v% and the thermal management of the cell

6. To simulate the cell performance the kinetic core described by equations 1.7-2.5 and the kinetic parameters reported in table 1.2 were used.

7. In the cell the fuel utilization factor (at the anode) is assumed to be 70%, while the CO_2 utilization factor (at the cathode) is assumed to be 90%.

8. The cells of the stack are considered to have an area of 1 m^2 each working with a current density of 1000 $A\,m^{-2}$.

9. The performance of the cell is calculated on the basis of the local SIMFC model described in the previous chapter.

10. To guarantee the presence of only CO_2 and H_2O in the gas outlet, at the anode outlet excess H_2 undergoes total combustion in a burner. H_2O is subsequently removed by condensation. The O_2 flow rate is optimized as a function of the operating conditions.

11. For the case with a membrane separation, it is assumed that the CO_2 removal efficiency is of 90% and that it produces a 95% pure CO_2 stream [88].

For this analysis, three different feeds have been studied to consider three different possible applications: blast furnace exhaust, gasified waste and syngas. Each composition is presented in Table 2.1.

Type of Fuel	H_2	CO	CO_2	H_2O	N_2	H_2S	HCN	NH_3
Blast furnace exhaust	0.048	0.228	0.190	0.062	0.472	$1.97\,10^{-5}$	$1.66\,10^{-4}$	$1.32\,10^{-5}$
Gasified waste	0.292	0.425	0.161	0.068	0.054	$3.6\,10^{-3}$	$9.95\,10^{-5}$	$2.5\,10^{-3}$
Syngas	0.282	0.350	0.139	0.198	0.031	$6.8\,10^{-3}$	–	$1.5\,10^{-3}$

Table 2.1: Molar fractions of the three kinds of fuel gas used for the simulation.

2.1.3. Simulation results

Since the interests of this study are the capture of CO_2 and the simultaneous exploitation of poor fuels, the main results presented will focus on the flow rate and the molar fraction of CO_2 released and captured during the process as well as the energy efficiency.

In Table 2.2, 2.3 and 2.4 the results of different simulations are presented. Table 2.2 shows the results of the calcium looping process without MCFCs to allow the comparison with the integration of the MCFC. Although this system ideally allows achieving a pure stream of captured CO_2, the emissions to the atmosphere still contain about 5% v/v of CO_2.

Table 2.3 shows the results considering the final enriched CO_2 stream after the calcium looping process, the fuel cell operation (anode outlet) and one of the further separation processes considered. In all the analyzed cases, the use of the condensation only is not sufficient to obtain a stream of CO_2 suitable for sequestration or other possible uses since it is still rich in other compounds (mainly N_2 and unreacted

Type of Fuel	Downstream Separation	CO_2 Molar Fraction	Flowrate CO_2 Flowrate in fuel	Flowrate MCFC Power Output $[kmol\ MW\ h^{-1}]$
Blast furnace	CO_2 released	0.060	0.288	6.635
	CO_2 captured	1.000	1.208	27.830
Gasified waste	CO_2 released	0.034	0.183	1.680
	CO_2 captured	1.000	0.979	8.980
Syngas	CO_2 released	0.050	0.344	2.628
	CO_2 captured	1.000	1.785	13.618

Table 2.2: Main results concerning the CO_2 captured and released in atmosphere for the simulation of the calcium looping process only.

H_2). The addition of a burner will favor the process, but the best solution is to add a further separation step that uses membranes. This not only produces a stream extremely rich in CO_2 (more than 90% v/v), but also reduces the final flow rate.

Type of Fuel	Downstream Separation	CO_2 Molar Fraction	Flowrate CO_2 Flowrate in fuel	Flowrate MCFC Power Output $[kmol\ MW\ h^{-1}]$
Blast furnace exhaust	With Condensation Only	0.351	1.767	24.421
	Burner + Condensation	0.444	1.985	27.446
	CO_2 Selective Membrane	0.950	1.590	21.979
Gasified waste	With Condensation Only	0.647	3.166	24.872
	Burner + Condensation	0.909	3.554	27.916
	CO_2 Selective Membrane	0.950	2.850	22.385
Syngas	With Condensation Only	0.687	3.510	28.048
	Burner + Condensation	0.941	3.886	31.052
	CO_2 Selective Membrane	0.950	3.159	25.243

Table 2.3: Simulation results for the three studied types of fuel gas.

Table 2.4 refers to the sum of all CO_2 present in all the streams that are released into the atmosphere for the overall process. In this case, the column "CO_2 Molar Fraction" indicates the molar fraction of CO_2 if all the emissions were grouped in one stream. As expected, for all three fuel gas cases, the lowest value of CO_2 emission is obtained when a membrane separation is used. It appears that there is no actual difference between the use of only condensation and burner coupled with condensation.

Finally Table 2.5 presents the global efficiency of the integrated solutions in terms of electrical energy and CO_2 capture for the three type of analyzed fuels. For all the gases, the efficiencies are similar and the segregation values reached are significantly high. The electrycal efficiency was calculated as in eq. 2.1, with LHV_{fuel} being the low heating value of the fuel $[W]$ and P_{cell} being the cell power $[W]$.

$$\eta = \frac{P_{cell}}{LHV_{Fuel}} \cdot 100 \qquad \text{(Eq. 2.1)}$$

These results show that, compared to the calcium looping only solution, the MCFC integrated solution allows for a greener solution with a much lower molar fraction of CO_2 emitted into the atmosphere (10^{-2} for calcium looping only and 10^{-3} for integrated system). In turn this can allow for larger savings on CO_2 emissions tax. On the basis of this analysis it is possible to say that the burner coupled with a condensation step and the membrane separation are the best scenario; the difference between the two would require a further economic analysis which is beyond the scope of this work.

Type of Fuel	Downstream Separation	CO_2 Molar Fraction	Flowrate CO_2 Flowrate in fuel	Flowrate MCFC Power Output $[kmol\ MW\ h^{-1}]$
Blast furnace exhaust	With Condensation Only	0.005	0.202	2.791
	Burner + Condensation	0.005	0.202	2.791
	CO_2 Selective Membrane	0.0009	0.379	5.233
Gasified waste	With Condensation Only	0.005	0.36	2.826
	Burner + Condensation	0.005	0.36	2.826
	CO_2 Selective Membrane	0.0011	0.676	5.313
Syngas	With Condensation Only	0.005	0.355	2.834
	Burner + Condensation	0.005	0.355	2.834
	CO_2 Selective Membrane	0.001	0.706	5.639

Table 2.4: Simulation results for the three studied types of gas concerning the captured CO_2.

Type of Fuel	Electrical energy efficiency	CO_2 segregation efficiency
Blast furnace exhaust	0.287	0.933
Gasified waste	0.286	0.922
Syngas	0.285	0.922

Table 2.5: Electrical energy and CO_2 segregation global efficiency of the integrated solution.

2.2. Integration of an Aspen Custom Modeler code in Aspen Plus

The second analyzed system consists in the retrofitting of MCFCs to a mid-size textile plant for the capture of the produced CO_2. The study was done using the software Aspen Plus with the code describing MCFC behavior developed in Aspen Custom Modeler.

The model within this study employs a 2D solver to simulate the MCFC performance. The cell was considered having a cross-flow configuration with anode and cathode coordinates discretized to allow simulation of local cell performance. Each unit was treated as an individual sub-unit with no diffusional mass transfer between sub-units. The development of the mass and energy balances was based on the following general assumptions: (i) adiabatic operation, (ii) feed temperature and velocity profiles fully developed, (iii) cell working in stationary state, (iv) pressure drop and gas cross-over neglected, (v) no reforming or parasitic reactions within the cell, (vi) WGS at equilibrium. Compared to the previous case, this study was conducted after the discovery of a mechanism that characterizes MCFCs working with wet cathode feeding that will be presented in the following chapters. The discovery of this mechanism proved that the kinetic core that considers water fed at the cathode side introduce in the previous chapter is not correct. As such, to avoid using an incorrect model, in this study case a previous model that does not consider the effect of water at the cathode side [4] was used. The polarization resistances are the following, with the kinetic parameters presented in table 2.6

$$R_{\Omega} = P_1 e^{\frac{P_2}{T}} \tag{Eq. 2.2}$$

$$R_{Cat,CO_2} = \frac{P_3\, T\, e^{\frac{P_4}{T}}}{p\, ln\left(1 - 1.5 y_{CO_2}\right)^{-} 1} \tag{Eq. 2.3}$$

$$R_{Cat,O_2} = \frac{P_5\, T\, e^{\frac{P_6}{T}}\, p^{0.5}\, y_{CO_2}\, y_{O_2}^{-0.5}}{p\, ln\left(1 - 3y_{O_2}\right)^{-}\, 1} \qquad \text{(Eq. 2.4)}$$

$$R_{An,H_2} = \frac{P_7 T e^{\frac{P_8}{T}}}{p \ln\left(1 + x_{H_2}\right)} \qquad \text{(Eq. 2.5)}$$

P_i	Value	Unit
P_1	0.01382	$\Omega\, cm^2$
P_2	3054	K
P_3	$2.25\,10^{-6}$	$\Omega\, cm^2\, K^{-1*}\, atm$
P_4	2743	K
P_5	$5.4\,10^{-8}$	$\Omega\, cm^2\, K^{-1*}\, atm^{0.5}$
P_6	10036	K
P_7	$3.4\,10^{-9}$	$\Omega\, cm^2\, K^{-1*}$
P_8	9362	K

Table 2.6: Kinetic parameters to simulate the performance of MCFCs as reported in [4].

2.2.1. Case study

A simplified schematic of the plant layout is illustrated in Figure 2.3. Within the schematic, the section below the dotted line details the original plant layout with the units above being the required retrofitted units for CO_2 capture. In the process scheme the bold lines signify the streams containing the main CO_2 flow.

At the bottom left of the scheme the coal enters the coal burner unit simulated in accordance with Aspen specification [89]. Then, the flue gas produced is utilized to preheat the burner air stream and to generate steam for use in the steam turbine energy generation unit producing 6.8 MW of electrical power. Once the required heat transfer is achieved in the vapor generator black box, the flue gas stream is ready for the CO_2 capture section.

Prior to entry to the MCFC stack, the flue gas stream must undergo a pre-treatment process. Different works have shown that many pollutants, especially sulfur compounds, can greatly harm MCFCs [90, 91]. The units implemented within this design were assumed being selective catalytic reduction and wet limestone scrubbing for flue gas pre-treatment for Nitrogen Oxides (NO_X) [92] and Sulfur Dioxide (SO_2) respectively [93, 94]. A detailed assessment of differing removal methods was not considered within this project scope and so the selection of these unit methods was a result of industrial prevalence and applicability to the process system. To provide a simplified simulation of MCFC feasibility it has been assumed that both the NO_X and SO_2 removal systems are 100% efficient, with scope for future works to deal with the effects of these contaminants on cell performance.

The flue gas stream is then sent as the cathode inlet stream (Catin) of the MCFC stack. The fuel cell anode inlet stream (Anin) was provided by a steam methane reformer (SMR) unit operating at a steam:CH_4 ratio of 3.28 : 1. The reformer unit was designed based on a fuel cell 75% H_2 utilization factor, with the reformer inlet flow rates iterated to provide the required H_2 flow rate in the Anin stream. The final separation of the concentrated CO_2 stream in the anode outlet (Anout) is performed by a dual stage condenser and cryogenic separation process. This unit selection was again based on industrial

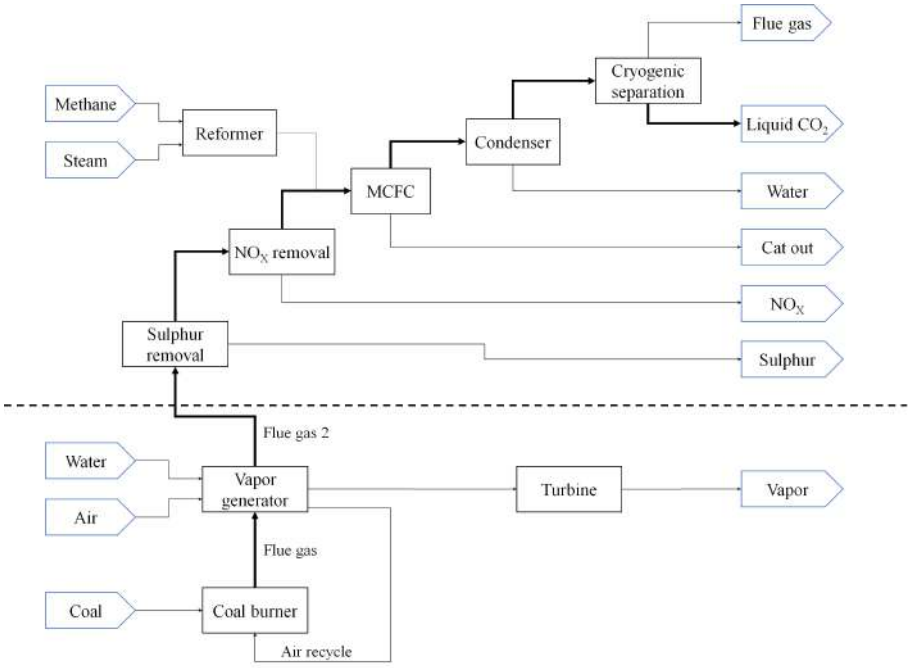

Figure 2.3: Schematic of the plant layout.

	Anode	Cathode
Flowrate [$kmol\ h^{-1}$]	469.7	2318.2
CH_4 [% mol/mol]	0.03	0
CO [% mol/mol]	9.88	0
CO_2 [% mol/mol]	6.06	9.1
H_2 [% mol/mol]	53.87	0
H_2O [% mol/mol]	30.16	4.44
N_2 [% mol/mol]	0	78.77
O_2 [% mol/mol]	0	7.69
Temperature [K]	923	923

Table 2.7: Cell inlet conditions.

prevalence and suitability for the design conditions with the potential for study using other operations in the future [95]. The cryogenic sizing and energy requirement were developed considering literature data to allow a 90% CO_2 capture capability [96, 97].

From plant process data the MCFC operating conditions examined within this feasibility study are depicted in Table 2.7.

The operating pressure was set at one atmosphere for all simulation tests as is often implemented in practice [64]. Although yield improvements can be observed at higher pressure this low operating pressure reduces the influence of unwanted side reactions such as the Boudouard reaction, allowing improvement of cell lifetime [98].

2.2.2. System modeling

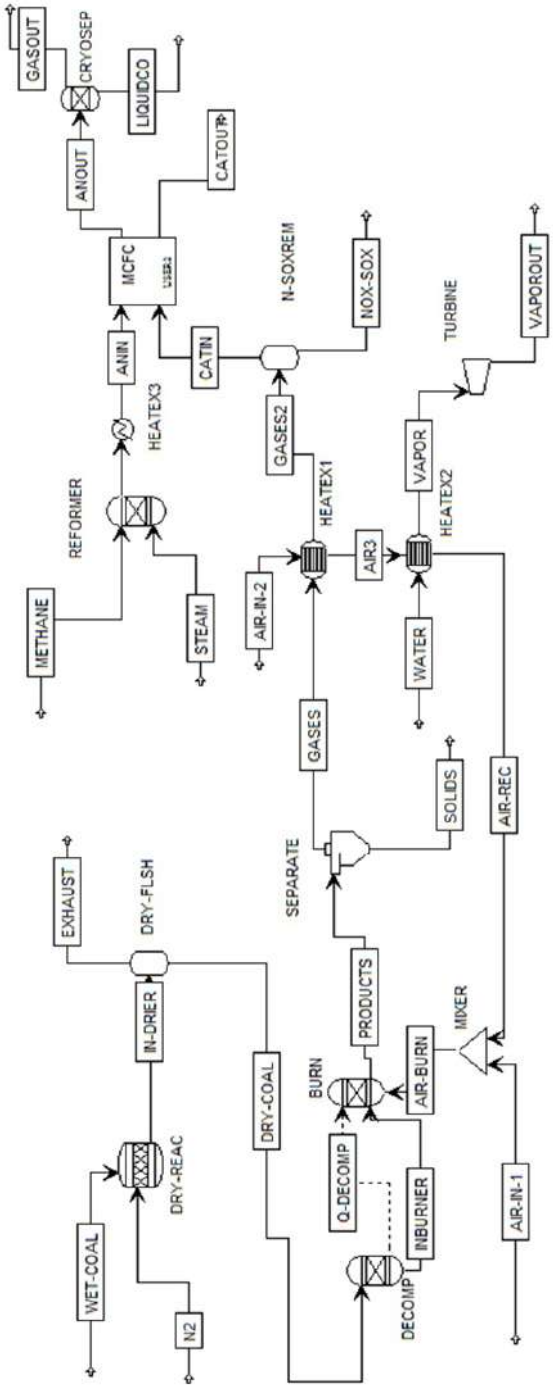

Figure 2.4: Aspen plus schematic representation of the retrofitting of MCFCs to a mid-size textile plant for the capture of the produced CO_2.

The system was simulated in Aspen plus using the scheme reported in Figure 2.4. The modeling process to simulate the existing plant environment employed data from a reference textile production plant as a basis. The data on the coal composition (Table 2.8) allowed simulation of the coal burner unit and necessary balance of plant in Aspen Plus. The coal was modeled as a non-conventional solid within the burner unit which was simulated as a two stage drying and decomposition process as suggested by the Aspen Plus guide. After treatment of impurities, the flue gas stream was preheated to the MCFC operating temperature of 923 K before entering the cathode inlet. The anode inlet stream was fed by a steam methane reformer with feed flow rates to the reformer unit iterated to provide a 75% hydrogen utilization factor within the MCFC. On user model integration, the effect of the MCFC unit could be directly assessed within the plant environment.

	Coal Flow
Flowrate [$kg\ h^{-1}$]	3591
C [% kg/kg]	70.6
Cl [% kg/kg]	0.02
H_2 [% kg/kg]	4.85
H_2O [% kg/kg]	8.29
N_2 [% kg/kg]	1.6
O_2 [% kg/kg]	8.5
S [% kg/kg]	0.58

Table 2.8: Coal flow and composition data.

There have been several literature studies of MCFC combined cycles considering integration as a topping cycle of a pre-existing steam turbine unit [99]. However, for this study one imposed constraint was the requirement for the MCFC unit and necessary balance of plant to be a stand-alone retrofit design with no direct integration of thermal or process streams. This requirement was specified to minimize the impact on the previously existing process streams. As a result, only heat integration within retrofit units is considered in this assessment.

2.2.3. Simulation results

The main global results of the simulation are presented in Table 2.9. The dual ability of MCFCs to generate power and simultaneously concentrate CO_2 concentration is clear. The MCFC combined with a simple condenser unit acts to concentrate the CO_2 concentration from the 9% mol/mol of the cathode inlet to 67% mol/mol of the anode outlet. This significant concentration increase simplifies the final separation process while at the same time the electrochemical cell generates 7.0 MW of electrical energy, a value comparable to that produced by plant steam turbine unit (6.8 MW). The simplified capture process and additional power generation capacity allows reduction in specific energy requirement for carbon capture. An estimation of this specific energy requirement considering heat integration within the retrofitted unit will be performed.

To provide with a quantitative estimate of the CO_2 capture specific energy requirement for the proposed system, a preliminary heat exchange network was designed to maximize efficiency while adhering to the constraint of no heat integration between existing and retrofitted sections. This energy recovery network is illustrated in Figure 2.5. The process streams are matched based on their temperature and heat capacity rates to provide a network that requires minimal heating and cooling utilities. The energy recovery network was designed based on a pinch temperature of 1073 K, with a requirement for no heating

Parameter	Unit	Value
SMR outlet T	K	1073
Steam turbine power	MW	6.8
Number of cells	-	10188
Cell area	m^2	1
Average J	$A\,m^{-2}$	1000
Cell potential	V	0.69
Total stack power	MW	7.0
Flue gas CO_2 segregated	%	90
Total flowrate CO_2 segregated	$[kmol\,h^{-1}]$	190
Anode outlet T	K	965
Cathode outlet T	K	952
MCFC outlet CO_2 concentration	$\%\ mol/mol$	34
Condenser Outlet CO_2 concentration	$\%\ mol/mol$	67

Table 2.9: Simulation results.

utility used below the pinch and no cooling utility used above the pinch temperature. A 10% energy loss during heat transfer between streams was assumed as a basis for the feasibility assessment.

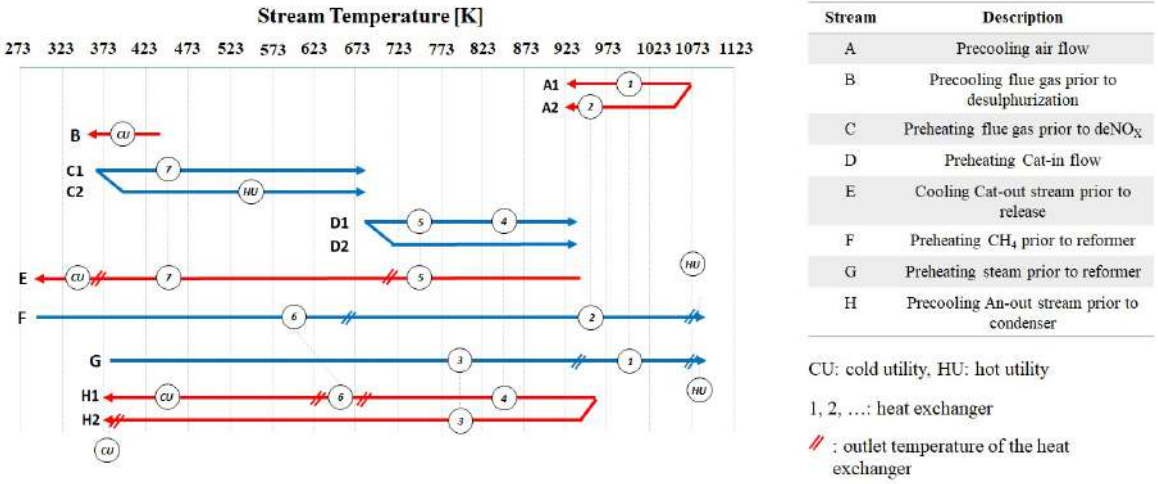

Figure 2.5: Heat exchange network.

Considering the implementation of the heat exchange network this equates to an approximated specific energy requirement prior to final CO_2 separation of $-0.39\ MJ\ kg_{CO_2}^{-1}$. Assuming a literature value for cryogenic CO_2 specific energy requirement of $1.80\ MJ\ kg_{CO_2}^{-1}$ [97], a calculated specific energy requirement of$1.41\ MJ\ kg_{CO_2}^{-1}$ can be obtained. Comparing this value to conventional Monoethanolamine (MEA) CO_2 capture technology having a requirement of $2.5 - 4.2\ MJ\ kg_{CO_2}^{-1}$ [100] significant improvements can be observed. This provides a positive viewpoint of the potential for MCFC carbon capture looking to the future with even isolated retrofit units showing high energy efficiency compared to conventional technology. In the event heat integration of the whole plant was considered the existing heating and cooling utility could allow further energy efficiency improvements for this capture method.

2.3. General considerations

In both cases the MCFC was simulated using a 2D model. This allowed the user to gain information on the local distribution of variables such as reactant concentration on the cell plane and current density as presented in Figure 2.6. The figure shows the distribution on the surface of a cell of the MCFC stack of the local bulk concentration of CO_2 and applied current density for one of the cell of the stack in case 1 using as initial gas the blast furnace exhaust. Information on the inlet is presented in Table 2.10.

	Anode inlet	Cathode inlet
Temperature $[K]$	923	923
x_{CO}	0.170	0
x_{CO_2}	0.084	0.069
x_{H_2}	0.192	0
x_{H_2O}	0.102	0.041
x_{N_2}	0.452	0.735
x_{O_2}	0	0.155
Mole flow $[kmol\ h^{-1}]$	307	1182

Table 2.10: MCFC stack inlet concentration for the case 1 using the blast furnace gas as initial fuel.

The two case studies show that the integration of MCFC for the capture of CO_2 can be fruitful to decrease emissions and increase the energy output. The use of a 2D model to simulate the MCFC stack allows to gain more information on the local variable behavior on the cell. This knowledge is fundamental as such information is not easy to obtain experimentally and since fuel cells simulation is not as developed as other unit operation thus it cannot be easily simplified.

However, the process here presented lack a specific dependence on the cell performance on a secondary possible reactant that has been almost not considered in literature and for which a model is absent: water. The next five chapters will consider this reaction in great detail, especially at low CO_2 concentrations.

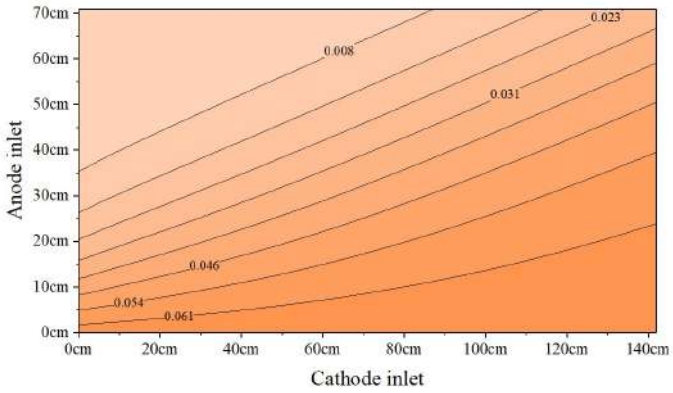

(A) Local CO_2 bulk concentration map.

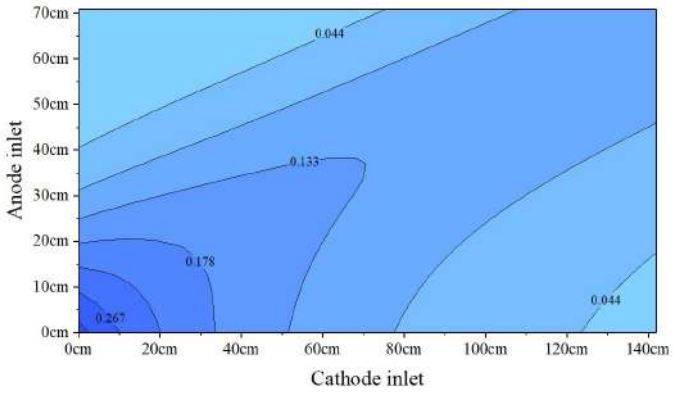

(B) Local J map.

Figure 2.6: Local map of CO_2 bulk concentration and J for a cell of the stack of case 1 fed using as initial gas the blast furnace gas.

3
The MCFC dual-anion model

New experimental evidence has shown that at particular working conditions of low CO_2 concentration and presence of H_2O in the cathode feed, MCFCs can operate exploiting a secondary path supported by hydroxide ions that sees the net cathode to anode migration of H_2O in addition to CO_2.

The understanding of the phenomena involved in this process is of particular importance: this secondary path affects MCFCs both in regard to their electrochemical performance and their carbon capture capability.

In this chapter, I will present an analysis of the available experimental data of cells working at these operating conditions to understand the process and establish a kinetic model that appropriately considers these new findings. The chapter will be structured as follow:

1. brief introduction of the issue of the presence of H_2O at the cathode inlet of an MCFC in correlation with experimental data;
2. introduction of the mechanisms considered to model MCFC performance at such working conditions;
3. development of the kinetic core of the model;
4. introduction of the base model form and presentation of the results of the simulation performed using it.

The results that will be presented have been published with the title "*New, Dual-Anion Mechanism for Molten Carbonate Fuel Cells Working as Carbon Capture Devices*" in the *Journal of Electrochemical Society* [101].

The experimental data presented in this chapter have been provided by EMRE and are presented in Appendix D in Table D.1.

3.1. The issue of wet cathode feed

The majority of literature studies on MCFC behavior considers cells working with dry cathode feeds. Only a few authors have analyzed the possible effects that H_2O addition at the cathode inlet may induce. They observed that the performance was higher with wet cathode feeds, compared to otherwise similar dry conditions [102, 47]. Like CO_2, H_2O can also act as an oxide ion acceptor [103, 104]. According to Nishina et al. [47], when the reaction between H_2O with O^{2-} is faster than the corresponding one involving CO_2 (a sub-step of the MCFC cathode reaction, Rxn. 1.7), OH^- ions can form in a layer adjacent the electrolyte surface. Successively, the equilibrium between species can enable the recovery of H_2O and formation of carbonate ions:

$$CO_2 + 2\,OH^- \longleftrightarrow CO_3^{2-} + H_2O \qquad \text{(R. 3.1)}$$

Following this argument, Nishina et al. [47] hypothesized that through these reactions (H_2O oxidation and recovery), the presence of H_2O can reduce the CO_2-induced polarization by decreasing its apparent

diffusion and enlarging the volume where the reactions can occur. However, according to Nishina's model, there was no net transfer of H_2O from the cathode to the anode.

Based on Nishina's work, in collaboration with the UNIPG, I took part in the development of a kinetic model to simulate MCFCs performance with water addition at the cathode side [3]. The experimental campaign for the model was conducted collecting data with low utilization of CO_2 (average 60%). Except for the higher voltage expected, no anomalies were observed for the experimental results, and consequently no particular attention was paid to the cathode and anode outlet compositions and flow rates. This work was completed prior to the engagement with ExxonMobil.

As mentioned in Chapter 1, recently EMRE has started studying the application of MCFCs as carbon capture devices. In this line of inquiry, EMRE tested the performance of MCFCs operating with cathode feeds at low CO_2 concentrations (2-6 % v/v), H_2O addition (roughly 10% v/v), high CO_2 utilization factors (>60%) and high current densities to simulate the desired capture conditions from gas-fired power plant flue gases.

For the experimental campaign [105], planar square single cells with active area of 250 cm^2 were used. Each cell had a NiO porous cathode lithiated *in situ*, a porous Ni-based anode, a porous $LiAlO_2$ matrix, and used an electrolyte mixture of Li_2CO_3 and Na_2CO_3. Both at the anode and at the cathode side, stainless steel structures doubled as flow fields and current collectors. The cells were compressed to 2.4 *bar* via pneumatic actuator in a stainless steel frame, providing active temperature control and gas connections. The cells were set up to work with a cross, co and counter-flow configurations. Unless specified, all the data and simulations presented hereon will refer to cross-flow configuration.

The main results of the campaign are presented in the graphs of Figure 3.1. The data presented in the graphs have been collected either at constant H_2O concentration (10% v/v) and varying CO_2 or at constant CO_2 (4% v/v) and varying H_2O. The cathode concentration of O_2 was kept fixed at 10% v/v, the one of N_2 was used to balance at 100%. The total cathode flow rate was adjusted to obtain the desired U_{CO_2} (utilization factor of CO_2) while keeping a current density of 90 $mA\ cm^{-2}$. The anode consisted of a H_2:CO_2:H_2O 72:18:10 mixture whose total flow rate was adjusted to keep the fuel utilization at 30% to limit the anode effects on the performance.

In accordance with the previous literature, EMRE observed that not only with increasing content of CO_2 (3.1A) but also with increasing concentration of H_2O (3.1B), the performance in terms of measured voltage and consequently output power increased. Moreover, they observed that it was possible for the cell to generate an electrical current that following Faraday's law of electrolysis (Eq. 3.1) would result in consumption of CO_2 higher than 100%, assuming that CO_3^{2-} is the only ion that can transfer ionic current through the electrolyte.

$$n_{el} = \frac{I\,t}{F\,z_e} \qquad \text{(Eq. 3.1)}$$

When the carbon capture efficiency was verified with detailed mass balances it was observed that the target value of carbon capture was underachieved (3.1C and 3.1D). For example, as shown in Figure 3.1C, when 90% was the target with an inlet CO_2 concentration of 4% only 70% capture was achieved. This result was confirmed through multiple tests. Also, it was observed that the inlet molar fractions of both CO_2 and H_2O have rather important influence on this variance: the higher the CO_2 the closer the resulting capture is similar to the target one (3.1C), while the higher the H_2O the further is the resulting capture (3.1D) from the target one.

Back diffusion of CO_2 from anode to cathode might explain this result since anode concentration is far larger than the cathode one. This could be accentuated by the presence of physical cracks in the matrix or poor sealing. However, tests on gas crossover ruled out this explanation. The absence of a physical leak was supported also by the coherent utilization of O_2 and H_2. Since Nishina suggested the presence of OH^- ions in the melt in the tested operating conditions, EMRE tested the possibility of having

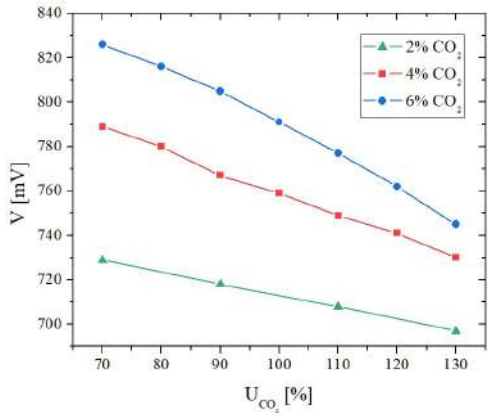

(A) Cell V as function of the target U_{CO_2} for different inlet CO_2 concentration.

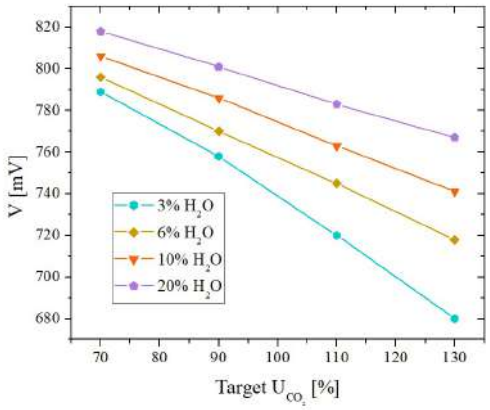

(B) Cell V as function of the target U_{CO_2} for different inlet H_2O concentration.

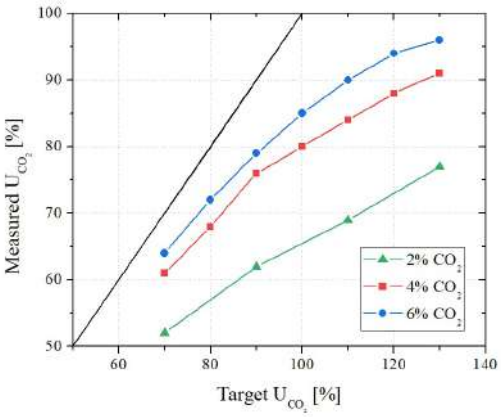

(C) Target vs. Measured U_{CO_2} for different inlet CO_2 concentration.

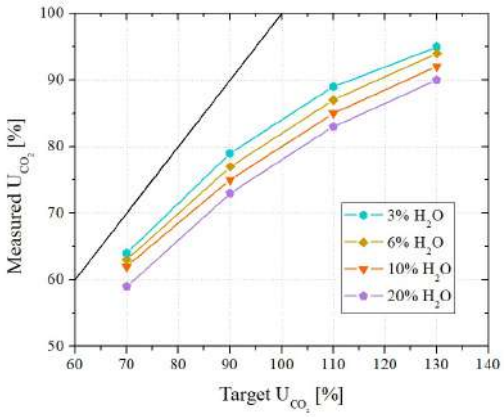

(D) Target vs. Measured U_{CO_2} for different inlet H_2O concentration.

Figure 3.1: Experimental results of the campaign to study the effects of H_2O addition at the cathode inlet.

OH^- as alternative ions for the additional current density. To verify this possibility mass transfer related experiment were performed. They showed that the anode outlet amount of H_2O was higher and CO_2 lower than the one expected. Moreover, considering the experimental error, the surplus of H_2O coincides with the quantity expected from its migration instead of the one of CO_2.

These findings demonstrated that the earlier model developed by my research group in collaboration with UNIPG cannot accurately simulate MCFCs working with reduced CO_2/H_2O cathode feed ratios since it does not account for the migration of H_2O. To construct a better model, it is necessary to identify the causes of these results and the mechanisms involved.

3.1.1. The possible mechanisms

The presence of both CO_2 and H_2O in the gas phase can alter the electrolyte composition, initially a carbonate melt, due to the carbonate-hydroxide equilibrium already observed by Nishina (Rxn. 3.1).

Generally, even in presence of very low CO_2 concentrations [106], this equilibrium favors the formation of carbonate ions over hydroxide. However, as CO_2 is depleted in the cathode gas, hydroxide ions can build up in the melt, particularly towards the cathode outlet.

It can be hypothesized that when the concentration ratio between CO_2 and H_2O reaches a certain value, the equilibrium would allow a non-negligible level of hydroxide ions to stabilize in the melt. This can establish a series of chained phenomena that can allow the net migration of H_2O to the anode side during energy production.

Two main possible reaction paths can be proposed and classified according to the nature of the cathode reaction of H_2O. They are presented schematically in Figure 3.2 and will be described in the following subsections.

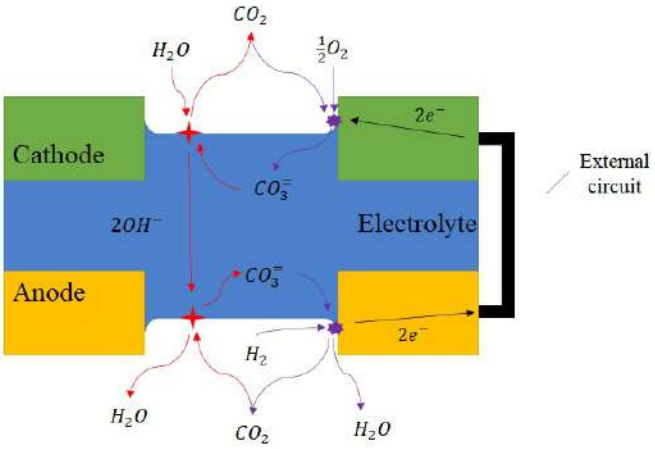

(A) Equilibrium driven H_2O reaction.

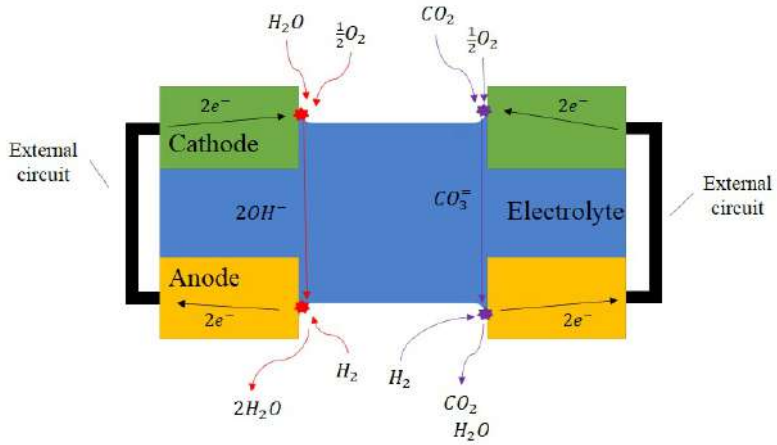

(B) Electrochemically driven H_2O reaction.

Figure 3.2: Possible reaction paths that describe MCFCs working with wet cathode feeds.

Cathodic chemical reaction of H_2O (A)

Close to the cathode outlet, OH^- ion concentration can become significant in the melt due to the depletion of CO_2 from the gas phase. These OH^- ions can migrate to the anode side carrying O_2 and electrons.

The anodic concentration of CO_2 is much higher than the cathodic one because the anode feed already has high CO_2 concentration (about 18% v/v), and anodic CO_2 is not depleted but enriched by the electrochemical reactions. This hinders the presence of stable OH^- in high concentration in the melt: the equilibrium will favor the formation of CO_3^{2-} to which corresponds the release of H_2O and the consumption of CO_2 and OH^-. Then, the newly formed CO_3^{2-} can electrochemically react with H_2 to reform CO_2 and release H_2O and two electrons completing the electrochemical carbonate reactions chain.

The overall mechanism is represented by the scheme of Figure 3.2A. The reaction chain that describes this path is the following:

- Cathode reactions:

$$H_2O + CO_3^{2-} \longrightarrow CO_2 + 2\,OH^- \tag{R. 3.2}$$

$$CO_2 + \frac{1}{2}\,O_2 + 2\,e^- \longrightarrow CO_3^{2-} \tag{R. 3.3}$$

- Overall cathode reaction:

$$H_2O + \frac{1}{2}\,O_2 + 2\,e^- \longrightarrow 2\,OH^- \tag{R. 3.4}$$

- Anode reactions:

$$CO_2 + 2\,OH^- \longrightarrow H_2O + CO_3^{2-} \tag{R. 3.5}$$

$$CO_3^{2-} + H_2 \longrightarrow CO_2 + H_2O + 2\,e^- \tag{R. 3.6}$$

- Overall anode reactions:

$$2\,OH^- + H_2 \longrightarrow 2\,H_2O + 2\,e^- \tag{R. 3.7}$$

- Overall Cell reactions:

$$H_2O_{\text{cathode}} + \frac{1}{2}\,O_2 + H_2 \longrightarrow 2\,H_2O_{\text{anode}} \tag{R. 3.8}$$

Cathodic electrochemical reaction of H_2O (B)

There is also the possibility that the H_2O reactions are completely electrochemically driven similar to those of CO_2. This mechanism is described in Figure 3.2B. The H_2O/OH^- electrochemical reaction chain is the following:

Cathode reaction:

$$H_2O + \frac{1}{2}\,O_2 + 2\,e^- \longrightarrow 2\,OH^- \tag{R. 3.9}$$

Anode reaction:

$$2\,OH^- + H_2 \longrightarrow 2\,H_2O + 2\,e^- \qquad \text{(R. 3.10)}$$

Overall reaction:

$$H_2O_{cathode} + \frac{1}{2}\,O_2 + H_2 \longrightarrow 2\,H_2O_{anode} \qquad \text{(R. 3.11)}$$

As in several other phenomena with competing reactions, in both cases the migration of CO_2 and H_2O from cathode to anode at the local level can take place both in series or in parallel. If the reactions happen in series, due to the working conditions, CO_2 will first react until, due to mass transport limitations, it can be considered completely depleted. Then H_2O will start migrating instead. In this case it will be possible to determine two defined consecutive areas where CO_2 reacts in the first one and H_2O reacts in the second one. If the reactions happen in parallel, it will not be possible to determine clear zones of CO_2 only or H_2O only reaction, but the migration of both anions will take place simultaneously over the cell entire surface. In this case the extent of the migration of one anion over the other will be determined by the local gas concentration that is related to both the equilibrium reaction and/or the polarization resistances.

However, the experimental data gave clear evidence that the carbonate and hydroxide paths operate simultaneously in parallel, but with a strong bias toward the carbonate path. Carbonate is strongly favored by thermodynamics without a potentially strong compensating effect from ionic conductivity. Consequently, the hydroxide path has not been observed in the past since it only manifests itself at measurable levels when the CO_2/H_2O ratio becomes low and at high current density, as in the case for high levels of CO_2 capture.

Either one or the other presented mechanism (equilibrium or electrochemically driven) might dominate or, most likely, the two take place simultaneously. Nevertheless, all possible scenarios yield the following overall reaction, with a and b being the extent of CO_2 and H_2O migration respectively:

$$a\,CO_{2,cathode} + b\,H_2O_{cathode} + \frac{a+b}{2}\,O_2 + a + b\,H_2 \longrightarrow a\,CO_{2,anode} + a + b\,H_2O_{anode} \qquad \text{(R. 3.12)}$$

With the current knowledge and the analysis of the experimental results, it is not possible to discriminate between the mechanisms to determine which one dominates. However, with appropriate fitting of the model parameters, I expect that all models would return similar results. Since, from a mathematical point of view it is easier to derive, I decided to build the model based on the electrochemical path with CO_2 and H_2O reacting in parallel.

3.2. The development of the Electrochemical Model

An MCFC operating at high CO_2 cathode feed conditions and moderate CO_2 utilization, typical in power generation mode, can be represented by the circuit in Figure 3.3. In the circuit, E $[V]$ stands for the cell equilibrium potential given by the Nernst equation (Eq. 1.6) and is the driving force of the electrochemical process. R_Ω $[\Omega\,cm^2]$ is the area-specific ohmic resistance of the cell, R_{An} and R_{Cat} $[\Omega\,cm^2]$ are the area-specific polarization resistances attributable to the anodic and cathodic electrochemical reactions respectively, J $[A\,cm^{-2}]$ is the current density, and V $[V]$ is the measured voltage of the closed circuit cell. This circuit represents a cell working with a single-anion mechanism, which means that only one anion, the carbonate, migrates from cathode to anode.

To simplify, from now on I will refer to the "area specific polarization resistances" just as "polarization resistances" or "resistances".

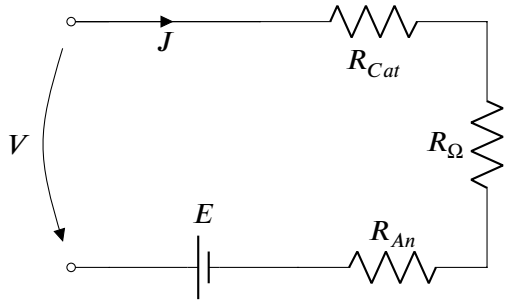

Figure 3.3: Circuit representing an MCFC working with single-anion mechanism.

However, this circuit cannot be applied in the case under study. As discussed above, this is due to a secondary path that involves the hydroxide ions in competition with carbonate ions. Therefore, a more appropriate circuit is needed to consider the driving forces and resistances of each path. I propose the one shown in Figure 3.4.

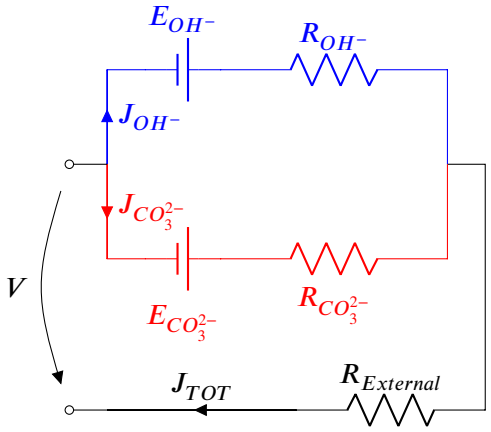

Figure 3.4: Circuit representing an MCFC working with dual-anion mechanism.

In the circuit E_m represents the equilibrium potential of the m-th path $[V]$, J_{TOT} the total current density that flows through the cell $[A\,cm^{-2}]$, J_m the current density flowing through the m-th anion path $[A\,cm^{-2}]$, $R_{External}$ is the sum of all the polarization resistances $[\Omega\,cm^2]$ that do not depend on the anion paths, and R_m is the sum of all the polarization resistances $[\Omega\,cm^2]$ characteristic of each m-th path.

From the Kirchhoff's law, the total cell current density and the current densities of the two anion paths are related as:

$$J_{TOT} = J_{CO_3^{2-}} + J_{OH^-} \qquad \text{(Eq. 3.2)}$$

If both members are divided by the total current density, the following equation is obtained:

$$1 = \frac{J_{CO_3^{2-}}}{J_{TOT}} + \frac{J_{OH^-}}{J_{TOT}} = t_{CO_3^{2-}} + t_{OH^-} \qquad \text{(Eq. 3.3)}$$

where t_m, defined as the ratio between the current density of the m-th path and the total current density, represents the transference number of the m-th anion $[-]$. Its value indicates the fraction of the total current density that is due to the considered m-th anion. I will use the carbonate transference number ($t_{CO_3^{2-}}$) as a principal parameter to evaluate cell performance and validate simulation results.

To describe the performance of a fuel cell, the following equation is usually considered:

$$V = E - J R_{TOT} \tag{Eq. 3.4}$$

This equation indicates that the measured voltage is obtained as the difference between the equilibrium potential given by the Nernst equation and the cell polarization that is the product of applied current and total resistance ($R_{TOT} = R_{Cat} + R_{\Omega} + R_{An}$).

However, in the case under study, Eq. 3.4 is not adequate to fully describe the system because at least the equilibrium potential, i.e. the driving force, of the two reactions should be considered. Thus, it is necessary to construct a system of equations where the voltage is a function of both the carbonate and hydroxide terms. In addition, Kirchhoff's law must be satisfied to guarantee that the sum of the currents of the two anion paths is equal to the cell total current. These conditions can be met by the following equation system:

$$\begin{cases} V = E_{CO_3^{2-}} - J_{CO_3^{2-}} R_{CO_3^{2-}} - J_{TOT}\, R_{External} & \text{(Eq. 3.5)} \\ V = E_{OH^-} - J_{OH^-} R_{OH^-} - J_{TOT}\, R_{External} & \text{(Eq. 3.6)} \\ J_{TOT} = J_{CO_3^{2-}} + J_{OH^-} & \text{(Eq. 3.7)} \end{cases}$$

It is important to note that Eqs. 3.4-3.6 should be expressed in polarization terms (η) rather than the corresponding resistances. However, resistance and polarization can be connected with the following relation:

$$R = \frac{d\eta}{dJ} \tag{Eq. 3.8}$$

If the cell is at steady state conditions, Eq. 3.8 can simplify to:

$$R = \frac{\eta}{J} \tag{Eq. 3.9}$$

Thus, if applied to steady state conditions only, as it is in this case, the use of said equations is correct.

The system described by Eqs. 3.5-3.7 has three equations with four unknown variables: V, J_{TOT}, $J_{CO_3^{2-}}$ and J_{OH^-}. Since the performance of a fuel cell is usually evaluated imposing the value of V or J_{TOT} (potentiostatic or galvanostatic mode), the number of unknown variables is reduced to three allowing to find unique solutions for both these operation modes. The solution for the potentiostatic mode can be found by solving the following system of equations:

$$\begin{cases} J_{TOT} = -\dfrac{\left(R_{CO_3^{2-}} + R_{OH^-}\right) V - E_{CO_3^{2-}} R_{OH^-} - E_{OH^-} R_{CO_3^{2-}}}{R_{External}\left(R_{CO_3^{2-}} + R_{OH^-}\right) + R_{CO_3^{2-}} R_{OH^-}} & \text{(Eq. 3.10)} \\ J_{CO_3^{2-}} = -\dfrac{R_{OH^-} V + \left(E_{OH^-} - E_{CO_3^{2-}}\right) R_{External} - E_{CO_3^{2-}} R_{OH^-}}{R_{External}\left(R_{CO_3^{2-}} + R_{OH^-}\right) + R_{CO_3^{2-}} R_{OH^-}} & \text{(Eq. 3.11)} \\ J_{OH^-} = -\dfrac{R_{CO_3^{2-}} V + \left(E_{CO_3^{2-}} - E_{OH^-}\right) R_{External} - E_{OH^-} R_{CO_3^{2-}}}{R_{External}\left(R_{CO_3^{2-}} + R_{OH^-}\right) + R_{CO_3^{2-}} R_{OH^-}} & \text{(Eq. 3.12)} \end{cases}$$

while the system below can be used for the galvanostatic mode:

$$\begin{cases} V = -\dfrac{R_{External}\left(J_{TOT}R_{OH^-}+J_{TOT}R_{CO_3^{2-}}\right)+R_{CO_3^{2-}}\left(J_{TOT}R_{OH^-}-E_{OH^-}\right)-E_{CO_3^{2-}}R_{OH^-}}{R_{OH^-}+R_{CO_3^{2-}}} & \text{(Eq. 3.13)} \\ J_{CO_3^{2-}} = \dfrac{J_{TOT}R_{OH^-} - E_{OH^-} + E_{CO_3^{2-}}}{R_{OH^-} + R_{CO_3^{2-}}} & \text{(Eq. 3.14)} \\ J_{OH^-} = \dfrac{J_{TOT}R_{CO_3^{2-}} + E_{OH^-} - E_{CO_3^{2-}}}{R_{OH^-} + R_{CO_3^{2-}}} & \text{(Eq. 3.15)} \end{cases}$$

Nonetheless, the calculation is not straightforward: as I will show in the following sections, some of the resistances are a function of the current density. This requires an iterative solution.

3.3. Evaluation of the Resistances

To solve the system of Eqs. 3.5-3.7, it is necessary to find the proper way to express the resistances. The resistances, or more specifically the polarizations, are usually considered to comprise three main components: ohmic, activation, and concentration.

The ohmic resistance (R_Ω , or polarization η_Ω) is the sum of the electrical resistances attributable to the cell materials, the circuit external to the cell, the various interconnections, and the ionic resistance of the electrolyte. In literature [107] it is usually expressed as function of the sole operating temperature with expressions such as:

$$R_\Omega = P_{\Omega,1}\, e^{\frac{P_{\Omega,2}}{T}} + P_{\Omega,3} \qquad \text{(Eq. 3.16)}$$

where $P_{\Omega,3}$ represents the resistance due to the external contacts and $P_{\Omega,1}\, e^{\frac{P_{\Omega,2}}{T}}$ represents the internal cell resistance. Since external contacts are usually negligible [108], I will neglect them in this analysis. Thus, the ohmic resistance will be considered as:

$$R_\Omega = P_{\Omega,1}\, e^{\frac{P_{\Omega,2}}{T}} \qquad \text{(Eq. 3.17)}$$

The activation resistance (R_{act}, or polarization η_{act}) represents the potential needed by the cell for the electrochemical reactions to take place.

The concentration resistance (R_{conc}, or polarization η_{conc}) represents the resistance offered by the mass transport.

To obtain a formulation for the activation and the concentration resistances, I started from the Butler-Volmer equation:

$$J = J_0\left[e^{(\alpha'_e z_e \eta F/RT)}\prod_i \frac{C_{i,sur}^{\alpha'_i}}{C_i^{\alpha'_i}} - e^{(\alpha''_e z_e \eta F/RT)}\prod_i \frac{C_{i,sur}^{\alpha''_i}}{C_i^{\alpha''_i}}\right] \qquad \text{(Eq. 3.18)}$$

where J_0 is the exchange current density $[A\, cm^{-2}]$; α'_e, α''_e, α'_i and α''_i are the reaction rate orders of the direct ($\prime$) and reverse ($\prime\prime$) reactions related to the electrons or the i-th reactant $[-]$, η is the polarization $[V]$; and C_i and $C_{i,sur}$ are, respectively, the concentration in the bulk and on the electrode surface of the i-th reactant $[mol\, m^{-3}]$. The focus of this investigation is the operation regime for carbon capture with high current density. At high current densities the forward reaction strongly dominates, thus the reverse

reaction can be neglected to simplify the model. This will have to be revised if someone would want to apply the model to include electrolysis or very low current densities (close to the OCV).

$$J = J_0 \left(e^{(\alpha'_e z_e \eta F / RT)} \prod_i \frac{C_{i,sur}^{\alpha'_i}}{C_i^{\alpha'_i}} \right) \tag{Eq. 3.19}$$

From the above equation, the polarization can be rendered explicit as:

$$\eta = \frac{RT}{\alpha'_e z_e F} \ln \left[\div \frac{J}{J_0} \prod_i \left(\frac{C_{i,sur}}{C_i} \right)^{-\alpha'_i} \right] \tag{Eq. 3.20}$$

According to the properties of the logarithms, the logarithm of a product is equal to the sum of the numbers being multiplied as shown in Eq. 3.21.

$$\ln (A \cdot B) = \ln A + \ln B \tag{Eq. 3.21}$$

In Eq. 3.20 it is possible to see the argument of the logarithm as products of two numbers as highlighted by the colors:

$$\eta = \frac{RT}{\alpha'_e z_e F} \ln \left[\frac{J}{J_0} \prod_i \left(\frac{C_{i,sur}}{C_i} \right)^{-\alpha'_i} \right] \tag{Eq. 3.22}$$

Thus, Eq. 3.22 can be separate in the sum of two contributions: activation (red in Eq. 3.22) and concentration (green in Eq. 3.22). The activation term can be expressed as:

$$\eta_{act} = \frac{RT}{\alpha'_e z_e F} \ln \frac{J}{J_0} \tag{Eq. 3.23}$$

The concentration term can be expressed as:

$$\eta_{conc} = \frac{RT}{\alpha'_e z_e F} \ln \prod_i \left(\frac{C_{i,sur}}{C_i} \right)^{-\alpha'_i} = - \sum_i \frac{\alpha'_i RT}{\alpha'_e z_e F} ln \left(\frac{C_{i,sur}}{C_i} \right) \tag{Eq. 3.24}$$

Because of the high operating temperatures of MCFCs (around 900 K), the activation term is often neglected [46, 109]. Following this approach, I reduced the analysis to the study of the concentration term only (Eq. 3.24).

In MCFCs the actual point where the reactions take place and species involved are not yet completely understood. Also, the relevant reactant concentrations cannot be readily determined due to the experimentally inaccessible diffusion resistances in the gas phase and in the electrolyte melt. Consequently, the ratio between the bulk and reacting surface concentration of the i-th reactant ($\frac{C_{i,sur}}{C_i}$) in Eq. 3.24 is not known. It is thus usually rewritten in terms of the ratio between the applied current density (J) and the limiting current density of the i-th reactant ($J_{L,i}$). The limiting current density of a reactant i is the maximum current density that can be obtained by its maximum attainable consumption rate controlled by the mass transport limitation. Applying a mass balance over the electrode surface, the current density and the limiting current density of the i-th reactant can be expressed as:

$$J = z_e F K_C \frac{\nu_e}{\nu_i} \left(C_i - C_{i,sur} \right) \tag{Eq. 3.25}$$

$$J_{L,i} = z_e F K_C \frac{\nu_e}{\nu_i} C_i \tag{Eq. 3.26}$$

where K_C is a mass transfer coefficient that considers the i-th reactant diffusion to the electrode surface $[m\,s^{-1}]$, and ν_e and ν_i are the stoichiometric coefficients of the electrons involved in the reaction and the i-th chemical component respectively $[-]$. Considering both equations, the concentration ratio can be expressed as:

$$\frac{C_{i,sur}}{C_i} = 1 - \frac{J}{J_{L,i}} \tag{Eq. 3.27}$$

If the ratio is substituted in Eq. 3.24, the following expression for the concentration polarization is obtained:

$$\eta_{conc} = -\sum_i \frac{\alpha_i' RT}{\alpha_e' z_e F}\, ln\left(1 - \frac{J}{J_{L,i}}\right) \tag{Eq. 3.28}$$

Dividing now by the cell current density, the concentration resistance can be expressed as:

$$R_{conc} = -\frac{1}{J}\sum_i \frac{\alpha_i' RT}{\alpha_e' z_e F}\, ln\left(1 - \frac{J}{J_{L,i}}\right) \tag{Eq. 3.29}$$

In both Eq. 3.28 and 3.29 the values of the reaction rate orders and the mass transfer coefficients are not available to determine $J_{L,i}$. To overcome this problem, I introduced fitting parameters ($P_i s$) that can be evaluated from experiments collected at variable gas concentrations, flow rates, and temperatures. Grouping all the unknown variables into fitted parameters, the concentration polarization of a reacting gas can be expressed as:

$$\eta_{conc,i} = -P_{i,1}\, T\, ln\left(1 - \frac{J}{P_{i,2} e^{\frac{P_{i,3}}{T}} p_i}\right) \tag{Eq. 3.30}$$

and the corresponding resistance as:

$$R_{conc,i} = -\frac{P_{i,1}\, T}{J} ln\left(1 - \frac{J}{P_{i,2} e^{\frac{P_{i,3}}{T}} p_i}\right) \tag{Eq. 3.31}$$

In this study, the resistances may depend on three different currents (J_{TOT}, $J_{CO_3^{2-}}$ and J_{OH^-}) based on the path where the reaction is involved. Thus, it is better to express Eq. 3.31 as:

$$R_{conc,i,m} = -\frac{P_{i,1}\, T}{J_m} ln\left(1 - \frac{J_m}{P_{i,2} e^{\frac{P_{i,3}}{T}} p_i}\right) \tag{Eq. 3.32}$$

where J_m represents the current density of the m-th path that affects the reactant. The non-linearity of Eq. 3.32 can complicate the calculations performed in the code to find a solution due to the difficulty in dealing with logarithms. Thus, if the consumption rate of the i-th reactant at the applied current J_m is not close to its limiting current ($J_{L,i}$), it is usually linearized using a Taylor expansion and keeping only the term with exponent equal to 1, as:

$$R_{conc,i} = \frac{P_{i,1}}{P_{i,2}}\, T\, e^{-\frac{P_{i,3}}{T}} p_i^{-1} = P_{i,1}^*\, T\, e^{\frac{P_{i,2}^*}{T}} p_i^{-1} \tag{Eq. 3.33}$$

For the sake of simplicity, when Eq. 3.33 is used instead of 3.32, the parameters $P_{i,1}^*$ and $P_{i,2}^*$ will be referred as $P_{i,1}$ and $P_{i,2}$.

3.4. Identification of the best circuit simplification

As introduced when presenting the circuit in Figure 3.4, $R_{External}$, $R_{CO_3^{2-}}$ and R_{OH^-} are the sums of the polarization resistances of the main branch and branches of the two parallel ionic paths. Consequently, they can be written as[1]:

$$R_{External} = R_{\Omega,External} + \sum_i R_{i,External} \quad \text{(Eq. 3.34)}$$

$$R_{CO_3^{2-}} = R_{\Omega,CO_3^{2-}} + \sum_i R_{i,CO_3^{2-}} \quad \text{(Eq. 3.35)}$$

$$R_{OH^-} = R_{\Omega,OH^-} + \sum_i R_{i,OH^-} \quad \text{(Eq. 3.36)}$$

These equations require a large number of kinetic parameters. Determining them would not be straightforward because it is challenging to isolate each effect. This may lead to an inability to perform meaningful parameter fitting. Also, it is possible that the main branch and the two anion paths do not account for all resistances.

Thus, it is necessary to identify which resistance is part of which path and, in case the system still maintain a high level of complexity, further simplify the circuit if possible.

First, the reactions that define the two anion paths have to be considered. The carbonate path (Rxns. 1.1, 1.2, and 1.7) has as main reactants CO_2 and O_2 at the cathode, and H_2 at the anode side. The hydroxide path (Rxns. 3.9, 3.10, and 3.11) has as main reactants H_2O, O_2 at the cathode, and H_2 at the anode side. Although there is interaction between CO_2 and H_2O through the carbonate/hydroxide equilibrium, they appear to have independent electrochemical paths. Consequently, I can assume that CO_2 and H_2O figure only in the carbonate and hydroxide path respectively. On the contrary, since both O_2 and H_2 are involved in both reactions, I can assume that each reactant resistance is present in each path. I can also assume that the reactant polarization resistances are only part of the branch of the respective anion paths and do not figure in the main branch. For the ohmic component I will have a resistance in the main branch representing the resistances of the anode, cathode, external circuits and different contacts, but each path will also see a specific ohmic resistance due to the different ionic conductivity of the two anions. On the base of what discussed above, I can rewrite the resistance equations as:

$$R_{External} = R_{\Omega,External} \quad \text{(Eq. 3.37)}$$

$$R_{CO_3^{2-}} = R_{\Omega,CO_3^{2-}} + R_{CO_2,CO_3^{2-}} + R_{O_2,CO_3^{2-}} + R_{H_2,CO_3^{2-}} \quad \text{(Eq. 3.38)}$$

$$R_{OH^-} = R_{\Omega,OH^-} + R_{H_2O,OH^-} + R_{O_2,OH^-} + R_{H_2,OH^-} \quad \text{(Eq. 3.39)}$$

This solution still presents with a large number of variables to fit. In an attempt of further simplification, I assessed the effects of each reactant gas on the carbonate transference numbers ($t_{CO_3^{2-}}$), and the cross-correlation effects that the transference number has on the internal resistance.

Before analyzing the experimental data, it is important to define three different CO_2 utilization factors that can be distinguished in an MCFC working with dual-anion mechanism: measured, apparent and simulated. The measured U_{CO_2} is the one experimentally measured as ratio between the CO_2 consumed in the cathodic reactions and the inlet CO_2 (Eq. 3.40). The apparent CO_2 utilization, $U_{CO_{2,apparent}}$, is calculated using Faraday's law (refer to Eq. 3.1) by assuming that all current is attributable to the carbonate path

[1]The reactant related resistances ($R_{i,m}$) should be expressed as sum between activation ($R_{i,act,m}$) and concentration ($R_{i,conc,m}$) contribution. However, since we decide to neglect the activation contribution, the reactant related resistance coincide with the concentration resistance only ($R_{i,m} = R_{i,conc,m}$).

(Eq. 3.41). Finally, there is simulated utilization factor (Eq. 3.42) that is equivalent to carbonate path current computed by the model. If the cathode feed does not contain water, thus the MCFC works only with carbonate ions, all three utilizations are equal. However, if the MCFC is fed with water-containing cathode gas, the apparent utilization will be always higher than the measured and the simulated one. The differences will depend on the CO_2/H_2O ratio. The lower it is the larger is the difference. In the equations F_{CO_2} represents the cathodic inlet or outlet molar flux of CO_2 [$mol\ s^{-1}$].

$$U_{CO_2,\ measured} = \frac{F_{CO_2,cat-in} - F_{CO_2,cat-out}}{F_{CO_2,cat-in}} \qquad \text{(Eq. 3.40)}$$

$$U_{CO_2,\ apparent} = \frac{F_{CO_2,cat-in} - \left(F_{CO_2,cat-in} - \frac{J_{TOT}\ A}{2F}\right)}{F_{CO_2,cat-in}} \qquad \text{(Eq. 3.41)}$$

$$U_{CO_2,\ simulated} = \frac{F_{CO_2,cat-in} - \left(F_{CO_2,cat-in} - \frac{J_{CO_3^{2-}}\ A}{2F}\right)}{F_{CO_2,cat-in}} \qquad \text{(Eq. 3.42)}$$

Figure 3.5 shows the $t_{CO3^{2-}}$ plotted against the cathode inlet concentrations of CO_2 (3.5A), H_2O (3.5B) and O_2 (3.5C), and the anode inlet concentration of H_2 (3.5D).

For each reactant, different data series were plotted to verify possible inconsistencies. In the figure, these data series are presented in the different colors and symbols.

Specifically, to reproduce the series of data at different H_2O and O_2 concentrations, the anode inlet flow rate, anode feed composition, cathode inlet flow rate, total applied current density, and H_2 and CO_2 theoretical utilizations (calculated using the Faraday's law for the current density applied to the cell) were kept constant. Different concentrations were obtained by balancing the necessary H_2O or O_2 changes with N_2, an inert gas in the electrochemical reactions.

To reproduce the series of data at different CO_2 and H_2 concentrations, the total generated current density, H_2 and CO_2 theoretical utilizations, anode (for H_2) and cathode (for CO_2) concentrations, and total anode inlet flow rates were kept the same. In this case, the concentrations of CO_2 and H_2 were varied by decreasing the total flow rate. To maintain a constant theoretical utilization of H_2 or CO_2, N_2 was used as balancing gas.

In both Figure 3.5A and Figure 3.5B, the transference numbers show an evident dependence on the concentrations of CO_2 and H_2O, shifting the current density contributions of the two paths. On the contrary, neither O_2 nor H_2 appears to influence the transference numbers, at least in the studied concentration ranges, as evidenced by Figure 3.5C and Figure 3.5D. It is possible O_2 and H_2 at a fundamental level change the current density distributions and therefore have a minor effect on transference number. For this reason, I could simplify the circuit without affecting model outputs by removing both the O_2 and H_2 resistances from the parallel paths and lumping them together in the main branch.

Similarly, the ohmic resistances can be plotted versus the carbonate transference numbers (see Figure 3.6) to verify whether the resistance can be affected by possible changes in the electrolyte composition. The experimental data were collected using different single cells to guarantee that possible time-dependent degradation would not affect the analysis. As a consequence, I obtained two series of ohmic resistance data that slightly differ for their values. In Figure 3.6 the black squares belong to a cell with ohmic resistance of about $0.3\,\Omega\,cm^2$ ($1.2\,\Omega$), while the red circles belong to a cell characterized by an ohmic resistance of about $0.25\,\Omega cm^2$ ($1.0\,\Omega$). The differences in ohmic resistances are due to the details of cell construction and this variation from cell to cell is well within the normal experimental uncertainty. At the maximum studied current density of $150\,mA\,cm^{-2}$ the polarization difference due to the different

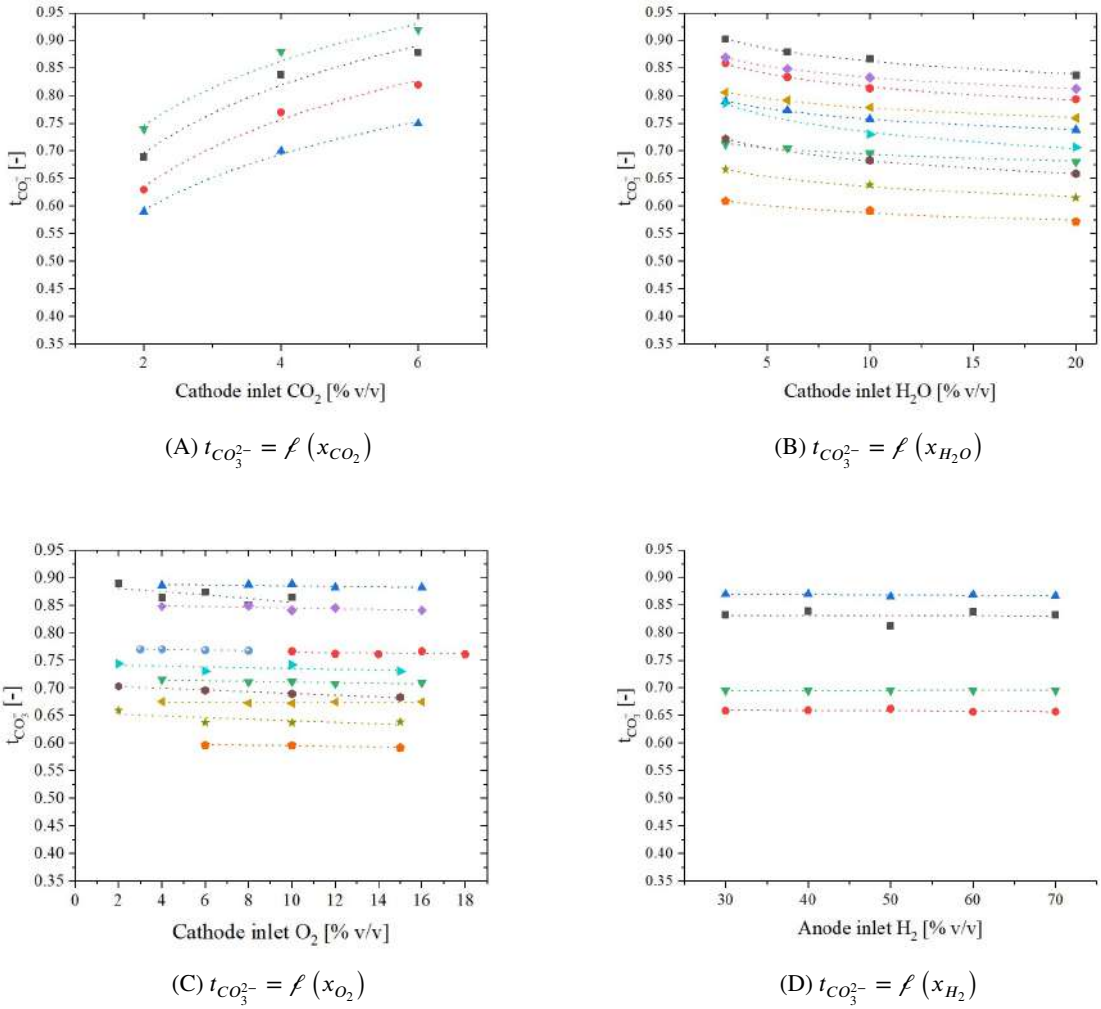

(A) $t_{CO_3^{2-}} = f\left(x_{CO_2}\right)$ (B) $t_{CO_3^{2-}} = f\left(x_{H_2O}\right)$

(C) $t_{CO_3^{2-}} = f\left(x_{O_2}\right)$ (D) $t_{CO_3^{2-}} = f\left(x_{H_2}\right)$

Figure 3.5: Carbonate ion transference number plotted as a function of inlet gas molar concentration as % v/v (cathode CO_2 (A), H_2O (B) and O_2 (C) and anode H_2 (D)). In the graphs different colors and symbols represent different inlet conditions in terms of total anode and cathode flow rates.

ohmic resistance of these two cell series is of less than $8\,mV$. This allows the results comparison of both series to be used without further considerations.

The trends of both series suggest that the ohmic resistance is not significantly influenced by changes in the transference number, with a difference between the lowest and highest values of resistance of about only $0.025\,\Omega\,cm^2$ ($0.1\,\Omega$). Therefore, to further simplify the model, the ohmic area specific resistances of the two paths ($R_{\Omega,CO_3^{2-}}$ and R_{Ω,OH^-}) were also lumped together in the ohmic area specific resistance already considered in the main branch (R_Ω). On the basis of this analysis, I simplified the equations for the resistances to:

$$R_{External} = R_\Omega + R_{O_2} + R_{H_2} \quad \text{(Eq. 3.43)}$$

$$R_{CO_3^{2-}} = R_{CO_2,CO_3^{2-}} = R_{CO_2} \quad \text{(Eq. 3.44)}$$

$$R_{OH^-} = R_{H_2O,OH^-} = R_{H_2O} \quad \text{(Eq. 3.45)}$$

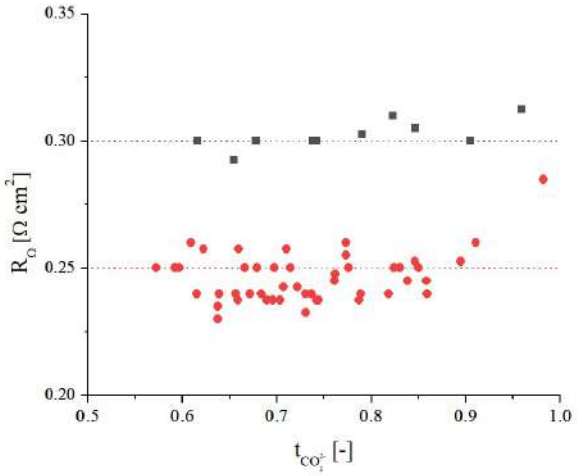

Figure 3.6: R_Ω as a function of carbonate transference number; the different colors represent results obtained with two different cells.

3.5. The base model

On the basis of the presented investigations, I established a base model for the simulation of MCFCs with a dual-anion path mechanism. The final circuit is presented in Figure 3.7.

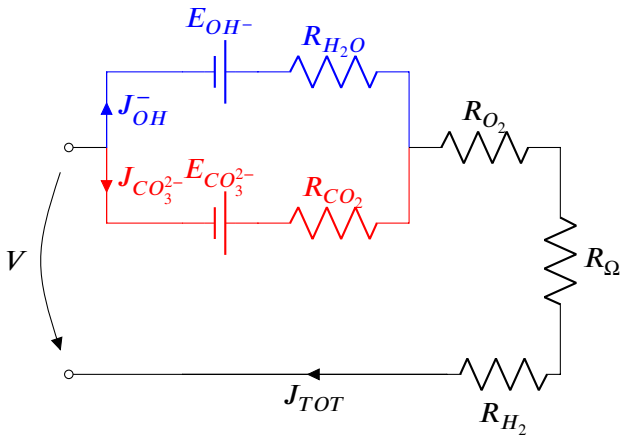

Figure 3.7: Circuit representing an MCFC working with dual-anion mechanism for the base model.

Following the development presented in the previous sections, I introduced the following expressions for the polarization resistances:

- R_Ω: Eq. 3.17 was used.

$$R_\Omega = P_{\Omega,1} e^{\frac{P_{\Omega,1}}{T}} \qquad \text{(Eq. 3.46)}$$

- R_{CO_2}: To describe the polarization resistance due to CO_2 I chose to use the non-linear formulation (Eq. 3.32). This choice depends on the fact that:

1. The utilization factors of CO_2 reach high values. This implies that using a linear form will underestimate the resistance value.
2. The most precise value possible is required to correctly evaluate the ratio between carbonate and hydroxide path.

Applied to this case Eq. 3.32 becomes:

$$R_{CO_2} = -\frac{P_{CO_2,1}T}{J_{CO_3^{2-}}} \ln\left(1 - \frac{J_{CO_3^{2-}}}{P_{CO_2,2}e^{\frac{P_{CO_2,3}}{T}} p_{CO_2}}\right) \quad \text{(Eq. 3.47)}$$

- R_{H_2O}: As done for the CO_2, I decided to use the non-linear formulation also to express the polarization resistance of H_2O. Since the water never reaches high consumption rate, this is done to estimate the more correct value to improve the evaluation of the carbonate/hydroxide migration ratio.

$$R_{H_2O} = -\frac{P_{H_2O,1}T}{J_{OH^-}} \ln\left(1 - \frac{J_{OH^-}}{P_{H_2O,2}e^{\frac{P_{H_2O,3}}{T}} p_{H_2O}}\right) \quad \text{(Eq. 3.48)}$$

- R_{H_2}: Since almost all the experimental data were collected at low H_2 utilization (about 30%), and since H_2 was excluded to determine the reacting path, I decided to describe its resistance using the linear formulation (Eq. 3.33).

  However, in previous works my research group has demonstrated that this formulation can be improved for H_2 [108]. At the anode side, the products (CO_2 and H_2O) diffuse from the electrode to the bulk. This products counter-diffusion penalizes the diffusion of H_2 from the bulk to the electrode. To consider this aspect, a correction factor ϵ (expressed as in Eq. 3.49, where i indicates the component) was introduced in the expression of the limit current density.[2]

$$\epsilon_{H_2} = \left(\ln\left(1 + x_{H_2}\right)\right)^{-1} \quad \text{(Eq. 3.49)}$$

  Consequently, the equation of the H_2 polarization resistance results:

$$R_{H_2} = \frac{P_{H_2,1}Te^{\frac{P_{H_2,2}}{T}}}{p\ln\left(1 + x_{H_2}\right)} \quad \text{(Eq. 3.50)}$$

- R_{O_2}: As for the H_2, since the consumption of O_2 considered is very low, I decided to use the linear formulation. However, in the case of O_2, literature showed that the limiting step in the O_2 reduction is not the diffusion of O_2 itself but the one of the intermediate ions that form in the melt. As discussed in Chapter 1, the actual steps of the O_2 reduction is not yet confirmed, and different authors suggest different paths. Experimental analysis are complicated by the fact that the ions are related by equilibria and many species are usually detected. Analysis at cell level considering the effects of O_2 or CO_2 are also not conclusive due to the different scale. In previous work, I assumed peroxide path (O_2^{2-}) and consequently I decided to apply it here too. If the concentration

[2] In Appendix B.1. "Induced fluxes" the reader can find a more detailed explanation on this correction factor.

of carbonate in the melt is assumed constant, the concentration of peroxide can be expressed as $C_{O_2}^{-0.5} C_{CO_2}$. The resulting equation for the O_2 resistance becomes:

$$R_{O_2} = P_{O_2,1} T e^{\frac{P_{O_2,2}}{T}} p^{0.5} \frac{x_{CO_2}}{x_{O_2}^{0.5}} \quad \text{(Eq. 3.51)}$$

However, the first group of collected experimental data did not have enough analysis of the cells at different operating temperatures. Moreover, the dimension of the cell studied ($250\,cm^2$), coupled with a good thermal control, allows for the assumption that the cell was working isothermally. For this reason, I initially decided to simplify the formulation removing the explicit dependence on the operating temperature by lumping it in the parameters.

The resistance equations describing the base model becomes:

$$R_\Omega = P_\Omega \quad \text{(Eq. 3.52)}$$

$$R_{CO_2} = -\frac{P_{CO_2,1}}{J_{CO_3^{2-}}} \ln\left(1 - \frac{J_{CO_3^{2-}}}{P_{CO_2,2}\, p_{CO_2}}\right) \quad \text{(Eq. 3.53)}$$

$$R_{H_2O} = -\frac{P_{H_2O,1}}{J_{OH^-}} \ln\left(1 - \frac{J_{OH^-}}{P_{H_2O,2}\, p_{H_2O}}\right) \quad \text{(Eq. 3.54)}$$

$$R_{H_2} = \frac{P_{H_2}}{p \ln\left(1 + x_{H_2}\right)} \quad \text{(Eq. 3.55)}$$

$$R_{O_2} = P_{O_2}\, p^{0.5} \frac{x_{CO_2}}{x_{O_2}^{0.5}} \quad \text{(Eq. 3.56)}$$

Completed the development of the base model, I used part of the experimental data to fit the kinetic parameters. Table 3.1 groups the results of the fitting.

P_i	Value	Unit
P_Ω	variable	$\Omega\, cm^2$
$P_{CO_2,1}$	1569.1	V
$P_{CO_2,2}$	69000	$A\, cm^{-2}\, atm^{-1}$
$P_{H_2O,1}$	5168.8	V
$P_{H_2O,2}$	8800	$A\, cm^{-2}\, atm^{-1}$
P_{H_2}	0.118	$\Omega\, cm^2\, atm$
P_{O_2}	0.046	$\Omega\, cm^2\, atm^{-0.5}$

Table 3.1: Kinetic parameters fitted for the base model.

The quality of model predictions for voltage (3.8A), CO_2 utilization factor (3.8B) and carbonate transference number (3.8C) are shown in the Figure 3.8 simulated vs. experimental parity plots. The average errors for the simulated data are: 2.9% for the voltage, 5.4% for the utilization factor of CO_2 and 5.1% for the carbonate ion transference number.

As shown in the left corner of the voltage graph (3.8A), most of the error emanates from the low experimental voltage data points. To understand why the error is higher for these runs, the operating conditions of these points must be considered. For example, the data with the highest errors were at high current density ($120\,mA\,cm^{-2}$) and high fuel utilization factors (85%) with low cathodic CO_2 inlet

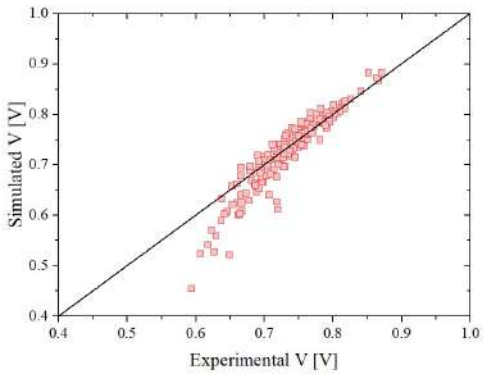

(A) Voltage.

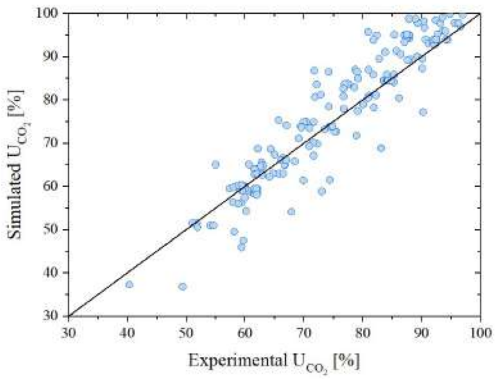

(B) CO_2 utilization

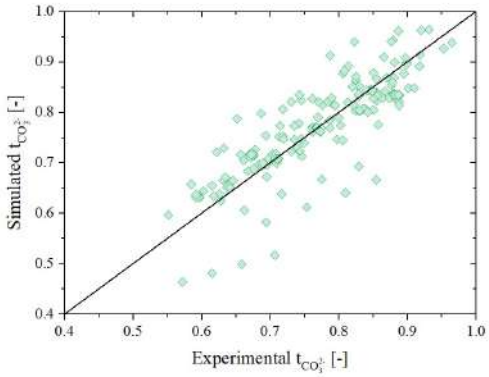

(C) Transference number

Figure 3.8: Parity plots of experimental and simulated data for measured voltage (A), CO_2 utilization factor (B) and carbonate ion transference number (C).

concentration (4% v/v). This led to 86% and 90% CO_2 utilization and carbonate ion transference numbers of about 0.66 at the higher and 0.60 at lower cathode flow rate. The CO_2 was highly depleted (in both cases less $<$ 1% v/v at the outlet) and there was a high concentration of water making the model more sensitive to the accuracy of the hydroxide parameters. Other elevated model error points were at similar, although somewhat less water rich and hydroxide ion mechanism favoring, operating conditions. Thus, I suspect that these points are inherently harder to model due to the small changes in CO_2, and H_2O, yielding significant relative outlet concentration and voltage changes.

For the CO_2 utilization factor and the carbonate ion transference number, the simulation may appear less satisfactory: not only the error is higher compared to voltage, but also the parity plots show a more scattered distribution. However, it should be considered that the relative analysis errors for the inlet and outlet gas compositions, from which the two values are determined, are higher at these low concentrations, thus the compounded experimental error could be high. Nonetheless, although more scattered, the results follow a clear trend. In addition, this 2D model simulations guarantee a far better simulation compared to previous attempts performed using a simpler 0D model that could not properly evaluate the polarization resistances and the parallel path split. For these reasons, I submit that the results of this first modeling are satisfactory.

However, in this form the model is capable to deal opportunely only for the simulation of data under load and not for Open Circuit Voltage (OCV) conditions.

First it is necessary to understand what happens at OCV conditions. The equilibrium voltage $E_{CO_3^{2-}}$ and E_{OH^-} can be expressed through the Nernst equation as:

$$E_{CO_3^{2-}} = E^0_{CO_3^{2-}} + \frac{RT}{z_e F} \ln\left(\frac{p_{H_2} p_{CO_{2,Cat}} p^{0.5}_{O_2}}{p_{CO_{2,An}} p_{H_2O_{An}}}\right) = \tag{Eq. 3.57}$$

$$E_{OH^-} = E^0_{OH^-} + \frac{RT}{z_e F} \ln\left(\frac{p_{H_2} p_{H_2O_{Cat}} p^{0.5}_{O_2}}{p^2_{H_2O_{An}}}\right) \tag{Eq. 3.58}$$

At the OCV the total cell current must be zero ($J_{TOT} = 0$). Therefore, the current densities of the two paths must be either both zero or equal in absolute value but opposite in sign. If both branch currents were zero, the equilibrium potentials for the two paths should be equal, thus:

$$E^0_{CO_3^{2-}} + \frac{RT}{z_e F} \ln\left(\frac{p_{H_2} p_{CO_{2,Cat}} p^{0.5}_{O_2}}{p_{CO_{2,An}} p_{H_2O_{An}}}\right) = E^0_{OH^-} + \frac{RT}{z_e F} \ln\left(\frac{p_{H_2} p_{H_2O_{Cat}} p^{0.5}_{O_2}}{p^2_{H_2O_{An}}}\right) \tag{Eq. 3.59}$$

Since in both paths the overall reaction ends in water evolution, the two standard potentials (E^0_m) must also be equal. This would imply that at the OCV the following condition must be met:

$$\frac{p_{CO_{2,Cat}}}{p_{CO_{2,An}}} = \frac{p_{H_2O_{Cat}}}{p_{H_2O_{An}}} \tag{Eq. 3.60}$$

It is evident that this equivalence is too conservative since it can only be met in a small number of cases and cannot be applied as OCV condition. Moreover, a variation of CO_2 content at the cathode exit has been experimentally observed even at OCV conditions. The behavior is shown in the graph of Figure 3.9, where the utilization of CO_2 is plotted versus its inlet molar fraction at the cathode side. It is interesting to notice that when the cathode concentration is particularly low (< 0.05) the CO_2 appears to migrate from the anode to the cathode side. This behavior is similar to the one observed in dual-phase membranes and in ceramic-carbonate nanocomposites as electrolyte for solid oxide fuel cells [110, 111, 112]. This is captured in the model that allows for negative current density. Together with the experimental data, Figure 3.9 also reports the simulated results. It can be observed that the model correctly predicts the experimentally observed trend. Nevertheless, the measured CO_2 utilization values are quite different from the calculated ones. This can be ascribed to the fact that, as presented in the development of the kinetic equations, I simplified the Butler–Volmer equation by considering only the direct reactions. However, since I have established the possibilities of negative current densities, which means reverse reactions, this simplification may prevent a precise evaluation of OCV conditions. In order to overcome this, the model should consider the reverse reactions also. Therefore, to expand the applicable condition range of the model, new data focusing on the OCV conditions should be collected. However, it is not in the scope of this work and has been neglected for the moment.

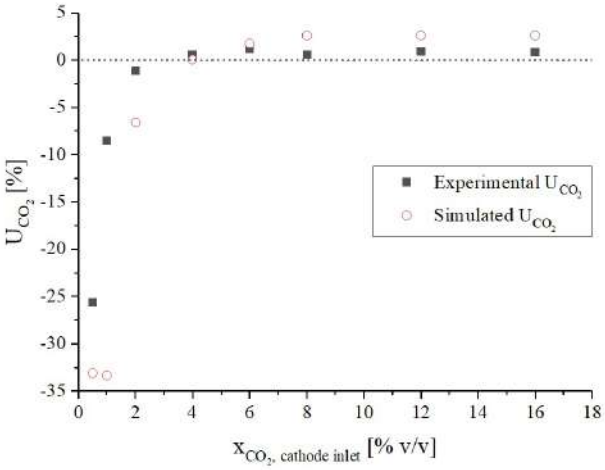

Figure 3.9: Cathode CO_2 mass balances under OCV conditions at different CO_2 inlet concentrations.

4
The effect of gas diffusion on the dual-anion model

The analysis of the experimental data has shown that the diffusion of the reactant gases not only affects the cell in terms of voltage/power performance, but also the split between the two competing anion fluxes. Specifically, the lower the concentration of CO_2 compared to H_2O, the more the hydroxide path will contribute to the overall anion flux through the cell penalizing carbon capture efficiency.

The model developed in the previous Chapter 3 is specific for cells that have the same structure (in terms of materials and geometrical features) and use the same gases as they highly affect the gas diffusion resistance. To model cells that are different, the empirical parameters must be re-tuned. However, this significantly limits the application window of the model. Clearly, there is a need for a term that accounts for the diffusion along the z-axis perpendicular to the cell plane. This should allow users to work with a fixed set of kinetic parameters, while adjusting only a diffusion parameter to describe different cell design, gas mixtures, etc. Also, with a better description of the reacting concentration of CO_2 and H_2O, I expect to reduce simulation errors.

This chapter will be organized as follow:

1. brief introduction of the diffusion issue in correlation with experimental data;
2. validation of the base model with new sets of parameters to fit experimental data collected with cell having different gas diffusion resistances;
3. development of a diffusion model;
4. additional analysis of experimental data collected with current collectors having different features.

The results of this chapter have been published with the title "*The Effects of Gas Diffusion in Molten Carbonate Fuel Cells Working as Carbon Capture Devices*" on the *Journal of Electrochemical Society* [113]. However, this article does not include the final discussion regarding current collectors with different features.

The experimental data presented in this chapter have been provided by EMRE and are presented in Appendix D in Tables D.1, D.3 and D.5.

4.1. The gas diffusion issue

As previously mentioned, one of the contributors to the loss in performance of MCFC is the resistance related to the mass transport of the reactants from the bulk to the reaction sites. To explore options for improved diffusion and to analyze the effects of diffusion on cell performance mainly in terms of CO_2 capture, a new experimental campaign was designed by EMRE [105]. In this new campaign, the cathode current collector (CC) was substituted by one with larger open area (from 35% to 90%), and in some runs N_2 was substituted with He as inert gas. The anode CC was not substituted since it was observed that the anode polarization resistances do not affect the anion transport split in the dual-anion mechanism and thus the CO_2 capture rate.

Measured cell voltages were higher with the CC having higher open area and with He in the cathode feed at otherwise similar conditions. This expected improvement can be attributed to improved gas transport afforded by the higher cathode open area and an increase of gas diffusion coefficient with the He-containing cathode gas mixture. Higher open cathode surface area and He also increased CO_2 utilization at a given current density indicating an increased contribution of the carbonate ion path. This is demonstrated in Fig. 4.1 by the higher measured CO_2 utilization factors with (i) He (blue dotted line) as compared to N_2 data (red line), and (ii) 90% (green dotted line) vs. the 35% (yellow line) open area CC . These results suggest that the contribution of one transference path over the other is greatly dependent on the local reactant concentrations at the gas-electrolyte interface within the cathode, which in turn is affected by diffusion. Since H_2O molecules are smaller than CO_2, their diffusion is less penalized in the more transport hindered conditions (N_2 and 35% open area CC) causing an increased H_2O utilization.

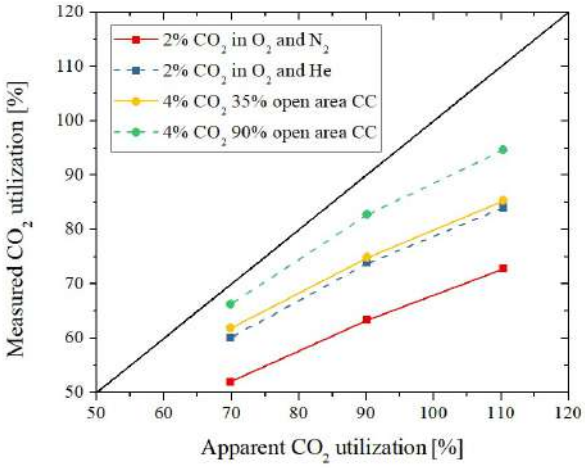

Figure 4.1: Comparison between apparent and measured CO_2 utilization factor of experimental data at same conditions but using different inert gas or CC open area.

In a graph like the one presented in Fig. 4.1, the further are the points below the parity line, the greater is the contribution of the hydroxide path. In the base model, this can only be addressed by refitting the kinetic parameters for different inert gases and CC open areas to properly fit the experimental data. This is exemplified in Table 4.1 that lists the kinetic parameters fitted for the original (as of Chapter 3, first column) and the new experimental data, the latter obtained with He instead of N_2 (second column) and with a current collector open area of 90% instead of 35% (third column).

P_i	N_2 and 35% open area	He and 35% open area	N_2 and 90% open area	Units
$P_{CO_2,1}$	1569.1	830.7	738.4	V
$P_{CO_2,2}$	69000	85000	200000	$A\,cm^{-2}\,atm^{-1}$
$P_{H_2O,1}$	5168.8	4707.3	3968.9	V
$P_{H_2O,2}$	8800	8000	8000	$A\,cm^{-2}\,atm^{-1}$
P_{H_2}	0.118	0.118	0.083	$\Omega\,cm^2\,atm$
P_{O_2}	0.046	0.042	0.042	$\Omega\,cm^2\,atm^{-0.5}$

Table 4.1: Base model kinetic parameters for different operating conditions.

Using the base model (Eqs. 3.52-3.56) and the new parameters, the experimental data were simulated.

The results are presented in the parity plots of Fig. 4.2.

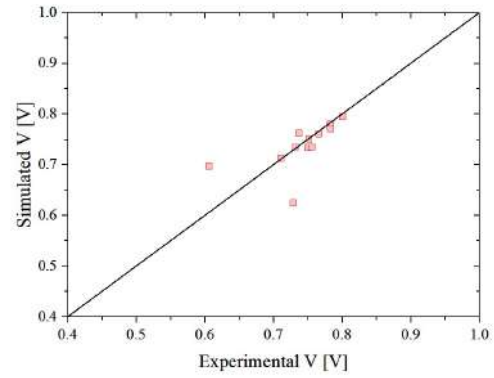

(A) Voltage

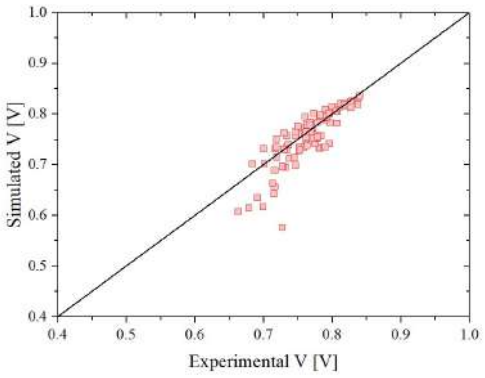

(B) Voltage

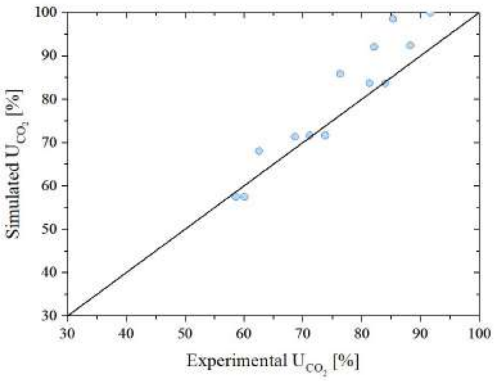

(C) CO_2 utilization

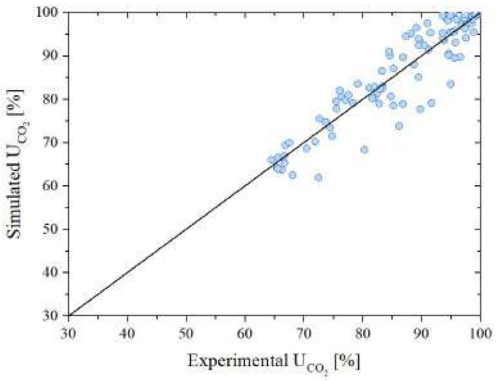

(D) CO_2 utilization

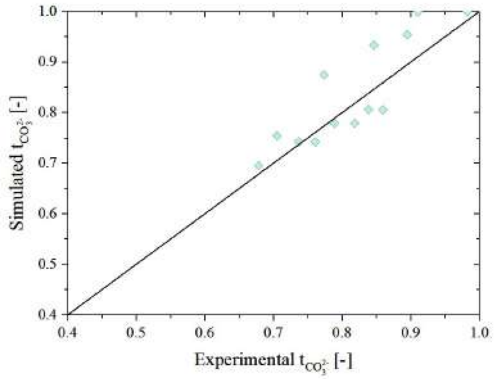

(E) Transference number

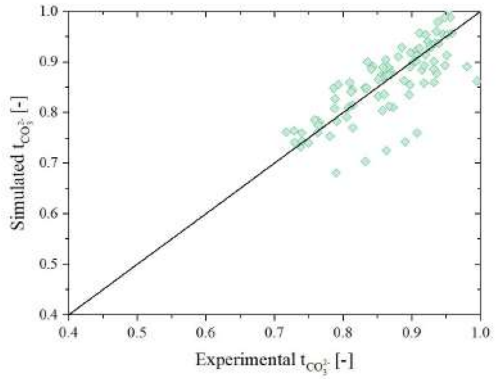

(F) Transference number

Figure 4.2: Simulated vs. experimental data of the He (4.2A, 4.2C and 4.2E) and CC with 90% open area (4.2B, 4.2D and 4.2F) data using the base model presented in Chapter 2. The kinetic parameters used for the simulation are presented in Table 4.1.

The He data (4.2A, 4.2C and 4.2E) show a good fit except for one data point collected with low cathode feed concentration of both CO_2 (2 vol %) and H_2O (3 vol %). At this operating condition the fitting for cell voltage is rather poor (the relative error is about 50%). This, however, might be due to increased experimental error at these low feed concentrations. The average errors for the He data are: 3.5% for the voltage (after excluding the aforementioned low concentration data point), 5.9% for the CO_2 utilization factor, and 5.3% for the carbonate ion transference. The data obtained using the cathode CC with 90% open area (4.2B, 4.2D and 4.2F) show a good fit with average errors of 3.9% for the voltages, 5.0% for the CO_2 utilization factors, and 4.4% for the carbonate ion transference numbers. In this case, the low voltage data points have worse fits compared to the high voltage data points; however, these data refer to more critical operating conditions (high utilization factors). These results confirm the applicability of the base model. However, having to generate a new set of kinetic parameters every time a variable affecting diffusion changes is rather inefficient. Clearly, it is desirable to include an explicit diffusion dependence of polarization resistances. To this end, I introduced a term addressing gas diffusion along the z-axis, perpendicular to the cell surface.

For this upgraded model, the following assumptions were made:

- steady state condition ($\frac{d}{dt} = 0$);
- mono-dimensional diffusion along the z coordinate, perpendicular to the cell plane ($\frac{d}{dx} = 0$ and $\frac{d}{dy} = 0$)
- convective fluxes negligible in the cathode pores ($\vec{v} = 0$);
- the cathode as homogeneous structure of pores and solid;
- current density constant alongside the z axis ($\frac{dJ}{dz} = 0$);
- temperature and pressure constant alongside the z axis ($\frac{dT}{dz} = 0$ and $\frac{dp}{dz} = 0$).

In Fig. 4.3, a schematic representation of the cathode side and the electrolyte+matrix of an MCFC is presented. From the gas diffusion perspective, three regions can be identified: (i) the top one represents the bulk gas phase flowing through the current collector, (ii) the middle one represents the porous cathode and (iii) the bottom one represents the electrolyte-filled cathode and matrix. The current collector is depicted as a black wavy line representing its transversal section. The cathode structure is represented by the green blocks where the open spaces between the blocks are the macropores. As it appears, some of the pores are filled or wetted with electrolyte (blue color). As mentioned above, the scope of this analysis does not include modeling of the micropores, that have not been represented, and the liquid diffusion in the electrolyte. The blue area below the dotted line signifies the electrolyte-filled matrix. The control volume assumed for the diffusion module is enclosed by the two dashed lines. Specifically, the area between the red dashed line and the cathode surface is the thin stagnant gas film where the bulk gas velocity can be assumed zero. The z axis is drawn on the right side of the picture. It shows that the axis is oriented from the bulk of the cathode gas towards the matrix; the origin ($z = 0$) is located at the interphase between the bulk flowing cathode gas and the stagnant gas film, which has a thickness of δ. The porous cathode thickness is ℓ.

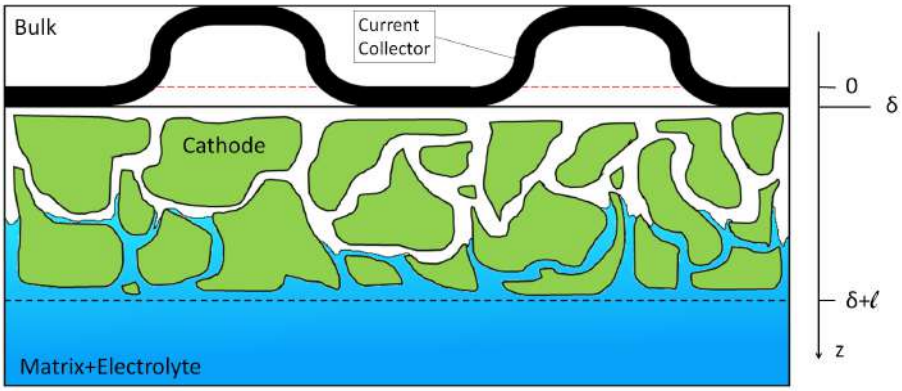

Figure 4.3: Comparison between apparent and measured CO_2 utilization factor of experimental data at same conditions but using different inert gas or CC open area.

As depicted in Fig. 4.3, the macropores are randomly oriented within the electrode. They form an interconnected 3D pattern along all spatial coordinates (x, y, and z). It is important to note that the cathode surface under the contacts with the current collector is blocked for direct gas transport from the bulk cathode gas phase. Hence, to transport gas under the current collector - cathode contacts, the gas must travel a longer distance in the porous cathode than in the cross section straight under the open cathode surface. This phenomenon has been called "shadow-effect". To consider all these issues whilst keeping only a simple one-dimensional diffusion model, an effective diffusion length $\ell_{eff} > \ell$ along the z axis will be used. It should be noted that it is dependent not only on electrode porosity and tortuosity, but also on the current collector design.

I specifically decided to not use the electrode models presented in Chapter 1 because they are far too detailed for the scope of this analysis.

4.2. Development of the gas diffusion model

4.2.1. Diffusion in the gaseous stagnant thin film

As mentioned above, to reach the bulk-cathode interface, the gases have to diffuse through a gaseous thin film of thickness δ where the cathode flow linear velocity can be assumed to be zero. The material balance that describes this section is:

$$\frac{dC_i}{dt} = -div\vec{N}_i \qquad \text{(Eq. 4.1)}$$

Where t is the time $[s]$, C_i is the concentration of the i-th gaseous component $[mol\ m^{-3}]$, $\vec{N}_i$ is the gas molar flux $[mol\ m^{-2}\ s^{-1}]$ and can be expressed as:

$$\vec{N}_i = C_i\vec{v} + \vec{j}_i \qquad \text{(Eq. 4.2)}$$

Where $\vec{v}$ is the gas velocity in the bulk $[m\ s^{-1}]$ and $\vec{j}_i$ is the molar flux due to the sole diffusion of the i-th component $[mol\ m^{-2}\ s^{-1}]$. Note that in this section, due to the absence of reactions, the formation or consumption of components is zero. Assuming steady state (i.e.: $\frac{d}{dt} = 0$) one-dimensional diffusion, and the absence of convective fluxes, the material balance can be simplified to:

$$\vec{j}_i = -\mathscr{D}_{i,mix}\frac{dC_i}{dz} \qquad \text{(Eq. 4.3)}$$

Considering the diffusion along the z-axis, $\vec{j}_i$ can be expressed as:

$$\vec{j}_i = -\mathscr{D}_{i,mix} \frac{dC_i}{dz} \tag{Eq. 4.4}$$

where $\mathscr{D}_{i,mix}$ is the diffusion coefficient of the i-th species in the cathode gas mixture [$m^2\ s^{-1}$] and z is the vertical axis coordinate [m]. Since I am considering gas diffusion at high temperature and low pressure, the concentration of the i-th component can be expressed by the ideal gas law, and the balance becomes:

$$\frac{d}{dz}\left(\mathscr{D}_{i,mix} \frac{d\frac{p\,x_i}{RT}}{dz}\right) = 0 \tag{Eq. 4.5}$$

where T and p are the operating temperature [K] and pressure [atm], R is the gas constant [8.314 $J\ mol^{-1}\ K^{-1}$], and y_i is the molar fraction of the i-th component. Assuming a constant temperature on the z-axis, and neglecting the pressure variations, the expression can be rewritten as:

$$\frac{p}{RT}\frac{d}{dz}\left(\mathscr{D}_{i,mix} \frac{dx_i}{dz}\right) = 0 \tag{Eq. 4.6}$$

The diffusion coefficients $\mathscr{D}_{i,mix}$ are a function of the local composition of the gas mixture[1]. Thus, to solve the equation, their variations along the z-axis should be considered. However, due to the excessive number of calculations and iterations this procedure would require, I assumed a constant diffusion coefficient ($\mathscr{D}_{i,mix,av}$) along the z-axis, locally evaluated on the 2D cell plane as the average between the diffusion coefficient at the bulk composition and at the composition after the diffusion. Consequently, Eq. 4.6 simplifies to:

$$\frac{p\mathscr{D}_{i,mix,av}}{RT}\frac{d^2x_i}{dz^2} = 0 \tag{Eq. 4.7}$$

And then ultimately, to the form:

$$\frac{d^2x_i}{dz^2} = 0 \tag{Eq. 4.8}$$

To solve equation 4.8, two boundary conditions must be considered:

1. at the interface between the bulk and the thin gas film ($z = 0$) the gas composition equals to that of the bulk gas phase:

$$x_i = x_{i,bulk} \tag{Eq. 4.9}$$

2. at the interface between the thin gas film and the cathode surface ($z = \delta$) the flux of the i-th reactant is equal to the consumption in the cathode volume:

$$\mathscr{D}_{i,mix,av}\frac{p}{RT}\frac{dx_i}{dz} = r_i \ell_{eff} \tag{Eq. 4.10}$$

r_i is the generation of the i-th component, expressed as:

$$r_i = -\frac{JA}{z_e F V_{Cat,eff}} \tag{Eq. 4.11}$$

where J is the current density [$A\,m^{-2}$], A is the cathode surface area [m^2], z_e is the number of electrons involved in the reaction [$-$], F is the Faraday's constant [96485 $A\,s\,mol^{-1}$], $V_{Cat,eff} = A\ell_{\text{eff}}$ is the cathode volume [m^3] related to the effective thickness ℓ_{eff} [m].

[1]The reader can find information on how I evaluated the diffusion coefficients in the Appendix B.2.: "Diffusion coefficients in the gas phase"

After solving the equation, the molar fraction profile of each reactant along the z-axis in the thin gas film over the cathode can be expressed by the following equation:

$$x_i = x_{i,bulk} - \frac{JART}{z_e F V_{Cat,eff} p \mathscr{D}_{i,mix,av}} \ell_{\mathrm{eff}} z \qquad \text{(Eq. 4.12)}$$

The value of the molar fraction of each reactant at the interface between bulk and cathode ($x_{i,interface}$) can be derived from Eq. 4.12 by substituting z with δ:

$$x_{i,inteface} = x_{i,bulk} - \frac{JART}{z_e F V_{Cat,eff} p \mathscr{D}_{i,mix,av}} \ell_{\mathrm{eff}} \delta \qquad \text{(Eq. 4.13)}$$

4.2.2. Diffusion in the cathode pores

After reaching the bulk-cathode interface, the gas can diffuse into the pores of the electrode and reach the point where it reacts. In the cathode macropores the material balance can be expressed as:

$$\frac{dC_i}{dt} = -div\vec{N}_i + r_i = -div\left(C_i\vec{v} + \vec{j}_i\right) + r_i \qquad \text{(Eq. 4.14)}$$

As done previously, I can assume steady state, one-dimensional diffusion, and an absence of convective fluxes, thus simplifying the balance expression to:

$$\frac{d\vec{j}_i}{dz} = r_i \qquad \text{(Eq. 4.15)}$$

The molar flux $\vec{j}_i$due to the sole diffusion of the i-th component is now expressed as:

$$\vec{j}_i = -\mathscr{D}_{i,mix,eff}\frac{dC_i}{dz} = -\mathscr{D}_{i,mix}\frac{\varepsilon}{\tau}\frac{dC_i}{dz} \qquad \text{(Eq. 4.16)}$$

where $\mathscr{D}_{i,mix,eff}$ represents the average effective diffusion coefficient of the i-th species in the gas mixture [$m^2\ s^{-1}$] that takes into account the porosity (ε) and the tortuosity (τ) of the cathode.

Then, using the ideal gas law and substituting Eq. 4.16 in Eq. 4.15, the following expression is obtained:

$$\frac{d}{dz}\left(-\mathscr{D}_{i,mix}\frac{\varepsilon}{\tau}\frac{d\frac{px_i}{RT}}{dz}\right) = -\frac{JA}{z_e F V_{Cat,eff}} \qquad \text{(Eq. 4.17)}$$

Finally, assuming constant T, p and the average $\mathscr{D}_{i,mix,av}$ alongside the z-axis, Eq. 4.17 can be rearranged as:

$$\frac{d^2x_i}{dz^2} = \frac{JART}{z_e F V_{Cat,eff} p \mathscr{D}_{i,mix,av}}\frac{\tau}{\varepsilon} \qquad \text{(Eq. 4.18)}$$

To solve Eq. 4.18, the following boundary conditions should be considered:

1. at the interface between the cathode surface and the thin film ($z = \delta$) the composition is the interface composition:

$$x_i = x_{i,interface} \qquad \text{(Eq. 4.19)}$$

2. at the end of the diffusion ($z = \delta + \ell_{eff}$, considering the effective diffusion length previously mentioned) the flux of the i-th reactant is equal to zero:

$$\frac{dx_i}{dz} = 0 \qquad \text{(Eq. 4.20)}$$

Thus, solving Eq. 4.18, the molar fraction profile of each reactant alongside the z-axis in the cathode macropores can be expressed with the following equation:

$$x_i = x_{i,bulk} - \frac{JART}{z_e F V_{Cat,eff} p \mathscr{D}_{i,mix,av}} \left[\frac{\tau}{\varepsilon} \left(\frac{z^2}{2} - z\ell_{eff} - z\delta + \delta\ell_{eff} + \frac{\delta^2}{2} \right) - \delta\ell_{eff} \right] \quad \text{(Eq. 4.21)}$$

Since the electrolyte can fill the pores randomly thus affecting where the reactions happen, for electrochemical model verification, we evaluated an average molar fraction between the beginning ($z = \delta$) and the maximum diffusion length ($z = \delta + \ell_{eff}$). Thus:

$$x_{i,average} = \int_{z=\delta}^{z=\delta+\ell_{eff}} \frac{\left\{ x_{i,bulk} - \frac{JART}{z_e F V_{Cat,eff} p \mathscr{D}_{i,mix,av}} \left[\frac{\tau}{\varepsilon} \left(\frac{z^2}{2} - z\ell_{eff} - z\delta + \delta\ell_{eff} + \frac{\delta^2}{2} \right) - \delta\ell_{eff} \right] \right\}}{\ell} dz \quad \text{(Eq. 4.22)}$$

Solving Eq. 4.22, the following expression for $x_{i,average}$ is obtained:

$$x_{i,average} = x_{i,bulk} - \frac{JART}{z_e F V_{Cat,eff} p \mathscr{D}_{i,mix,av}} \left(\frac{\ell_{eff}^2}{3} \frac{\tau}{\varepsilon} - \delta\ell_{eff} \right) \quad \text{(Eq. 4.23)}$$

4.3. Integration of the reactants z-axis diffusion in the model

The equations for the polarization resistances already presented in the base model of Chapter 3 were rewritten in terms of average reacting molar fraction ($x_{i,average}$) to obtain the kinetic core of the z-axis diffusion model. However, only the cathode gas molar fractions were changed (CO_2, H_2O and O_2), while the H_2 molar fraction on the anode side was kept equal to the bulk.

As mentioned, this was done because the current collector and feed component changes were applied only at the cathode side, assuming the anode having no influence on the transference number.

$$R_{conc,CO_2} = -\frac{P_{CO_2,1}}{J_{CO_3^{2-}}} \ln\left(1 - \frac{J_{CO_3^{2-}}}{P_{CO_2,2}\, p\, x_{CO_2,average}} \right) \quad \text{(Eq. 4.24)}$$

$$R_{conc,H_2O} = -\frac{P_{H_2O,1}}{J_{OH^-}} \ln\left(1 - \frac{J_{OH^-}}{P_{H_2O,2}\, p\, x_{H_2O,average}} \right) \quad \text{(Eq. 4.25)}$$

$$R_{conc,H_2} = \frac{P_{H_2}}{p \ln\left(1 + x_{H_2}\right)} \quad \text{(Eq. 4.26)}$$

$$R_{conc,O_2} = P_{O_2} p^{0.5} \frac{x_{CO_2,average}}{x_{O_2,average}^{0.5}} \quad \text{(Eq. 4.27)}$$

$$R_{\Omega} = P_{\Omega} \quad \text{(Eq. 4.28)}$$

To simulate the data a unique set of kinetic parameters was refitted. The final values are presented in Table 4.2.

To validate the new model, all data (the original data set as well as the new results obtained with He or with the higher open area cathode current collector) were simulated. The results for voltages (4.4A), CO_2 utilization factors (4.4B), and carbonate ion transference numbers (4.4C) are shown in Figure 4.4. The

Parameters	Value	Units
$\ell_{35\%\ open\ area}$	4.2	mm
$\ell_{90\%\ open\ area}$	0.9	mm
δ	20	μm
$P_{CO_2,1}$	2953.6	V
$P_{CO_2,2}$	350000	$A\,cm^{-2}\,atm^{-1}$
$P_{H_2O,1}$	8307	V
$P_{H2O,2}$	16000	$A\,cm^{-2}\,atm^{-1}$
P_{H_2}	0.111	$\Omega\,cm^2\,atm$
P_{O_2}	0.0415	$\Omega\,cm^2\,atm^{-0.5}$
$\frac{\varepsilon}{\tau}$	0.3	-

Table 4.2: Kinetic parameters fitted for the z-axis diffusion model. P_Ω depends on the cell used.

average errors are: 3.9% for the voltages, 3.5% for the CO_2 utilization factors, and 3.5% for the carbonate ion transference numbers.

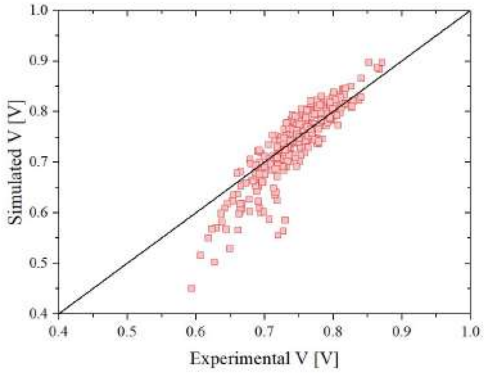

(A) Voltage

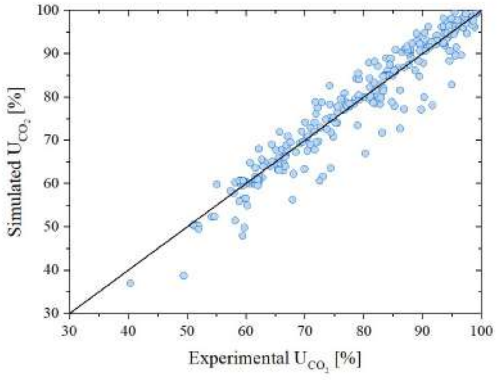

(B) CO_2 utilization

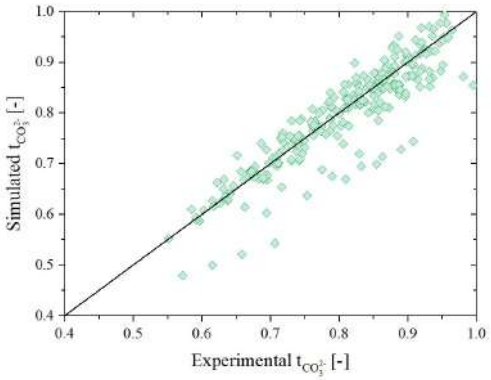

(C) Transference number

Figure 4.4: Parity plots comparing the experimental and simulated data in terms of voltage (A), utilization factor of CO_2 (B) and carbonate ions transference number (C) evaluated using the model with detailed diffusion analysis.

The model shows satisfactory results for all studied parameters. However, a "tail" can be identified in the voltage results at low voltage values. These data points correspond to experimental conditions of high CO_2 utilization and low transference number. A possible way to cope with this issue will be presented in the next chapters.

Finally, the model was tested to simulate a new set of experimental data collected with two other kinds of CCs. Both CCs have 70% open area, but two different screen features, identified as screen 1 and screen 2. After analysis of the experimental data, the effective diffusion lengths of these two sets were determined to be:

$$screen\ 1\ \ell_{eff} = base\,(flipped)\,\ell_{eff} \times 1.7 = 0.153\ cm \quad \text{(Eq. 4.29)}$$

$$screen\ 2\ \ell_{eff} = base\,(flipped)\,\ell_{eff} \times 1.25 = 0.1125\ cm \quad \text{(Eq. 4.30)}$$

where $base\,(flipped)\,\ell_{eff} = 0.6cm$ is the ℓ_{eff} of the 90% open area CC (flipped 35% open area CC). The measured-simulated parity values are depicted in Fig. 4.5 for screen 1 (4.5E, 4.5C and 4.5E) and screen 2 (4.5F, 4.5D and 4.5F). The average errors of the simulations are: 4% for the voltage, and 5.2% for both utilization factor and transference number. I tried to vary the ℓ_{eff} value, while keeping the same set of kinetic parameters as in Table 4.2, however I could not obtain better results. However, due to the low number of analyzed data, I deemed the fitting satisfactory.

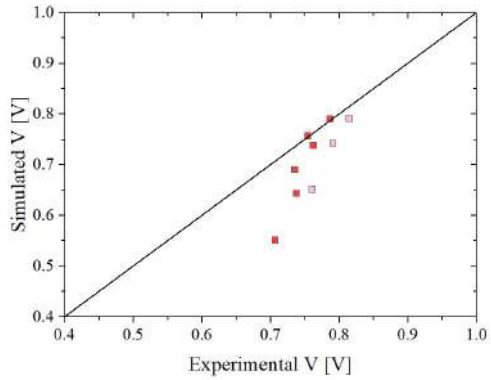

(A) Voltage

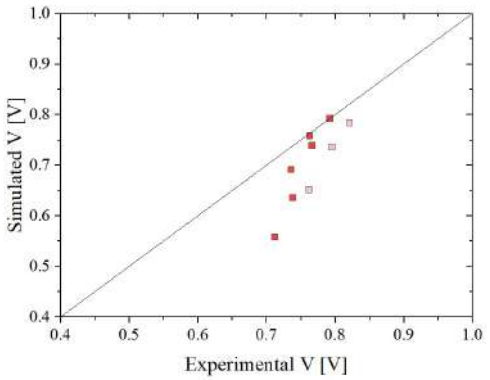

(B) Voltage

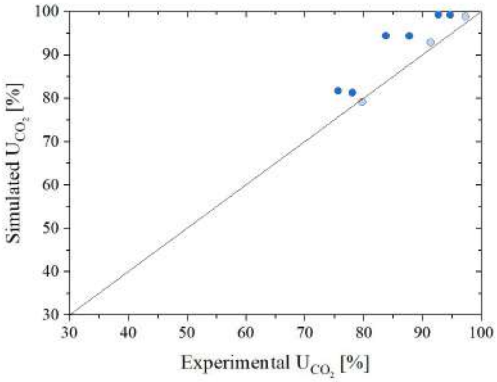

(C) CO_2 utilization

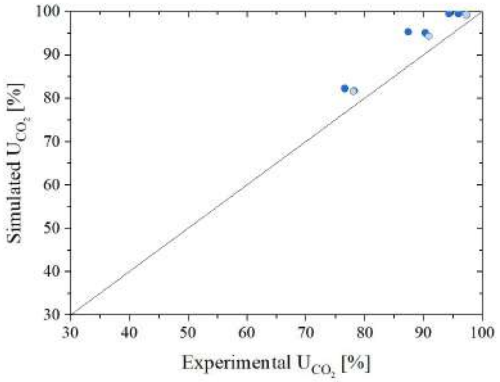

(D) CO_2 utilization

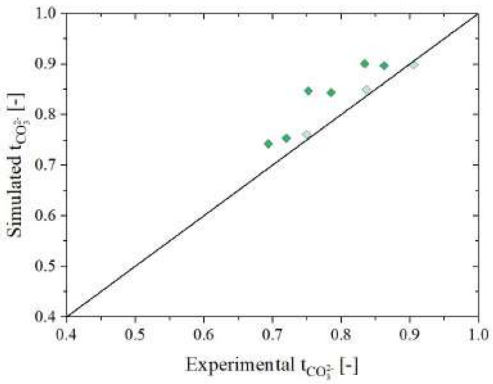

(E) Transference number

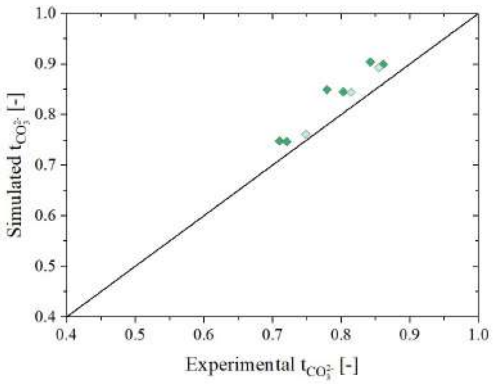

(F) Transference number

Figure 4.5: Simulated vs. measured cell performance parameters with CC screen 1 and 2 (the dark data points were collected using N_2 as inert gas, while the light ones were collected using He).

5
Model parameter sensitivity analysis

The kinetic core of the z-axis diffusion dual-anion model proposed in the previous Chapter 4 is composed of five equations with a total of eleven parameters that the users must identify from experimental data before being able to us it.

This number of parameters is not small considering also the fact that temperature dependence is not yet included in the model and each resistance will require a new parameter to define it. This can be regarded as an issue for a simplified use of the model. A large number of parameters not only means that a large set of experimental data is required to properly fit them, but also that they can induce biases due to their over- or underestimation.

If the fitting issue only depends on the user's will to acquire a sensible number of experimental data for the parameters tuning, the theoretical derivation of the kinetic core ensure that the number of parameters is not excessive. However, depending on the user's desired operating conditions it could be possible to reduce the number of parameters for an easier access to the model.

In this chapter, I will present a series of sensitivity analyses to show which parameters are effected and when they could be neglected. To perform such analysis I decided to integrate the code into Aspen Plus as this software offers an easy way to perform such sensitivity analysis that the initial Fortran code was not considering[1]. However, I decided not to use directly the SIMFC code, but a simplified version with simplified energy balances as in this state the model does not consider the temperature dependence. This was one mostly to simplify the integration process of the code into Aspen Plus.

The results of this chapter have been published with the title "*Process analysis of molten carbonate fuel cells in carbon capture applications*" in the *International Journal of Hydrogen Energy*[114].

5.1. Methodology

To perform the sensitivity analyses on the parameters of the model, five different data were used as reference points. Table 5.1 lists the reference current densities and feed rates of these points. For all data the anode and cathode compositions were the same: CO_2:H_2O:O_2:N_2 in ratio 0.04:0.10:0.10:0.76 at the cathode, and CO_2:H_2O:H_2 in ratio 0.18:0.10:0.72 at the anode. The names of the different tests indicate the values of current density [$A\,m^{-2}$] and CO_2 apparent utilization factor [%]. Each condition was tested for the two different current collector designs with different open areas (35% and 90%).

Starting from these reference conditions, different simulations were performed to improve the understanding of the behavior of the fuel cells and to identify the minimal set of parameters that could sufficiently define the outcomes. Each parameter was analyzed singularly keeping the values of all the others constant.

[1] In the SIMFC code it is necessary to manually modify the desired variable each time.

Test	J $[A\,m^{-2}]$	Cathode n_{TOT} $[mol\,h^{-1}]$	Anode n_{TOT} $[mol\,h^{-1}]$
900J_70%Uc	900	14.6	1.9
900J_90%Uc	900	11.4	1.9
900J_110%Uc	900	9.3	1.9
1200J_70%Uc	1200	19.5	2.5
1200J_90%Uc	1200	15.1	2.5

Table 5.1: Reference current density, and cathode and anode feed rates. (Name in the table: $[A\,m^{-2}]$ J current density_[%] Uc CO_2 utilization factor)

5.2. Current collector geometrical parameters

The current collector geometrical parameters are the two parameters that are dependent on the current collector's geometry and consequently have a high impact on the gas diffusion: δ and ℓ_{eff}.

As explained in the previous Chapter, δ is the thickness of the stagnant gas film over the cathode surface. Its value depends on the height of the current collectors and the distribution of its holes and blockages. The higher is its value the more laminar is the gas flux and the more penalized is the gas diffusion from bulk to electrode. For this analysis the value was varied between 0 and 0.01 cm. The δ in the reference case was assumed to be one order of magnitude lower than a usual sheet constituting a typical current collector (0.1 cm) [115].

ℓ_{eff} represents the effective cathode diffusion path that depend on the shadow effects of the CC used. The higher is its value the more extreme is the shadow effects and thus the more penalized is the gas diffusion inside the cathode pore structure. For this analysis the value was varied from 0.0 up to 0.5 cm. When ℓ_{eff} is zero, the concentration in the electrode is the same everywhere and the reacting and bulk concentrations are equal. On the other hand, when ℓ_{eff} is 0.5 cm, the cathodic CC strongly penalizes diffusion by forcing the reactant to follow a path about ten times the usual thickness of a cathode (0.5 mm) [116].

As introduced in the previous Chapter, the value of ℓ_{eff} is used to distinguish between CCs having different open areas. The data have shown that to different open areas correspond different R_Ω values (higher open areas have lower ohmic resistance). To take this aspect into account, a new correlation to represent the dependence of the R_Ω on the open area was introduced when ℓ_{eff} was varied:

$$R_\Omega = -0.303\,\ell_{eff} + 0.3773 \qquad \text{(Eq. 5.1)}$$

The equation corresponds to a straight line passing through two experimental points available at this time corresponding to R_Ω measured at ℓ_{eff} of 0.42 and 0.09 cm. The effects of the electrolyte composition and fill level, and/or the electrode conductivity are not represented, but were kept constant in the present study. It is also important to note that the open area is not the only factor that can affect the effective diffusion length. For example, other features such as the shape and distribution of the CC holes and contact areas should be also considered since they affect the mean diffusion length in the cathode.

These two parameters, δ and ℓ_{eff}, were chosen for this analysis because their values can be easily modified in MCFC by using different kind of CCs. However, it is important to emphasize that trying to decrease the ℓ_{eff} values by using very high open areas (>90%) or particular geometric designs can result in worse overall cell performance due to potential mechanical issues. This presents a challenge since a current collector with low open area is desired for increased mechanical strength and will have a lower ohmic resistance, while high open area is beneficial for enhanced gas diffusion with a higher ohmic resistance due to poor cathode-CC electrical contacting.

5.2.1. Results and discussion

Figure 5.1 shows the cell voltage (5.1A) and transference number (5.1B) values as function of δ. In the chart, test "900J_70%Uc" and test "1200J_70%Uc" were depicted as the representatives of low and high current density, respectively. Dashed lines refer to the CC with 35% open area, while continuous lines refer to the CC with 90% open area. Table 5.2 lists the maximum percentage variation for both the voltage and the transference number in each case as a function of δ.

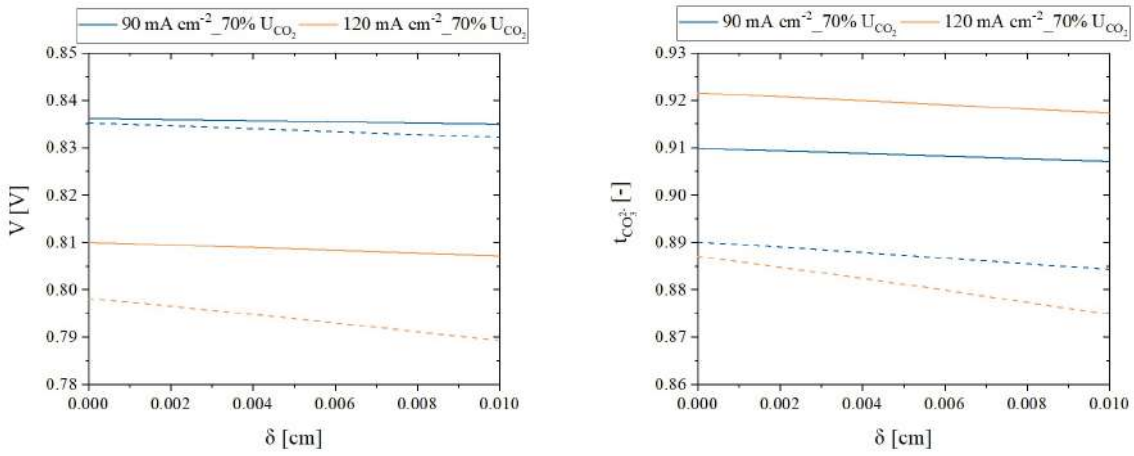

(A) Voltage

(B) Transference number

Figure 5.1: V and $t_{CO_3^{2-}}$ simulation results as a function of stagnant cathode gas film thickness, δ. Dashed lines refer to the CC with 35% open area, while continuous lines refer to the CC with 90% open area.

Test	Open Area [%]	V maximum % variation [%]	$t_{CO_3^{2-}}$ maximum % variation [%]
900J_70%Uc	35	0.36	0.65
	90	0.16	0.29
900J_90%Uc	35	0.58	0.98
	90	0.24	0.41
900J_110%Uc	35	0.85	1.33
	90	0.38	0.58
1200J_70%Uc	35	1.10	1.38
	90	0.35	0.46
1200J_90%Uc	35	1.74	2.06
	90	0.56	0.70

Table 5.2: Maximum variations of voltage and transference number with two CC designs having 35% or 90% open cathode CC areas as a function of stagnant cathode gas film thickness, δ. (Name in the table: $[A\,m^{-2}]$ J current density_[%] Uc CO_2 utilization factor).

It is evident that δ has a negligible effect on the MCFC performance especially when the cathodic CC with an open area of 90% is used. This suggests that the diffusion resistance is more likely related to the transport within the electrode pores characterized by the effective diffusion length, ℓ_{eff}. The variation

Test	V maximum % variation [%]	$t_{CO_3^{2-}}$ maximum % variation [%]
900J_70%Uc	0.29	3.43
900J_90%Uc	1.29	4.89
900J_110%Uc	2.63	6.67
1200J_70%Uc	2.69	6.16
1200J_90%Uc	5.49	9.17

Table 5.3: Maximum voltage and transference number variations at selected current density-CO_2 utilization combinations obtained by changing the ℓ_{eff} parameter between 0 and $0.5cm$. The numbers in red represent the values that exceeded the 5% set threshold. (Name in the table: $[A\,m^{-2}]$ J current density_[%] Uc CO_2 utilization factor).

as a function of δ was always much lower than 5%, thus it is reasonable to assume that the term in the kinetic model associated with parameter δ can be omitted without adversely affecting the results.

Figure 5.2 shows the cell voltage (5.2A) and transference number (5.2B) values as function of ℓ_{eff}. In this analysis the R_Ω was also varied according to Eq.5.1. The results show a large dependence on the reactants diffusion through the cathode pores of the transport resistance. This is demonstrated by the fact that both voltage and transference number significantly vary with ℓ_{eff}. It is worth noting that higher effective diffusion lengths correspond to lower current collector open areas available for gas-electrode contact resulting in longer mean diffusion paths. Increasing effective diffusion lengths in turn result in reduced voltages and CO_2 transference numbers. In the investigated ℓ_{eff} range, the maximum observed drops were 5.5% and 9.1% for the voltage and the transference number, respectively (refer to Table 5.3).

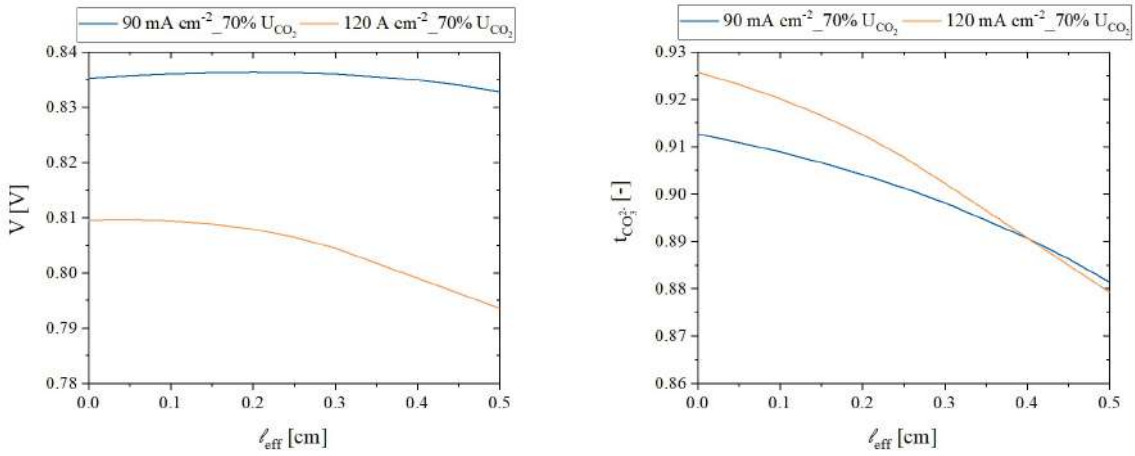

(A) Voltage

(B) Transference number

Figure 5.2: V and $t_{CO_3^{2-}}$ simulation results as a function of the effective diffusion length, ℓ_{eff}.

The graphs of Figure 5.2 also show that cathode CCs with lower open areas cause a progressively larger penalty both in power generation and carbon capture, as indicated by the decreasing voltage and CO_2 transference number. Moreover, the results of this analysis suggest that the effect of increasing diffusion resistance is larger than that of the related R_Ω drop given in Eq. 5.1. In other words, the gain from reduced ohmic losses afforded by increased contact area between the CC and cathode cannot compensate for the increased transport resistance caused by the associated increase in the mean diffusion path. This trade off can be improved by changing the CC design by optimizing the mean path via geometric

and open area adjustments.

In addition, it can be noted that when ℓ_{eff} increases, both the voltage and the $t_{CO_3^{2-}}$ decrease faster in the tests with a higher current density (for instance in case 1200J_70%Uc). This is in line with the predictably higher transport resistance losses at higher gas fluxes through the cathode at increased current densities and higher capture rates. It is satisfying that the model simulations can properly predict what follows from physical reality. Considering that a variation of the results higher than 5% as a function of the ℓ_{eff} was observed, the term ℓ_{eff} was assumed as non-negligible in the kinetic model.

5.3. Electrode physical parameters

The electrode physical parameters are the two parameters that consider the effect of the porous structure on the cell performance: porosity (ε) and tortuosity (τ).

These two parameters affect the reactant concentrations at the gas-liquid interface inside the cathode. To assess their effects on cell performance, the ratio between cathode porosity and tortuosity was varied based on literature inputs [1, 117] between 0.25 and 0.7. This range was also chosen considering that the minimum value of tortuosity is 1, and porosity extremes are between 0 (only solid and no pores) and 1 (no electrode). This ratio was chosen as its value can, to some degree, be controlled and opportunely adjusted during the manufacturing process.

5.3.1. Results and discussion

The results of the sensitivity analysis related to the porosity/tortuosity ($\frac{\varepsilon}{\tau}$) ratio are reported in Figure 5.3 depicting two representative cases at low ($900\,A\,m^{-2}$) and high ($1200\,A\,m^{-2}$) current density. In addition, Table 5.4 shows the maximum variation for both the voltage and the transference number for each current density. As in previous simulations varying ℓ_{eff}, the results at higher current density show steeper responses confirming the dominating influence of diffusion.

The response to $\frac{\varepsilon}{\tau}$ seems negligible with the cathode current collector of 90% open area. However, with a lower, 35%, open area, the performance of the fuel cell notably decreases as the ratio decreases. When the effect of $\frac{\varepsilon}{\tau}$ is significant, the performance shows an asymptotic increase towards high $\frac{\varepsilon}{\tau}$ ratios (refer to the results for 35% open area in Figure 5.3). This confirms that $\frac{\varepsilon}{\tau}$ is a controlling factor of the diffusion contribution because high $\frac{\varepsilon}{\tau}$ ratios allow better diffusion as can be seen in the Eq. 4.23. In addition, the high current density results suggest that the performance of a fuel cell with a current collector of 35% open area can be improved to nearly reaching the performance of a cell operating with a current collector of 90% open area by increasing the ratio between porosity and tortuosity. Of course, there are practical limits to how much the cathode porosity can be increased. Thus, while the studied $\frac{\varepsilon}{\tau}$ range indicates that the potential exists for improving cell performance by maximizing $\frac{\varepsilon}{\tau}$ (especially with a value above 0.45), a specific target that can be implemented in practice cannot be inferred from this analysis.

Similar results can be observed in Table 5.4 that presents the maximum percentage variation for both the measured voltage and transference number at varying $\frac{\varepsilon}{\tau}$. As expected, the variation of the studied ratio is negligible for CCs having high open areas (the variation is lower than the fixed discrimination threshold), while it is larger for low open area CCs, especially for higher current densities and CO_2 utilization factors (the variation is higher than the fixed threshold).

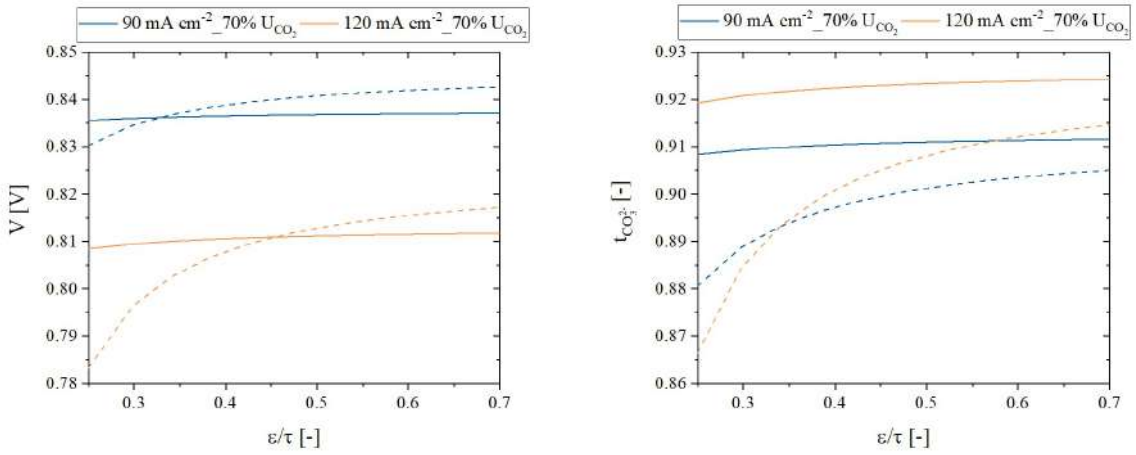

(A) Voltage

(B) Transference number

Figure 5.3: V and $t_{CO_3^{2-}}$ results obtained by the sensitivity analyses on the parameter $\frac{\varepsilon}{\tau}$ within a range between 0.25 and 0.7. Dashed lines refer to open area equal to 35%, continuous lines refer to open area equal to 90%.

Test	Open Area [%]	V maximum % variation [%]	$t_{CO_3^{2-}}$ maximum % variation [%]
900J_70%Uc	35	1.49	2.78
	90	0.19	0.35
900J_90%Uc	35	2.11	3.69
	90	0.29	0.49
900J_100%Uc	35	3.63	5.81
	90	0.45	0.69
1200J_70%Uc	35	4.34	5.56
	90	0.41	0.54
1200J_70%Uc	35	7.09	8.59
	90	0.65	0.81

Table 5.4: Maximum voltage and transference number variations with two current collector designs having 35% or 90% open cathode current collector areas at selected current density-CO_2 utilization combinations obtained by the sensitivity analyses on parameter $\frac{\varepsilon}{\tau}$. The numbers in red represent the values that exceed the 5% set threshold. (Name in the table: $[A\,m^{-2}]$ J current density_[%] Uc CO_2 utilization factor).

5.4. Kinetic parameters

In the non-linear expression for the polarization resistance two parameters can be identified: a pre-logarithmic and logarithmic.

The pre-logarithmic parameter is connected mainly to a series of constants (R, F and z_e) corrected for the data fitting and the carbonate-hydroxide equilibrium. Thus, other than the electrochemistry, this parameter can be influenced by the electrolyte composition. Consequently, changes to this parameter may be obtained by modifying the electrolyte compositions or by changing the electrocatalyst materials. Of all the variables that can be analyzed, this is probably the hardest one to be controlled efficiently.

The logarithmic one is connected mainly to the mass transport of the reactant in the liquid phase. However, some effects of the gas mass transport and of the dissolution of the gas into the melt are included. An effective way to modify the value of this parameter could be to work on the electrolyte material to find melts that can promote the dissolution of the reactants in the melt.

In the linear expression, there is only one parameter that combines both effects. In addition, P_Ω is used to represent the ohmic resistance.

These parameters were tested in a $\pm 10\%$ range around the identified values. This analysis allows testing the sensitivity to those parameters and through it, improving the quality of the kinetic model fit and identifying the parameters most influencing the outcomes.

5.4.1. Results and discussion

The effects of the kinetic parameters P_Ω, P_{H_2}, P_{O_2}, $P_{CO_2,1}$, $P_{CO_2,2}$, $P_{H_2O,1}$ and $P_{H_2O,2}$ on cell performance, with the cathode CC of 90% open area, are shown in Figure 5.4 and Table 5.5. The voltage and transference number variations are clearly presented in the bar charts of Figure 5.4. These show the maximum and minimum percentage differences in terms of voltage and transference number when the kinetic parameters are increased or decreased by 10% with reference to the values reported in Table 4.2.

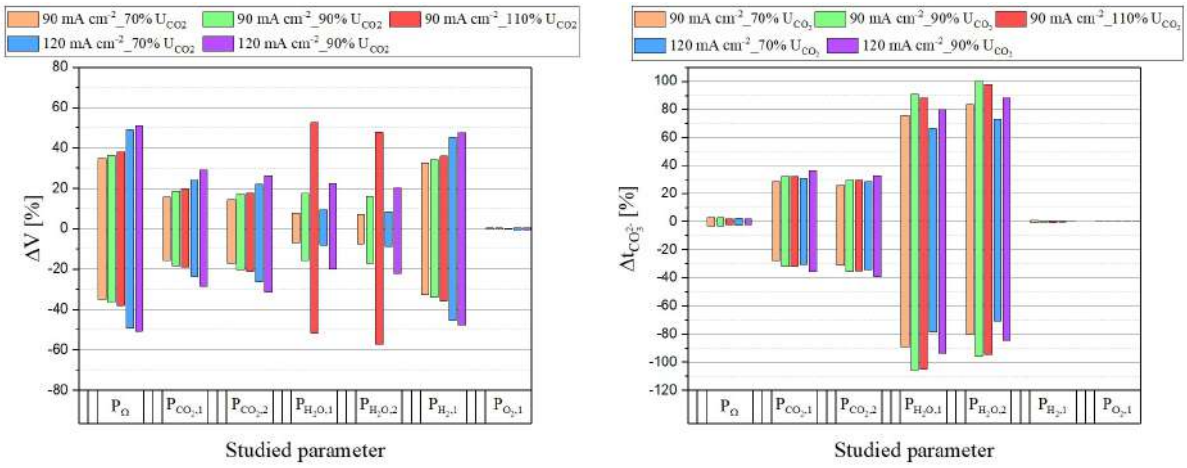

(A) Change in Voltage

(B) Change in transference number

Figure 5.4: Voltage and transference number changes when increasing or decreasing the kinetic parameters by 10% vs. the reference values listed in Table 4.2.

P_i	Test	ΔV [%] using P_i decreased by 10%	ΔV [%] using P_i increased by 10%	$\Delta t_{CO_3^{-2}}$ [%] using P_i decreased by 10%	$\Delta t_{CO_3^{-2}}$ [%] using P_i increased by 10%
P_Ω	900A_70%Uc	0.35	-0.35	-0.35	0.03
	900A_90%Uc	0.36	-0.36	-0.03	0.03
	900A_110%Uc	0.38	-0.38	-0.02	0.02
	1200A_70%Uc	0.49	-0.49	-0.03	0.02
	1200A_90%Uc	0.51	-0.51	-0.02	0.02
$P_{CO_2,1}$	900A_70%Uc	0.16	-0.16	0.28	-0.28
	900A_90%Uc	0.19	-0.18	0.32	-0.32
	900A_110%Uc	0.20	-0.19	0.32	-0.32
	1200A_70%Uc	0.24	-0.24	0.31	-0.31
	1200A_90%Uc	0.29	-0.28	0.36	-0.35
$P_{CO_2,2}$	900A_70%Uc	-0.17	0.14	-0.31	0.26
	900A_90%Uc	-0.20	0.17	-0.35	0.29
	900A_110%Uc	-0.21	0.18	-0.35	0.30
	1200A_70%Uc	-0.26	0.22	-0.34	0.28
	1200A_90%Uc	-0.31	0.26	-0.39	0.33
$P_{H_2O,1}$	900A_70%Uc	0.08	-0.07	-0.89	0.76
	900A_90%Uc	0.18	-0.16	-1.06	0.91
	900A_110%Uc	0.53	-0.52	-1.05	0.88
	1200A_70%Uc	0.09	-0.08	-0.79	0.66
	1200A_90%Uc	0.22	-0.2	-0.94	0.8
$P_{H_2O,2}$	900A_70%Uc	-0.07	0.07	0.83	-0.81
	900A_90%Uc	-0.17	0.16	1.00	-0.96
	900A_110%Uc	-0.57	0.48	0.97	-0.94
	1200A_70%Uc	-0.09	0.08	0.73	-0.71
	1200A_90%Uc	-0.22	0.20	0.88	-0.85
P_{H_2}	900A_70%Uc	0.33	-0.33	-0.01	0.01
	900A_90%Uc	0.34	-0.34	-0.01	0.00
	900A_110%Uc	0.36	-0.36	-0.01	0.01
	1200A_70%Uc	0.46	-0.46	-0.01	0.00
	1200A_90%Uc	0.48	-0.48	0.00	0.00
P_{O_2}	900A_70%Uc	0.00	0.00	0.00	0.00
	900A_90%Uc	0.00	0.00	0.00	0.00
	900A_110%Uc	0.00	0.00	0.00	0.00
	1200A_70%Uc	0.00	0.00	0.00	0.00
	1200A_90%Uc	0.00	0.00	0.00	0.00

Table 5.5: Maximum voltage and transference number variations at selected current density-CO_2 utilization combinations obtained with the 90% open area current collector. The numbers in red exceed the 0.5% threshold. (Name in the table: $[A\,m^{-2}]$ J current density_[%] Uc CO_2 utilization factor).

As shown in Figure 5.4 and Table 5.5, the sensitivity of the modeling results to the input parameters is relatively minor. For the cell potential, the greatest response is -0.57%, which translates to only 4 mV. For carbonate transference, the sensitivity shows only a 1% deviation. These results demonstrate that, in general, the model is quite robust in terms of the exact choice of parameters.

The parameters related to the carbonate path and the ones that are common to both anion paths (P_Ω, P_{H_2}, P_{O_2}, $P_{CO_2,1}$, $P_{CO_2,2}$) show similar trends in all the examined tests: the voltage shifts are typically more prominent at higher current density. The parameters related to the hydroxide path ($P_{H_2O,1}$, $P_{H_2O,2}$) also show significant voltage shifts at lower molar feed rates ($\sim 5\,mV$). The model indicates a marked dependence on the parameters related to the water effect. For instance in the "900J_110%Uc" case with

90% of open area, the maximum variation is higher than 0.5%. This test is characterized by a high (110%) theoretical CO_2 utilization factor, a total flow rate of 20-35% lower than the other tests, and a particularly low (< 80%) transference number. This is the only test where the CO_2 feed is less than what is necessary to guarantee the obtained carbonate current density. The observation suggests that it is important to focus on tuning the parameters $P_{H_2O,1}$ and $P_{H_2O,2}$ to properly simulate these operating conditions.

These results indicate that the kinetic parameters related to the resistances of the common path (P_Ω, P_{H_2}, P_{O_2}) do not influence the transference number significantly. This is in agreement with the previous analysis of the experimental results that allowed the construction of the model in Chapter 3. In particular, the P_{O_2} kinetic parameter affects voltage significantly less than the others. In addition, it can be concluded from the results in Table 5.5 that anion paths external parameters P_Ω, P_{H_2}, and P_{O_2} generate similar responses: when their values increase, the voltage decreases and the transference number stays constant or just slightly changes, which is also in agreement with the experimental results.

The parameter related to the carbonate path shows an opposite response: if $P_{CO_2,1}$ increases, the voltage and the transference number decrease; on the contrary, if $P_{CO_2,2}$ increases, the voltage and the transference number increases. This behavior can be explained considering the nature of the two parameters. $P_{CO_2,1}$ includes the activation dependencies that increase the resistance at an increasing parameter value. $P_{CO_2,2}$ lumps the contribution of reactant diffusion in the electrolyte. Thus, in this latter case an increasing value corresponds to increasing diffusion, and consequently, to a lower resistance. The two parameters related to the hydroxide path present the same voltage trend as the parameters of the carbonate one, but a reverse trend for the transference number. Specifically, when $P_{H_2O,1}$ increases the carbonate ions transference number increases, and when $P_{H_2O,2}$ increases the transference number decreases. The explanation of this fact is similar to the CO_2 response, but in this case the competing ions are the hydroxides.

5.5. Operating conditions

The examined molar fractions of H_2O and O_2 in the cathode feed were in the range of 0.05 and 0.20 representing the typical cathode feed compositions of MCFCs. For carbon capture cases, the molar fraction of CO_2 in the cathode feed was examined in a lower range, between 0.03 and 0.07. The molar fraction of H_2 in the anode feed was between 0.36 and 0.72. Constant total molar flow rate was maintained by making the appropriate adjustments in the inert nitrogen feed component. This analysis may yield the best inlet composition and operating window at which the MCFCs can operate without overly hindering performance.

5.5.1. Results and discussion

The cathode CO_2, H_2O, and O_2 molar fractions were varied between 0.03 and 0.08, 0.05 and 0.20, 0.05 and 0.20 respectively. The anode H_2 molar fraction was varied between 0.36 and 0.72. To keep the feed flow rates constant, the variation of a reacting gas molar fraction was compensated for by the opposite variation of the inert N_2 molar fraction. All other variables were kept constant.

The effects of inlet composition changes with the cathode current collector of 90% open area are shown in Figure 5.5. The figure has four different charts representing the molar fraction variations of CO_2, H_2O, O_2 in the cathode and H_2 in the anode feeds. The graphs show only the results for the 900J_70%Uc case, but the other conditions yielded similar trends. Table 5.6 details the maximum voltage and trans-

ference number variations for all the simulated feed composition cases.

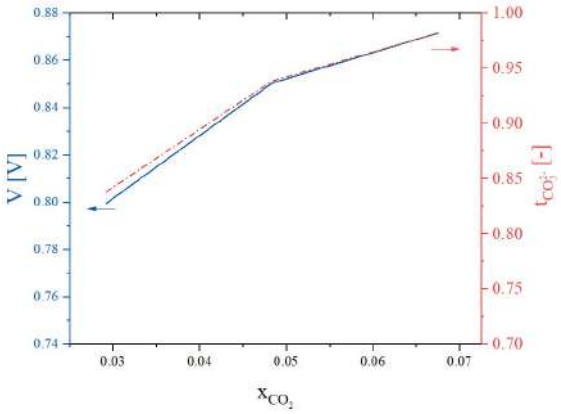

(A) Voltage as function of inlet x_{CO_2}

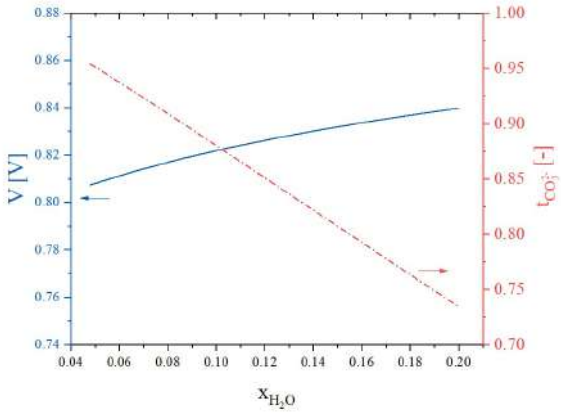

(B) Voltage as function of inlet x_{H_2O}

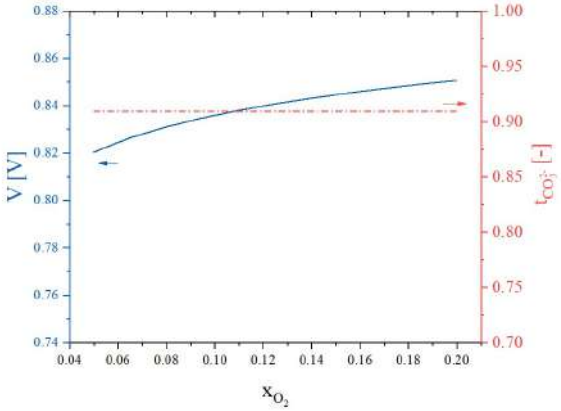

(C) Voltage as function of inlet x_{O_2}

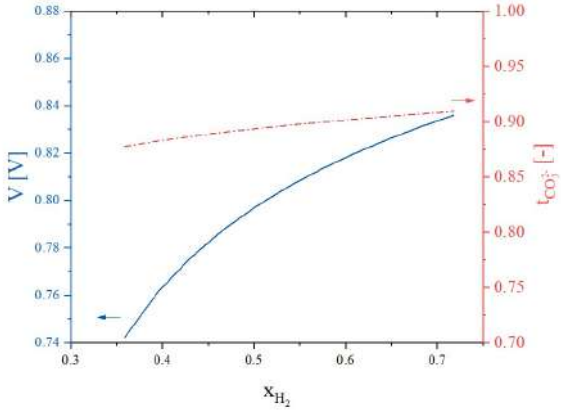

(D) Voltage as function of inlet x_{H_2}

Figure 5.5: V and $t_{CO_3^{2-}}$ results obtained by the sensitivity analyses on the molar fractions of: a) CO_2 within a range between 0.03 and 0.07; b) H_2O within a range between 0.05 and 0.20; c) O_2 within a range between 0.05 and 0.20 and d) H_2 within a range between 0.36 and 0.72. Dashed lines refer to the transference number, continuous lines refer to the voltage1.

Test	x_{CO_2} ΔV [%]	x_{H_2O} ΔV [%]	x_{O_2} ΔV [%]	x_{H_2} ΔV [%]	x_{CO_2} $\Delta t_{CO_3^{-2}}$ [%]	x_{H_2O} $\Delta t_{CO_3^{-2}}$ [%]	x_{O_2} $\Delta t_{CO_3^{-2}}$ [%]	x_{H_2} $\Delta t_{CO_3^{-2}}$ [%]
900A_70%Uc	12.55	1.72	3.56	11.21	21.69	20.04	0.01	3.50
900A_90%Uc	17.27	3.86	3.56	11.44	29.05	23.06	0.01	3.59
900A_110%Uc	25.75	12.95	4.07	11.57	40.95	20.57	0.03	3.01
1200A_70%Uc	15.74	2.15	3.70	13.54	20.19	18.18	0.01	2.80
1200A_70%Uc	22.85	4.57	3.92	14.00	28.37	19.29	0.01	2.98

Table 5.6: Maximum voltage and transference number variations at selected current density-CO_2 utilization combinations with the 90% open area current collector obtained by changing the molar fractions as listed in Figure 5.5. The numbers in red represent the values that exceed the 5% set threshold. (Name in the table: [A m-2] J current density_[%]Uc CO_2 utilization factor).

As expected, both the fuel cell voltage and transference number increase as the feed CO_2 molar fraction increases. In addition, increases in the H_2O molar fraction provides a voltage rise of up to 4% in the studied range, but at the same time leads to a decrease in the CO_2 transference number. This is useful for understanding the optimal conditions in industrial applications. For example, it may be better to work with a high molar fraction of H_2O in power generation, while the opposite may be more favorable in carbon capture applications. However, in practice, it may not be feasible to adjust the H_2O concentration in the cathode feed gas, or there may be additional efficiency implications and costs associated with doing so. This can be analyzed through the lens of process optimization. Overall, the results show a large variation in the transference numbers both for CO_2 and H_2O. As previously shown [101], the reason for this is the shift between the contributions from the carbonate and hydroxide paths.

O_2 and H_2 resistances are outside of the two parallel anion paths. The model was constructed this way because the experimental data and their analysis showed that neither gas has influence on the carbonate/hydroxide transference ratio. Consequently, as shown in Figures 5.5C and 5.5D, their main influence is manifested in the cell voltage, but not in the transference number value. In particular, the voltage increases with increasing O_2 molar fraction showing a moderate maximum variation of 3.5%, which is lower than our discrimination threshold of 5%. Similarly, the anode H_2 concentration mainly affects cell voltage. Specifically, a value of $0.74\,V$ is obtained with 36 vol. % H_2 and $0.83\,V$ with 72 vol. % H_2. Interestingly, a moderate increase in the CO_3^{2-} transference number can also be observed at increasing hydrogen concentrations with a recorded maximum of 3.6% in the examined range (see Table 5.6). This change in the transference number cannot be attributed to a direct effect of H_2 on the ratio between the two anion paths. It would be impossible considering the model construct. Rather, the different inlet concentrations yield different polarization resistances that modify the current distribution and consequently the reactant concentration profile on the 2D cell plane. In particular, a lower initial H_2 resistance due to higher inlet concentration allows for higher front-end current density that permits an increased local transfer of carbonate ions thus increasing the overall carbonate path contribution over that of the hydroxide. O_2 could show a similar behavior, but it did not manifest itself because, in the analyzed condition range, O_2 resistance is extremely low compared to other reactant resistances. This and the result from the O_2 resistance term suggest that the O_2 effect is negligible in agreement with literature that highlighted the negligible influence of the O_2 related resistance when O_2 is in large excess [4].

It is important to note that these experiments, and this model, are for a fully reformed feed. The results may be different, although the trend will be similar, with in-situ reforming of natural gas resulting in non-isothermal conditions and different anode concentration profiles. Similarly, these results are for a cross-flow cell geometry and the basic conclusions are likely transferable to a co- or counter-flow geometry, but the specific results will be slightly different.

5.6. Final considerations on the parameters relevance

The analyses performed in this Chapter indicate that all the parameters used in the model have relevance and cannot be neglected to simplify the model. The two exceptions are δ and P_{O_2}.

In the case of δ the analyses show that it could be removed without causing any relevant issue.

In the case of P_{O_2} there are two possible solutions. The easiest one is to completely neglect it as the resistance due to O_2 is very low compared to the ones ascribable to the other reactants. Otherwise, it is possible to assume a constant value independent of the concentration for R_{O_2}. However, it is important to remember that when O_2 is a limiting reactant its influence may be much greater and not negligible.

These sensitivity analyses do not offer only a view on how to simplify the model, but can also be used to study and understand how the cell can be improved to maximize the desired performance. indeed, all the studied parameters can be influenced by manufacturing.

$P_{i,1}$[2]

As shown in the development of the model, this first parameter is connected mainly to a series of constant (gas constant, Faraday's constant and number of reacting electrons) corrected for the data fitting and the carbonate-hydroxide equilibrium.

Changes in this parameter may be obtained by modifying the electrolyte compositions. For example, using a melt with additions of components that can slow the formation of stable hydroxide in the melt. Also, improvements in the electrode catalysts material may slightly influence this number value. Of all the variables that can be analyzed is probably the hardest one to be controlled efficiently.

$P_{i,2}$

This second parameter is connected mainly to the mass transport of the reactant in the liquid phase. However, some effects of the gas mass transport, the dissolution of the gas into the melt, the absorption of the reactant on the electrode, and the activation energy of the electrochemical reactions are included. There are two effective way to modify the value of this parameter. The first is to work on the electrolyte material to find melts that can promote the dissolution of CO_2 (or also O_2, H_2, H_2O) in the melt. The second one is to work on the cell constituent materials. There are two main ways to proceed: (1) dope the electrodes with appropriately studied catalysts, (2) study completely new base materials to design the electrodes. Due to the extensive literature studied on the matter, the best would be to work on doping already existing electrodes. This can also be helpful to improve mechanical properties while keeping approximately the same material characteristic such as thermal conductivity and thermal expansion coefficients.

[2] P_{H_2} and P_{O_2} include both $P_{i,1}$ and $P_{i,2}$

δ

δ is a parameter that describe the thickness of the film over the cathode where the velocity of the gas approximates zero. The sensitivity analysis has shown that its value does not particularly affect the performance. If necessary, it can be controlled by increasing or decreasing the turbulence of the gas in the bulk, for example by operating on the geometry of the current collectors.

ℓ_{eff}

ℓ_{eff} represents the effective diffusion length of the cathodic gas in the porous cathode structure. There are two ways to affect this value: (i) modify the porous structure of the cathode to decrease the actual real length of the pores, or (ii) modify the geometry of the current collectors.

In the previous Chapter 4, it was presented how a higher open area can highly improve the performance compared to a lower one. However, the open area percentage has a maximum limit: the current collectors need to cover sufficient area to collect and distribute the current density without increasing the ohmic resistance and must have enough mechanical stability.

In the work presented, the holes of the current collectors had constant area and they were evenly distributed on the current surface. However, the use of current collectors having also with different opening area or different distribution may greatly affect the performance. Also the extent of the hydroxide path increases moving from the cathode inlet to the outlet. For this reason, having current collectors with low open area in correspondence of the cathode inlet and higher towards the outlet may provide with different and better performances.

ε/τ

This parameter represents the ratio between the cathode tortuosity and porosity. As shown in the sensitivity analyses, fluctuations of its value can have high effect on the cell performance. The only way to affect this value is to directly operate on the manufacturing process of the electrode. The higher is the porosity and lower the tortuosity the higher will be the cell performance thanks to reduced muss transfer resistance. However, it is necessary to balance the porosity to avoid mechanical instability of the material.

$\mathscr{D}_{i,mix,av}$

This value represents the diffusion coefficient of the reactants in the gas phase. The higher is this number, the lower will be the mass transport resistance and consequently the performance will improve. The only way to alter this value is to use different inert gas with dimension lower than N_2 such as He. However, this is not practical in real applications.

P_{Ω}

The main way to affect the ohmic resistance is to work on the cell overall materials (electrode, current collectors, eletrolyte, etc.). FoIt is also important to consider the current collectors open area that make the resistance increases when its value increases according to the Ohm's law. In addition, component thickness can be modified as well as porosity to minimize ionic diffusion.

6
Temperature dependent model

The base model developed in Chapter 3 and the z-axis diffusion model developed in Chapter 4 do not explicitly consider a dependence on the operating temperature in the polarization resistance expressions. This is a relevant issue that hinders the possibility to apply the model to real cases that are not small laboratory scale cells with good thermal insulation or to disparate conditions that may be experienced in practical systems.

For this reason, based on experimental data, in this Chapter I will introduce an explicit dependence in the equation resistances and fit the necessary parameters to expand the model applicability. This chapter will be organized as follows:

1. introduction of a non-linear formulation for the H_2 polarization resistance to expand the applicability of the model to high fuel utilization cases;
2. brief introduction of the effects of the temperature on the dual-anion mechanism;
3. analysis of the R_Ω as a function of the operating temperature;
4. result of the fitting using a model with explicit temperature dependence.

The results of this chapter will be submitted for publication with the title "*Experimental and modelling investigation of CO_3^{2-} and OH^- equilibrium effects on Molten Carbonate Fuel Cell performance in carbon Capture applications*" in the *Frontiers in Energy Research* [118].

The experimental data presented in this chapter have been provided by EMRE and are presented in Appendix D in Tables D.1, D.3, D.5, D.2 and D.4.

6.1. H_2 non-linear polarization

In Chapter 3, the polarization resistances due to the reactants were derived from the Butler-Volmer equation. The use of said methodology allows the expression of the polarization resistances with a formulation having a non-linear dependence on the applied current density (refer to Eq. 3.31). However, when the applied current density is sufficiently lower than the limiting current density for the analyzed reactant, it is possible to linearize the formulation considering only the first term of the Taylor's series expansion (refer to Eq. 3.33).

In the development of the dual-anion model, both in its base form (Chapter 3) and in the z-axis diffusion one (Chapter 4), a non-linear formulation was considered to express the resistances of CO_2 and H_2O, and a linear one to express the resistances of O_2 and H_2. The CO_2 and H_2O resistances were considered in their non-linear form because for many experimental data the utilization factors of CO_2 were so high (>85%) that the limiting current density was of the same magnitude of the applied one and thus neglecting the non-linear term would have potentially led to greatly underestimate its value and poor modeling results. Moreover, because these two reactants are the ones that determine which anion path is followed, it is important to have the best and most accurate definition of their values. In contrast, the O_2 and H_2 resistances were simplified to a linear form because neither values seem to particularly affect the

anion paths, nor were their utilizations were particularly high to justify limiting diffusion issues for the analyzed experimental data.

In the case of H_2, I decided to reconsider this assumption for wider applicability of the model. In real applications, fuel cell working conditions characterized by high H_2 utilizations or low H_2 concentrations are likely to be encountered. Thus, I decided to rewrite the H_2 resistance in the following non-linear formulation to improve the model reliability:

$$R_{conc,H_2} = -\frac{P_{H_2,1}}{J_{TOT}} \ln\left(1 - \frac{J_{TOT}}{P_{H_2,2}\, p\, \ln\left(1 + x_{H_2}\right)}\right) \qquad \text{(Eq. 6.1)}$$

6.2. Temperature dependence

Both the simplified base model and initial z-axis diffusion model do not explicitly consider the dependence on the operating temperature in the polarization resistance expressions. This approach was followed (i) because I wanted to understand more in depth the effects of the gas concentration and diffusion on the occurring phenomena, and (ii) because the vast majority of the data were collected at the constant operating temperature of 923 K. Neglecting the temperature effects was also possible because the single cells used in the experimental campaign had a relatively small dimension that could allow for negligible temperature gradient on the plane.

However, the integration of an explicit temperature dependence is essential if the model is to be applied for industrial applications and practical process optimization of the fuel cell. These require the use of full scale fuel cells (area of about 1 m^2) in stack designs (>30 cells) for which the average operating temperature may vary, and relevant temperature gradients may be encountered if a proper energy management is not considered.

One of the most effective ways to understand the extent of the dual-anion mechanism is to analyze the utilization factor of CO_2 (U_{CO_2}). Fig. 6.1A presents a square graph "apparent vs. measured utilization factor of CO_2", where the axes have been adjusted to adequately show the data. In the graph, five sets of four experimental data (A, B, C and D) at different operating temperature are presented, with the black line representing the parity line of the graph. Information about the four conditions are shown in Table 6.1.

Data		A	B	C	D
Cathode flow rate	$Nm^3\, h^{-1}$	0.488	0.349	0.285	0.241
Cathode inlet concentration (v/v %)	CO_2:H_2O:O_2:N_2	4:10:10:76			
Anode flow rate	$Nm^3\, h^{-1}$	0.055			
Anode inlet concentration (v/v %)	CO_2:H_2:H_2O	18:72:10			
J	$mA\, cm^{-2}$	120			
Apparent U_{CO_2}	%	70	90	110	130

Table 6.1: Data used in the analysis of the temperature effects on the dual-anion mechanism.

In such a graph the greater the difference between the parity line and the measured utilization, the

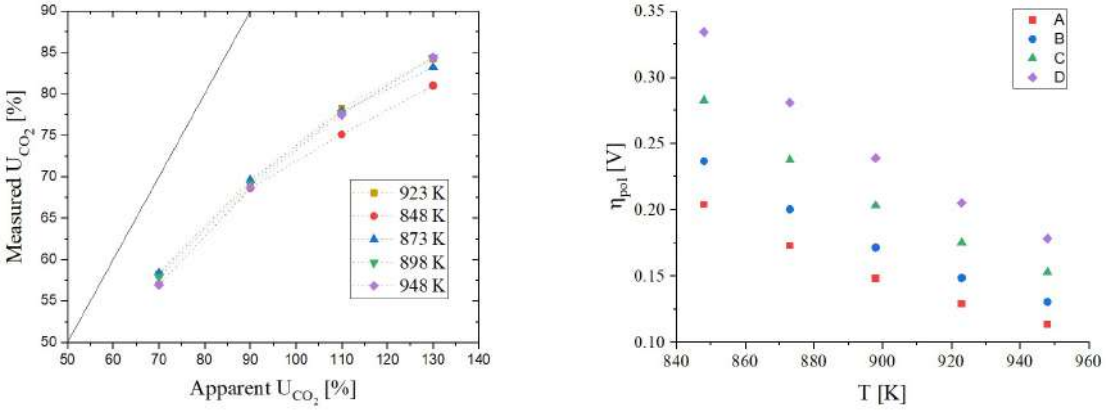

Figure 6.1: Experimentally measured utilization of CO_2 vs apparent utilization of CO_2 calculated considering all the current due to the carbonate anion path only (A). Cell polarization resistance losses ($R_{pol} = OCV - V_{experimental} - R_{\Omega}$) of different experimental data with same operating conditions of flows, composition, applied current and reactant utilizations but different operating temperature (B).

greater is the extent of the hydroxide path. Points on the parity line would represent MCFC operating with a carbonate only pathway as is traditionally described in non-carbon capture applications. The graph shows that at different operating temperatures the measured utilization factors are nearly identical. This indicates that the temperature has a negligible effect on the choice between the carbonate or the hydroxide path. This result is in agreement with what was observed in the previous sections, where it was established that the extent of one path over the other is highly dependent on the diffusion process in the gas phase (which is only slightly affected by the temperature in the studied range). The only two data counter to this result are the two data points at high CO_2 utilization at 848 K which may indicate a very slight dependence of one or both pathways. However, the reproducibility of this data is uncertain, and the temperature is also low compared to the desired one for MCFC operations which are targeted to operate between 873 and 923 K.

In Fig. 6.1B, the polarization resistances, obtained as differences between the OCV values and the sum of the measured voltages and the measured ohmic resistances, are plotted against the operating temperatures. The trend is the same with resistance values increasing with decreasing temperature as in normal MCFC operations.

These two graphs show that the operating temperature has an effect on the polarization resistances similar to the one of cells working on carbonate ions only (low resistances correspond to high operating temperatures), but that it does not seem to have any major influence regarding the extent of one path other the other. As presented in Chapter 3, the following equations represent the z-axis diffusion model with an explicit temperature dependence:

$$R_{conc,CO_2} = -\frac{P_{CO_2,1}T}{J_{CO_3^{2-}}} \ln\left(1 - \frac{J_{CO_3^{2-}}}{P_{CO_2,2}e^{\frac{P_{CO_2,3}}{T}}\, p\, x_{CO_2,average}}\right) \qquad \text{(Eq. 6.2)}$$

$$R_{conc,H_2O} = -\frac{P_{H_2O,1}T}{J_{OH^-}} \ln\left(1 - \frac{J_{OH^-}}{P_{H_2O,2}e^{\frac{P_{H_2O,3}}{T}}\, p\, x_{H_2O,average}}\right) \qquad \text{(Eq. 6.3)}$$

$$R_{conc,H_2} = -\frac{P_{H_2,1}\,T}{J_{TOT}} \ln\left(1 - \frac{J_{TOT}}{P_{H_2,2}\, e^{\frac{P_{H_2,3}}{T}}\, p\ \ln\left(1 + x_{H_2}\right)}\right) \qquad \text{(Eq. 6.4)}$$

$$R_{conc,O_2} = P_{O_2,1} T e^{\frac{P_{O_2,2}}{T}}\, p^{0.5} \frac{x_{CO_2,average}}{x_{O_2,average}^{0.5}} \qquad \text{(Eq. 6.5)}$$

For the ohmic resistance, I considered the previously introduce equation (Eq. 3.17):

$$R_\Omega = P_{\Omega,1} e^{\frac{P_{\Omega,2}}{T}} \qquad \text{(Eq. 6.6)}$$

To fit the parameters of the ohmic resistance, I used experimental data collected at different operating temperature as reported in Fig. 6.2. Two series of data for two independent cells are reported. The trends of both series are the same, but the values are slightly different for the two cells due to minor experimental variation. Considering an average value to determine the parameters is possible and does not particularly affect the results.

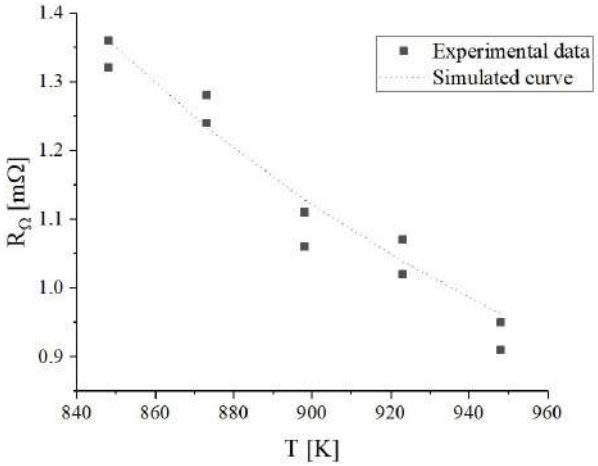

Figure 6.2: R_Ω of experimental points at different operating temperature (black points) and curve used to fit according to Eq. 6.6.

A new set of kinetic parameters to be used in the equations for the non-isothermal dual-anion model has been re-evaluated and is reported in Table 6.2.

Using this temperature dependent model, I simulated the experimental data at different operating temperatures. In Table 6.3, some of the main results of the simulations are presented to verify whether the dependence shown in the graphs of Fig. 6.1 are respected by the developed model. In the first columns the measured voltage, the simulated voltage and the % error (in absolute value) are presented. For most of the data the model agrees with the experimental results with less than 2% error. Only for a few data points collected with apparent utilization of CO_2 higher than 110% the errors increase with a maximum of 13% for the data at 848 K. However, this result aligns with findings from previous chapters that data collected with high CO_2 utilization factors had the highest errors. I attributed this to the very low concentration of CO_2 of these points that are characterized by having a pronounced influence of the hydroxide path. In the last column, the experimentally measured and the simulated utilization factors are presented with the corresponding percentage errors. In Figure 6.1A, the simulated utilization factors agree with the measured

ones both in terms of values and trend. The worst results are the ones for high utilization of CO_2 at low temperature (848 K). However, as previously mentioned, the use of MCFCs at these conditions is almost non-existent due to the low temperature. Therefore, from a practical standpoint, the minor offset in this region is negligible.

Paramter	Values	Units
$P_{CO_2,1}$	1.3	$V\ K^{-1}$
$P_{CO_2,2}$	8.98 E9	$A\,cm^{-2}\,atm^{-1}$
$P_{CO_2,3}$	-10200	K
$P_{H_2O,1}$	5.6	$V\ K^{-1}$
$P_{H_2O,2}$	1.37 E8	$A\,cm^{-2}\,atm^{-1}$
$P_{H_2O,3}$	-9200	K
$P_{H_2,1}$	0.00816	$V\ K^{-1}$
$P_{H_2,2}$	1141970	$A\,cm^{-2}\,atm^{-1}$
$P_{H_2,3}$	-8500	K
$P_{O_2,1}$	8.53E-10	$\Omega\,cm^2\,K^{-1}\,atm^{-0.5}$
$P_{O_2,2}$	10036	K
$P_{\Omega,1}$	0.033	$\Omega\,cm^{-2}$
$P_{\Omega,2}$	1341	K
$\ell_{35\%\ open\ area}$	4.2	mm
$\ell_{90\%\ open\ area}$	0.9	mm
δ	20	μm
$\frac{\varepsilon}{\tau}$	0.3	$-$

Table 6.2: Kinetic parameters used for the temperature dependent dual-anion model with non-linear resistance equations for CO_2, H_2O and H_2 and linear resistance expression for O_2.

Data	V $[V]$	Simulated V $[V]$	% error on V	$U_{CO_2,measured}$ [%]	$U_{CO_2,simulated}$ [%]	% error on U_{CO_2}
923 K_A	0.774	0.766	1.0	58.3	55.7	4.5
923 K_B	0.733	0.741	1.1	69.3	68.2	1.6
923 K_C	0.711	0.709	0.3	78.3	78.6	0.4
923 K_D	0.697	0.672	3.6	84.3	86.1	2.2
848 K_A	0.705	0.713	1.2	57.0	56.0	1.8
848 K_B	0.684	0.676	1.2	68.6	68.7	0.1
848 K_C	0.667	0.624	6.4	75.1	79.3	5.6
848 K_D	0.650	0.565	13.0	81.0	87.0	7.4
873 K_A	0.727	0.737	1.4	58.4	55.9	4.4
873 K_B	0.707	0.705	0.3	69.6	68.5	1.5
873 K_C	0.687	0.661	3.7	77.9	79.1	1.5
873 K_D	0.669	0.611	8.6	83.2	86.7	4.3
898 K_A	0.744	0.754	1.4	57.9	55.8	3.6
898 K_B	0.720	0.726	0.9	69.1	68.3	1.1
898 K_C	0.699	0.688	1.5	77.7	78.9	1.5
898 K_D	0.684	0.646	5.6	84.4	86.5	2.5
948 K_A	0.762	0.773	1.5	56.9	55.5	2.3
948 K_B	0.740	0.752	1.6	68.8	67.9	1.2
948 K_C	0.723	0.723	0.0	77.5	78.3	1.1
948 K_D	0.708	0.691	2.4	84.4	85.8	1.7

Table 6.3: Results of the temperature dependent model fitting for data A, B, C and D at different operating temperatures.

Figure 6.3 presents the results for voltage (6.3A), CO_2 utilization factor (6.3B), and carbonate ions transference numbers (6.3C) simulation for the data A,B,C and D. The average errors are: 2.85% for the voltages, 2.51% for the CO_2 utilization factors, and 2.16% for the carbonate ion transference numbers.

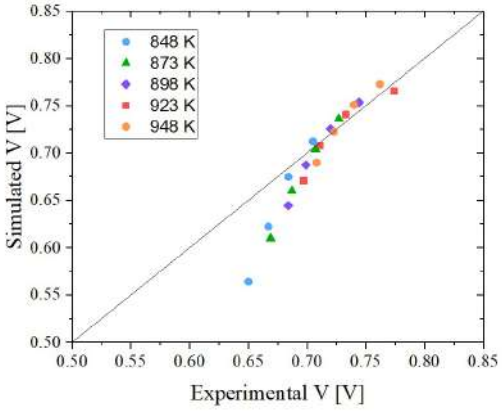

(A) Voltage

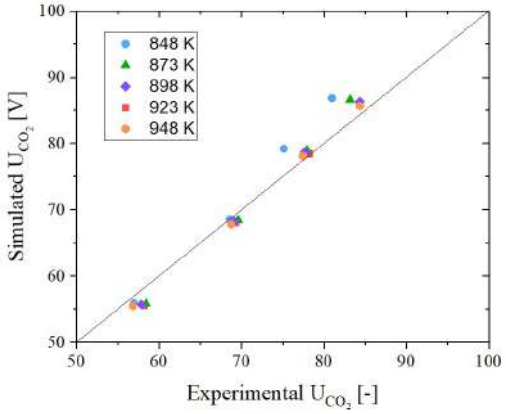

(B) CO_2 utilization

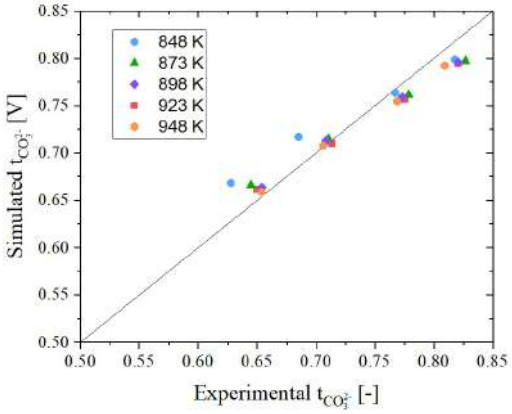

(C) Transference number

Figure 6.3: Parity plots comparing the experimental and simulated data for voltage (A), utilization factor of CO_2 (B) and carbonate ions transference number (C) evaluated using the model with explicit temperature dependence for the data A, B, C and D of Table 6.1.

Finally, Figure 6.4 shows the comparison between the experimental and the simulated data using the model with explicit dependence on the operating temperature. Figure 6.4A shows the results of the voltage simulation with an average percentage error changes of 6.75%. Figure 6.4B shows the results of the utilization factor of CO_2 simulation with an average percentage error of 4.39%. Figure 6.4C shows the results of the carbonate ions transference number simulation with an average percentage error changes of 3.95%.

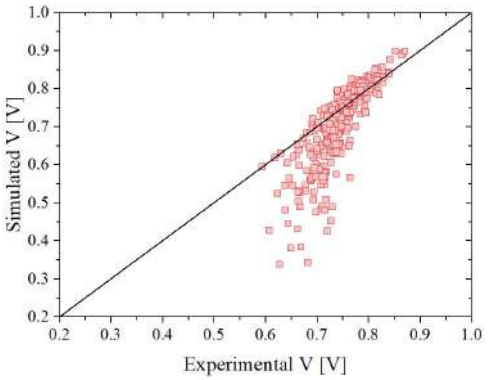

(A) Voltage

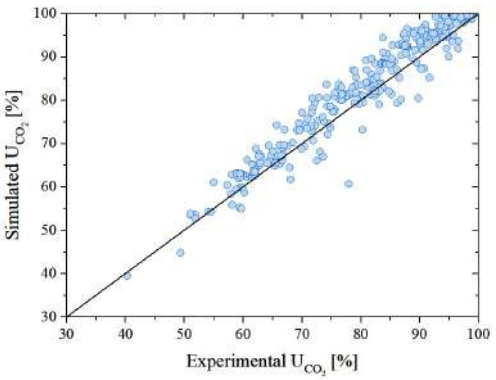

(B) CO_2 utilization

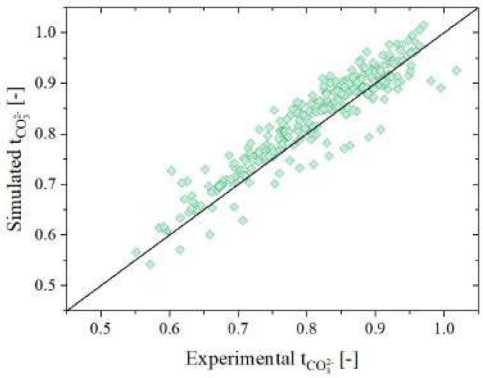

(C) Transference number

Figure 6.4: Parity plots comparing the experimental and simulated data for voltage (A), utilization factor of CO_2 (B) and carbonate ions transference number (C) evaluated using the model with explicit temperature dependence for the all the experimental data.

It is clear from the graph of the voltage, that the model has problems in simulating data at low measured voltage generating a "tail". In Figure 6.5, the same voltage simulation is represented highlighting the different data with different colors according to the experimental measured values of utilization factor of CO_2 (Figure 7.7A) and carbonate ions transference number (7.7B). The graph clear show that the "tail" is due to data having high utilization factors of CO_2 or low carbonate ions transference number. This issue will be discussed in the next chapter.

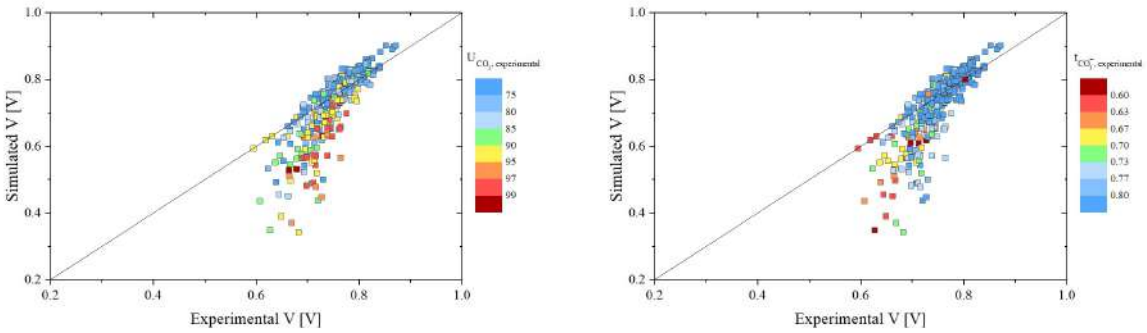

(A) Voltage parity plot as function of the U_{CO_2}.

(B) Voltage parity plot as function of the $t_{CO_3^{2-}}$.

Figure 6.5: Parity plots showing the comparison between experimental and simulated data for the voltage.

7
Further modeling improvements

The model developed until the previous Chapter considers the z-axis diffusion of the reactant gases from the bulk to the three-phase-boundary where the reactions occur and the temperature dependence on the polarization resistances. It was demonstrated to be a powerful way to simulate MCFCs working with dual-anion mechanism obtaining good results in the fitting of voltage, utilization factor of CO_2 and carbonate transference number of the experimental data.

However, it was also shown to have issues in dealing with the fitting of data with high utilization factor of CO_2 or low carbonate transference number. These are operating conditions at which the hydroxide path starts to be more significant in the cell. This may be due to a lack of an explicit dependence of the polarization resistance on the carbonate/hydroxide equilibrium that governs the presence of hydroxide in the melt.

In this Chapter, I am going to present additional experimental evidence to prove the model validity and use them to improve the expression of the polarization resistances. Also, I will show that the model is capable to deal with cells working in flow configurations different from cross-flow.

This chapter will be organized as follow:

1. analysis of new experimental evidence on the carbonate/hydroxide equilibrium;
2. analysis of the effects of the hydroxide presence in the melt over the ohmic resistance;
3. development of a new "equilibrium" model;
4. simulation results of the new model;
5. introduction of new flow configuration;
6. result of the simulations of co- and counter-flow operating cells;
7. brief comparison of the dual-anion model results to the non-dual-anion model previously developed by my research group.

The results of this chapter will be submitted for publication with the title "*Experimental and modelling investigation of CO_3^{2-} and OH^- equilibrium effects on Molten Carbonate Fuel Cell performance in carbon Capture applications*" in the *Frontiers in Energy Research* [118].

The experimental data presented in this chapter have been provided by EMRE and are presented in Appendix D in Tables D.1, D.3, D.5, D.2, D.4, D.6 and D.7.

7.1. Experimental evidences of the presence of OH^- in the melt

By considering the total mass balances performed between cathode and anode inlet and outlet, the presence of OH^- ions in the melt was assumed but never directly confirmed.

The issue presented at the end of the previous Chapter highlight the need to investigate more on the hypothesized carbonate/hydroxide equilibrium to improve the resistance expressions. Particularly, the impact of CO_2 and H_2O concentrations in the gas phase on the electrolyte should be studied. In this

line of inquiry, Raman spectroscopy was performed by ExxonMobil colleagues to analyze the changes in composition of the electrolyte at equilibrium. In particular, a molten carbonate eutectic mixture was exposed to water vapor (10%) and different amounts of CO_2, ranging from 0 – 15% while N_2 was used to balance the gas. Each condition was allowed to equilibrate for several hours until stable spectra could be collected.

The spectra were collected using a Horiba Jobin-Yvon LabRAM Aramis confocal micro-Raman spectrometer with a 532 nm diode pumped solid state laser and an 1800 grooves mm^{-1} grating. The confocal microscope was coupled to a $460 - mm$ focal length spectrograph equipped with a 180° backscattered arrangement. The microscope was a free space Olympus BXFM. The CCD was a Peltier-cooled $1024x256$, back-illuminated deep-depletion. The objective used was a Mitutoyo M Plan APO, SL20x (NA 0.42) with a working distance of 20 mm. A 15-second integration time was used with 3 scans averaged per spectrum and a collection range of $100 - 4000\,cm^{-1}$. The data was analyzed using the software package Grams AI. Band fitting was done using the Gaussian-Lorentz function on the carbonate and hydroxyl peaks in the $900 - 1200$ and $3400 - 3800\,cm^{-1}$ region of the spectrum, respectively.

The cell used for experiment was a Linkam CCR1000 high temperature catalyst cell reactor. The molten carbonate eutectic was loaded into a sapphire crucible and placed on a ceramic cloth inside of the sample holder. The sample holder was then loaded into the CCR100 cell and assembled with a quartz window and lid. The composition of the eutectic electrolyte studied was 52 mol% Li_2CO_3/48 mol% Na_2CO_3. All spectra were taken at 923 K. In the analysis below, the ratio of peak areas was used to account for changes in absolute peak intensity that can occur due to changes in focusing distance over the course of an experiment.

In Figure 7.1 a spectrum representative of the results obtained for all the analyzed compositions is presented. The major peak at $1064\,cm^{-1}$ corresponds to symmetric stretching vibration of CO_3^{2-} and is typically the most intense of the other carbonate related peaks ($1049\,cm^{-1}$ and $698\,cm^{-1}$) [119, 120]. Additionally, a hydroxide related peak at about $3500\,cm^{-1}$ was observed for all the range of studied conditions [121]. This suggests that even under normal molten carbonate fuel cell operations, hydroxide is present in the electrolyte due to the high water content at the cathode side.

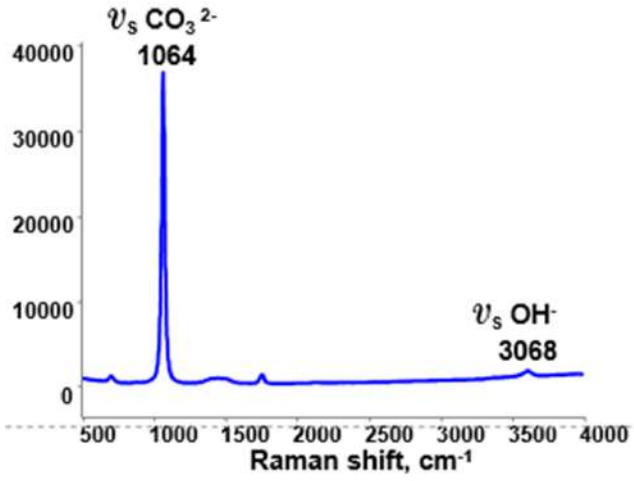

Figure 7.1: Raman spectra of lithium/sodium carbonate eutectic under 10% v/v water vapor, balanced with N_2 at 923 K.

The analysis of the peaks area can provide experimental estimates of the equilibrium constants asso-

ciated with the hydroxide/carbonate equilibrium in the melt.

$$2OH^-_{(melt)} + CO_{2(gas)} \leftrightarrow H_2O_{(gas)} + CO^{=}_{3\,(melt)} \quad \text{(Eq. 7.1)}$$

Assuming the reaction comes to equilibrium, the equilibrium constant K_{eq} can be expressed as:

$$K_{eq} = \frac{\left[H_2O\right]\left[CO_3^{=}\right]}{\left[CO_2\right]\left[OH^-\right]^2} \quad \text{(Eq. 7.2)}$$

where "$[i]$" represents the activity of the i-th component. Because the water concentration was kept constant through these experiments, the slope of a plot of $[CO_3^{2-}]/[OH^-]^2$ vs $[CO_2]$ would equal the equilibrium constant divided by $[H_2O]$. Attempts at creating a calibration curve of hydroxide species at these elevated temperatures have not been feasible to produce as hydroxide concentrations vary under most gas compositions and hydroxides can decompose at elevated temperatures. Nonetheless, because the spectroscopy provides with peak areas instead of concentrations, an estimate can be obtained. This is shown below in Figure 7.2.

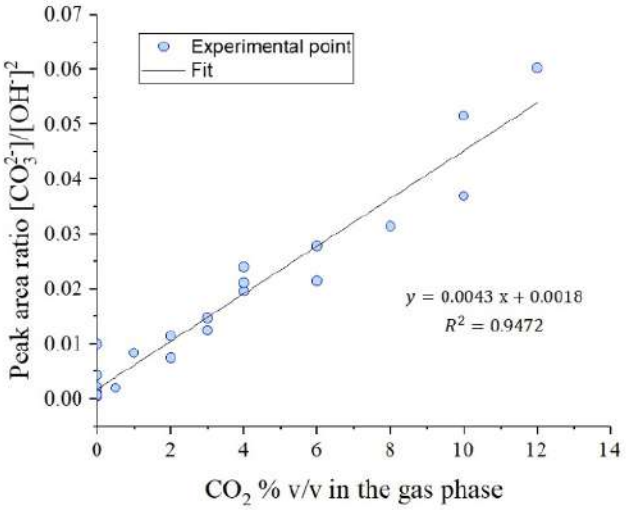

Figure 7.2: Peak Area Ratios vs CO_2 in gas phase to estimate carbonate/hydroxide equilibrium constant.

From this estimation the equilibrium constant can be assumed to be close to $0.0043\,atm^{-1}$ which indicates that the equilibrium is highly shifted toward formation of carbonate. Nonetheless, this result should be considered only from a qualitative point of view. This is in line with experimental observations on molten hydroxide fuel cells in which very small presence of CO_2 are poisonous to the cell as they completely turn into carbonate modifying the electrolyte [106, 122, 123].

From this analysis, it is possible to conclude that the cathode gas concentration has a significant influence on the electrolyte composition that is altered in accordance with the carbonate/hydroxide equilibrium. Although this aspect was mentioned in the discussions previously presented, the presented results confirmed the assumptions.

7.2. Hydroxide anion effect on the ohmic resistance

The presence of OH^- should influence the ohmic resistance (R_Ω) of the cell as it alters the electrolyte composition and thus its ionic conductivity. Since the melt equilibrium is determined by the gas phase as shown by the Raman results presented above, this means that the inlet gas composition should have an effect on the R_Ω. This dependence has not been adequately studied in literature and usually the MCFC ohmic resistance is considered as a function solely of operating temperature [46, 54].

To experimentally measure R_Ω of an MCFC, Electrochemical Impedance Spectroscopy (EIS) or Current Interruption Technique are usually performed. For the experimental campaigns, initially only a few values were measured mainly to assess the degradation level of the used cells. For this reason, initially, R_Ω was assumed to have a constant value or depend solely on the operating temperature.

However, for the data collected with cells having a CC with 90% open area, R_Ω values were measured more consistently. Consequently, for these data, I decided to examine how the simulation results would be affected by assuming the measured values of R_Ω compared to the constant values. In particular, I wanted to verify whether and how the results of the voltage simulation would be affected.

Figure 7.3 shows the simulation comparison between the data simulated using a fixed average value for R_Ω (▫) and the data using the EIS measured experimental value of R_Ω for each data (◇). The graph shows that the difference between the two simulations is not particularly significant. However, the fitting performed with the R_Ω of which we knew the exact values (◇) consistently shows simulated values closer to the parity line compared to the ones where the R_Ω was fixed (▫). In particular, if the low voltage data are considered, it appears that the EIS evaluated R_Ω is consistently lower than the average one. These low voltage data usually correspond to experimental points with low cathode concentration of CO_2 due to either high U_{CO_2} ($> 90\%$) or low $t_{CO_3^{2-}}$ (< 0.7). Thus, for these data points, the concentration of hydroxide in the melt is mostly higher compared to the other data. This is in accordance with the literature [124] that mentions that the hydroxides are more conductive compared to the corresponding carbonate ones (i.e.: KOH and K_2CO_3). For example for a melt of KOH and K_2CO_3 at 953 K if the KOH is in 97.9% mol than the conductance is 2.32 $\Omega^{-1}\,cm^{-1}$, and it decreases to 1.94 $\Omega^{-1}\,cm^{-1}$ when the KOH mol % in the melt is of 91.5%.

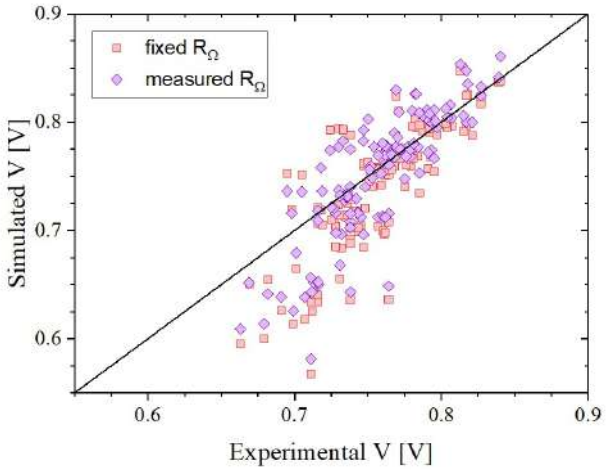

Figure 7.3: Square graph (Experimental vs. Simulated data) comparison between the data simulated using a fixed values for the internal resistance (▫) and using the values obtained from the EIS (◇).

Although, the graph of Figure 7.3 shows that a more precise value of R_Ω can increase the simulation results, this value cannot be always known without time intensive experimental testing. Thus, I decided to investigate the dependence of R_Ω on the gas composition since it was not observed before in the literature and to verify whether the EIS measured values could be predictable.

The main parameters that can influence the presence and the amount of hydroxide ions in the melt are the concentrations of CO_2 and H_2O which in fact are responsible to shift from a carbonate to a hydroxide driven path. For this study, I decided to analyze the dependence of R_Ω as function of the average (inlet-outlet) molar fractions of CO_2 ($\overline{x_{CO_2}}$ and its ratio with that of H_2O, U_{CO_2} and $t_{CO_3^{2-}}$. In Figure 7.4 the dependences of R_Ω versus all these variables are represented. The different colors and shapes of the dots indicate different series of experimental data: similar conditions with only one variable changed at a time. Dependence on H_2O molar fraction was not considered as in the studied conditions, despite its migration to the anode side, the different between inlet and outlet is not significant.

Graph 7.4A shows the dependence of R_Ω on the average molar fraction of CO_2 focusing on the range $0.0175 \leq \overline{x_{CO_2}} \leq 0.030$. On average the R_Ω increases with increasing average CO_2 molar fraction as more carbonates become present in the melt. Graphs 7.4B presents the dependence of R_Ω on the ratio between the average molar fraction of CO_2 and the average molar fraction of H_2O. On average the R_Ω increases with increasing ratio, due to the lower presence of hydroxide in the melt. Graphs 7.4D and 7.4C show the dependence of R_Ω on U_{CO_2} and $t_{CO_3^{2-}}$. On average, R_Ω decreases with decreasing transference number and increasing CO_2 utilization. Indeed, the first signifies an increasing utilization of water in the reactions and thus an increasing presence of OH^- in the melt, while the second represents high depletion of CO_2 and thus an increasing possible formation of hydroxide in the melt.

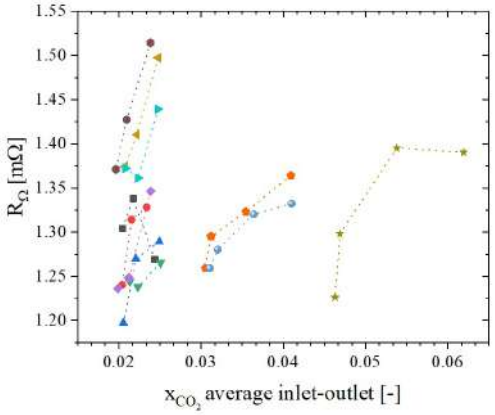

(A) [R_Ω as function of the inlet-outlet average x_{CO_2} molar fraction.

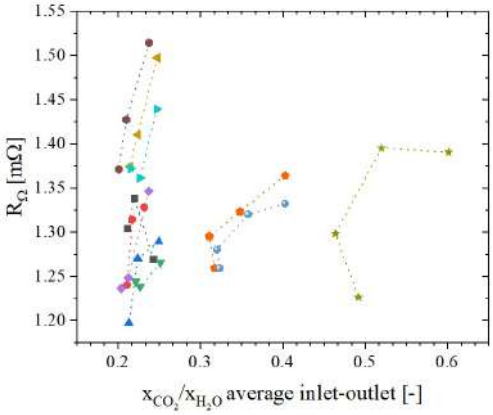

(B) R_Ω as function of the ratio between inlet-outlet average x_{CO_2} and x_{H_2O} molar fraction.

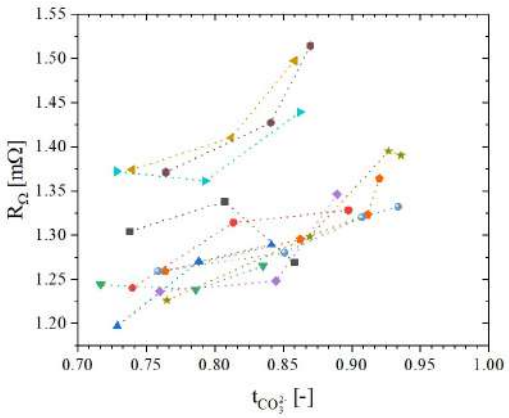

(C) R_Ω as function of the $t_{CO_3^{2-}}$.

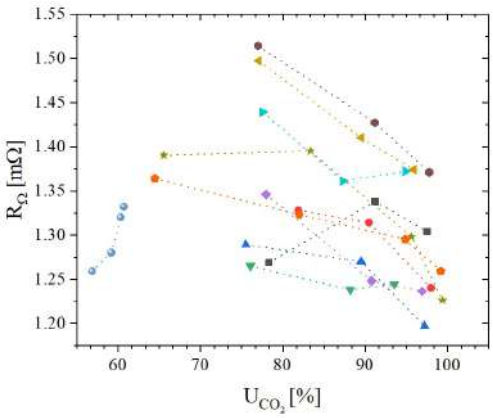

(D) R_Ω as function of the U_{CO_2}.

Figure 7.4: R_Ω dependence on the different variables that affect or result from the presence of OH^- in the electrolyte melt. Each series represented in the graphs by different colors and symbols represent a set of experimental data where all points have been collected in the same conditions with the exception of an analyzed single variable (i.e.: CO_2 inlet concentration, CO_2 utilization factor, etc.).

Thus, from the analysis of all the graphs presented in Figure 7.4, it is possible to conclude that the lower presence of CO_2 due to either a low initial concentration, high consumption, or a higher presence of the hydroxide path reduces the values of R_Ω due to an increasing amount of OH^- in the electrolyte melt. This result is particularly important because it suggests that in some sections of the operating cell, where the OH^- concentration is relatively high, the resistance can be lower compared to the cell average.

Consequently, to improve the model, a proper formulation that relates the value of R_Ω to the studied variables should be identified. R_Ω can be considered as sum of two different contributions: the resistance due to the electrolyte $R_\Omega, melt$ and the resistance due to everything else $R_\Omega, non-melt$.

$$R_\Omega = R_{\Omega,melt} + J_{TOT} R_{\Omega,non-melt} \qquad \text{(Eq. 7.3)}$$

However, there is no information to distinguish between these two contributions. Thus, I initially decided

to hypothesize all the R_Ω as only due to one function related to the electrolyte composition.

$$R_\Omega = R_{\Omega,0} + f\left(t_{CO_3^{2-}}, x_{CO_2}, \dots\right) \quad \text{(Eq. 7.4)}$$

Between all the considered variables, the carbonate ions transference number is the one that shows the clearest dependence. Therefore, for simplicity, I decided to consider only it to find a possible dependence of R_Ω on the melt composition.

The more plausible functions that can describe the dependence of R_Ω on $t_{CO_3^{2-}}$ are an exponential function (A) and a sigmoidal function (B) as presented in the graph of Figure 7.5. It is important to underline that the set of data represented in the two graphs is the same, but a final fictitious point (in blue in the graph 7.5B) was added to complete the sigmoidal graph to properly fit the curve. This was done because this second trend is more plausible since we can expect the resistance to shift from a hydroxide lower resistance to a carbonate higher resistance at increasing $t_{CO_3^{2-}}$.

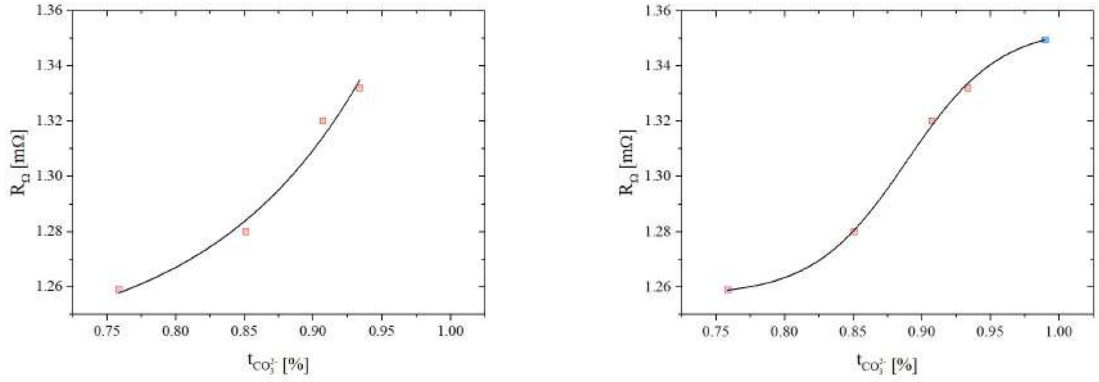

(A) Exponential behavior.

(B) Sigmoidal behavior.

Figure 7.5: Possible dependence of the R_Ω on the carbonate ions transference number. A fictious point has been introduced in graph 7.5B to better show sigmoidal behavior.

The exponential equation is of the form of:

$$R_\Omega = R_{\Omega,0} + Y_1\, e^{\frac{t_{CO_3^{2-}}}{Y_2}} \quad \text{(Eq. 7.5)}$$

and considering an average value that takes into account all the available data, it can be fitted as:

$$R_\Omega = 0.33 + 1.6 \bullet 10^{-9}\, e^{\frac{t_{CO_3^{2-}}}{0.051}} \quad \text{(Eq. 7.6)}$$

$$R_\Omega = 0.375 + 1.6 \bullet 10^{-9}\, e^{\frac{t_{CO_3^{2-}}}{0.051}} \quad \text{(Eq. 7.7)}$$

The sigmoidal equation is of the form of:

$$R_\Omega = R_{\Omega,0} + \frac{Y_3 - R_{\Omega,0}}{1 + Y_5 \bullet 10^{Y_4 - t_{CO_3^{2-}}}} \quad \text{(Eq. 7.8)}$$

and considering an average value that takes into account all the available data, it can be specific as:

$$R_\Omega = 0.3 + \frac{0.365 - 0.3}{1 + 12.89 \bullet 10^{0.889 - t_{CO_3^{2-}}}} \quad \text{(Eq. 7.9)}$$

$$R_\Omega = 0.37 + \frac{0.45 - 0.37}{1 + 12.89 \bullet 10^{0.889 - t_{CO_3^{2-}}}} \qquad \text{(Eq. 7.10)}$$

In both cases, I obtained two final expressions for the R_Ω because there were two series of data with significantly different resistance. Substituting Eqs. 7.6, 7.7, 7.9 and 7.10 for the R_Ω expression, the experimental data were refitted using the temperature dependent z-axis diffusion model.

Figure 7.6 shows the results as comparison between different data fitting using different formulation for the R_Ω: average value of the data series, EIS measured value for each data, exponential and sigmoidal formulation.

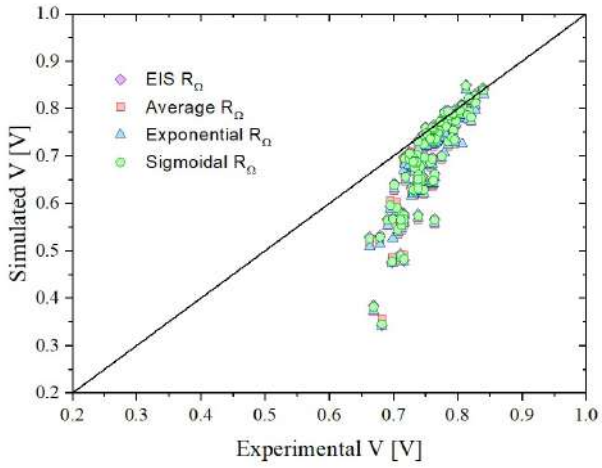

Figure 7.6: Comparison between simulation and experimental data using different solutions for how to express R_Ω.

As expected, the graph shows that (i) none of the different solutions offer a fitting that is significantly more accurate than using the average value, and that (ii) a more accurate expression for the R_Ω does not appear to solve the "tail" issue of the voltage simulation. From this analysis on the ohmic resistance, it can be concluded that the R_Ω of an MCFC is influenced by the inlet gas composition when it can lead to changes in the electrolyte compositions, and thus this phenomenon was not evidenced in past works. In the analyzed case, water forms hydroxides that substitutes the carbonates of the melts. This allow the R_Ω to decrease in accordance with [104]. However, although this result is interesting, it does not offer a better solution in the fitting of the data. For this reason, for all the next simulations I decided to continue using an R_Ω average value for the old series of data that missed the R_Ω value measured through EIS, and to use the R_Ω value measured with EIS for the data for which this is known.

7.3. Final optimized model

As shown in the graphs presented at the end of the previous Chapter, the model has a problem in properly dealing with the voltage simulation of data at high utilization of CO_2 (>90%) or low transference number of carbonate ions (<0.7). This may be because the carbonate-hydroxide equilibrium has not been properly introduced in the resistance equations. Assuming fast kinetics, the equilibrium should regulate the presence of hydroxide in the melt, thus controlling when the hydroxide path can increase. Since the simulations of the utilization factor of CO_2 and the one of the carbonate ions transference number do not show similar behavior, I think the problem is that we overestimate the hydroxide resistance when

the hydroxide path increases its extent, thus underestimating the voltage. The polarization resistance equations of both CO_2 and H_2O are written in the following form:

$$R_{conc,i} = -\frac{P_{i,1}\,T}{J_m}\ln\left(1 - \frac{J_m}{P_{i,2}\,e^{\frac{P_{i,3}}{T}}\,p_i}\right) \qquad \text{(Eq. 7.11)}$$

In this form, in the logarithmic part, the ratio between the bulk and the reacting concentration is represented. Thus, as explained in the model development, $P_{i,2}\,e^{\frac{P_{i,3}}{T}}$ groups the mass transfer resistance that involves dissolution of the reactants in the melt, diffusion of reactant in the melt, etc.

The pre-logarithmic $\frac{P_{i,1}\,T}{J_m}$ is actually $\frac{\alpha_i' RT}{\alpha_e' z_e F J_m}$, where $P_{i,1}$ groups the following expression of constant: $\frac{\alpha_i' R}{\alpha_e' z_e F}$. This should have a value of about $4.3\,10^{-5}\ J\ K^{-1}\ s^{-1}\ A^{-1}$ without taking into account of the correction due to the ratio between α_i' and α_e' whose values should be around 1. However, as mentioned in the literature [125], the experimentally fitted value of $P_{i,1}$ is usually higher than the calculated one. This is the same in the model here developed (refer to Table 6.2) for the $P_{i,1}$ of CO_2, H_2O, but also H_2. However, although in the case of H_2 the value is still close to the one calculated, for both CO_2 and H_2O this value greatly differs. I think that in the development of the model, to properly fit the data, I unconsciously included a correction to consider the equilibrium, consequently altering the resistance values. However, since this is not properly specified and is constant all over the cell plane, I think that it resulted in overestimating the resistances values (especially of H_2O) especially where the extent of the hydroxide path is more prominent than the carbonate one.

Therefore, to properly express the polarization resistances of CO_2 and H_2O, I should consider a more precise way to include the equilibrium effects on the anions. I can assume the polarization resistances of both CO_2 and H_2O as the product between the pure electrochemical resistance and a function of the concentration of the related anion in the melt that increases or decreases the apparent resistance value according to the melt composition. I assume this function as the one presented in Eq. 7.12, being "i" the gas component (CO_2 or H_2O) and "m" the related anion (CO_3^{2-} or OH^-).

$$R_i = \not{\ell}\left(C_m\right) \times R_{i,\ electrochemical} \qquad \text{(Eq. 7.12)}$$

However, I do not know how to accurately express the anion concentrations in the melt. Thus, considering the carbonate-hydroxide equilibrium reactions, I can express the two functions as dependent on the ratio between the two anions concentrations multiplied by a constant for conversion (Υ_m) as:

$$\not{\ell}_{CO_3^{2-}}\left(\frac{C_{CO_3^{2-}}}{C_{OH^-}^2}\right) = \Upsilon_{CO_3^{2-}}\left(\frac{C_{H_2O}}{C_{CO_2}}\right)\frac{1}{K_{eq}} \qquad \text{(Eq. 7.13)}$$

$$\not{\ell}_{OH^-}\left(\frac{C_{OH^-}^2}{C_{CO_3^{2-}}}\right) = \Upsilon_{OH^-}\left(\frac{C_{CO_2}}{C_{H_2O}}\right)K_{eq} \qquad \text{(Eq. 7.14)}$$

To simplify these functions and make them more manageable I added the following assumptions:

1. Since the MCFC operating temperature range is limited, K_{eq} can be assumed to be a constant value, thus we can group it together with $\Upsilon_{CO_3^{2-}}$ and Υ_{OH^-} reducing the actual number of parameters we must identify.

2. The gas concentration can be expressed as molar fraction considering the Henry's Law constant that can be assumed having a constant value in the temperature range of MCFC, thus allowing to group them with $\Upsilon_{CO_3^{2-}}$ and Υ_{OH^-}.

Therefore, I can obtain two more fairly simple formulations (Eqs. 7.15 and 7.16) that require the identification of only two additional parameters.

$$\ell_{CO_3^{2-}}\left(\frac{C_{CO_3^{2-}}}{C_{OH^-}^2}\right) = \Upsilon_{CO_3^{2-}}\left(\frac{x_{H_2O}}{x_{CO_2}}\right) \tag{Eq. 7.15}$$

$$\ell_{OH^-}\left(\frac{C_{OH^-}^2}{C_{CO_3^{2-}}}\right) = \Upsilon_{OH^-}\left(\frac{y_{CO_2}}{y_{H_2O}}\right) \tag{Eq. 7.16}$$

Substituting Eqs. 7.15 and 7.16 in Eqs. 7.13 and 7.14 we can obtain the polarization resistances of CO_2 and H_2O. Since both $A\prime_m$ and $P_{m,1}$ are constant parameters that need to be evaluated I grouped them together as: $P_{m,1} = P_{m,1}A\prime_m$.

$$R_{conc,CO_2} = -\left(\frac{x_{H_2O,average}}{x_{CO_2,average}}\right)\frac{P_{CO_2,1}\,T}{J_{CO_3^{2-}}}\ln\left(1 - \frac{J_{CO_3^{2-}}}{P_{CO_2,2}\,e^{\frac{P_{CO_2,3}}{T}}\,p\,x_{CO_2,average}}\right) \tag{Eq. 7.17}$$

$$R_{conc,H_2O} = -\left(\frac{x_{CO_2,average}}{x_{H_2O,average}}\right)\frac{P_{H_2O,1}\,T}{J_{OH^-}}\ln\left(1 - \frac{J_{OH^-}}{P_{H_2O,2}\,e^{\frac{P_{H_2O,3}}{T}}\,p\,x_{H_2O,average}}\right) \tag{Eq. 7.18}$$

$$R_{conc,H_2} = -\frac{P_{H_2,1}\,T}{J_{TOT}}\ln\left(1 - \frac{J_{TOT}}{P_{H_2,2}\,e^{\frac{P_{H_2,3}}{T}}\,p\,\ln\left(1 + x_{H_2}\right)}\right) \tag{Eq. 7.19}$$

$$R_{conc,O_2} = P_{O_2,1}Te^{\frac{P_{O_2,2}}{T}}\,p^{0.5}\frac{x_{CO_2,average}}{x_{O_2,average}^{0.5}} \tag{Eq. 7.20}$$

$$R_{\Omega} = P_{\Omega,1}e^{\frac{P_{\Omega,2}}{T}} \tag{Eq. 7.21}$$

A final set of kinetic parameters have been identified and the new values are presented in Table 7.1. Using these new set and Eqs. 7.17 (R_{conc,CO_2}), 7.18 (R_{conc,H_2O}), 7.20 (R_{conc,O_2}), 7.19 (R_{conc,H_2}) the experimental data collected in cross flow were refitted to verify whether an improvement can be obtained.

P_i	Value	Units
$P_{CO_2,1}$	0.333	$V\ K^{-1}$
$P_{CO_2,2}$	5.34 E8	$A\,cm^{-2}\,atm^{-1}$
$P_{CO_2,3}$	-7000	K
$P_{H_2O,1}$	38.5	$V\ K^{-1}$
$P_{H_2O,2}$	2.36 E6	$A\,cm^{-2}\,atm^{-1}$
$P_{H_2O,3}$	-6000	K
$P_{H_2,1}$	0.00816	$V\ K^{-1}$
$P_{H_2,2}$	8715.5	$A\,cm^{-2}\,atm^{-1}$
$P_{H_2,3}$	-4000	K
$P_{O_2,1}$	8.53E-10	$\Omega\,cm^2\,K^{-1}\,atm^{-0.5}$
$P_{O_2,1}$	10036	K

Table 7.1: Kinetic parameters used for temperature dependent dual-anion "equilibrium" model.

In Figure 7.7 the results of the simulation of the voltage data are presented in four different graphs. To allow a better comparison, graphs 7.7A and 7.7B show the simulation done using the temperature dependent model without equilibrium correction already presented at the end of the previous Chapter. Graphs 7.7C and 7.7D show the simulation done with the new temperature dependent equilibrium model. Graphs 7.7A and 7.7C are color coded according to the experimental values of CO_2 utilization, while 7.7B and 7.7D are color coded according to the experimental values of transference number. Clearly, the new model improves the results highly reducing the "tail", with an average voltage percentage error of about 4.5%, from the 6.75% of the model that did not include the "equilibrium" correction.

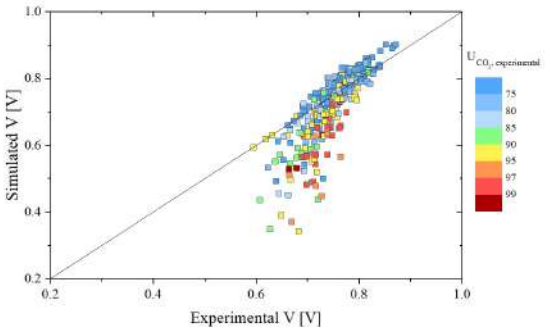

(A) Voltage parity plot as function of the U_{CO_2} using the model without equilibrium correction.

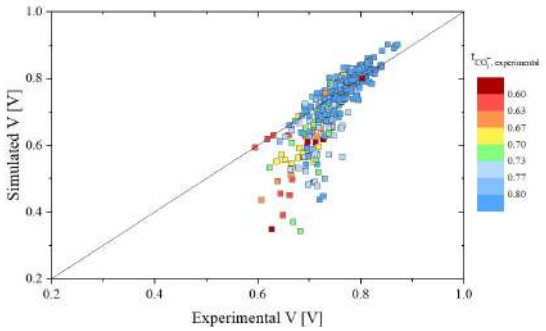

(B) Voltage parity plot as function of the $t_{CO_3^{2-}}$ using the model without equilibrium correction.

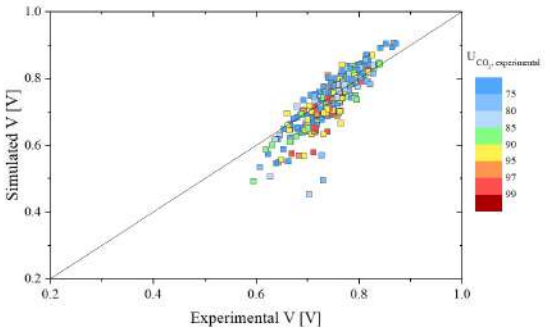

(C) Voltage parity plot as function of the U_{CO_2} using the model with equilibrium correction.

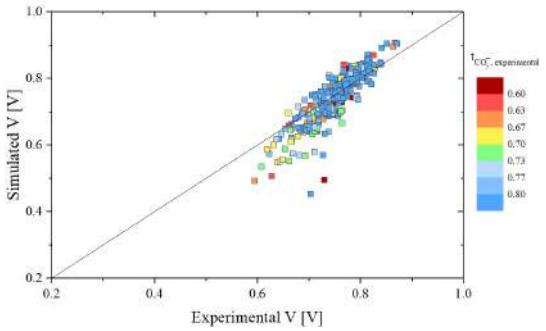

(D) Voltage parity plot as function of the $t_{CO_3^{2-}}$ using the model with equilibrium correction.

Figure 7.7: Parity plots showing the comparison between experimental and simulated data for the voltage.

Finally in Figure 7.8, the comparison between experimental data for voltage (7.8A and 7.8B), utilization factor of CO_2 (7.8C and 7.8D) and carbonate ions transference number (7.8E and 7.8F) are presented. The data has been separated according to the different CC used: 35% open area for 7.8A, 7.8C and 7.8E, and 90% open area for 7.8B, 7.8D and 7.8F. The results are satisfactory with average percentage error of 4.39% for the voltage, 5.13% for the utilization factor, and 5.33% for the carbonate ions transference number for the data with 35% open area, and of 4.63% for the voltage, 3.79% for the utilization factor, and 3.79% for the carbonate ions transference number for the data with 90% open area. Nevertheless, I encountered some numerical issue in dealing with data having very high utilization factors of CO_2 (> 95%) that I could not simulate.

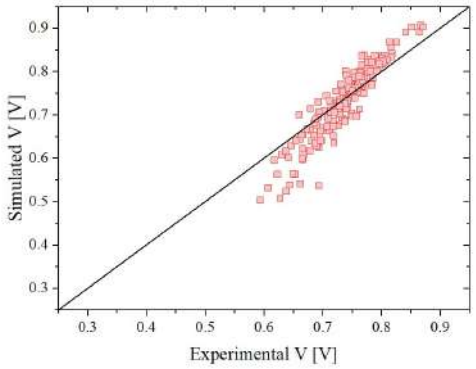

(A) Voltage, 35% CC open area.

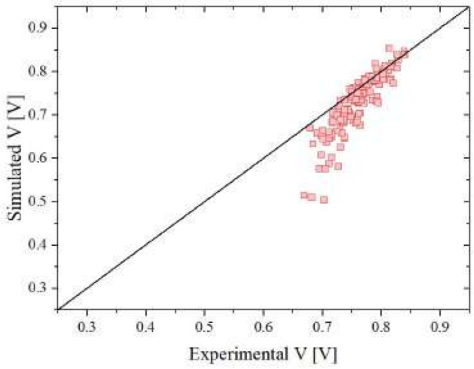

(B) Voltage, 90% CC open area.

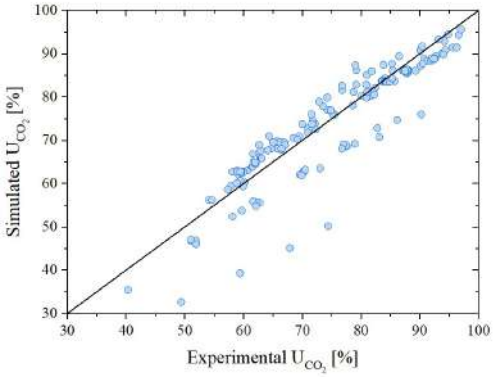

(C) U_{CO_2}, 35% CC open area.

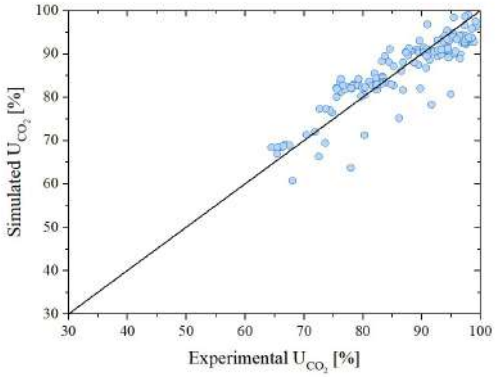

(D) U_{CO_2}, 90% CC open area.

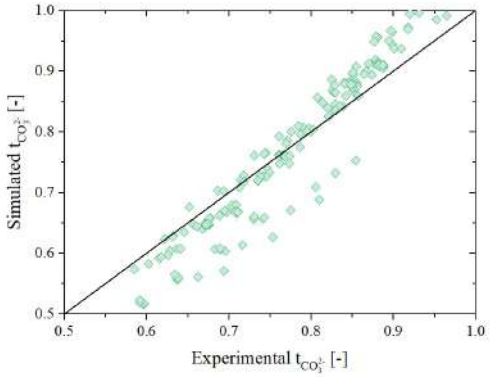

(E) $t_{CO_3^{2-}}$, 35% CC open area.

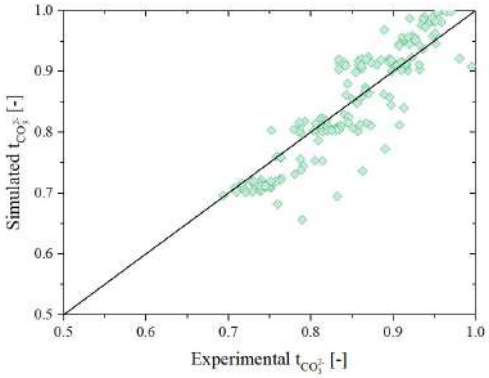

(F) $t_{CO_3^{2-}}$, 90% CC open area.

Figure 7.8: Parity plots showing the comparison between experimental and simulated data for all data sets in terms of voltage (A, B), utilization factor of CO_2 (C,D) and carbonate ions transference number (E,F) evaluated using the "equilibrium" model (H_2 non-linear) for the cross-flow data. Graphs A, C and E are for the data collected with 1st generation CC (35% open area), while B, D, and F for the one collected with the 2nd generation CC (90% open area).

7.4. Application to different flow configurations

The experimental data analyzed until this point were collected using single cells working in a cross-flow configuration. In this kind of configuration, the cathode and anode flows move in perpendicular directions as forming a cross from which the name derives (refer to Figure 7.9A).

In experimental or real application apparatus, there are three main configurations that can be encountered: co-, counter- and cross-flow. In a co-flow configuration, the cathode and anode inlet are located at the same side of the fuel cells and the two gaseous streams flow in the same direction towards the outlet (refer to Figure 7.9B). In a counter-flow configuration, the anode and cathode streams flow in the same direction but in opposite verse. Cathode inlet corresponds to anode outlet and vice versa (refer to Figure 7.9C).

From a manufacturing standpoint cross-flow is the easiest to construct due to manifolding of the fuel cell stack. Therefore traditionally commercial fuel cells have been in a cross-flow configuration. From an experimental point of view, the co-flow is the easiest in term of temperature management, since, according to its conformation the temperature will increase from inlet to outlet without possible hot-spot in the middle of the cell (unless degradation or malfunctioning interfere with proper operations). However, it is the one that provide the worst performance since the driving force of the process decreases moving from inlet to outlet. The counter-flow represents the best solution in terms of both performance and temperature management. Both co- and counter-flow configurations are difficult to construct especially when more cells are stacked together. The cross-flow configuration has performance in the middle between co and counter and can be more easily constructed compared to a counter flow. However, cross-flow configuration is the one where the steepest temperature gradient can be found.

The model developed to simulate dual-anion mechanism working MCFC is a 2D model. To simplify, this means that it evaluates the local cell variables on the cell plane alongside the coordinate x and y. To do that, the cell is divided in a series of sub-cells as shown by the scheme in Figure 7.9. To do the calculations, the known variables are the total cathode and anode inlet flows. In the cross flow case studied until now, this mean that calculations can start only from the common sub-cell of which both cathodic and anodic inlet are known (colored in magenta in Figure 7.9A). To evaluate the performance of a cell working in co-flow configuration, calculations can start from all the first row of sub-cells (colored in magenta in Figure 7.9B) that correspond to the anodic and cathodic inlet. However, as is clear from Figure 7.9C, there is no starting sub-cell of whose inlet flows are known because anode and cathode inlet are at opposite sides. To evaluate the cell performance, it is necessary to proceed as follow:

1. Hypothesize one of the two outlets
2. Calculate the cell performance using the known inlet and the hypothesized outlet
3. Verify whether the resulting evaluated inlet is equal to the real one
4. If they are the same but for a previously specified error, then the performance has been evaluated; if not, a new hypothesized outlet should be considered and performance re-evaluated.

This process makes the calculation of counter-flow cells more complex. Additionally, although the SIMFC code already foresees the possibility to work in both co- and counter-flow mode, I had to add additional iteration loops for the initialization of the carbonate ions transference number.

I tested the model to simulate both newly collected data in co- and counter-flow configuration. These data were collected using cell having CC with 90% open area.

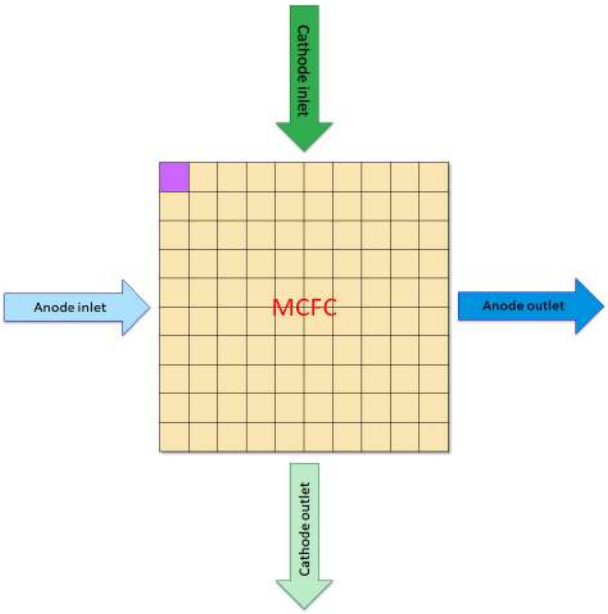

(A) Cross-flow configuration.

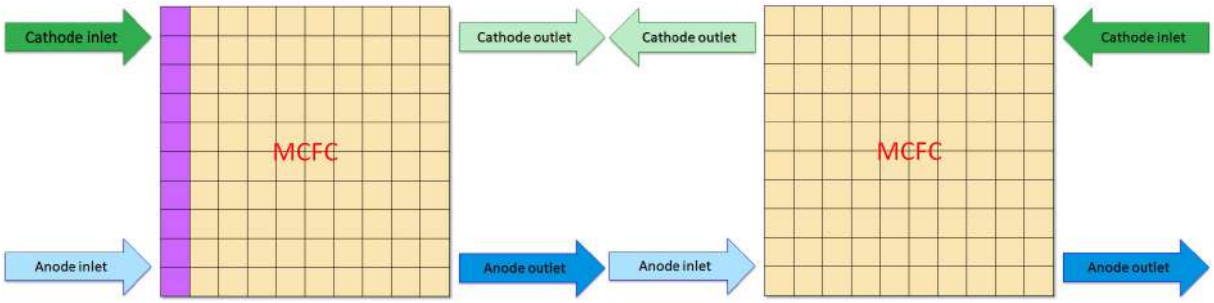

(B) Co-flow configuration.

(C) Counter-flow configuration.

Figure 7.9: MCFC flow configurations. The yellow arrows indicate the cathode inlet and outlets.

Figure 7.10 shows the results for the co-flow data for voltage (7.10A and 7.10B), utilization factor of CO_2 (7.10C and 7.10D) and carbonate ions transference number (7.10E and 7.10F) using the temperature dependent model with and without equilibrium correction.

The model without equilibrium correction shows satisfactory results, as in cross-flow configuration, with average percentage error of 4.48% for the voltage, 1.49% for the utilization factor, and 2.56% for the carbonate ions transference number. As for the previously presented cross-flow simulations, there is still the issue of the "tail" in the voltage simulation. Also the model with equilibrium correction shows satisfactory results with average percentage error of 3.15% for the voltage, 3.27% for the utilization factor, and 3.49% for the carbonate ions transference number. However, some data with high utilization of CO_2 ($> 95\%$) could not be simulated.

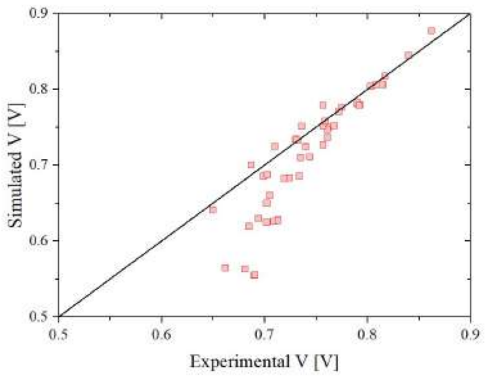

(A) Voltage, model without equilibrium correction.

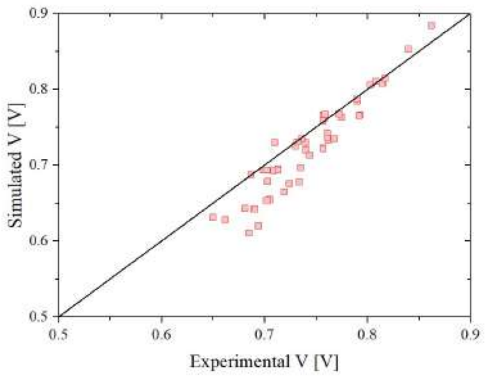

(B) Voltage, model with equilibrium correction.

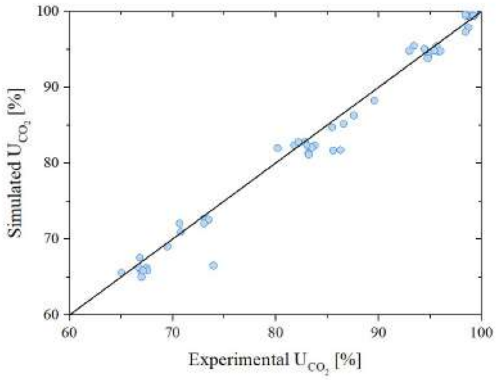

(C) U_{CO_2}, model without equilibrium correction.

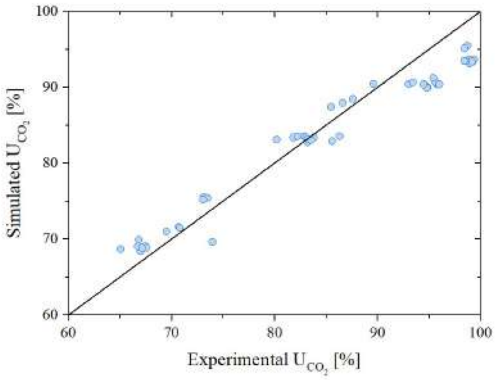

(D) U_{CO_2}, model with equilibrium correction.

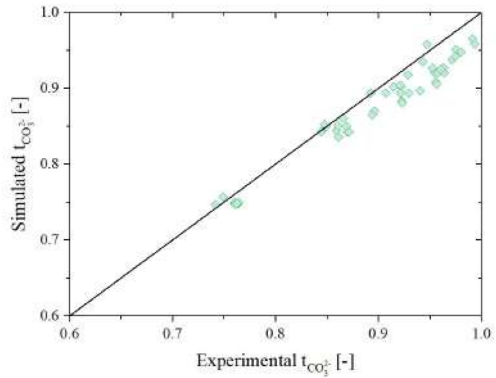

(E) $t_{CO_3^{2-}}$, model without equilibrium correction.

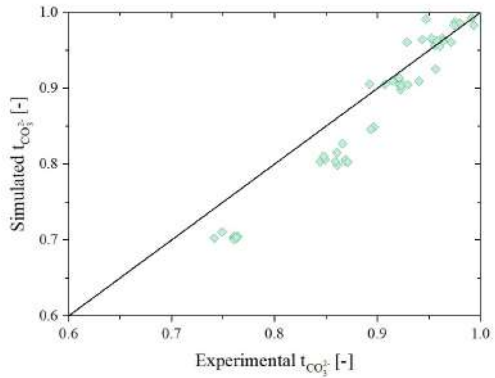

(F) $t_{CO_3^{2-}}$, model with equilibrium correction.

Figure 7.10: Parity plots showing the comparison between experimental and simulated data for all data sets in terms of voltage, utilization factor of CO_2 and carbonate ions transference number evaluated using both temperature dependent models with and without equilibrium correction for the co-flow data.

Figure 7.11 shows the results for the counter-flow data for voltage (7.11A and 7.11B), utilization factor of CO_2 (7.11C and 7.11D) and carbonate ions transference number (7.11E and 7.11F) using the

temperature dependent model with and without equilibrium correction.

The model without equilibrium correction shows satisfactory results, as for the cross-flow configuration, with average percentage error of 3.04% for the voltage, 1.20% for the utilization factor, and 2.48% for the carbonate ions transference number. Also in this case, the "tail" issue in the voltage simulation is present as expected. The model with equilibrium correction shows satisfactory results with average percentage error of 2.89% for the voltage, 2.30% for the utilization factor, and 1.73% for the carbonate ions transference number. In this case the number of data that could not be fitted is much higher. This is due to mathematical issues in dealing with the loops and the initialization of the transference number and is encountered in data with high utilization of CO_2 ($> 90\%$) or low utilization factor (< 0.75).

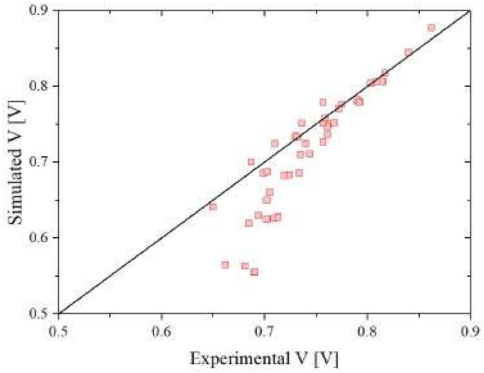

(A) Voltage, model without equilibrium correction.

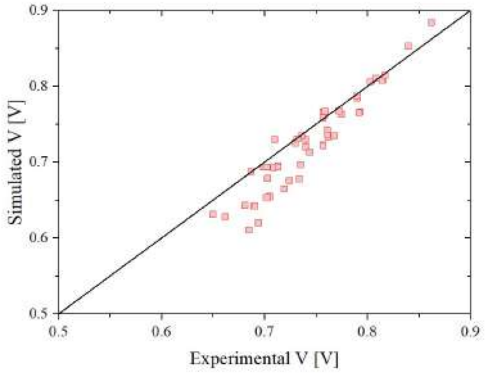

(B) Voltage, model with equilibrium correction.

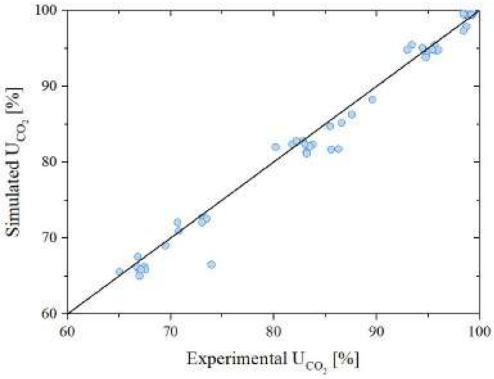

(C) U_{CO_2}, model without equilibrium correction.

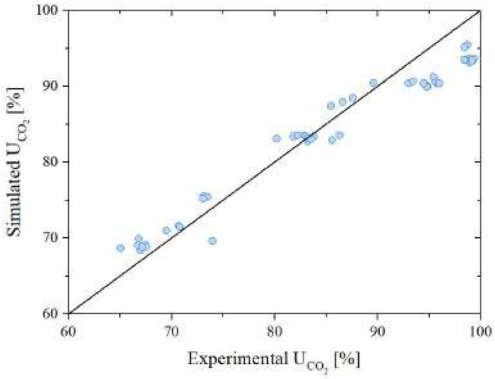

(D) U_{CO_2}, model with equilibrium correction.

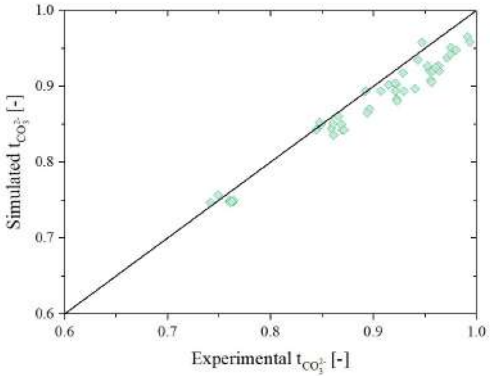

(E) $t_{CO_3^{2-}}$, model without equilibrium correction.

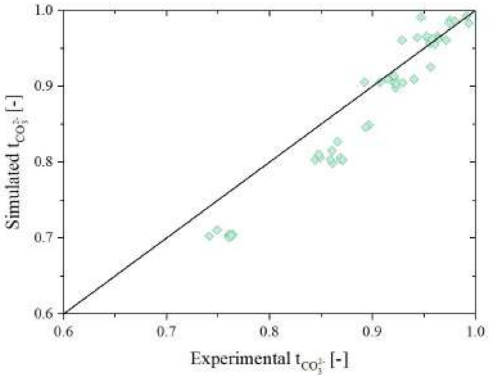

(F) $t_{CO_3^{2-}}$, model with equilibrium correction.

Figure 7.11: Parity plots showing the comparison between experimental and simulated data for all data sets in terms of voltage, utilization factor of CO_2 and carbonate ions transference number evaluated using both temperature dependent models with and without equilibrium correction for the counter-flow data.

8
Integration of Internal Reforming applied to Solid Oxide Fuel Cells

As mentioned in Chapter 1, MCFCs can work with anode inlet fuels containing CH_4 or other light hydrocarbons thanks to reforming units typically integrated within or near them. They therefore can self-produce the H_2 required by the electrochemical reactions. In the dual-anion model developed in the previous Chapter, CH_4 was not considered as inlet gas, and H_2 was used instead. However, this is not problematic if dual-anion model and internal reforming reaction occur simultaneously in an MCFC as the former depends on the cathode side inlet and the latter on the anode side one.

For this reason, I decided to integrate into SIMFC the code necessary to take this reaction into account. In this chapter I will present first a brief introduction to the reforming and how I decided to consider its inclusion in the model, and subsequently I will present the result of the simulations focusing on how the model can be used to study the catalysts distribution in terms of performance degradation and optimization.

However, the work will be presented in regard to Solid Oxide Fuel Cells (SOFCs) and not MCFCs. There are three main reason for this choice:

1. from a coding/modeling point of view the code to integrate the reforming process is the same for MCFCs and SOFCs. As both cells would use similar catalysts based on Ni, the reaction kinetics would be similar and the study of both typology can be unified. The main difference is the operating temperature. Moreover the use of SOFCs allow us to neglect the dual-anion model and focus on the analysis of reforming only.

2. this study was performed in collaboration with Fiammetta Bianchi, a colleague Ph.D. student, whose focus of study is SOFCs and with whom I collaborate to set up a model for Reversible Solid Oxide Cells [126].

3. during my Ph.D. experience I had the opportunity to spend 8 months at the Korea Institute of Science and Technology in South Korea. There I took part in two experimental studies: one on innovative SOFCs materials (also in collaboration with University of Cassino), and one on SOFCs materials for dry-reforming of CH_4 under sulfur poisoning that will be presented in the next Chapter.[1]

The results of this chapter have been published with the title "*2D Simulation for CH_4 Internal Reforming-SOFCs: An Approach to Study Performance Degradation and Optimization*" in *Energies* [129].

Initially it was consider to validate the model developed in this Chapter using an experimental campaign that was supposed to be conducted during the program final year using SOFCs made using the catalysts material studied at KIST during the first year. However, the spread of the COVID-19 prevented this from happening.

[1] On these works two paper were published: [127] and [128]

8.1. Fuel Cells and Reforming

A relevant limit to the wide spread of high temperature fuel cells on the energy market is the lack of a proper network for the distribution of low cost H_2 [130]. Several existing processes are continuously revamped to develop a more efficient and sustainable H_2 production route. For instance, steam reforming of hydrocarbons, the main approach used at industrial level, has been enhanced to obtain a higher quality outlet syngas thanks to the introduction of new reactor designs including catalytic membranes or sorption enhanced steam reforming [131, 132]. Partial oxidation reaction has been introduced in different applications thanks to the need for lower working temperature and higher fuel conversion obtained through the introduction of self-sustained electrochemical promoted catalysts [133]. Gasification of biomass has also gained literature attention in the last decades, considering its wide diversity and overall availability [134]. Water electrolysis is also becoming a competitive application through the integration with renewable sources in order to reduce requested external power and operating costs [135].

An alternative path to overcome this issue is the possibility to use directly light hydrocarbons such as CH_4 or CH_3OH as fuel. As introduced in Chapter 1, MCFCs, but also SOFCs, can work with light hydrocarbons exploiting reforming processes for the production of the H_2 needed for the electrochemical reactions.

The use of alternative fuels makes high temperature fuel cells safer due to the highly flammability and volatility of pure H_2. In addition, from an environmental perspective, it means that these fuel cells can operate using renewable fuel such as biogas reducing the total carbon print in the atmosphere.

For the integration of reforming with fuel cells there are three possible configurations that can be considered as presented in Figure 8.1:

1. External reforming (ER): the fuel cell and reforming units are two distinct blocks. In the reforming reactor, H_2 is produced from light hydrocarbons and consequently fed to the fuel cell anode inlet (Figure 8.1A);

2. Indirect internal reforming (IIR): the cell and reforming units are two neighboring blocks in order to favor thermal exchanges (Figure 8.1B);

3. Direct internal reforming (DIR): the reforming takes places inside the cell using the Ni-based anode material as catalyst (Figure 8.1C).

While the first option is the easiest to operate thanks to the lack of interactions between two different units, the others are more efficient as the heat needed for the endothermic reforming can be provided by the exothermic electrochemical process. At the same time, the amount of cell cooling provided by flowing excess air decreases because the reforming prevents an excessive temperature rise, increasing the efficiency of the system. Additionally, capital and operating costs are reduced without the use of separate external units [136]. Compared to IIR, the DIR configuration also allows further process optimization as the continuous electrochemical consumption of H_2 enhances the hydrocarbon conversion thus resulting in a more uniform H_2 distribution [137]. However, this design is characterized by considerable temperature gradients and relevant carbon deposition [138]. The high Ni anodic content, at these temperatures, favors a reforming process faster than the electrochemical one. Consequently, hydrocarbon conversion is usually complete within a small distance from the cell inlet, leading to initial severe cooling effects. Even if proper cell materials are used to reduce the mismatch among thermal expansion coefficients, the subsequent temperature gradient on the fuel cell plane may induce system failure [139]. Indeed, creep formation is favored using brittle ceramics. However, it also occurs in the metallic interconnects that are characterized by a thermal behavior strongly dependent on temperature [140]. Appropriate modifications of the anodic

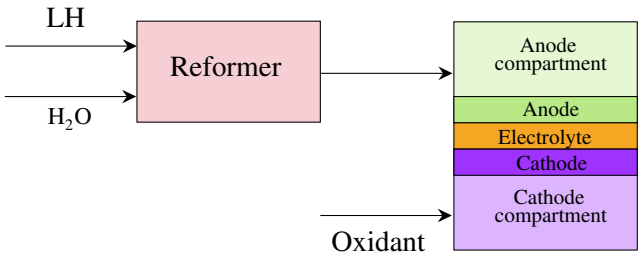

(A) External reformer.

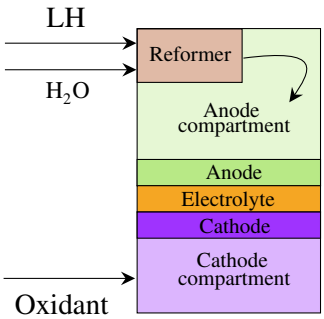

(B) Indirect internal reformer.

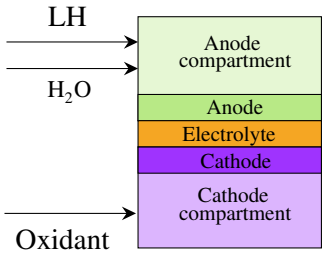

(C) Direct internal reformer.

Figure 8.1: Possible integration of fuel cell and reforming.

structure, such as the partial poisoning of active sites or doping processes [141], are under investigation to decrease the reforming rate.

Another common problem is the carbon deposition that is catalyzed by the presence of Ni and results in decreasing the active sites. This phenomenon is reversible and can be minimized by increasing the inlet steam to carbon ratio (S/C ratio) without a high fuel dilution to avoid the reduction of electrical efficiency [142].

A further issue is the presence of pollutants in the fuel stream that can degrade cell materials and deeply reduce both reforming and electrochemical performance. As for their amount, the type of such pollutants highly depends on the fuel source and usually consists of sulfur-based and chlorine-based compounds [143]. If biogas is used as fuel, siloxanes might represent relevant issues [144] too. Among these numerous compounds, H_2S is the most common poison for catalyst activity. The adsorption of S and the subsequent formation of secondary Ni−S phases can cause serious but reversible degradation [145], making fuel pre-treatment fundamental. To lessen the possible damage, alternative sulfur tolerant materials, such as metal sulfides [146], are under investigation.

For process improvement, all three configurations of MCFC and SOFC reforming integration have been analyzed in the literature using different levels of details. Such experimental and theoretical studies focus on both new industrial power generation systems and on their integration into existing plants. In different works, the simulation is usually performed considering ER or IIR units or, when DIR configurations are presented, simplifying the cell through 0D [147, 148] and 1D [142, 149] approaches. Although effective in a first feasibility analysis, such models disregard local effects, especially in terms of temperature and current density. This may lead users to contemplate possible solutions that could in reality bring the cell to failure.

A more detailed analysis is performed through 2D simulation. Considering a planar geometry, cross-section is commonly assumed as system domain to evaluate the main changes in chemical-physical features in flow direction and along cell thickness [138, 150, 151]. These studies guarantee a quite good overview of cell behavior in co- and counter-flow configurations, since flow channels can be approxi-

mated as plug flow model, whereas in the case of cross-flow design, the analysis should consider occurring gradients on cell plane section that is a less common assumption [152]. The complete knowledge of the system is reached only through a 3D approach [153, 154]. This permits a more detailed modeling but requires long computational times to reach a solution penalizing its use. On the other hand, when a tubular cell is simulated, 2D modeling is sufficient to describe completely system behavior [155].

A further step consists of the analysis of occurring degradation and poisoning phenomena. In literature, they have been mostly investigated with experimental tests on both single cells [156] and stacks [157] as well as in terms of regeneration [158]. However, there are few modeling efforts that evaluate coking and H_2S poisoning influence on electrochemical performance based on empirical [159] or theoretical formulation [160].

In the following, I am going to present how I integrated the internal steam reforming of CH_4 inside the SIMCF code for the simulation of DIR-SOFC in industrial applications using a biogas type fuel (mixture of CH_4, CO, CO_2, H_2, and H_2O).

8.2. Reforming kinetics

In the literature three different modeling approaches are mainly followed to describe the reforming reaction[137]:

1. equilibrium;
2. power law kinetic formulation;
3. surface reaction kinetic model.

The equilibrium approach assumes that the reforming reaches the thermodynamic equilibrium as indicated by Eq. 8.1, where $K_{eq,SR}$ is the equilibrium constant, and $p_{i,eq}$ are the partial pressures of the reactants at the equilibrium [161].

$$K_{eq,SR} = \frac{p_{COeq} p^3_{H_2,eq}}{p_{CH_4,eq} p_{H_2O,eq}} \qquad \text{(Eq. 8.1)}$$

The equilibrium constant is usually expressed according to either a rigorous Van't Hoff formulation (Eq. 8.2) [162] or a simplified semi-empirical approach (Eq. 8.3) [163].

$$\Delta G = -RT \ln K_{eq,SR} \qquad \text{(Eq. 8.2)}$$

$$K_{eq,SR} = e^{(30.114 - \frac{26830}{T})} \qquad \text{(Eq. 8.3)}$$

where ΔG is the Gibbs free energy variation [$J\ mol^{-1}$], R the ideal gas constant, and T the temperature.

Experimental results show that the actual conversion of CH_4 is lower than the equilibrium one [164]. Hence, the use of this approach may require appropriate corrections to properly reproduce experimental data. This is usually done through a temperature approach that consists in assuming a different temperature than the operating one for the evaluation of the equilibrium constant. Since the results are independent from catalyst amount and distribution, this approach can be effectively used to describe 0D systems.

A power law kinetic formulation approach is based on semi-empirical equations, as described in Eq. 8.4. The SR reaction rate (r_{SR}) is usually expressed as the product between a kinetic constant (k_{SR}) and

the partial pressure of reactants elevated to different exponents. Both kinetic constant and exponents are fitted through analysis of experimental data.

$$r_{SR} = k_{SR} A p_{CH_4}^{\alpha} p_{H_2O}^{\beta} p_{H_2}^{\gamma} p_{CO_2}^{\delta} p_{CO}^{\varepsilon} \quad \text{(Eq. 8.4)}$$

The dependence on H_2, CO_2, and CO is usually negligible (that is, γ, δ, and ε are close to zero), thus the reaction rate is usually assumed as a function of CH_4 and H_2O. Consequently, α and β values may vary among different studies [165, 141]. The literature generally agrees that the reforming has a first order dependence on CH_4 partial pressure, while the order of water seems highly influenced by the S/C ratio. It can be positive for low S/C ratio, zero for S/C close to two, and negative for higher values of S/C [166]. This is explained by the negative effects that large amounts of water has on the CH_4 adsorption on the catalyst surface [164]. This approach does not require the knowledge of the mechanisms involved and can be easily applied when a large number of experimental data are available for model tuning. However, results are specific to the analyzed case and cannot be directly applied to different systems.

The surface reaction kinetic model approach describes the different mechanisms as a sequence of intermediate phenomena, consisting of adsorption, surface reaction, and desorption of all present species. The rate of the total kinetics is determined by the slowest phenomenon that changes at different temperatures and reactant-product compositions. Such kinetics are usually modeled following the Langmuir–Hinshelwood or the Hougen–Watson approaches. The first one assumes a bimolecular reaction between two reactants adsorbed on neighboring sites as the rate-limiting step and the water dissociation into atomic H and hydroxyl groups OH (Eq. 8.5) [167].

$$r_{SR} = \frac{k_{SR} A \prod p_i^{\varphi_i}}{\left(1 + \sum K_i p_i^{\varphi_i}\right)^{\chi}} \left(1 - \frac{Q_{SR}}{K_{eq,SR}}\right) \quad \text{(Eq. 8.5)}$$

The second approach also takes into account the sorption and the reaction of intermediates (Eq. 8.6) [167].

$$r_{SR} = \frac{k_{SR} A \prod \frac{p_i^{\varphi_i}}{p_j^{\lambda_j}}}{\left(1 + \sum K_i \frac{p_i^{\varphi_i}}{p_j^{\lambda_j}}\right)^{\chi}} \left(1 - \frac{Q_{SR}}{K_{eq,SR}}\right) \quad \text{(Eq. 8.6)}$$

In both Eqs. 8.5 and 8.6, the numerator shows the kinetics dependency on involved gases, while the denominator considers the availability of active sites through adsorption isotherm. The last term, expressed as the ratio between the reaction quotient Q_{SR} (Eq. 8.7) and the equilibrium constant $K_{eq,SR}$, represents the driving force of the overall process.

$$Q_{SR} = \frac{p_{CO} p_{H_2}^3}{p_{CH_4} p_{H_2O}} \quad \text{(Eq. 8.7)}$$

Both kinetic k_{SR} and adsorption K_i coefficients can be described by an Arrhenius type dependency on the operating temperature (Eqs. 8.8 and 8.9).

$$k_{SR} = k_0 exp^{-\frac{E_{act,SR}}{RT}} \quad \text{(Eq. 8.8)}$$

$$K_i = K_{0,i}^{-\frac{\Delta H_{ads,i}}{RT}} \quad \text{(Eq. 8.9)}$$

where k_0 and $K_{0,i}$ are the pre-exponential coefficients, E_{act} the activation energy of SR reaction, and ΔH_{ads} the adsorption enthalpy variation. In DIR fuel cell modeling, Eq. 8.6 is commonly used, considering the values detected for $Ni-MgAl_2O_3-$spinel catalysts as reference of kinetics parameters [161].

Since the process rate is strongly influenced on catalyst features, such as the support used, Ni percentage, and particle size, this approach is not always effective for SR occurring inside a fuel cell due to the higher Ni content compared to the traditional SR catalyst needed to guarantee a good conductivity [141].

Experimental data suggest that, for Ni/YSZ, the material usually employed as the SOFC anode, the rate-limiting step is the CH_4 dissociative adsorption. Thus, a first order expression function of only CH_4 partial pressure is formulated in accordance with power law models. Under the assumption that the surface cannot be covered by other components, the adsorption dependency is neglected, and the kinetic rate is expressed through Eq. 8.10 as reported indifferent works [164, 141, 167].

$$r_{SR} = k_{SR} A p_{CH_4} \left(1 - \frac{Q_{SR}}{K_{eq,SR}}\right) \qquad \text{(Eq. 8.10)}$$

The kinetics constant k_{SR} usually depends on available catalyst active area. These kinetics have been validated over a wide range of temperatures and S/C ratios.

For this work, I decided to implement in the code both equilibrium (Eq. 8.1) and surface reaction kinetics approach (Eq. 8.10). It is important to underline that the first is independent of the specific used catalyst, while the second one is expressed in function of its distribution on cell plane.

8.3. Simulation of IR-SOFC

For the simulation a planar cross-flow anode-supported SOFC with active surface of 1 m^2 (anode inlet length = 71 cm, cathode inlet length = 142 cm) was considered. The main cell features assumed for the cell are presented in Table 8.1.

Property	Anode	Electrolyte	Cathode
Material	Ni/YSZ	YSZ	LSC
Density [$g\ cm^{-3}$]	7.7	6	5.3
Heat Capacity [$J\ mol^{-1}\ K^{-1}$]	209.2	121.3	142.3
Porosity [−]	0.4	0.01	0.35
Thickness [μm]	350	5	30
Tortuosity [−]	4	-	n.a.

Table 8.1: Physical and micro-structural properties of different SOFC layers considered for the IR simulation.

As kinetic core to describe SOFC performance, the following equation was used [5]:

$$V = E - R_\Omega J - R_{act,An} J - R_{act,Cat} J - R_{conc} J \qquad \text{(Eq. 8.11)}$$

where E is the equilibrium potential [V], J is the cell current density [$A\,cm^{-2}$], $R_{act,An}$, $R_{act,Cat}$ and R_{conc} are respectively the activation resistance of anode and cathode and the total concentration resistance [$\Omega\,cm^2$]. As it was done in the MCFC case previously presented, the ohmic resistance can be expressed in an exponential form with the following equation, being P_1 and P_2 empirical parameters:

$$R_\Omega = P_1\, T\, e^{\frac{P_2}{T}} \qquad \text{(Eq. 8.12)}$$

The activation resistances of anode and cathode can be expressed with the following equations:

$$R_{act,An} = \frac{RT}{F} \sinh^{-1}\left(\frac{J}{2J_{0,An}}\right) \qquad \text{(Eq. 8.13)}$$

$$R_{act,Cat} = \frac{RT}{2F} \sinh^{-1}\left(\frac{J}{2J_{0,Cat}}\right) \quad \text{(Eq. 8.14)}$$

where $J_{0,An}$ and $J_{0,Cat}$ are the anodic and cathodic exchange current densities expressed as follows:

$$J_{0,an} = P_3 \left(y_{H_{2,an}}\right)^A \left(y_{H_2O,an}\right)^B e^{-\frac{E_{act,An}}{RT}} \quad \text{(Eq. 8.15)}$$

$$J_{0,cat} = P_4 \left(y_{O_2,cat}\right)^C e^{-\frac{E_{act,Cat}}{RT}} \quad \text{(Eq. 8.16)}$$

where P_3 and P_4 are empirical parameters, A, B and C are the anode and cathode reactants reactions order, $E_{act,An}$ and $E_{act,Cat}$ and are the activation overpotentials of the anodic and cathodic reaction $[kJ\ mol^{-1}]$. Finally the concentration resistance can be expressed with the following formulation:

$$R_{conc} = \frac{RT}{2F} ln \left(\frac{\left(1 + \frac{RT d_{an} J}{6F D_{eff,H_2O} p_{H_2O,an}}\right)^{2B}}{\left(1 - \frac{RT d_{an} J}{6F D_{eff,H_2} p_{H_{2,an}}}\right)^{2A}} \right) \quad \text{(Eq. 8.17)}$$

where D_{eff,H_2} and D_{eff,H_2O} are respectively the effective diffusion of H_2 and H_2O in the gas mixture in the electrode pores $[m^2\ s^{-1}]$, and d_an is the anode thickness $[m]$.

The parameters used in the SOFC kinetic core are presented in table 8.2

P_i	Value	Unit
P_1	$3.53\ 10^{-11}$	$\Omega\, m^2\, K^{-1}$
P_2	6309.8	K
P_3	$2.8\ 10^{-9}$	$A\, m^{-2}$
P_4	$4\ 10^{-10}$	$A\, m^{-2}$
$E_{act,An}$	110	$kJ\ mol^{-1}$
$E_{act,An}$	120	–
A	0.55	–
B	0.5	K
C	0.25	–

Table 8.2: Kinetic parameters to simulate the performance of SOFCs as reported in [5].

The SOFC performance has been studied setting up a current density load of 0.15 $A\ cm^{-2}$ coupled with an H_2 utilization of about 75%, common target values according to numerous SOFC producers [168]. The proposed feed conditions, with inlet S/C ratio of about two (safety condition to avoid carbon deposition at the cell operating temperature [169]), are represented in Table 8.3.

8.3.1. Base simulation

The comparison between DIR-SOFC simulation assuming reforming reaction at the equilibrium or kinetics driven is presented in terms of local maps on the cell surface in Figure 8.1. Specifically, the maps of the H_2 molar fraction (equilibrium 8.2A and kinetics 8.2B), the temperature of the solid structure (equilibrium 8.2C and kinetics 8.1D), and the applied current density (equilibrium 8.1E and kinetics 8.1F)

Inlet Conditions	Anode	Cathode
T $[K]$	1023	1023
N $[Nm3\,h^{-1}]$	0.75	8.6
x_{CH_4} [-]	0.25	-
x_{CO} [-]	0.03	-
x_{CO_2} [-]	0.13	-
x_{H_2} [-]	0.04	-
x_{H_2O} [-]	0.51	-
x_{N_2} [-]	0.04	0.79
x_{O_2} [-]	-	0.21

Table 8.3: Inlet operating conditions for the IR-SOFC simulations.

are presented. In both cases, CH_4 is almost completely consumed in proximity of the anode inlet (about $10\,cm$), thus its mapping on the cell plane is not reported here.

As verified before, the high operating temperature allows for a rapid conversion of CH_4. This is confirmed in the literature, where CH_4 is observed consuming in the so called "reforming zone" [138]. The equilibrium conversion represents the maximum value that can be theoretically achieved. This is evident in the kinetics reaction rate expression (refer to Eq. 8.10), where the imbalance between actual and equilibrium composition represents the driving force of the process ($\frac{Q_{SR}}{K_{eq,SR}}$). The consequence is that the equilibrium case foresees a slightly faster SR to form H_2 and CO, reducing local temperature. However, in both approaches, the newly formed H_2 electrochemically reacts to produce H_2O at the anode, while CO mainly produces additional H_2 via WGS. Both reactions are exothermic and balance the local decrease in temperature caused by reforming. As a result, almost all CH_4 converts in close proximity of the anode inlet. H_2 is immediately produced by reforming and rapidly depletes along the cell plane to sustain the electrochemical reactions (Figure 8.2A and 8.2B). As expected, the temperature (Figure 8.2C and 8.1D) decreases at the inlet due to the reforming endothermicity and increases moving towards the anode and, to a lesser degree, the cathode outlet where both exothermic electrochemical and WGS reactions occur [170]. Due to the cross-flow configuration, inlet cathodic gas (bottom left corner of maps) reduces the anode inlet temperature proceeding toward the cathode outlet. This in turn penalizes the reforming and the subsequent anodic reactions, limiting any further temperature increase. In both cases, the current density (Figure 8.1E and 8.1F) increases moving from the anode inlet thanks to the H_2 produced that allows the reactions and then decreases with decreasing CH_2 after a peak moving towards the outlet.

The kinetics assumed have a relevant influence on the electrochemical processes. If the fastest equilibrium reforming kinetics induce an initial peak of H_2 production followed by a slow electrochemical conversion (Figure 8.2A), in the surface kinetics formulation a wider H_2 conversion zone (Figure 8.2B) is detected, causing lower peaks of temperature and local current density (Figure 8.1D and 8.1F). However, as shown in Table 8.4, the macroscopic results of the simulation are not particularly dissimilar, thus both approaches can be used as preliminary analysis.

Reforming operating conditions	Equilibrium	Kinetics
$V\ [V]$	0.747	0.856
$J_{max}\ [A\ cm^{-2}]$	0.88	0.42
$T_{max}\ [K]$	1110	1084
$T_{min}\ [K]$	873	828
$T_{average}\ [K]$	1037	1034
$x_{CH_4,max}\ [-]$	0.048	0.196
$x_{H2,max}\ [-]$	0.402	0.525
Cell Power $[W]$	1121	1284

Table 8.4: Main results of the DIR-SOFC simulations based on equilibrium and surface reaction mechanism approaches.

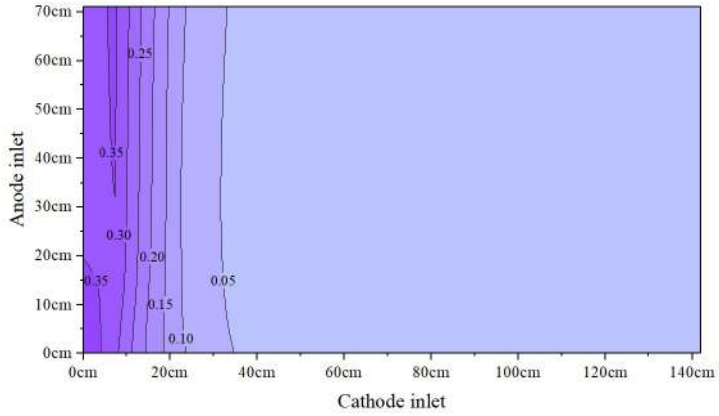

(A) $x_{H_2}\ [-]$ map for equilibrium.

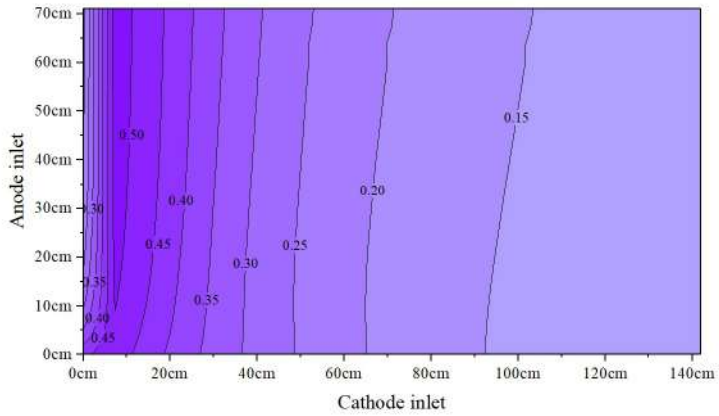

(B) $x_{H_2}\ [-]$ map for kinetics.

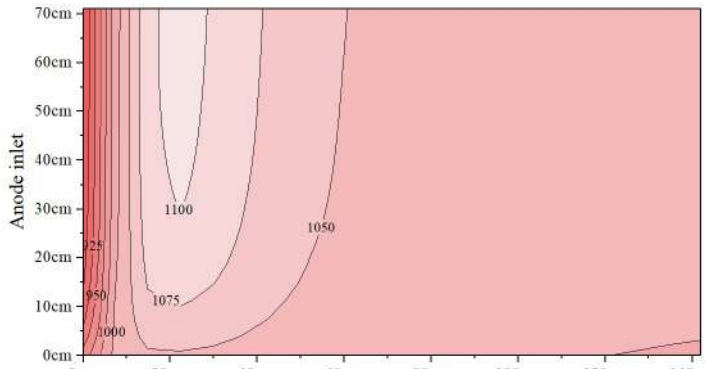

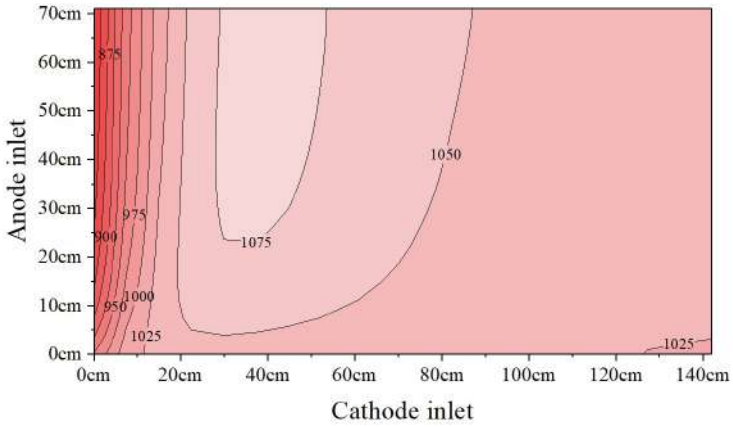

(D) T $[K]$ map for kinetics.

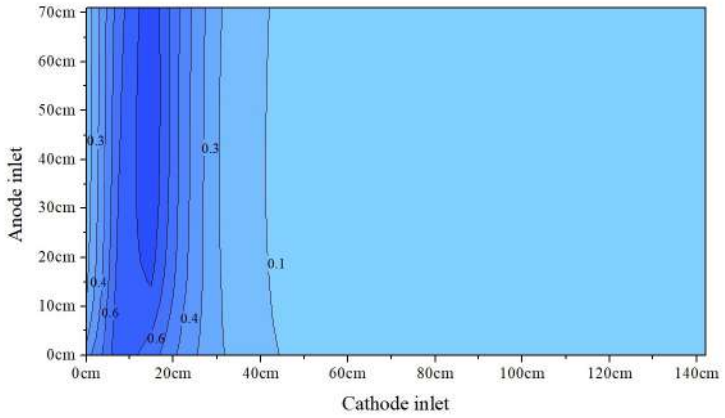

(E) J $[A\,cm^{-2}]$ map for equilibrium.

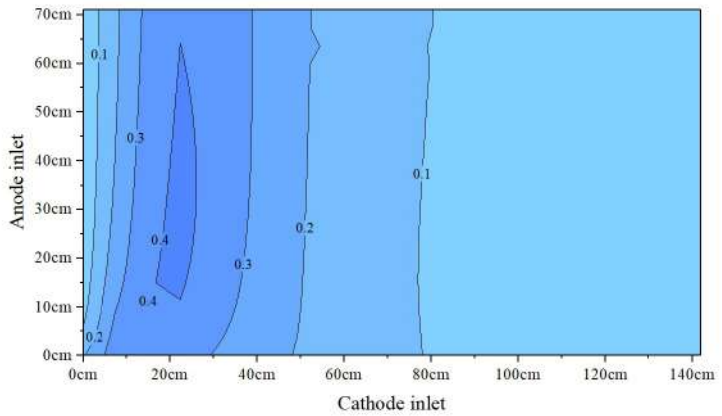

(F) J $[A\,cm^{-2}]$ map for kinetics.

Figure 8.1: Local results of the DIR-SOFC simulation using SR equilibrium (A, C, E) and kinetics formulation (B, D, F)

However, these results are not completely satisfactory. As previously mentioned and shown in Figure 8.1, the rapid conversion of CH_4 near the anode inlet induces a steep temperature gradient with a difference between maximum and minimum temperature of more than 200 K in the equilibrium case and more than 250 K in the kinetics case. This, coupled with the very high peak current density, can greatly speed up the degradation processes limiting the cell lifetime.

For this reason, the catalysts active area is usually reduced by a partial poisoning or by changing the material microstructure [141].

8.3.2. Simulation of catalyst's degradation and poisoning

As already underlined, the local simulation has several advantages: it allows for a detailed knowledge of the main chemical-physical features on the cell plane and also a local description of system structure. Consequently, using a local modeling approach, the degradation of the reforming catalyst and how it affects the cell performance can be studied.

To simulate the catalysts deactivation that can occur due to phenomena such as sintering, poisoning induced by sulfur and other pollutants, or carbon deposition, a coefficient (σ), as shown in Eq. 8.18, can be introduced to adjust the reforming kinetics. This coefficient represents a corrective parameter that allows considering a reduced active area or an unevenly distributed catalyst. Since the equilibrium kinetics is independent from the active area dimension, this correction has been added only in the surface reaction approach.

$$r_{SR} = k_{SR}\sigma A p_{CH_4}\left(1 - \frac{Q_{SR}}{K_{eq,SR}}\right) \qquad \text{(Eq. 8.18)}$$

An uneven distribution of the SR active sites due to advanced degradation processes can be introduced considering local values of σ to differentiate the cell areas. This is specifically important when there is the need to simulate long-term applications, where such deactivation phenomena cannot be neglected. To demonstrate this possibility, I introduced into the code a matrix of σ, as presented in Figure 8.3. The cell surface has been divided into a $20\,x\,20$ mesh, each one has an area equal to $25\,cm^2$: the degradation process starts at the anode inlet where the sigma value is the smallest. Moving towards the anode outlet the sigma value increases reflecting a milder degradation effect. Such distribution may derive for instance from carbon deposition that starts at the anode inlet of the cell, where the reactions initially take place, and then sequentially shifts to the outlet. Other possible causes could be the poisoning effects of sulfur compounds and trace compounds present in fed biogas in view of long exposition. It is well known that sulfur can react with the catalysts thus inhibiting its properties [145]. The local results of the simulation are reported in Figure 8.4.

0.00001	0.00001	0.00001	0.00001	0.01	0.01	0.01	0.01	0.02	0.02	0.02	0.02	0.7	0.7	0.7	0.7	0.7	0.7	0.7	0.7
0.00001	0.00001	0.00001	0.00001	0.01	0.01	0.01	0.01	0.02	0.02	0.02	0.02	0.7	0.7	0.7	0.7	0.7	0.7	0.7	0.7
0.00001	0.00001	0.00001	0.00001	0.01	0.01	0.01	0.01	0.02	0.02	0.02	0.02	0.7	0.7	0.7	0.7	0.7	0.7	0.7	0.7
0.00001	0.00001	0.00001	0.00001	0.01	0.01	0.01	0.01	0.02	0.02	0.02	0.02	0.7	0.7	0.7	0.7	0.7	0.7	0.7	0.7
0.00001	0.00001	0.00001	0.00001	0.01	0.01	0.01	0.01	0.02	0.02	0.02	0.02	0.7	0.7	0.7	0.7	0.7	0.7	0.7	0.7
0.00001	0.00001	0.00001	0.00001	0.01	0.01	0.01	0.01	0.02	0.02	0.02	0.02	0.7	0.7	0.7	0.7	0.7	0.7	0.7	0.7
0.00001	0.00001	0.00001	0.00001	0.01	0.01	0.01	0.01	0.02	0.02	0.02	0.02	0.7	0.7	0.7	0.7	0.7	0.7	0.7	0.7
0.00001	0.00001	0.00001	0.00001	0.01	0.01	0.01	0.01	0.02	0.02	0.02	0.02	0.7	0.7	0.7	0.7	0.7	0.7	0.7	0.7
0.00001	0.00001	0.00001	0.00001	0.01	0.01	0.01	0.01	0.02	0.02	0.02	0.02	0.7	0.7	0.7	0.7	0.7	0.7	0.7	0.7
0.00001	0.00001	0.00001	0.00001	0.01	0.01	0.01	0.01	0.02	0.02	0.02	0.02	0.7	0.7	0.7	0.7	0.7	0.7	0.7	0.7
0.00001	0.00001	0.00001	0.00001	0.01	0.01	0.01	0.01	0.02	0.02	0.02	0.02	0.7	0.7	0.7	0.7	0.7	0.7	0.7	0.7
0.00001	0.00001	0.00001	0.00001	0.01	0.01	0.01	0.01	0.02	0.02	0.02	0.02	0.7	0.7	0.7	0.7	0.7	0.7	0.7	0.7
0.00001	0.00001	0.00001	0.00001	0.01	0.01	0.01	0.01	0.02	0.02	0.02	0.02	0.7	0.7	0.7	0.7	0.7	0.7	0.7	0.7
0.00001	0.00001	0.00001	0.00001	0.01	0.01	0.01	0.01	0.02	0.02	0.02	0.02	0.7	0.7	0.7	0.7	0.7	0.7	0.7	0.7
0.00001	0.00001	0.00001	0.00001	0.01	0.01	0.01	0.01	0.02	0.02	0.02	0.02	0.7	0.7	0.7	0.7	0.7	0.7	0.7	0.7
0.00001	0.00001	0.00001	0.00001	0.01	0.01	0.01	0.01	0.02	0.02	0.02	0.02	0.7	0.7	0.7	0.7	0.7	0.7	0.7	0.7

Anode inlet

Cathode inlet

Figure 8.3: Matrix of σ to consider the active area reduction due to deactivation processes such as carbon deposition and poisoning effect.

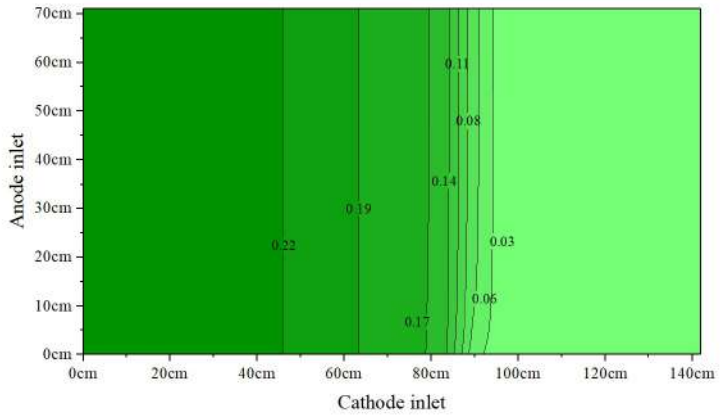

(A) x_{CH_4} [−] map.

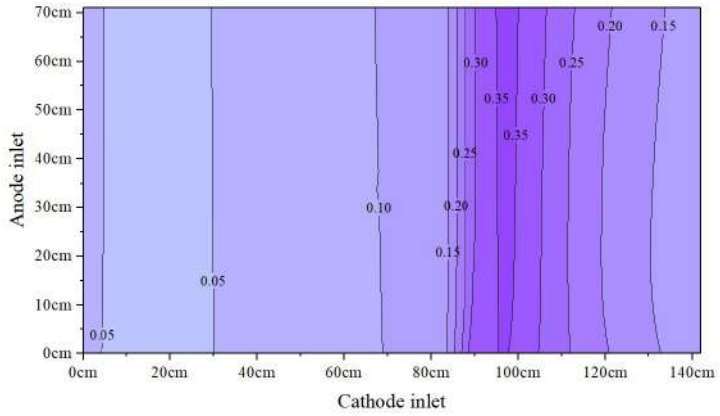

(B) x_{H_2} [−] map.

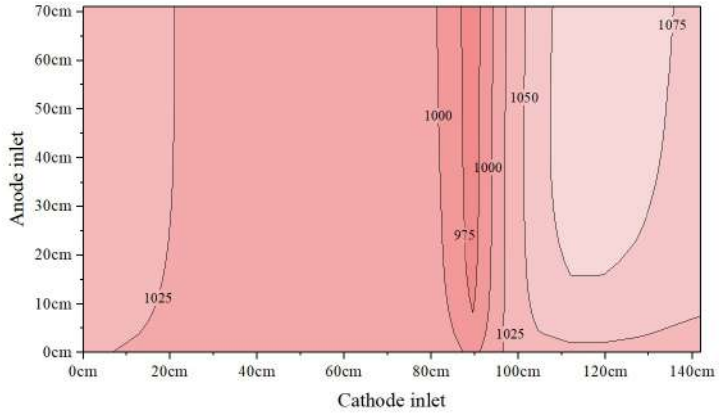

(C) T $[K]$ map.

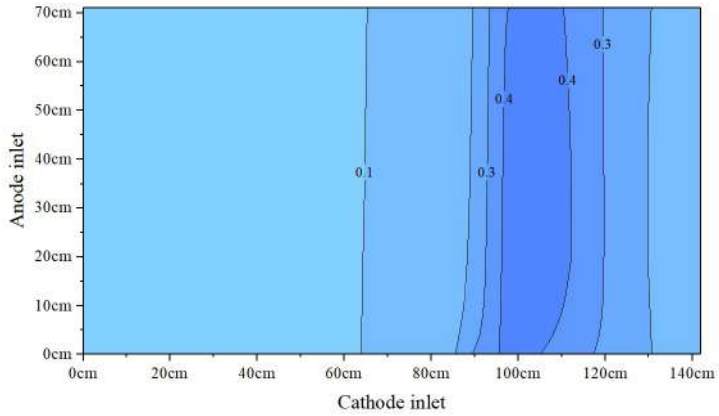

(D) J $[A\,cm^{-2}]$ map.

Figure 8.4: Results of the DIR-SOFC simulation using the SR kinetics approach correcting the catalysts actual surface area to simulate the cell degradation.

In proximity to the anode inlet, the conversion of CH_4 is negligible due to the highly reduced catalytic surface area that corresponds to a value of 0.00001 in the σ matrix. This can be interpreted as extremely deactivated or poisoned catalyst. As in Figure 8.5A, then moving towards the anode outlet, the conversion increases as the flow encounters catalyst with more open active area (σ from 0.01 to 0.07 progressively). The maps of H_2, current density and temperature on the cell plane are also influenced, resulting in more uniform distribution (Figures 8.5B, 8.4C and 8.4D). As Table 8.5 shows, the global performance variation is not hugely different compared to the normal equilibrium and kinetics cases described in Table 8.4, still an inefficient use of catalyst occurs.

Reforming operating conditions	Degradation
$V\ [V]$	0.823
$J_{max}\ [A\,cm^{-2}]$	0.47
$T_{max}\ [K]$	1088
$T_{min}\ [K]$	962
$T_{average}\ [K]$	1034
$x_{CH_4,max}\ [-]$	0.25
$x_{H_2,max}\ [-]$	0.373
Cell Power $[W]$	1234

Table 8.5: Main results of the DIR-SOFC simulation considering the catalyst degradation.

It is important to underline that the decrease of the temperature gradient (less than 150 K between maximum and minimum values) and the lower peak current density should not be interpreted as positive outcomes. They are the results of highly deactivated catalysts that penalizes the performance in terms of power output, which decreases of about 50 W in comparison with kinetics case. The degradation effects on electrochemical reactions were not considered here, and they could be added with available experimental data and would more highly affect the power losses.

Through a similar local approach, it is possible to identify the optimized catalyst distribution that can result in relatively lower temperature gradient compared to the previous solutions without degradation (kinetics case), thus improving the cell stability in time and its durability. In considered working conditions, the followed framework has been detected in terms of *sigma* value (Figure 8.5). These uneven distributions can be obtained in the manufacturing process controlling the catalysts amount and/or by a light poisoning.

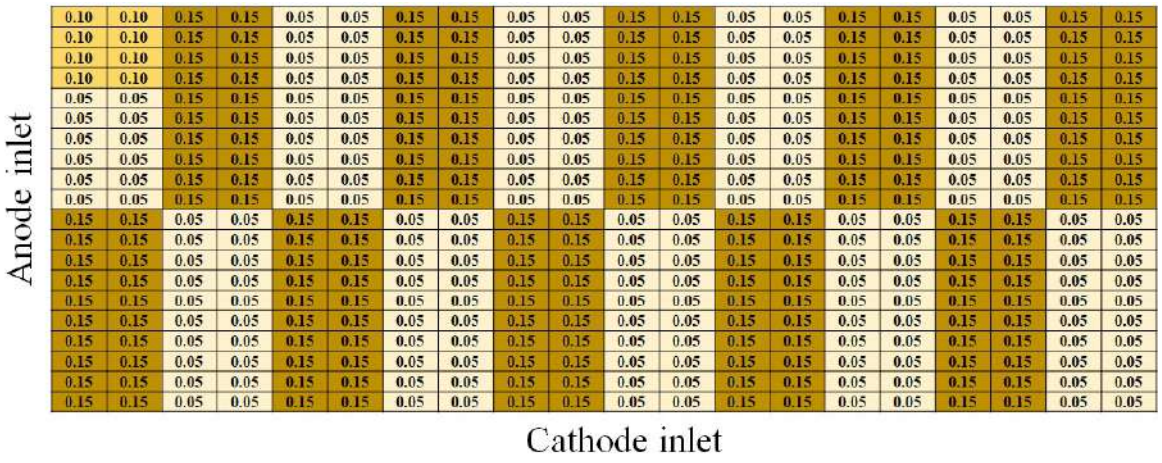

Figure 8.5: Matrix of σ to optimize the cell performance in terms of even distribution of temperature and current density.

In Figure 8.6 a more uniform temperature distribution is predicted on the cell plane, improving also the global performance as shown in Table 8.6. It is estimated that about 30% of the physical stresses are due to thermal gradients, highlighting the relevant of this improvement to guarantee a long-term application [171]. In this case, the difference between the highest and the lowest temperature points is only of about 100 K, while it is of more than 250 K with uniform catalysts distribution and no degradation (kinetics case). This result is obtained by expanding the CH_4 reforming zone in order to have a more uniform

conversion. Compared to the previous solutions (equilibrium and kinetics cases), the maximum current density and H_2 molar fraction are also lower, signifying less stressed cell working conditions. Whereas, for the obtained power, whose value is not penalized by this uneven catalyst distribution, the reduction is only of about $14\,W$.

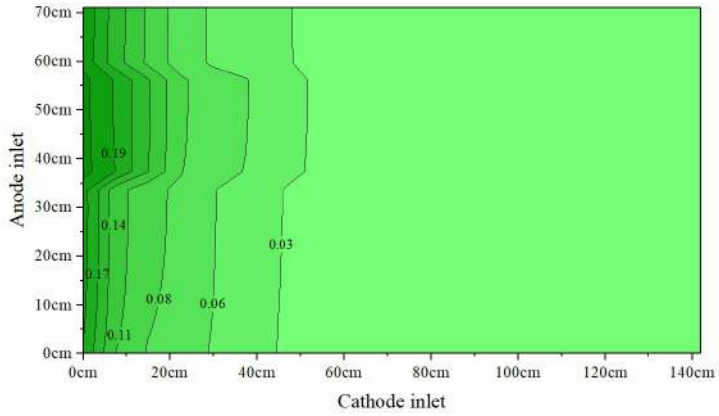

(A) x_{CH_4} [-] map.

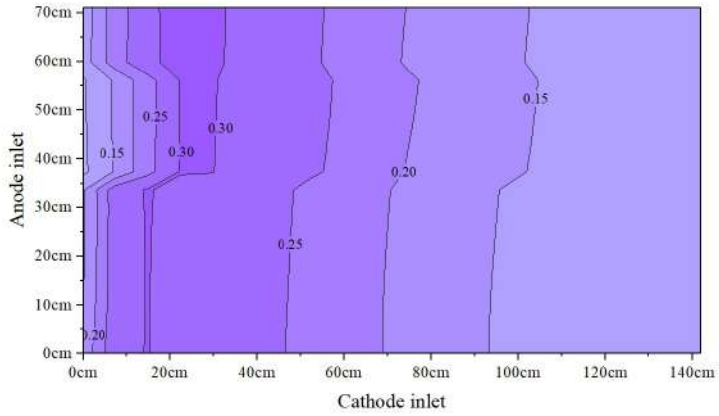

(B) x_{H_2} [-] map.

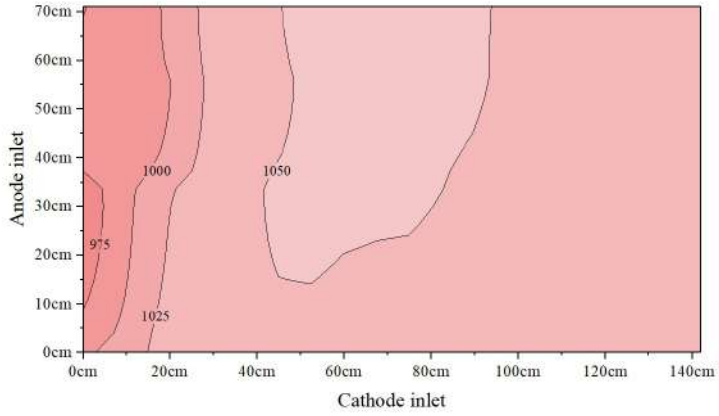

(C) T $[K]$ map.

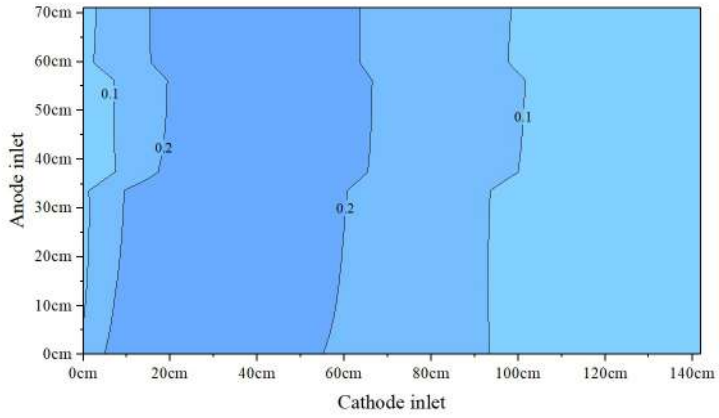

(D) J $[A\,cm^{-2}]$ map.

Figure 8.6: Results of the DIR-SOFC simulation using the SR kinetics approach correcting the catalysts actual surface area to obtain cell performance optimization.

Reforming operating conditions	Optimized configuration
V $[V]$	0.847
J_{max} $[A\,cm^{-2}]$	0.29
T_{max} $[K]$	1059
T_{min} $[K]$	963
$T_{average}$ $[K]$	1034
$x_{CH_4,max}$ $[-]$	0.233
$x_{H_2,max}$ $[-]$	0.322
Cell Power $[W]$	1270

Table 8.6: Main results of the DIR-SOFC simulation considering the catalyst optimized configuration.

9
Perovskite materials for dry CH_4 reforming

The study of new materials is extremely important to enhance the spread of high temperature fuel cells on the energy market. Indeed, new materials can support the reduction of the cell operating temperature (especially in the case of SOFC), the increase of the cell operation time before failure, the increase of the cell performance by reduction of the activation energy required for the reactions to occur, and the increase of the resistance toward poisonous gases that may be contained in the feeds.

In this Chapter I am going to present an experimental study to analyze the performance of a Rh doped perovskite materials as catalyst for SOFC anode to sustain CH_4 dry-reforming reaction. This work was conducted at the Center for Hydrogen and Fuel Cell Research of the Korea Institute of Science and Technology in Seoul (South Korea) and was supported by the Global Research Laboratory Program (Grant Number NRF-2009-00406) funded by the Ministry of Education, Science and Technology of Korea and the Hydrogen Energy Innovation Technology Development Program of the National Research Foundation of Korea (NRF) funded by the Korean government (Ministry of Science and ICT(MSIT)) (No. 2019M3E6A1104113).

After a brief introduction of these perovskite base catalysts, I will present the description of how the catalysts powders were obtained. It will follow an analysis of the effects that the catalysts reduction time and temperature have on the performance to reaction of CH_4 dry reforming. To conclude, the effects of sulfur poisoning as H_2S will be presented to show the recovery capability of this kind of catalyst.

The results of this chapter have been published with the title "*In situ exsolution of Rh nanoparticles on a perovskite oxide surface: Efficient Rh catalysts for Dry reforming*" on the *Korean Journal of Chemical Engineering* [128].

9.1. Metal-exsolved perovskite catalysts

Recently, metal-exsolved perovskite catalysts have attracted considerable interest in the catalysis field, due to the strong metal support interaction and high dispersibility of their nanoparticles on the perovskite oxide surface. The formation of these exsolved nanoparticles derives from a phenomenon where the B-sites of the perovskite oxides (structure: ABO_3) are firstly substituted by transition metals (main examples are Ru, Rh and Ni) under oxidizing conditions, and subsequently released as metal nanoparticles when exposed to reducing atmosphere [172].

These surface-exsolved nanoparticles catalysts have demonstrated several advantages over the conventional impregnated material-based catalysts. For example, Wei et al. [173] compared two different Ni supported on $LaMnO_3$-based perovskite catalysts: the first synthesized by the impregnation and the second by the exsolution method. They observed not only that the Ni-exsolved catalysts exhibited higher CH_4 conversion but also higher stability with a lower extent of coking, compared with the impregnated ones. These high catalytic activity and stability exhibited by the exsolved catalyst were ascribed to the high dispersion of the Ni particles, their uniform size distribution, and stronger Ni-surface bonds.

In a similar work, Neagu et al. [174] demonstrated the high coke resistance of Ni nanoparticles supported on an LST perovskite oxide (La doped $SrTiO_3$). The Ni-exsolved particles were more embedded in the oxide support compared to the impregnated ones. For this reason, they contained more anchoring sites connecting the metal and the perovskite surface, that resulted in a lower tendency to agglomerate or

coke.

These metal-exsolved perovskite catalysts have shown great potential for many real-world applications, such as CH_4 partial oxidation [175], electrolysis of CO_2 [176]. and O_2 transport membranes [177].

Various studies on CH_4 reforming have been reported in literature. Zubenko et al. [178] studied a perovskite $LaFeO_3$-based catalyst with exsolved Re-alloy nanoparticles that exhibited a stable and efficient CH_4 conversion (more than 90% at an operating temperature of 1173 K). Chai et al. [179] investigated a Ni-exsolved nanoparticle perovskite ($La_{0.46}Sr_{0.34}Ti_{0.9}Ni_{0.1}O_3$) with a bimodal size distribution that exhibited better and more stable results compared to the non-exsolved Ni-based catalysts, although the CH_4 conversion was low. Oh et al. [180] analyzed different $LaCrO_3$-based catalysts with Ir, Co, and Rh-exsolved nanoparticles that exhibited a very promising performance; particularly, Ir produced over 90% CH_4 conversion at an operating temperature of 1173 K.

The metal-exsolved nanoparticles were also found to show high sulfur resistance. For instance, Papaioannou et al. [181] stated that their perovskite-based catalysts with Fe-Ni-exsolved nanoparticles exhibited higher sulfur resistance in the CO oxidation reaction compared to the commercial Ni catalysts and achieve an almost complete recovery once the poisoning was interrupted.

SYT ($Sr_{0.92}Y_{0.08}Ti_2O_{3-\delta}$)-based perovskite oxides have been used as anode constituent for solid oxide fuel cells attributed to its high electronic conductivity as well as stability under high temperatures. It was recently reported that facile exsolution of metal nanoparticles is feasible over non-stoichiometric SYT-based perovskites. For example, Kim et al. showed successful exsolution of Ni [182], Ru [183] and Rh [184] nanoparticles from SYT perovskite structure to the oxide surface using different metal loadings. Although their works showed good results, they never conduced a study to determine the best conditions in terms of time and temperature for the reduction of the catalysts to exsolve the metal particles. In the following, a meticulous analysis of the effects of these two variables on the powder reductions will be presented for a 5% Rh doped SYT with the final porpoise of catalyze the reaction of CH_4 dry reforming.

9.2. Catalyst preparation

The $Sr_{0.92}Y_{0.08}Ti_{1.95}Rh_{0.05}O_{3-\delta}$ perovskite catalyst powders (SYTRh5) were prepared using Pechini's method [182, 183, 184]. This is a type of sol-gel synthesis technique that is frequently employed to obtain well-dispersed metal ions entrapped in a covalent polymer network through an esterification of citric acid with ethylene glycol. Once the polymer matrix is removed by thermal treatment, a highly homogeneous complex metal oxide is obtained.

The first step of the synthesis involved the preparation of the following three solutions:

1. yttrium nitrate [$Y(NO_3)_3{\cdot}_6H_2O$ (Junsei), 0.502 g] and strontium nitrate [$Sr(NO_3)_3$ (Sigma-Aldrich), 3.191 g] in 100 g of deionized water

2. titanium isopropoxide [$Ti(OCH(CH_3)_2)_4$ (Junsei), 9.085 g] dissolved in 100 g of ethylene glycol

3. rhodium chloride hydrate [$RhCl_3{\cdot}xH_2O$ (Alfa Aesar), 0.198 g] and citric acid [$C_6H_8O_7$ (Sigma-Aldrich), 100 g] dissolved in deionized water

The three solutions were slowly mixed in a beaker at 353 K, resulting in the formation of a precipitate. Solution and precipitate were dried at 383 K overnight to facilitate gelation and subsequently calcined at 573 K for 6 hours under air to remove any remaining organic species. The obtained solid was grounded and subsequently calcined once more at 923 K for 10 hours in air to obtain the SYTRh5 perovskite powder (5 g). A schematic of the process is presented in Figure 9.1. For comparison, a reference SYT perovskite was prepared without adding the Rh precursor during the synthesis procedure.

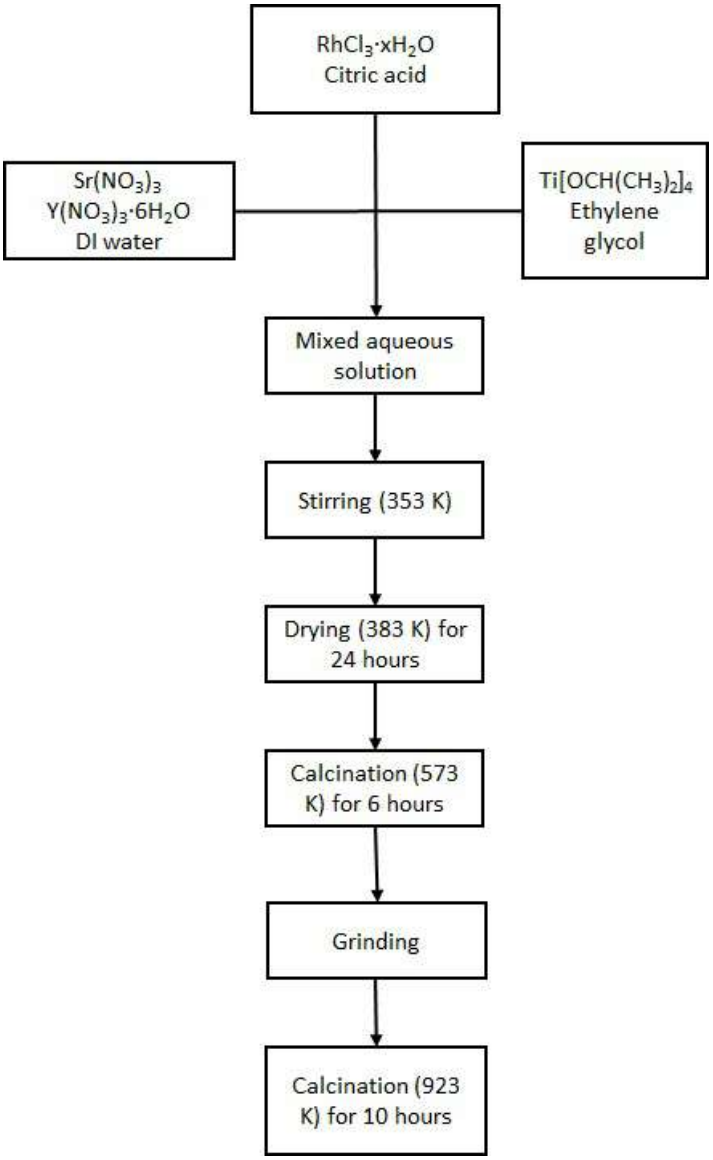

Figure 9.1: Schematic of the synthesis process of the SYTRh5 catalyst powders.

To conclude the powder preparation, after calcination, each sample was reduced. The reduction process was conducted ex-situ, at different reduction temperatures and times, under a flux of H_2:N_2 in the ratio 40 : 60 ($80\,mL\,min^{-1}$) in a heating furnace. The samples reduced at 1073 K, 1173 K, and 1273 K for 24 hours have been represented as SYTRh5 (1073), SYTRh5 (1173), and SYTRh5 (1273), while the samples reduced at 1173 K for 4, 12, and 24 hours have been represented as SYTRh5 (4), SYTRh5 (12), and SYTRh5 (24), respectively.

9.3. Catalyst characterization technique

To analyze the characteristics of the obtained catalyst powders the following techniques and the machineries were used:

1. *Brunauer–Emmett–Teller (BET) Surface Area, Pore Volume and Pore Size*: a N_2 physisorption technique in a Micromeritics ASAP2000 (accelerated surface area and porosimetry system) instrument was used. Depending on the expected surface area, a known amount of catalyst was first measure and transferred to a sample tube. The sample tube was exposed to a vacuum environment where the catalyst was degassed at 343 K for 2 hours and 523 K for 12 hours in order to remove any impurities on the catalyst surface. The sample tube was then moved to the analysis port and N_2 physisorption was carried out at 77 K. The Barrett-Joyner-Halenda (BJH) pore size distribution was constructed based on the desorption branch of the isotherm.

2. *Temperature-Programmed Reduction (TPR)*: BELCAT-M chemisorption analyzer (MicrotracBEL Corp) was used to conduct temperature-programmed reduction of the SYTRh5 catalysts. The sample was placed in a quartz reactor tube equipped with a thermocouple to monitor the temperature of the catalyst bed. Pure Ar with a flowrate of 70 $mL\ min^{-1}$ was introduced to the reactor at room temperature and the reactor temperature was increased to 523 K. The pretreatment of the sample was maintained for 2 hours to eliminate the adsorbed water on the catalyst surface. The temperature of the reactor was then decreased to room temperature while flowing pure Ar. For TPR, 70 $mL\ min^{-1}$ of 5% H_2/Ar was used where the reactor temperature was increased from 323 K to 1123 K at a ramp rate of 10 $K\ min^{-1}$. The outstream of the reactor was connected to a thermal conductivity detector (TCD) to estimate hydrogen consumption due to the catalyst.

3. *X-ray Diffraction (XRD)*: XRD patterns of the as-prepared SYTRh5 catalysts powders and of the samples reduced in different conditions of time and temperature were collected using a Miniflex II diffractometer (Rigaku Co., Japan) with CuKα radiation (wavelength $\lambda = 1.5418$ Å). The diffraction patterns were collected in the 2θ range of $20-90^{\circ}$ and the identification of the crystallographic phases was performed using PDXL software.

4. *Transmission Electron Microscopy (TEM)*: to analyze the morphology of the studied catalysts powders, S-TEM images were taken using a TEM Tecnai F20 (FEI Co., USA) equipped with a high brightness field emission electron gun (FEG) operated at 200 kV. Before conducting the analysis, the catalysts powders were suspended in ethanol and sonicated for 15 minutes to obtain a homogeneous mixture. A single drop putted on a grid was used to investigate the morphology of the powders.

5. *X-ray Photoelectron Spectroscopy (XPS)*: to confirm the presence of Rh or S on the catalysts powder surface, XPS spectra were collected using a K-Alpha+ XPS System (Thermo Scientific Co.). The samples were loaded in the chamber using carbon tape and the chamber was evacuated for 2.5 hours. A survey scan was taken for each sample to identify all the elements present on the powders surface. Following the survey scan, spectra for the specific C 1s, O 1s, Ti 2p, Y 3d, Sr 3d, Rh 3d and S 2p regions were collected. Prior to the data analysis, the charging effect was corrected based on the C 1s binding energy of 284.5 eV.

9.4. Dry-reforming activity testing

The catalytic activity of the SYTRh5 catalysts was studied under dry reforming conditions in a fixed-bed vertical quartz reactor at atmospheric pressure. The gas flow was fed into the top of the tube while the bottom served as an exhaust line directly connected to a gas chromatograph (GC). To ensure that no water could reach the GC, the outlet stream was cooled down to a temperature of 277 K. The catalyst

bed was placed in the middle of the tube and for each test 0.2 g of catalyst were used. The composition of the dry off-gas was measured by GC with a TCD and two separated columns Plot Q and Molesieve (both 30 m in length), using He and Ar, respectively, as carrier gases to determine the concentrations of H_2, CO, CO_2 and CH_4. A schematic representation of the system is presented in Figure 9.2.

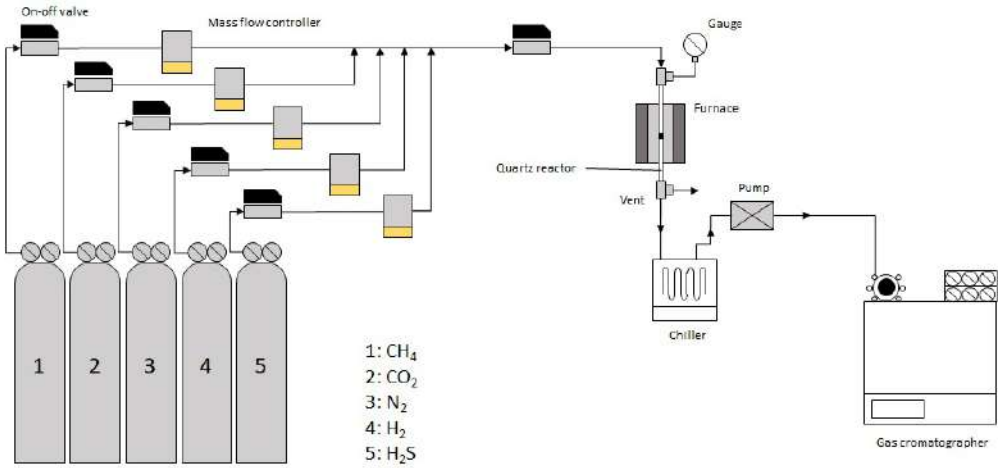

Figure 9.2: Schematic of the system use to conduct the CH_4 dry reforming experiments.

The feed consisted of a CH_4:CO_2:N_2 mixture at a ratio of $1:1:2$ in total flow rate of 80 $mL\,min^{-1}$. The gas hourly space velocity was of $1.2\,10^4\ h^{-1}$.

All the ex-situ reduced SYTRh5 catalysts at different reduction temperature and time were once more reduced in-situ using the same reduction procedures of the catalyst preparation prior to the dry reforming reaction except the sample reduced at 1273 K as the temperature exceed the limit of the reaction testing furnace.

Dry reforming of CH_4 was carried out in the temperature range of 873 K to 1173 K with 50 K temperature increments. At each temperature, 2 hours of reaction was carried out while multiple GC injections were made. Once the pre-reduction was completed, the reaction temperature was adjusted to 1173 K and the reaction was carried out from 1173 K to 873 K. The activity testing was repeated from 873 K to 1173 K in order to investigate thermal cycling stability of the catalysts. Lastly, for H_2S supply, N_2 balanced 400 ppm H_2S cylinder were used. Additional N_2 was added to the reactant in order to obtain the amount of 100 ppm of H_2S. Overall, a mixture of H_2S, CH_4, CO_2, N_2 was introduced to the catalysts bed for a prolonged time to estimate the sulfur-resistance of the SYTRh5 reduced at different reduction temperature and time. Once a stable activity was achieved under H_2S conditions, the inlet of H_2S was stopped to observe whether the catalyst recovers the original activity.

To examine the performance of the catalysts we referred to the conversion rate of CH_4 and CO_2, and the ratio between the produced H_2 and CO. To evaluate these number, the following equations have been used:

$$Methane\ Conversion = \frac{n_{CH_4,in} - n_{CH_4,out}}{n_{CH_4,in}} \qquad \text{(Eq. 9.1)}$$

$$Carbon\ Dioxide\ Conversion = \frac{n_{CO_2,in} - n_{CO_2,out}}{n_{CO_2,in}} \qquad \text{(Eq. 9.2)}$$

$$^{H_2}/_{CO} = \frac{n_{H_2,out}}{n_{CO,out}} \qquad \text{(Eq. 9.3)}$$

9.5. In-situ growth of Rh nanoparticles on SYT surface

The SYTRh5 catalysts must undergo a reduction process for substituted Rh in the perovskite structure to exsolve on the surface forming homogenously dispersed Rh nanoparticles. At first, TPR experiment was conducted in order to understand the exsolution behavior of SYTRh5 at different reduction temperatures. As shown in Figure 9.3, multiple reduction peaks were revealed especially near the low temperature region. The first peak was assigned to the surface RhO_x species that were not incorporated into the perovskite structure thereby remaining on the catalyst surface. It has been reported that the intensity of this peak increases with high Rh loading indicating that the substitution of Ti sites to Rh are limited to some extent leading to formation of non-exsolved surface Rh nanoparticles [185]. The second peak of the TPR profile exhibits exsolution of Rh that are present in the vicinity of the catalyst surface. The substituted Rh cations that are located near the surface of the perovskite structure is considered to have less diffusion restriction moving to the surface compared to bulk Rh species thus showing high degree of exsolution at relatively lower temperatures. On the other hand, a broad peak was obtained between 573 K to 1173 K linked to the bulk Rh exsolution. The bulk Rh reduction takes place at much higher temperatures in wider temperature range. This demonstrates that higher temperature and longer reduction time are possibly needed to fully exsolve the Rh species from the B sites of the perovskite lattice structure. Incomplete exsolution of Rh due to short reduction time and low reduction temperature can significantly influence the catalytic activity of SYTRh5 for dry reforming giving inconsistency of the catalytic results.

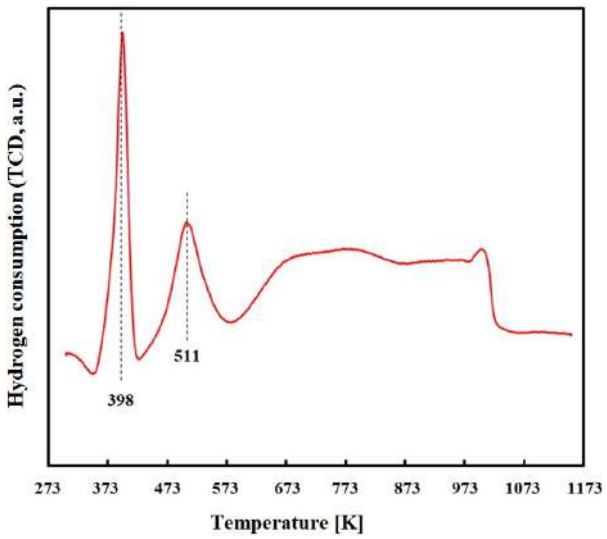

Figure 9.3: TPR Profile of SYTRh5 catalysts (exsolution of Rh).

9.6. Effect of reduction time

Firstly, the effects that time has on the reduction process were investigated. For these samples the reduction temperature was fixed at 1173 K.

9.6.1. Particle size of Rh and extent of exsolution

TEM images of the SYTRh5 catalysts reduced at different reduction times were collected to confirm the exsolution of Rh particles from the SYT perovskite oxide. Figure 9.4 shows the SYTRh5 sample after reduction performed for 4 (9.4B), 12 (9.4C) and 24 (9.4D) hours at 1123 k. To allow comparison, in Figure 9.8A the power before reduction process is also presented. Compared to the non-reduced SYTRh5 sample, the sintering level of the SYT support increased with the reduction time. The particle size of the SYT support increased from an average diameter of 18 *nm* (non-reduced) to 50 *nm* for SYTRh5 (4). When the reduction time was increased to 12 hours, the final powders reached an average diameter of 80 *nm* that remained approximately the same up to reduction time of 24 hours.

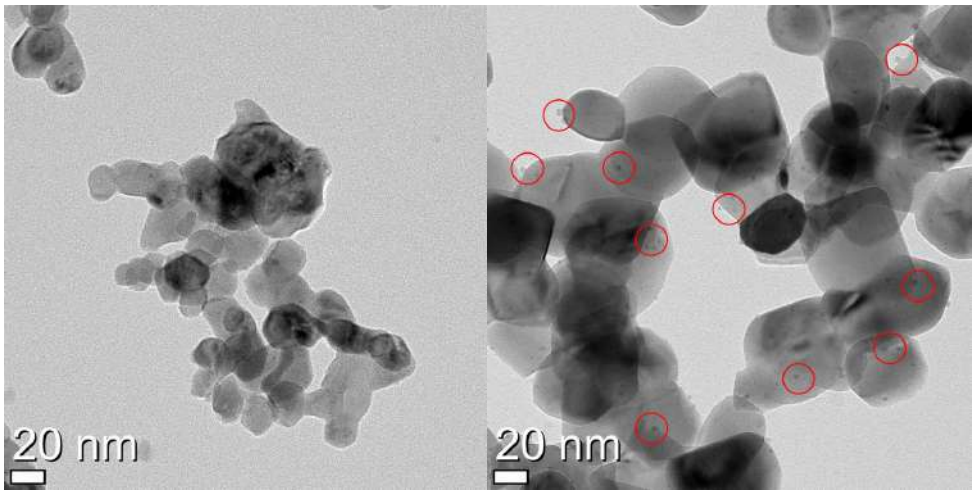

(A) SYTRh5 catalysts before reduction.

(B) SYTRh5 (4).

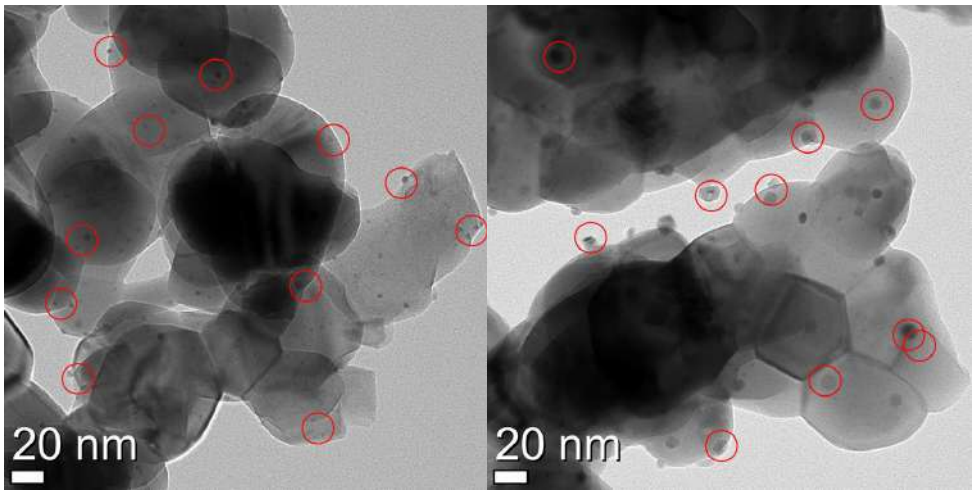

(C) SYTRh5 (12).

(D) SYTRh5 (24).

Figure 9.4: TEM images of the SYTRh5 catalysts before (9.8A) and after reduction at 1173 K for 4 (9.4B), 12 (9.4C), and 24 hours (9.4D) for the same scale bar. The red circles on the image indicate Rh-exsolved nanoparticles formed on the SYT oxide surface.

Similarly, the exsolution of Rh particles to the SYTRh5 surface resulted to be greatly time dependent.

The SYTRh5 sample before reduction show no formation of Rh particles indicating that most of the Rh species were incorporated inside the perovskite structure after catalyst synthesis. After 4 hours of reduction, the SYTRh5 (4) shows low extent of Rh exsolution leading to segregated Rh nanoparticles on the surface with average dimension of 2 *nm*, spotted in red circles on the TEM images. The Rh nanoparticles average diameter increased to 3 *nm* after 12 hours of reduction, and finally reached dimension between 5 to 10 *nm* over the SYTRh5 (24) catalysts. Compared to the non-reduced SYTRh5 samples, the presence of Rh particles on the catalyst surface indicates that exposing the catalyst to a reducing environment is essential to exsolve Rh species. Interestingly, tiny Rh particles were also observed especially on SYTRh5 (24) (Figure 9.4D). This is likely attributed to the difference in the rate of exsolution of Rh between bulk and surface and/or immobile Rh particles that are significantly stable under high reduction temperature compared to others. Furthermore, the possibility of existence of Rh particles close to single-atom size should not be ruled out for all tested SYTRh5 catalysts since these sites are hardly visible in the TEM images. Based on these results, a conclusion was reached that longer reduction time should be given to completely exsolve most of the Rh to the catalyst surface.

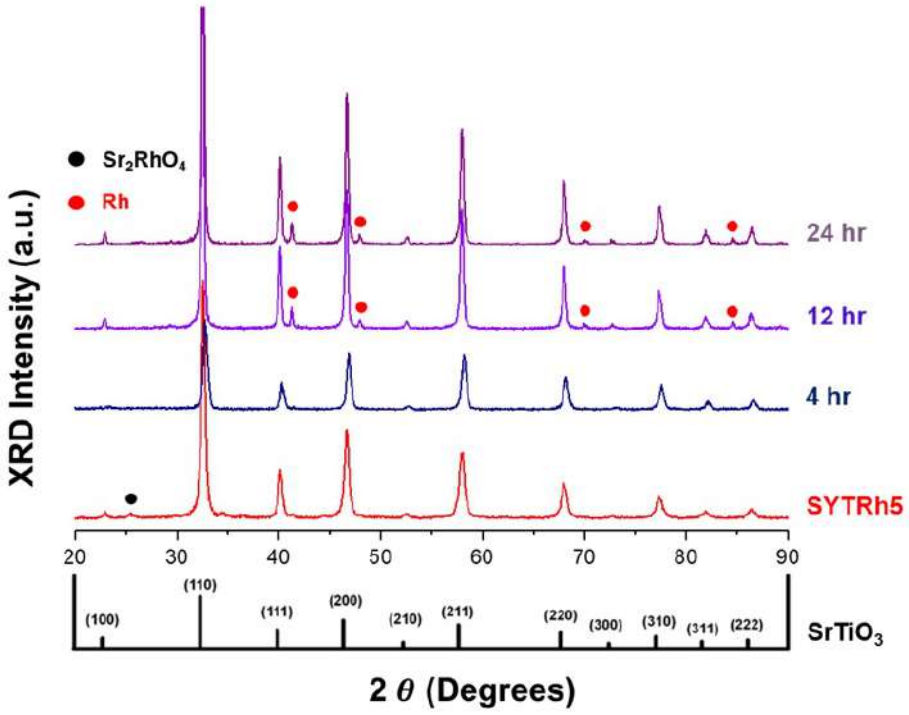

Figure 9.5: XRD patterns of the as-prepared SYTRh5 catalysts and SYTRh5 reduced at 11373 *K* 4 hours, 12 hours and 24 hours. The reference spectra of the $SrTiO_3$ perovskite is shown at the bottom to allow comparison.

In Figure 9.5 the XRD spectra of the SYTRh5 catalyst samples are presented. In comparison to the reference spectra of $SrTiO_3$ (JCPDS 35-0734), the XRD pattern of the as-prepared SYTRh5 does not show any major peaks related to the formation of byproducts such as RhO_2 except negligible amount of Sr_2RhO_4, thus suggesting that the Rh was successfully substituted in the SYT lattice. The spectrum of SYTRh5 after 4 hours of reduction only reports the peaks related to the perovskite structure without any secondary peaks that can suggest high stability of the perovskite structure of the SYTRh5 under harsh reduction conditions. Although approximately 2 *nm* Rh particles were observed in the TEM images for SYTRh (4) catalyst, the size of the Rh nanoparticles were too small to be detected using XRD due to

short-range ordering. With respect to the SYTRh5 (12) and SYTRh5 (24) catalysts, peaks related to the metallic Rh clearly appear and the intensity of these peaks increase as longer reduction was carried out over the sample. In good agreement with the TEM results, this explicitly suggests that the extent of exsolution is extremely dependent on the reduction time.

9.6.2. Oxidation states of exsolved Rh particles

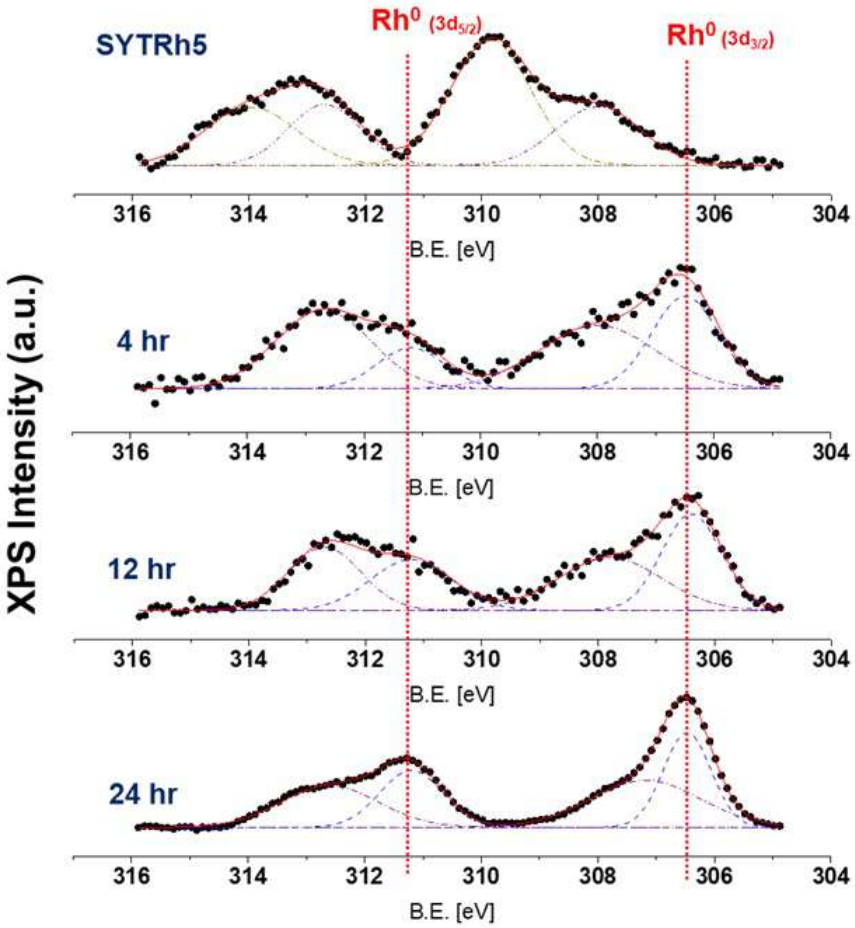

Figure 9.6: XPS Rh 3d fitted spectra of the as-prepared SYTRh5 catalysts and SYTRh5 reduced at 1173 K for 4, 12 and 24 hours.

The electronic characteristic of the SYTRh5 treated under different reduction time was examined by XPS. Figure 9.6 shows the fitted Rh 3d photoelectron XPS spectra of as-prepared SYTRh5 and SYTRh5 (4), SYTRh5 (12) and SYTRh5 (24) samples. Three doublet peaks were observed in the spectra. The doublet at 306.5 eV and 311.5 eV correspond to the $3d_{3/2}$ and $3d_{5/2}$ orbitals of metallic Rh (Rh^0) whereas other peaks appearing at higher binding energies are attributed to the oxidized Rh states (Rh^{x+}) [185, 186, 187]. In the case of as-prepared SYTRh5 sample, majority of Rh species were oxidized and no formation of metallic Rh were observed on the catalyst surface. However, with longer reduction time, significant increase in peak intensity for metallic Rh were acquired revealing exsolution of Rh particle to

the surface of STYRh5 catalyst. Analysis of the relative areas shows that with increasing reduction time the percentage of metallic Rh increased compared to the one related to the oxide (Rh metal/Rh oxide ratio was 38:62 after 4 hours, 50:51 after 12 hours and 53:47 after 24 hours) confirming is higher presence on the surface due to exsolution. It should be noted that the resolution of the XPS spectra enhances with increasing reduction time. This is likely ascribed to the increasing surface concentration of Rh located on the catalyst surface again signifying the exsolution of Rh during the reduction process.

9.6.3. Dry reforming reactivity of SYTRh5 (4, 12, 24)

The SYTRh5 (4, 12, 24) catalysts were tested for CH_4 dry reforming in a fixed-bed reactor system changing the operating temperature from 1173 K to 873 K and back to 1173 K at constant time intervals. The outlet gas was analyzed by GC to quantify the CH_4 conversion, CO and CO_2 and H_2 yields. The results are plotted in the Figure 9.7A, and the averaged CH_4 conversion values obtained from two temperatures ranges are reported in Figure 9.7B. The catalytic activity data of all the catalysts tested for this study can be seen in Table 9.1. Among the catalysts reduced with different reduction time, the SYTRh5 (4) showed significantly lower catalytic performance regarding the CH_4 conversion. The catalytic stability was also found low. As shown in the Figure, lower CH_4 conversions were achieved over SYTRh5 (4) when the reaction was repeated at equal reaction temperatures. The deactivation of the catalyst was predominantly attributed to the significant carbon formation on the catalyst surface, which was verified in the post-catalysis analysis. Compared to the SYTRh (4) catalyst, SYTRh5 (12) indicated slightly better catalytic performance at all reaction temperature range. Also, similar CH_4 conversions were obtained while increasing the reaction temperature demonstrating high stability of the catalyst. Lastly, SYTRh5 (24) catalyst exhibited the best performance reaching close to 100% conversion at 1123 K and completely repeatable activity results between the two temperature ranges.

The acquired order of reactivity ($4 < 12 < 24$ hours) under dry reforming condition indicate that the high catalytic activity is closely related to the higher extent of exsolution of Rh. At longer reduction time, higher surface concentration of Rh leading to increased number of active sites. On the other hand, shorter reduction time results in lower surface concentration of Rh on the catalyst surface resulting lower catalytic activity. Another factor that should be taken into account is the effect of Rh particle size. For example, Zhang et al. [186] studied the effect of Rh particle size on the catalytic activity of Rh supported on various supports such as YSZ, Al_2O_3, TiO_2, SiO_2, La_2O_3 and MgO under dry reforming conditions. In their results, significantly faster deactivation rate was obtained as the particle size of Rh decreases from 6 nm to 1 nm. Particularly on Al_2O_3 and SiO_2 supports, the deactivation rate rapidly rises from a point of 2.5 nm. Similar conclusion was made by Ligthart et al. [185] where they found that Rh nanoparticle smaller than 2.5 nm deactivate faster under steam methane reforming reaction compared to others of $4 \sim 9$ nm particles. This was explained by the small particle size of Rh that contain lower density of step edge sites. The step sites are predominantly responsible for C-O recombination to remove deposited carbon on the catalyst surface under methane reforming reaction. In the case of SYTRh5 (4) sample, which was fairly unstable over the thermal cycling process, the particle size of Rh was close to 2 nm. Therefore, these results are in good agreement with the aforementioned studies suggesting that the high catalytic activity of SYTRh5 reduced at higher temperatures is attributable to the higher surface concentration of Rh and the larger particle size.

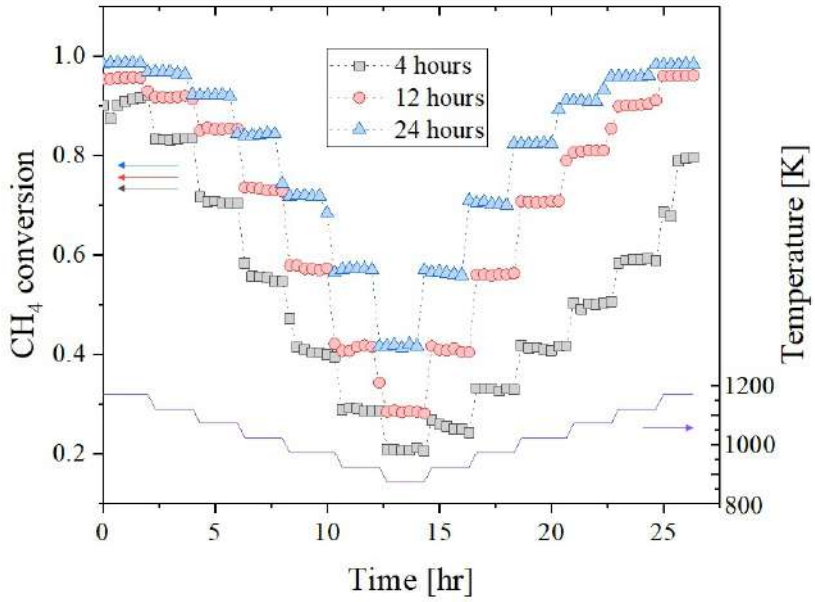

(A) CH_4 conversion at different operating temperatures.

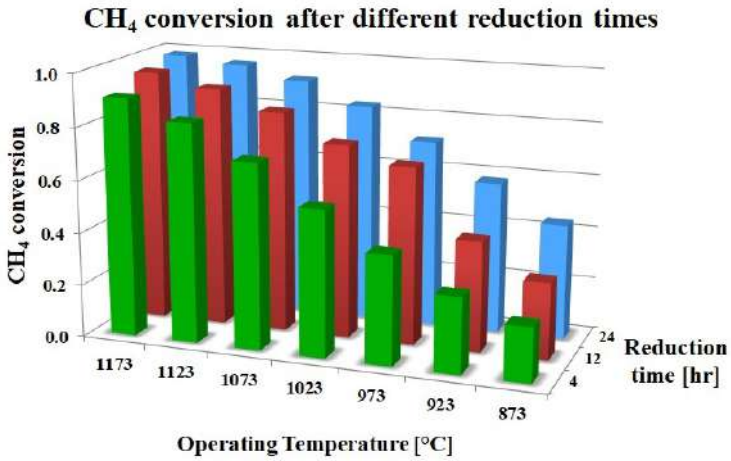

(B) Averaged CH_4 conversion obtained from thermal cycling.

Figure 9.7: Catalytic activity of SYTRh5 (4, 12, 24) catalysts under dry reforming conditions. It should be noted that the SYTRh5 (4) sample does not recover its original catalytic activity.

9.7. Effect of reduction temperature

As second step, the effects that temperature has on the reduction process were investigated. For these samples the reduction time was fixed at 24 hours as it resulted the best according to the previously

SYTRh5 reduced at X K for Y hours (X/Y)					
Temperature (K)	1173/4	1173/12	1173/24	1073/24	1273/24
(a) CH_4 conversion (%)					
873	20.7	29.2	43.8	19.4	49.1
923	27.1	41.1	57.6	25.1	66.2
973	36.9	58.8	71.3	34.5	80.6
1023	50.1	73.6	83.3	49.1	90.0
1073	66.5	83.9	91.5	64.6	94.9
1123	81.2	91.1	96.2	81.1	97.3
1173	90.8	95.8	98.4	91.6	98.3
(b) CO_2 conversion					
873	19.2	30.3	44.5	16.5	58.1
923	27.8	45.2	61.0	24.5	73.0
973	40.2	65.0	76.0	36.7	86.4
1023	54.8	79.8	87.4	53.5	94.2
1073	71.3	89.0	94.4	70.9	98.0
1123	85.2	95.1	97.9	85.9	99.7
1173	94.1	98.8	99.5	94.3	99.8
(c) H_2/CO ratio					
873	0.49	0.70	0.73	0.40	0.72
923	0.60	0.88	0.78	0.52	0.80
973	0.67	0.86	0.84	0.61	0.86
1023	0.75	0.87	0.88	0.71	0.90
1073	0.82	0.91	0.92	0.80	0.92
1123	0.87	0.93	0.93	0.87	0.93
1173	0.91	0.95	0.94	0.91	0.94

Table 9.1: Summary of the dry reforming reactivity of the tested SYTRh5 catalysts.

presented analysis.

9.7.1. Particle size of Rh and extent of exsolution

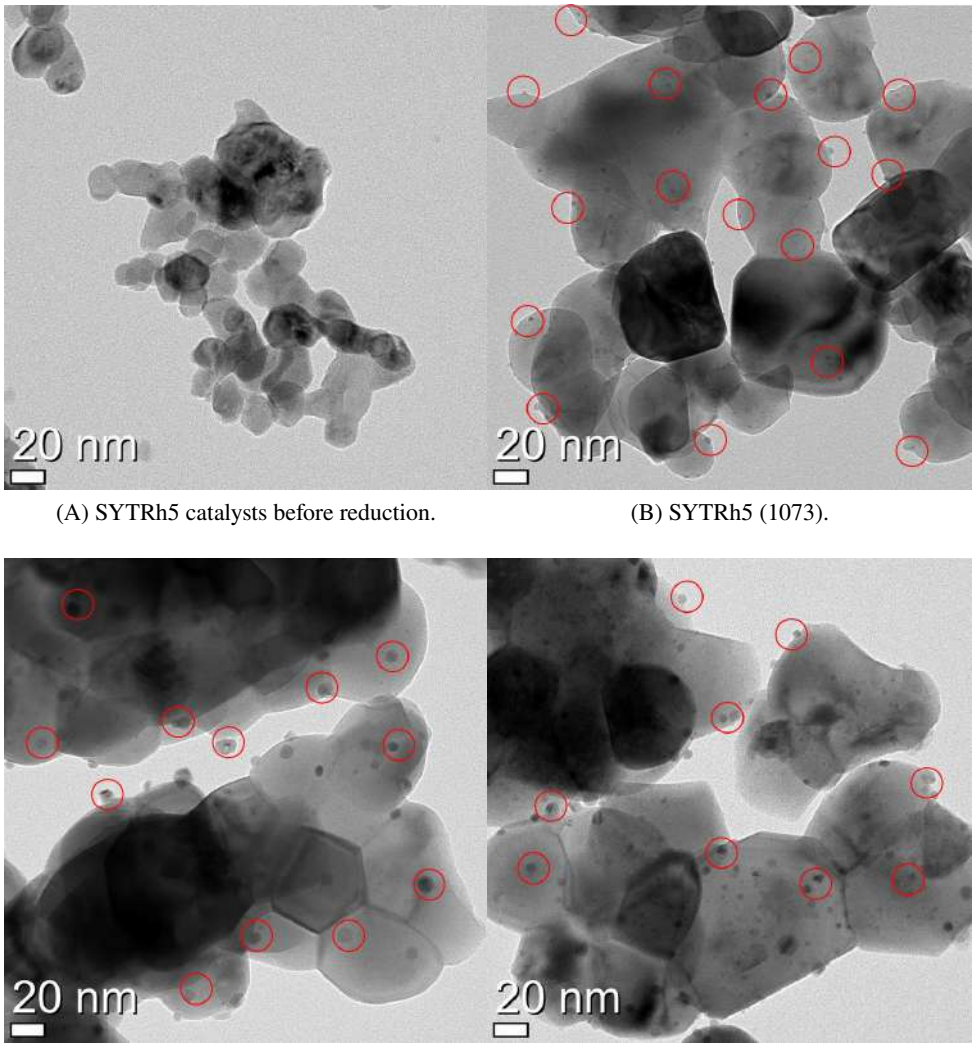

(A) SYTRh5 catalysts before reduction.

(B) SYTRh5 (1073).

(C) SYTRh5 (1173).

(D) SYTRh5 (1273).

Figure 9.8: TEM images of the SYTRh5 catalysts before (9.8A) and after reduction at 1073 K (9.8B), 1073 K (9.8C), and 1073 K (9.8D) for 24 hours for the same scale bar. The red circles on the image indicate Rh-exsolved nanoparticles formed on the SYT oxide surface.

The TEM images of the as-prepared SYTRh5 catalysts (9.8A) and of the samples reduced at 1073 K (9.8B), 1173 K (9.8C) and 1273 K (9.8D) are shown in Figure 9.8. Based on the TPR results shown above, reduction temperatures lower than 1073 K were not considered. As shown in the Figure, it was found that the increase in reduction temperature significantly affects the particle size and number of nanoparticles exsolved on the catalyst surface. It was found that the average diameters of the SYT support vary from 40 nm (at 1073 K) to 50 nm (at both 1173 K and 1273 K), while the Rh nanoparticles size increase from

average values of 2 *nm* for SYTRh5 (1073 *K*) up to 12 *nm* for the ones reduced at 1273 *K*. The particle size between SYTRh5 (1173) and SYTRh5 (1273) are comparable pointing out that the exsolved Rh particles with close to 10 *nm* size are reasonably stable at this temperature range. However, higher number of Rh particles were observed in the same region of the TEM images over SYTRh5 (1273) catalyst. These results again clearly indicate that the temperature of the reducing environment is important in order to improve the extent of Rh exsolution as well as to control the sintering level of the Rh particles.

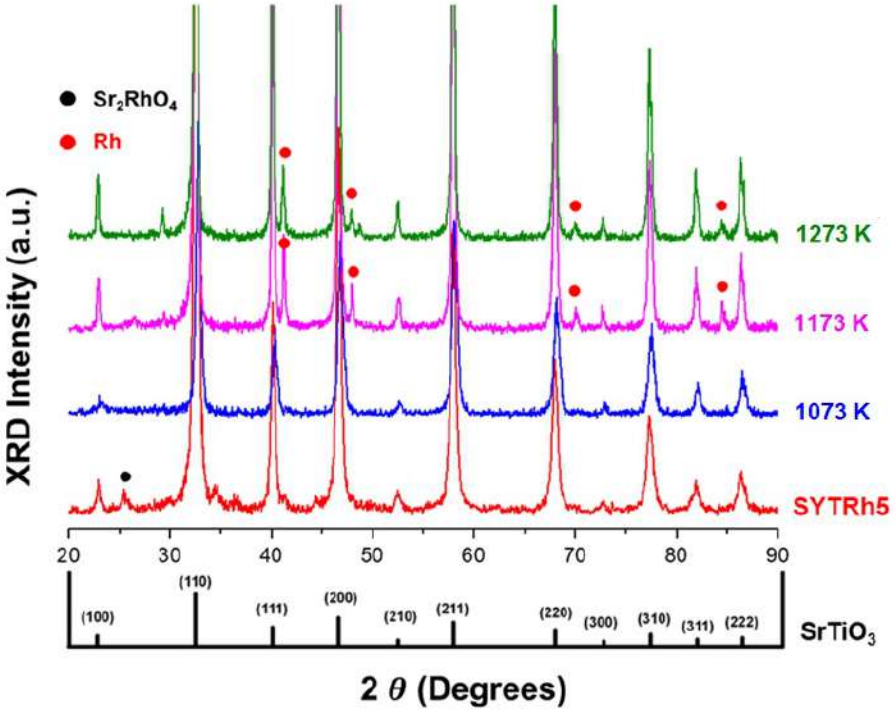

Figure 9.9: XRD patterns of the as-prepared SYTRh5 catalysts and SYTRh5 reduced at 1073 *K*, 1173 *K* and 1273 *K* for 24 hours. The reference spectra of the $SrTiO_3$ perovskite is shown at the bottom to allow comparison.

The XRD spectra of the SYTRh5 reduced at different temperatures are shown in Figure 9.9. For the SYTRh5 (1073), as expected, only the peaks related to the perovskite structure were observed due to the extremely small size of the Rh nanoparticles, while the SYTRh5 (1173, 1273) catalysts reveal peaks assigned to metallic Rh. The arise of these metallic Rh peaks again indicate exsolution of Rh from the bulk perovskite structure forming Rh nanoparticles on the surface as shown in the TEM images.

9.7.2. Oxidation states of exsolved Rh particles

Similar conclusion was reached in the XPS spectra. The fitted Rh 3d photoelectron spectra of the SYTRh5 catalysts after reduction at 10373 *K*, 11373 *K* and 12373 *K* are reported in Figure 9.10 . As mentioned in the previous XPS section binding energy of 306.5 *eV* and 311.5 *eV*, are ascribable to the Rh metal form [187]. Analysis of the relative areas shows that with increasing reduction temperature the percentage of metallic Rh increases confirming its higher presence on the surface due to exsolution. The intensity of the Rh 3d XPS spectra significantly increases as observed previously in the effect of reduction time study indicating that higher surface concentration of Rh was acquired when reduced at

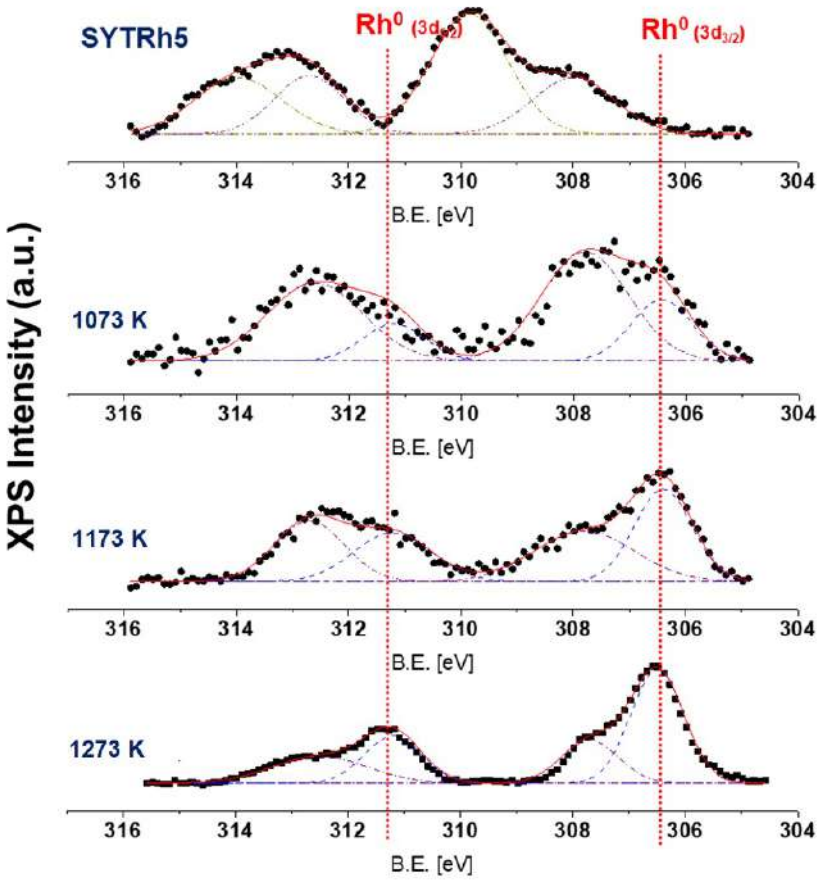

Figure 9.10: XPS Rh 3d fitted spectra of the as-prepared SYTRh5 catalysts and SYTRh5 reduced at at 10373 K, 11373 K and 12373 K for 24 hours.

higher temperatures.

9.7.3. Dry Reforming Reactivity of SYTRh5 (1073, 1173, 1273)

Dry reforming of CH_4 was carried out to investigate the effect of reduction temperature on the catalytic activity of SYTRh5 catalysts. The reaction conditions and procedures were the same of the previously tested samples at different reduction times. The catalytic activity data of all the catalysts tested for this study can be seen in Table 9.1.

As shown in Figure 9.11A, higher CH_4 conversions were obtained using SYTRh5 catalysts that are reduced at higher temperatures. For example, the SYTRh5 (1173) and SYTRh5 (1273) catalysts showed considerably higher CH_4 conversions at equal temperature of 873 K in comparison with SYTRh5 (1073). As the operating temperature increases, this difference in the CH_4 conversion reduces and complete conversion of CH_4 is reached for all catalysts. The greater catalytic activity of SYTRh5 (1173) and SYTRh5 (1273) is due to the higher surface concentration of Rh through exsolution from the perovskite oxide. This indicates that not only the reduction time but also the reduction temperature determines the (i) surface concentration of Rh, (ii) particle size of Rh and (iii) metal-support interaction by facilitating exsolution

of Rh.

Thermal cycling tests were also performed to examine the stability of these catalysts by changing the reaction temperature from 1173 *K* to 873 *K* and repeating the experiment from 873 *K* to 1173 *K*. While both SYTRh5 (1173) and SYTRh5 (1273) returned to the initial conversion values, SYTRh5 (1073) could not showing lower stability. This is attributable to the lower level of exsolution achieved through reduction at 1073 *K*.

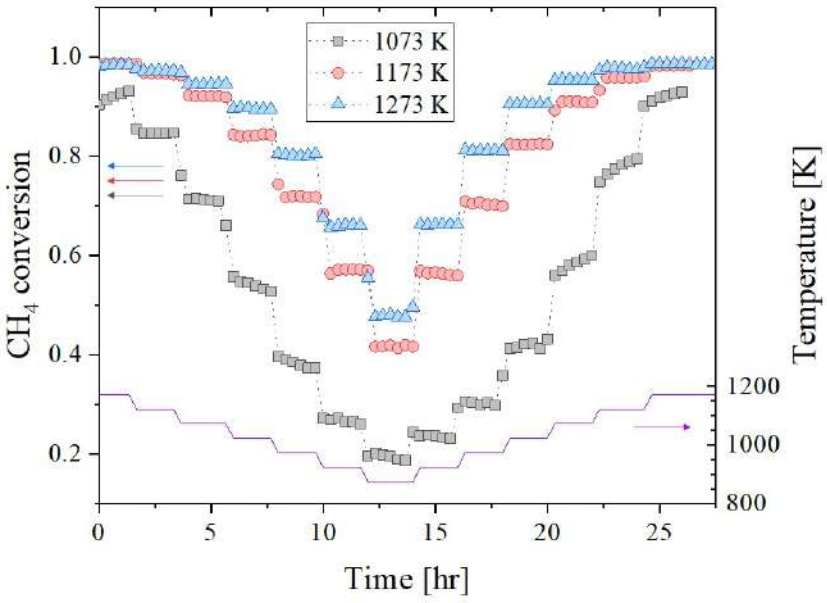

(A) CH_4 conversion at different operating temperatures.

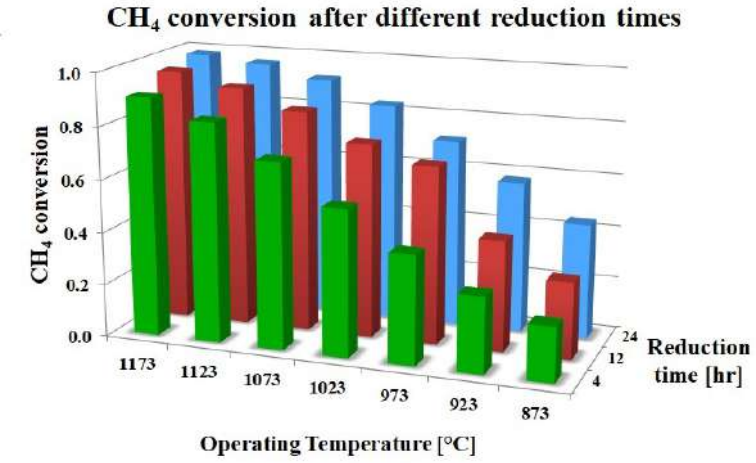

(B) Averaged CH_4 conversion obtained from thermal cycling.

Figure 9.11: Catalytic activity of SYTRh5 (1073, 1173, 1273) catalysts under dry reforming conditions.

9.8. Post-test analysis

A post-catalysis analysis was conducted on the SYTRh5 samples that were collected after dry reforming to identify the primary cause for catalyst deactivation over time. In Figure 9.12, the TEM images of the post-catalysis SYTRh5 samples after 4 hours (9.12A), 12 hours (9.12B), and 24 hours (9.12C) reduction at 1173 K, and after 24 hours reduction at 1273 K (9.12D) are presented.

Formation of carbon species as nanotubes is observed in all four cases. However, with increasing reduction time and temperature, the carbon coking appears significantly limited. The high resistance to coke formation could be attributed to the stronger metal-support interaction of the exsolved SYTRh5 catalyst, which is not easily achievable over the conventional metal-deposited catalysts. For example, Neagu et al. [174] reported nano-socketed Ni particles grown through exsolution, which are highly coke-resistant under CH_4 reforming conditions. The authors stated that because these Ni particles are socketed into the perovskite surface, "base growth" carbon coking is preferred. This growth mechanism, instead of lifting the metal particles upwards, leads to a carbon formation that is horizontal to the surface. This is due to the significantly strong adhesion between the metallic phase and the support. Regarding the SYTRh5 catalyst, the high coke resistance of the SYTRh5 (24) and SYTRh5 (1273) catalysts is therefore possibly attributed to the formation of larger Rh-exsolved particles whose Rh particles are significantly more attached to the SYT support, leading to a stronger metal-support interaction. Furthermore, limited agglomeration of the Rh-exsolved particles were observed over the SYTRh5 (24) and SYTRh5 (1273) catalysts whereas for SYTRh5 (4) and SYTRh5 (12), the size of the Rh-exsolved particles increased after dry reforming.

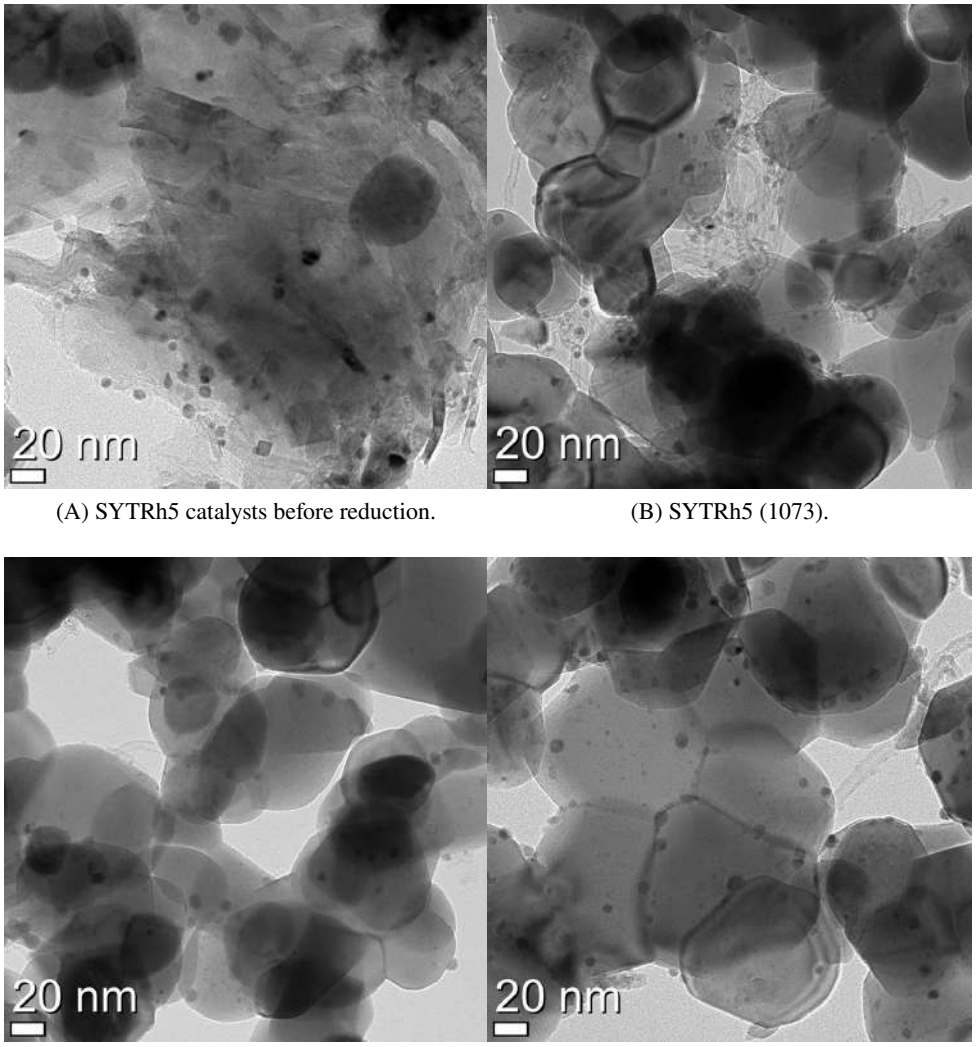

(A) SYTRh5 catalysts before reduction.

(B) SYTRh5 (1073).

(C) SYTRh5 (1173).

(D) SYTRh5 (1273).

Figure 9.12: TEM images of the SYTRh5 catalysts after dry-reforming activity tests SYTRh5 (4) (9.12A), SYTRh5 (12) (9.12B), SYTRh5 (24) (9.12C), SYTRh5 (1273) (9.12D).

9.9. Recovery of catalytic activity of the SYTRh5 after sulfur poisoning

The recovery characteristics of SYTRh5 from sulfur poisoning was investigated by flowing a mixture of H_2S, CH_4 and CO_2 into the reactor at 1173 K. The samples reduced at different temperatures were subjected to the testing: SYTRh5 (1073), SYTRh5 (1173), and SYTRh5 (1273).

As displayed in Figure 9.13, the CH_4 conversion of the catalysts reduced at different reduction temperatures significantly decrease after introduction of H_2S into the reactant stream. This was fairly expected considering the high concentration of H_2S (100 *ppm*). Although, all three catalyst were severely deactivated under H_2S conditions, it was found that the SYTRh5 (1273) showed slightly higher CH_4 conversion of about 29%.

When the H_2S feed was interrupted, a complete regeneration of the catalyst was achieved in both cases

of SYTRh5 (1173), and SYTRh5 (1273), and the CH_4 conversions quickly returned to the original level. On the other hand, the SYTRh5 (1073) catalyst could not recover its original activity even after a few hours of reaction revealing limited recovery, producing a conversion of about 75% (versus the initial 85%). It should be noted that all three catalysts deactivated under H_2S conditions. The remarkably high recovery rate of the SYTRh5 (1173) and SYTRh5 (1273) catalysts is attributed to the higher degree of exsolution of the Rh particles, which is a result of the higher reduction temperature, that are strongly anchored to the SYT catalyst support. This strong synergy effect between the metallic Rh and SYT support possibly increases the electron deficiency of the active sites, thereby lowering the desorption energy of the sulfur species to the metal.

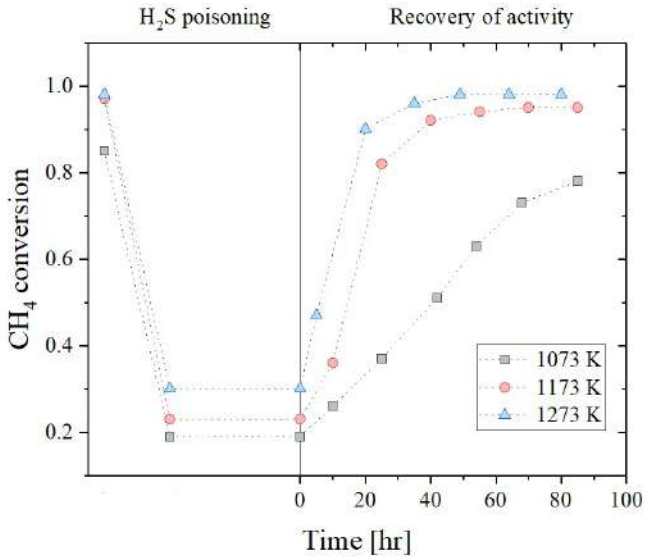

Figure 9.13: H_2S poisoning and recovery test results of SYTRh5 (1073, 11730, 1273 reduced for 24 hours) catalysts at operating temperature of 1173 K for dry reforming.

Summary & Conclusions

A recent experimental campaign performed by ExxonMobil and FuelCell Energy to explore the possible use of Molten Carbonate Fuel Cells in Carbon Capture applications has revealed a secondary electrochemical path involving the migration of OH^- in competition with CO_3^{2-} ions. This so-called dual-anion mechanism is of fundamental importance as it can greatly affect the cell performance in terms of both energy produced and CO_2 capture rate. As it was never described before in the literature, it needed to be studied in particular to derive a model for its simulation. In fact, the modeling of physical and chemical systems is of extreme importance to understand phenomena, improve or develop new and more sustainable processes, and design or control industrial plants.

Firstly, I studied the experimental data to understand their effects on the occurrence of the OH^- driven electrochemical path. From this analysis I was able to identify a circuit to schematize this dual-anion mechanism. Then, starting from the Butler-Volmer equation, I derived the expression for the polarization resistance on each reactant. This allowed to establish a base model to simulate cells working at these conditions. For testing, the model was integrated into an existing Fortran home-made code developed by my research group for the simulation of high temperature fuel cells called SIMFC. It tested positively with good fitting of the main studied parameters: voltage, utilization factor of CO_2 and carbonate transference number.

Once the basic model was developed, it was recognized that gas diffusion has an extreme significance in determining the extent of one path over the other. In particular, experimental evidence performed using cells having different current collectors or different inert gas at the cathode side showed that the more gas diffusion is hindered, the more also is the carbonate path. As H_2O is smaller than CO_2 its diffusion is less penalized at similar conditions. This allows for higher H_2O concentrations at the gas/electrolyte interface favoring higher formation of OH^-. To underline this aspect and allow an easier use of the model, a new formulation was derived for the polarization resistances of the cathodic reactants. In particular a gas diffusion term along the z-axis perpendicular to the cell plane was made explicit. Again, this new formulation was positively tested on different experimental data sets.

This new formulation including z-axis diffusion has a high number of empirical parameters to be determined for adequate use. However, they are all fundamental to properly describe the system. This was shown in Chapter 5 by performing a sensitivity analysis.

At this point the kinetic core of the model lacked an explicit dependence on the operating temperature. The model was developed as such to focus on the effects of the reactants and the diffusion. However, with such formulation, the model cannot be applied without significant errors to real applications. Consequently, additional data collected at different temperatures were used to study possible effect on the dual-anion mechanism and integrate the temperature dependence in the model. The analysis proved that temperature has a negligible effect on the occurrence of one path over the over, and only influence the overall cell performance in term of measured voltage.

Also, this final model having explicit temperature dependence provided with good fitting of the experimental data. However, a fair number of data points showed high errors. These data were collected either with a high utilization factor of CO_2 or low carbonate ions transference number. This meant that the model had issues in dealing with the simulation of data where the hydroxide path extent grows. This was ascribed to a lack of a proper method to relate the polarization resistance with the carbonate/hydroxide equilibrium. So, the polarization resistance of CO_2 and H_2O were redeveloped to better consider this aspect and the final formulation was tested with satisfying results.

As result of this analysis, the dual-anion model developed can be successfully used for the simulation

of Molten Carbonate Fuel Cells with both water and CO_2 presence in the cathode compartment exhibit this newly discovered dual-anion mechanism in a large range of operating conditions and flow configurations. This newly developed model is of significant importance as it correctly takes into account the effects of water at the cathode side and its migration to the anode and thus fundamental to describe MCFC systems particularly for CCS applications. For example, at the end of Chapter 2, I showed the local results of a cell fed with blast furnace gas. Using the model previously developed that does not account for the dual-anion mechanism, the simulated voltage obtained was of $662\,V$ and the CO_2 was of 90%. Using the newly developed dual-anion model with explicit temperature dependence and equilibrium correction and considering CC with open area equal to 35% the simulated voltage increases to $684\,V$ and the CO_2 utilization decreases to 88.9% with a carbonate transference number of 0.94. Although the electrochemical performance slightly increases and the capture rate only slightly decreases, these changes can be extremely significant in plant or in case the cathode outlet has higher H_2O content.

In the following Table a summary of the progression in the development of the dual-anion model is presented. The table includes the number of experimental data used for fitting the parameters for each intermediate model, the average simulation error for voltage and carbonate ion transference number, the percentage of outliers (data with a simulated error higher than 10%), and the strengths and limits of each mode.

To complete the modeling of high temperature fuel cells, in the eighth chapter I integrated into the SIMFC code a formulation to deal with direct internal steam reforming of CH_4. This was done to allow studies on catalyst distribution and degradation. For this part of the work, I considered Solid Oxide Fuel Cells. Nonetheless, the same formulation with small corrections can be also applied to Molten Carbonate.

Overall, this thesis describes the development of a complete kinetic model for the simulation of high temperature fuel cells.

Finally, in the last chapter, the analysis of a Rh doped SYT catalysts for CH_4 dry reforming to be used as SOFC anode was presented. The first part of the analysis provided with specific results to determine the best reduction conditions to obtain the catalyst that gives the best performance in term of CH_4 conversion and stability. The second part showed the high recovery of these kind of catalysts after sulfur poisoning. This is particularly important if these catalysts are used with biogas or other fuel feeds that might contain sulfur derived pollutants.

Model	Number of data used	Average % error V	Average % error $t_{CO_3^{2-}}$	% of Outliers V	% of Outliers $t_{CO_3^{2-}}$	Strengths & limits
Base dual-anion model	<200	3%	5%	4%	10%	1^{st} model that captures the dual-anion mechanism Kinetic parameters must be re-evaluated for (1) different cell geometry, (2) different inlet gas mixtures, and (3) different operating temperatures (reference value: 923 K) The model applies to isothermal operation only
Dual-anion model with z-axis diffusion	~300	6%	5%	4%	6%	Cathode current collector configurations are modeled using geometric factors The model is applicable to different inlet gas mixtures Kinetic parameters must be re-evaluated for different operating temperatures The model applies to isothermal operation only
Dual-anion model with dependence of R_Ω on the gas pahse	400	6%	4%	23%	3%	The model incorporates the dependence of ohmic resistance on the electrolyte composition that is influenced by the cathode gas concentrations Anode H_2 resistance is extended to full non-linear equation, covering operation at low fuel utilization Kinetic parameters must be re-evaluated for different operating temperatures The model applies to isothermal operation only
Dual-anion model with explicit temperature dependence	450	7%	4%	23%	3%	Describes both isothermal and non-isothermal operations, using a single set of kinetic parameters for a range of operating temperatures (tested range 848 – 948 K)
Final dual-anion model with temperature dependence and hydroxide-carbonate equilibrium	450	4%	5%	8%	10%	The model includes an explicit dependence of the cathode polarization resistance on the carbonate-hydroxide equilibrium

Progress of the dual-anion model.

List of publications

- B. Bosio, T. Barckholtz, P.H. Kalamaras, G. Kiss, J. Rosen, D. Bove, and E. Audasso,Experimental and modelling investigation of CO_3^{2-} and OH^- equilibrium effects on Molten Carbonate Fuel Cell performance in carbon Capture applications, *submitted*.
- R. Cooper, D. Bove, E. Audasso, M.C. Ferrari, and B. Bosio., "A feasibility assessment of a retrofit Molten Carbonate Fuel Cell coal-fired plant for flue gas CO_2 segregation.", International Journal of Hydrogen Energy, 2020, doi: DOI.
- D. Bove, E. Audasso, T. Barckholtz, G. Kiss, J. Rosen, and B. Bosio, "Process analysis of molten carbonate fuel cells in carbon capture applications.", International Journal of Hydrogen Energy, 2020, doi: 10.1016/j.ijhydene.2020.08.020.
- F. Bianchi, A. Baldinelli, L. Barelli, G. Cinti, E. Audasso, and B. Bosio, "Multiscale modeling for reversible solid oxide cell operation.", Energies, 2020, 13, 1–16, doi:10.3390/en13195058.
- E. Audasso, F. Bianchi, B. Bosio, "2D simulation for CH_4 internal reforming-SOFCs: An approach to study performance degradation and optimization", Energies, 2020, 13, 4116, doi: 10.3390/en13164116
- E. Audasso, B. Bosio, D. Bove, E. Arato, T. Barckholtz, G. Kiss, J. Rosen, H. Elsen, R. Blanco, Gutierrez, L. Han, T. Geary, C. Willman, A. Hilmi, C. Y. Yuh, and H. Ghezel-Ayagh, "The Effects of Gas Diffusion in Molten Carbonate Fuel CellsWorking as Carbon Capture Devices.", Journal of The Electrochemical Society, 2020, 167, 114515, doi: 10.1149/1945-7111/aba8b6.
- E. Audasso, B. Bosio, D. Bove, E. Arato, T. Barckholtz, G. Kiss, J. Rosen, H. Elsen, R. Blanco Gutierrez, L. Han, T. Geary, C. Willman, A. Hilmi, C.Y. Yuh, and H. Ghezel-Ayagh. "New, Dual-Anion Mechanism for Molten Carbonate Fuel Cells Working as Carbon Capture Devices.", Journal of The Electrochemical Society, 2020, 167, 084504, doi: 10.1149/1945-7111/ab8979.
- E. Audasso, Y. Kim, J. Cha, V. Cigolotti, H. Jeong, Y.S. Jo, Y. Kim, S.H. Choi, S.P. Yoon, S.W. Nam, and H. Sohn. "In situ exsolution of Rh nanoparticles on a perovskite oxide surface: Efficient Rh catalysts for dry reforming.", Korean Journal of Chemical Engineering, 2020, 37, 1401–1410, doi: 10.1007/s11814-020-0592-4.
- L. Spiridigliozzi, G. Accardo, E. Audasso, B. Bosio, S.P. Yoon, and G. Dell'Agli, "Synthesis of easily sinterable ceramic electrolytes based on bi-doped 8ysz for it-sofc applications", AIMS Materials Science, 2019, 6, 610–620, doi: 10.3934/matersci.2019.4.610.
- E. Audasso, P. Campbell, M. Della Pietra, M.C. Ferrari, B. Bosio, and E. Arato, "Molten carbonate fuel cells in integrated systems for the exploitation of poor fuels and the segregation of CO_2.", Bulgarian Chemical Communications, 2018, 50, 99-107, http://www.bcc.bas.bg/BCC_Volumes/Volume_50_Special_D_2018/BCCvol50_SpecD_paper12.pdf

A
Nomenclature

Latins

Symbol	Meaning	Units
A	Active area/surface	m^2
Arr	Arrhenius pre-exponential factor	$\Omega\, cm^2$
A, B, C, D, E	Exponential in the definition of the area specific polarization resistance[1]	–
$\mathscr{a}$, $\mathscr{b}$	Extent of the two anion paths[2]	–
C	Concentration	$mol\, m^{-3}$
Cp	Specific heat	$J\, mol^{-1}\, K^{-1}$
$\mathscr{D}$	Diffusion coefficient	$m^2\, s^{-1}$
E	Equilibrium potential	V
ΔE	Activation Energy	$J\, mol^{-1}$
F	Faraday's constant	$s\, A\, mol^{-1}$
F	Molar flux	$mol\, s^{-1}$
G	Gibbs free energy	$J\, mol^{-1}$
h	Coefficient of heat transfer for convection	$W\, m^{-2}\, K^{-1}$
H	Enthalpy	$J\, mol^{-1}$
$\mathscr{H}$	Henry's constant	$atm\, m^3\, mol^{-1}$
J	Current density	$A\, cm^{-2}$
j	Gas molar flux due to sole diffusion	$mol\, m^{-2}\, s^{-1}$
J_0	Exchange current density	$A\, cm^{-2}$
k	Kinetic constant	$mol\, s^{-1}\, m^{-2}\, atm^{-x3}$
K	Adsorption coefficient	–
K_0	Adsorption pre-exponential coefficient	–
K_C	Mass transfer coefficient	$m\eta s^{-1}$
K_eq	Equilibrium constant	$atm{-}x^4$
l	Passageway height	m
$\mathscr{l}$	Cathode thickness	mm
M	Molar mass	$kg\, mol^{-1}$
M, N	Fluid-dynamic coefficients	–
n	Gas flow rate per lenght unit	$mol\, m^{-1}\, s^{-1}$
N	Gas molar flux	$mol\, m^{-2}\, s^{-1}$
n_{el}	Moles generated by electrolysis according to Faraday's law	$mol\, s^{-1}$
ox	Oxidated species	–
p	Preassure	atm
P_i	Empirical parmaters	$variable$

[1] Refer to Eqs. 1.3 and 1.4
[2] Refer to Eq. 3.12
[3] The exponent of the *atm* depend on the reaction rate of the reactants.
[4] The exponent of the *atm* depend on the reaction rate of the reactants.

Symbol	Meaning	Units
Q	Thermal power density	$W\ m^{-2}$
$q_{cross-over}$	Cross-over flow rate	$mol\ s^{-1}$
Q_{SR}	SR reaction quotient	atm^2
R	Area specific polarization resistance	$\Omega\, cm^2$
R	Gas constant	$J\ mol^{-1}\ K^{-1}$
r	Generation rate	$mol\ m^{-2}\ s^{-1}$
r	Reaction rate	$mol\ s^{-1}$
Re	Reynolds number	–
red	Reduced species	–
s	Specific gas-solid interface ratio	–
T	Temperature	K
t	Anion transference number	–
t	Time	s
U	Utilization factor	–
V	Voltage	V
v	Gas velocity	$m\ s^{-1}$
V_{Cat}	Cathode volume	m^3
$\sum v$	Atomic diffusion volume	m^3
w	Vertical celocity component on the cell plane	$m\ s^{-1}$
x	Spatial coordinate	m
x	Molar fraction	–
y	Spatial coordinate	m
Y_i	Coefficients in the expressions of R_Ω	$variable$
z	Spatial coordinate	m
Z	Cell geometry, materials and flow regime coefficients	–
z_e	Electron exchanged in the electrochemical reactions	–

Greeks

Symbol	Meaning	Units
α	Reaction order	–
$\alpha, \beta, \gamma, \delta, \varepsilon$[5]	Power law kinetic coefficients	–
δ	Stagnant film thickness	μm
ϵ	Correction factor for induced fluxes	–
ε	Porosity	–
η	Polarization	V
ϑ	Friction factor	–
ϑ	Water correction factor	–
λ	Thermal conductivity	$W\ m^{-1}\ K^{-1}$
λ	Wavelength	Å
λ, ϕ	Steam reforming kinetic orders	–
μ	Gas viscosity	$Pa\ s$
ν	Stoichiometric coefficient	–

[5]Refer to Eq. 8.4

Symbol	Meaning	Units
ξ	Cross-over parameter	$Nm^3\ atm^{-1}\ h^{-1}\ cm^{-2}$
σ	Active area coefficient	–
τ	Tortuosity	–
Υ	Coefficient to correlate ions concentration in the melt and gas phase	–

Subscripts

Symbol	Meaning
act	Related to the activation
ads	Adsorption
An	Related to the anode
av	Average
$average$	Evaluated at the average point of diffusion
$bulk$	In the bulk
Cat	Related to the cathode
$conc$	Related to the concentration
$cond$	Related to the conduction
$cross-over$	Related to the cross-over
e	Reated to the electrons
eff	Effective
eq	At the equilibrium
$External$	External to the anion paths
$g-l$	Gas-liquid interface
i	Related to the i-th reactant
in	Inlet
$interface$	At the gas-liquid interface
j	Related to the j-th component
L	Longitudinal
L	Limit
m	Related to the m-th anionic path
mix	Gas mixture
n	Related to the n-th component
out	Outlet
ox	Related to the oxidated species
$reac$	Related to the reaction
red	Related to the reduced species
S	Related to the solid
SR	Related to the steam reforming
sur	At the electrode surface
T	Transversal
TOT	Total
x	Related to the spatial coordinate x
y	Related to the spatial coordinate y
Ω	Related to the Ohmic resistance

Superscript

Symbol	Meaning
ε	Related to the reverse reaction
$'$	Related to the direct reaction
$*$	Similar
γ	Fluid-dynamic coefficient
σ	Fluid-dynamic coefficient
0	Related to the standard state

Abbreviations

Symbol	Meaning
BET	Brunauer–Emmett–Teller
CC	Current collector
CCS	Carbon Capture and Storage
DIR	Direct internal reforming
EIS	Electrochemical Impedance Spectroscopy
EMRE	ExxonMobil's Research and Engineering
ER	External reforming
FCE	FuelCell Energy
GC	Gas cromatograph
IIR	Indirect internal reforming
LST	La-substituted $SrTiO_3$ perovskite
MCFC	Molten carbonate fuel cells
OCV	Open circuit voltage
POP	Peroxide path
S/C	Steam to carbon ratio
SIMFC	Simulation of Fuel Cells
SOP	Superoxide path
SR	Steam reforming
STEM	Scanning transmission electron microscope
SYT	$Sr_{0.92}Y_{0.08}Ti_2O_3$ perovskite
TCD	Thermal conductivity detector
TEM	Transmission electron microscope
TPB	Three phase boundary
TPR	Temperature-Programmed Reduction
UNIGE	University of Genoa
UNIPG	Univerity of Perugia
WGS	Water-gas-shift reaction
XPS	X-ray Photoelectron Spectroscopy
XRD	X-ray diffraction

B
Additional modeling information

B.1. Induced fluxes

Due to the non-equimolar consumption or production of reactants in the electrochemical reactions other the electrode surface, induced convective fluxes originate to balance the net volume flow. As a result, according to the mole disparity in the reactions, the reactant diffusive fluxes going to the electrode will be penalized or promoted. In the developed model, I can consider the presence of this induced fluxes in the expression for the limit current density:

$$J_{L,i} = z_e F K_C \frac{\nu_e}{\nu_i} C_i \varepsilon_i \tag{Eq. B.1}$$

where ϵ_i is a correction factor function of the reactant concentration and stoichiometry that allows to consider the induced fluxes. It can be expressed as:

$$\epsilon_i = \frac{1}{\left(1 - \sum_k \frac{\nu_k}{\nu_i} x_i\right)_m} \tag{Eq. B.2}$$

where ν is the stoichiometric coefficient, k scans all chemical reactants and products involved in the studied reaction and m indicates the logarithmic mean between the bulk and the reacting site.

The logarithmic mean between two variables y and z is expressed as:

$$M_{log} = \frac{z - y}{\ln\left(\frac{z}{y}\right)} \tag{Eq. B.3}$$

Thus, the ε_i can be expressed as:

$$\epsilon_i = \frac{\ln\left(\frac{\left(1-\sum_k \frac{\nu_k}{\nu_i} x_i\right)_{reacting\ site}}{\left(1-\sum_k \frac{\nu_k}{\nu_i} x_i\right)_{bulk}}\right)}{\left(1 - \sum_k \frac{\nu_k}{\nu_i} x_i\right)_{reacting\ site} - \left(1 - \sum_k \frac{\nu_k}{\nu_i} x_i\right)_{bulk}} \tag{Eq. B.4}$$

For each possible reactant the corresponding correction factor becomes:

$$\epsilon_{CO_2} = \frac{\ln\left(1 - 1.5\ x_{CO_2}\right)^{-1}}{1.5\ x_{CO_2}} \tag{Eq. B.5}$$

$$\epsilon_{H_2O} = \frac{\ln\left(1 - 1.5\ x_{H_2O}\right)^{-1}}{1.5\ x_{H_2O}} \tag{Eq. B.6}$$

$$\epsilon_{H_2} = \frac{\ln\left(1 + x_{H_2}\right)}{x_{H_2}} \tag{Eq. B.7}$$

$$\epsilon_{O_2} = \frac{\ln\left(1 - 3\ x_{O_2}\right)^{-1}}{3x_{O_2}} \qquad \text{(Eq. B.8)}$$

From the expression it appears that in MCFC case, the reactant diffusion is exalted at the cathode, since the reactants disappears, and penalized at the anode, since the products formation hinder the reactant diffusion.

In a previous works [108], my research group has observed that considering the convective induced fluxes for H_2 greatly improve the model simulation. Thus, I decided to keep them in the development of the dual-anion mechanism model when we considered the linear expression for the polarization of H_2.

On the other hand, although considering them slightly improve the performance [4], I chose to neglect them for CO_2 and O_2. This because for CO_2 I considered a non-linear term for the polarization and thus I wanted to light the model, and for the O_2 because in the considered operating conditions the resistance is so low that inclusion of the fluxes would be negligible.

Since I can assume a similar behavior for H_2O as for CO_2, and since I considered a non-linear expression for its resistance, I decided to neglect also the induced convective fluxes for the it.

B.2. Diffusion coefficients in the gas phase

To evaluate the concentration of the reactant gas after diffusion in the gas phase, I introduced the diffusion coefficient of each gas "i" in the gas mixture "m": $\mathscr{D}_{i,m}$. In the model, this coefficient was simplified assuming an average value $\mathscr{D}_{i,m,av}$ between the diffusion coefficient at the bulk composition and the one at the composition after the diffusion, due to too many required calculations to evaluate it locally alongside the z-axis.

The diffusion coefficient of a gas "i" in a mixture of gas "m" can be expressed according to the following equation [188]:

$$\mathscr{D}_{i,m} = \left(\sum_{i \neq j} \frac{x_j}{\mathscr{D}_{i,j}}\right)^{-1} \left(1 - x_i\right) \qquad \text{(Eq. B.9)}$$

where $\mathscr{D}_{i,j}$ is the diffusion coefficient of the binary mixture "i,j", and x_j and x_i are the molar fraction of j and i in the mixture. Thus, to evaluate the diffusion coefficient $\mathscr{D}_{i,m}$ of each species (CO_2, H_2O, O_2, N_2 and He) in the mixture, it is necessary to assess the diffusion coefficient for each couple. In the literature different approaches can be found for determining the diffusion coefficients of a given component in a binary mixture [189, 190, 191, 192]. The methods are all semi-empirical and the formulation mainly differ according to the nature of the species involved. In this work, we applied the equation derived by Fuller [191] that was developed to evaluate the diffusivity when polar gas components, such as H_2O, are present. According to Fuller [191], the equation that describes the diffusion coefficient of the binary mixture i,j ($\mathscr{D}_{i,j}$) is the following:

$$\mathscr{D}_{i,j} = \frac{0.00143\ T^{1.75}}{p\ M_{i,j}^{0.5}\left[\left(\sum v\right)_i^{\frac{1}{3}} - \left(\sum v\right)_j^{\frac{1}{3}}\right]^2} \qquad \text{(Eq. B.10)}$$

where $\sum v$ is the sum of the atomic diffusion volumes of each component of the mixture, and $M_{i,j}$ is the harmonic mean of the molar mass of the components i and j.

The binary coefficients for all the considered species are the following:

$$\mathscr{D}_{CO_2,N_2} = 1.172\ cm^2\ s^{-1}$$

$$\mathscr{D}_{CO_2,He} = 4.192\ cm^2\ s^{-1}$$

$$\mathscr{D}_{CO_2,H_2O} = 1.506\ cm^2\ s^{-1}$$

$$\mathscr{D}_{CO_2,O_2} = 1.472\ cm^2\ s^{-1}$$

$$\mathscr{D}_{H_2O,N_2} = 1.862\ cm^2\ s^{-1}$$

$$\mathscr{D}_{H_2O,He} = 6.080\ cm^2\ s^{-1}$$

$$\mathscr{D}_{H_2O,O_2} = 2.214 cm^2\ s^{-1}$$

$$\mathscr{D}_{O_2,N_2} = 1.802\ cm^2\ s^{-1}$$

$$\mathscr{D}_{O_2,He} = 5.603\ cm^2\ s^{-1}$$

The diffusivity of each gas in the mixture cannot be shown since it varies in all the points being dependent of the local composition.

B.3. Diffusion in the liquid phase

In the development of the z-axis diffusion model (Chapter 4), the diffusion of the reactants in the liquid electrolyte melt was not considered and it was masked in the kinetic parameters of the resistances. During the development of the model I tried to insert this aspect, however lack of proper information regarding the cell, the mixture and the physical properties did not allow for a good simulation.

In the following I will present the development that I tried to apply to the model.

As shown in the Chapter 3, according to the Butler-Volmer equation, the mass transport polarizations term of the i-th gas can be expressed as function of the ratio between the bulk and the reacting concentration as:

$$\eta_{conc,i} = -\frac{\alpha_i' RT}{\alpha_e' z_e F}\, ln\left(\frac{C_{i,sur}}{C_i}\right) \qquad \text{(Eq. B.11)}$$

With the introduction of the z-axis liquid phase diffusion it will be possible to evaluate the concentration at the liquid (electrolyte)-solid (electrode) interface. The use of this representation also permits to differentiate between the mass transport polarization due to the gas and the liquid diffusion, providing interesting information both to understand where the cell may need improvements and to evaluate the improvements made on the cell. In the following equation the term due to the gas transfer will be marked in purple, while the one of the liquid will be marked in green.

$$\eta_{conc,i} = -\frac{\alpha_i' RT}{\alpha_e' z_e F}\left[ln\left(\frac{C_{i,g-l}}{C_{i,bulk}}\right) + ln\left(\frac{C_{i,TPB}}{C_{i,\ g-l}}\right)\right] \qquad \text{(Eq. B.12)}$$

where $C_{i,bulk}$ is the concentration in the bulk, $C_{i,g-l}$ is the concentration at the gas-liquid interface, and $C_{i,TPB}$ is the concentration at the three-phase boundary (TPB) where the reactions take place.

From the development in Chapter 4, $C_{i,g-l}$ can be formulated as:

$$C_{i,g-l} = \left(x_{i,bulk} - \frac{JART}{z_e F V_{Cat,eff} p \mathscr{D}_{i,mix,av} \frac{\varepsilon}{\tau}}\left(\frac{\ell_s}{3} + \delta\right)\right) \qquad \text{(Eq. B.13)}$$

To express $C_{i,TPB}$ it is necessary to start studying from the bass balance in the electrolyte:

$$\frac{dC_i}{dt} = -div\vec{N}_i + r_i \tag{Eq. B.14}$$

If steady state conditions are assumed, it simplifies to:

$$div\vec{N}_i = r_i \tag{Eq. B.15}$$

The two terms can be rewritten as:

$$\frac{d^2C_i}{dz^2} = \frac{JA}{z_eFV} \tag{Eq. B.16}$$

To solve this equation, the following boundary conditions must be considered:

1. At the gas-liquid interface the composition is the Henry's law corrected gas composition ($z = \ell_{g-l} \rightarrow C_i = C_{i,g-l,H}$), being $y_{i,g-l}\, p = C_{i,g-l,H}\, \mathscr{H}_i$.
2. At the bottom of the pore where we assume there is no flux: $z = \ell_s \rightarrow \frac{dC_i}{dz} = 0$.

Solving Eq. B.16, the following expression is obtained to describe the concentration gradient:

$$C_i = C_{i,g-l,H} + \frac{JA}{z_eFV\mathscr{D}_{i,mix}}\left(\frac{z^2}{2} - \ell_s z - \frac{\ell_{g-l}^2}{2} + \ell_s\ell_{g-l}\right) \tag{Eq. B.17}$$

where $\mathscr{D}_{i,m,l}$ represent the diffusion coefficient of the i-th gas in the liquid melt. Since the pore can be filled randomly affecting the position of TPB along the z-axis, we decided to assume an average concentration between the beginning of the liquid phase and the maximum distance of the TPB:

$$C_{i,TPB} = \int_{\ell_{g-l}}^{\ell_s} \frac{C_{i,g-l,H} + \frac{JA}{z_eFV\mathscr{D}_{i,mix}}\left(\frac{z^2}{2} - \ell_s z - \frac{\ell_{g-l}^2}{2} + \ell_s\ell_{g-l}\right)}{\ell_s - \ell_{g-l}}\, dz \tag{Eq. B.18}$$

$$C_{i,TPB} = C_{i,g-l,H} + \frac{JA}{z_eFV\mathscr{D}_{i,mix}} \int_{\ell_{g-l}}^{\ell_s} \frac{\left(\frac{z^2}{2} - \ell_s z - \frac{\ell_{g-l}^2}{2} + \ell_s\ell_{g-l}\right)\, dz}{\ell_s - \ell_{g-l}} \tag{Eq. B.19}$$

$$C_{i,TPB} = C_{i,g-l,H} + \frac{JA}{z_eFV\mathscr{D}_{i,mix}} \left.\frac{\left(\frac{z^3}{6} - \ell_s\frac{z^2}{2} - \frac{\ell_{g-l}^2}{2}z + z\ell_s\ell_{g-l}\right)}{\ell_s - \ell_{g-l}}\right|_{\ell_{g-l}}^{\ell_s} \tag{Eq. B.20}$$

$$C_{i,TPB} = C_{i,g-l,H} + \frac{JA}{z_eFV\mathscr{D}_{i,mix}}\left(\frac{\left({\ell_s}^3 - {\ell_{g-l}}^3\right) - 3\ell_s\left({\ell_s}^2 - {\ell_{g-l}}^2\right) - 3\ell_{g-l}^2\left(\ell_s - \ell_{g-l}\right) + 6\left(\ell_s - \ell_{g-l}\right)\ell_s\ell_{g-l}}{6\left(\ell_s - \ell_{g-l}\right)}\right) \tag{Eq. B.21}$$

$$C_{i,TPB} = C_{i,g-l,H} + \frac{JA}{z_eFV\mathscr{D}_{i,mix}}\left(\frac{2{\ell_{g-l}}^3 - 2{\ell_s}^3 + 3{\ell_s}^2\ell_{g-l} - 3\ell_s\ell_{g-l}^2}{6\left(\ell_s - \ell_{g-l}\right)}\right) \tag{Eq. B.22}$$

$$C_{i,TPB} = C_{i,g-l,H} + \frac{JA}{6z_eFV\mathscr{D}_{i,mix}}\left(\frac{\left(\ell_s - \ell_{g-l}\right)\left(2{\ell_s}^2 - \ell_s\ell_{g-l} + {\ell_s}^2\right)}{\left(\ell_s - \ell_{g-l}\right)}\right) \tag{Eq. B.23}$$

$$C_{i,TPB} = C_{i,g-l,H} + \frac{JA\left(2{\ell_s}^2 - \ell_s \ell_{g-l} + {\ell_s}^2\right)}{6 z_e F V \mathscr{D}_{i,mix}} \tag{Eq. B.24}$$

If then this expression is substituted in the formula for $C_{i,g-l,H}$:

$$C_{i,\ell_{l-s}} = \frac{y_{i,g-l}\, p}{\mathscr{H}_i} + \frac{JA\left(2{\ell_s}^2 - \ell_s \ell_{g-l} + {\ell_s}^2\right)}{6 z_e F V \mathscr{D}_{i,mix}} \tag{Eq. B.25}$$

If Eq. B.25 and Eq. B.13 are substituted in Eq. B.12 the mass transfer polarization of i-th component becomes:

$$\eta_{conc,i} = -\frac{\alpha_i' RT}{\alpha_e' z_e F}\left[ln\left(\frac{x_{i,bulk} - \frac{JART}{z_e F V_{Cat,eff} p \mathscr{D}_{i,mix,av} \frac{\varepsilon}{\tau}} \left(\frac{\ell_s}{3} + \delta\right)}{x_{i,bulk}} \right) + ln\left(\frac{\frac{x_{i,g-l}\, p}{\mathscr{H}_i} + \frac{JA\left(2{\ell_s}^2 - \ell_s \ell_{g-l} + {\ell_s}^2\right)}{6 z_e F V \mathscr{D}_{i,mix}}}{\mathscr{H}\left(x_{i,bulk} - \frac{JART}{z_e F V_{Cat,eff} p \mathscr{D}_{i,mix,av} \frac{\varepsilon}{\tau}} \left(\frac{\ell_s}{3} + \delta\right)\right)} \right)\right] \tag{Eq. B.26}$$

Although valid, it was not possible to obtain to fit proper parameters to obtain satisfying results or, in same cases, the model conversion.

C
Appendix: Intermediate models

In this Appendix I will present the models to describe MCFC working with dual-anion mechanism analyzed in terms of circuit and resistance equations before establishing the final model with no z-axis diffusion as described in Chapter 3.

C.1. Model 1

In my first approach to the modeling of the dual-anion mechanism both path were considered having each the resistances of all the reactants while sharing a common Ohmic resistance as shown in Figure C.1.

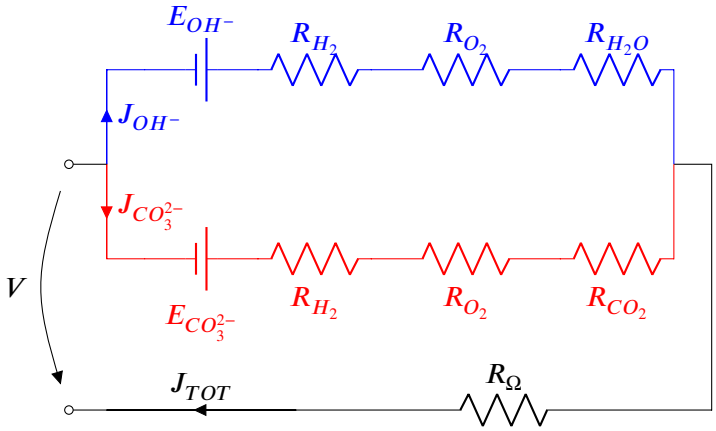

Figure C.1: Circuit representing an MCFC working with dual-anion mechanism, Model 1.

The resistances of each path are described by the following equations and were considered all in their linear form:

$$R_{External} = R_\Omega \tag{Eq. C.1}$$

$$R_{CO_3^{2-}} = R_{CO_2,CO_3^{2-}} + R_{O_2,CO_3^{2-}} + R_{H_2,CO_3^{2-}} \tag{Eq. C.2}$$

$$R_{OH^-} = R_{H_2O,OH^-} + R_{O_2,OH^-} + R_{H_2,OH^-} \tag{Eq. C.3}$$

with specifically:

$$R_\Omega = P_{\Omega,1} e^{\frac{P_{\Omega,2}}{T}} \tag{Eq. C.4}$$

$$R_{CO_2,CO_3^{2-}} = P_{CO_2,1}\, T\, e^{\frac{P_{CO_2,2}}{T}}\, p_{CO_2}^{-1} \tag{Eq. C.5}$$

$$R_{H_2O,OH^-} = P_{H_2O,1}\, T\, e^{\frac{P_{H_2O,2}}{T}}\, p_{H_2O}^{-1} \tag{Eq. C.6}$$

$$R_{H_2,m} = \frac{P_{H_2,1,m} e^{\frac{P_{H_2,2,m}}{T}}}{p \ln\left(1 + y_{H_2}\right)} \tag{Eq. C.7}$$

$$R_{O_2,CO_3^{2-}} = P_{O_2,1,CO_3^{2-}}\, T\, e^{\frac{P_{O_2,2,CO_3^{2-}}}{T}}\, p^{0.5}\, y_{CO_2}\, y_{O_2}^{0.5} \tag{Eq. C.8}$$

$$R_{O_2,OH^-} = P_{O_2,1,OH^-}\, T\, e^{\frac{P_{O_2,2,OH^-}}{T}}\, p^{0.5}\, y_{CO_2}\, y_{O_2}^{0.5} \tag{Eq. C.9}$$

Due to the high number of empirical parameters (P_i) required for the evaluation of the resistances, this model was discarded to identify a simpler solution.

C.2. Model 2

As the reaction between CO_2 and O_2 is not direct, but involves a series of different steps that foresee the formation of O_2 ions as intermediates, it is assumable that similar steps will occur for the corresponding one between H_2O and O_2.

However, it is possible that the O^{2-} ions form reacting with CO_3^{2-} can then react both with CO_2 to form CO_3^{2-} or H_2O to form OH^-. The same happens in the case of the O^{2-} formed by reaction with OH^-. This model takes into account these possibilities further differentiating the R_{O_2} inside the anion paths.

The final circuit thought for this model is presented in Figure C.2.

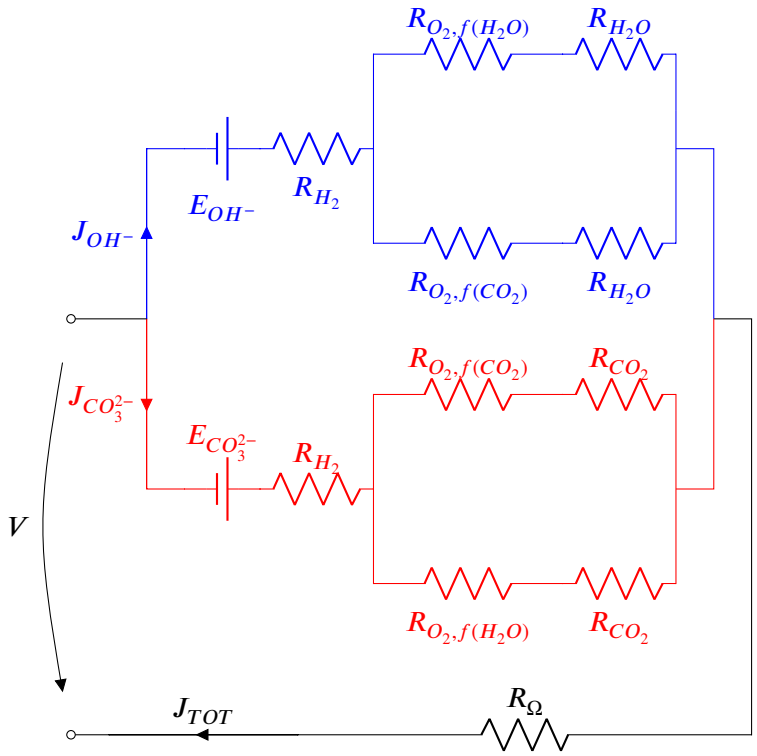

Figure C.2: Circuit representing an MCFC working with dual-anion mechanism, Model 2.

While the structure is basically the same of Model 1, the O_2-related resistances have to be rewritten to take into account the aforementioned considerations. Assumed Q_1, Q_2, Q'_1 and Q'_2 as functions of local variables such as the melt concentration that weight the magnitude of the source of O^{2-} in each resistance.

$$R_{O_2,CO_3^{2-}} = P_5 e^{\frac{P_6}{T}} \left[Q_1 \left(p^{0.5} p_{O_2}^{-0.5} p_{CO_2} \right) + Q_2 \left(p^{0.5} p_{O_2}^{-0.5} p_{H_2O} \right) \right] \quad \text{(Eq. C.10)}$$

$$R_{O_2,OH^-} = P'_5 e^{\frac{P'_6}{T}} \left[Q'_1 \left(p^{0.5} p_{O_2}^{-0.5} p_{CO_2} \right) + Q'_2 \left(p^{0.5} p_{O_2}^{-0.5} p_{H_2O} \right) \right] \quad \text{(Eq. C.11)}$$

As for Model 1, due to the high number of empirical parameters (P_i) required for the evaluation of the resistances the model was discarded.

Moreover, it is theoretically possible to observe that this "mixed O_2 paths" cannot occur.

In fact, if these “mixed paths” could occur, they can be schematized by the following cathodic reactions:

1. O_2 activated species from carbonate and electricity from H_2O:

$$\frac{1}{2}\,O_2 + CO_3^{2-} \longrightarrow O_2^{2-} + CO_2 \quad \text{(R. C.1)}$$

$$O_2^{2-} + 2\,H_2O + 2\,e^- \longrightarrow 4\,OH^- \quad \text{(R. C.2)}$$

From the sum of Rxns. C.1 and C.2 and the carbonate decomposition reaction ($M_2CO_3 \longrightarrow 2\,M^+ + CO_3^{2-}$), the complete mechanism becomes:

$$\frac{1}{2}\,O_2 + 2\,H_2O + 2\,e^- + M_2CO_3 \longrightarrow 2\,M^+ + 2\,CO_2 + 4\,OH^- \quad \text{(R. C.3)}$$

2. O_2 activated species from hydroxide and electricity from CO_2:

$$\frac{1}{2}\,O_2 + 2\,OH^- \longrightarrow O_2^{2-} + 2\,H_2O \quad \text{(R. C.4)}$$

$$O_2^{2-} + 2\,CO_2 + 2\,e^- \longrightarrow 2\,CO_3^{2-} \quad \text{(R. C.5)}$$

From the sum of Rxns. C.4 and C.5 and the water decomposition reaction ($2\,H_2O \longrightarrow 2\,H^+ + 2\,OH^-$), the complete mechanism becomes:

$$\frac{1}{2}\,O_2 + 2\,CO_2 + 2\,e^- \longrightarrow 2\,H^+ + 2\,CO_3^{2-} \quad \text{(R. C.6)}$$

However, the stoichiometry of the reactions seems to not allow for such combined path. The charge must be equilibrated and the paths should balance each other. This does not happen showing the impossibilities of this mixed path solution. The anode reactions are in fact:

$$2\,H_2 + 2\,CO_3^{2-} \longrightarrow 2\,CO_2 + 2\,H_2O + 4\,e^- \quad \text{(R. C.7)}$$

$$2\,H_2 + 4\,OH^- \longrightarrow 4\,H_2O + 4\,e^- \quad \text{(R. C.8)}$$

It is clear that the electrons obtained in Rxns. C.7 and C.8 are double the ones required bu Rxns. C.3 and C.6. The mix paths are thus not properly balanced and consequently or secondary unknown reduction reactions occur, or carbonate and water are formed again, so that the two mixed paths must proceed much the same to balance the charges.

C.3. Model 3

Compared to the previous model, I decided to assume the H_2 resistance as common resistance as not affecting the initial cathode CO_3^{2-}/OH^- split. The circuit that describes this model is presented in Figure C.3.

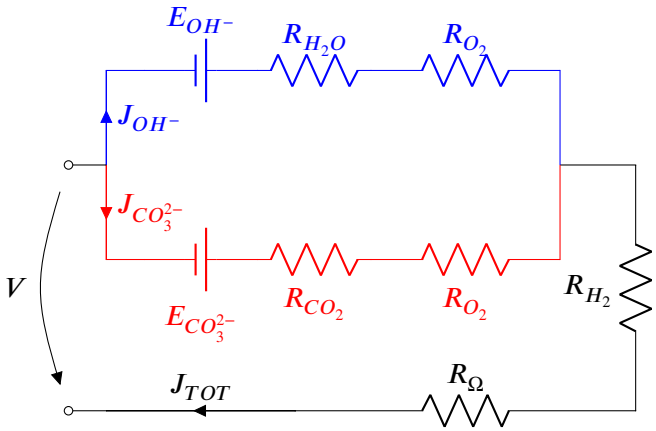

Figure C.3: Circuit representing an MCFC working with dual-anion mechanism, Model 3.

The resistances of each path are described by the following equations:

$$R_{External} = R_\Omega + R_{H_2} \tag{Eq. C.12}$$

$$R_{CO_3^{2-}} = R_{CO_2,CO_3^{2-}} + R_{O_2,CO_3^{2-}} \tag{Eq. C.13}$$

$$R_{OH^-} = R_{H_2O,OH^-} + R_{O_2,OH^-} \tag{Eq. C.14}$$

with specifically:

$$R_\Omega = P_{\Omega,1} \tag{Eq. C.15}$$

$$R_{H_2} = \frac{P_{H_2,1} T e^{\frac{P_{H_2,2}}{T}}}{p \ln\left(1 + y_{H_2}\right)} \tag{Eq. C.16}$$

$$R_{CO_2,CO_3^{2-}} = P_{CO_2,1} T e^{\frac{P_{CO_2,2}}{T}} p_{CO_2}^{-1} \tag{Eq. C.17}$$

$$R_{H_2O,OH^-} = P_{H_O,1} T e^{\frac{P_{H_2O,2}}{T}} p_{H_2O}^{-1} \tag{Eq. C.18}$$

To express the resistance of O_2, two different approaches have been considered.

C.3.1. Model 3.A

To express the concentrations of O_2 ions, the following equation can be used:

$$C_{O_2^{2-}} = K_{O_2^{2-}} C_{CO_3^{2-}} C_{O_2}^{0.5} C^{-1} 1_{CO_2} \quad \text{(Eq. C.19)}$$

Since CO_3^{2-} ions are consumed to form OH^-, the concentration is not constant. It can be assumed to depend on the transference number as:

$$C_{CO_3^{2-}} = C^0_{CO_3^{2-}} t_{CO_3^{2-}} \quad \text{(Eq. C.20)}$$

Thus:

$$R_{O_2,m} = P_{m,O_2,1}\, e^{\frac{P_{m,O_2,2}}{T}}\, p^{0.5}\, y_{O_2}^{-0.5}\, y_m\, t_m^{-1} \quad \text{(Eq. C.21)}$$

C.3.2. Model 3.B

It is possible to simplify assuming that in both paths the ions are provided only by reaction with CO_2. Also the CO_3^{2-} concentrations can be assumed constant because much higher compared to the OH^- one.

Thus we can expressed the R_{O_2} as:

$$R_{O_2,m} = P_{m,O_2,1}\, e^{\frac{P_{m,O_2,2}}{T}}\, p^{0.5}\, y_{O_2}^{-0.5}\, y_{CO_2} \quad \text{(Eq. C.22)}$$

Both Models 3.A and B were discharged as assuming the linear formulation for the resistances of CO_2 and H_2 resulted problematic in dealing with experimental data with high oxidant utilization factors.

C.4. Model 4.A

Model 4.A was developed from the previous model 3.B, assuming resistances of CO_2 and H_2O in their non-linear forms. The circuit used is schematized in Figure C.4.

The resistances equations were expressed as:

$$R_\Omega = P_{\Omega,1} e^{\frac{P_{\Omega,2}}{T}} \quad \text{(Eq. C.23)}$$

$$R_{CO_2,CO_3^{2-}} = -\frac{P_{CO_2,1} T}{J_{CO_{2-}^{=}}} \ln\left(1 - \frac{J_{CO_3^{2-}}}{P_{CO_2,2} e^{\frac{P_{CO_2,3}}{T}} p_{CO_2}}\right) \quad \text{(Eq. C.24)}$$

$$R_{H_2O,OH^-} = -\frac{P_{H_2O,1} T}{J_{OH^-}} \ln\left(1 - \frac{J_{OH^-}}{P_{H_2O,2} e^{\frac{P_{H_2O,3}}{T}} p_{H_2O}}\right) \quad \text{(Eq. C.25)}$$

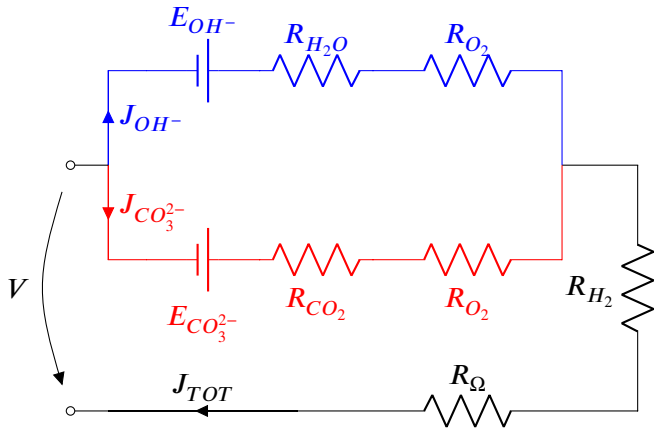

Figure C.4: Circuit representing an MCFC working with dual-anion mechanism, Model 4.A.

$$R_{H_2} = \frac{P_{H_2,1} T e^{\frac{P_{H_2,2}}{T}}}{p \ln\left(1 + y_{H_2}\right)} \tag{Eq. C.26}$$

$$R_{O_2,m} = P_{m,O_2,1}\, T, e^{\frac{P_{m,O_2,2}}{T}}\, p^{0.5}\, y_{O_2}^{-0.5}\, y_{CO_2} \tag{Eq. C.27}$$

C.5. Model 4.B

In this model, I decided to consider the H_2 resistance inside the anion paths and the O_2 resistance in the main branch. The O_2 resistance was written as function of the CO_2 only. The circuit used is schematized in Figure C.5.

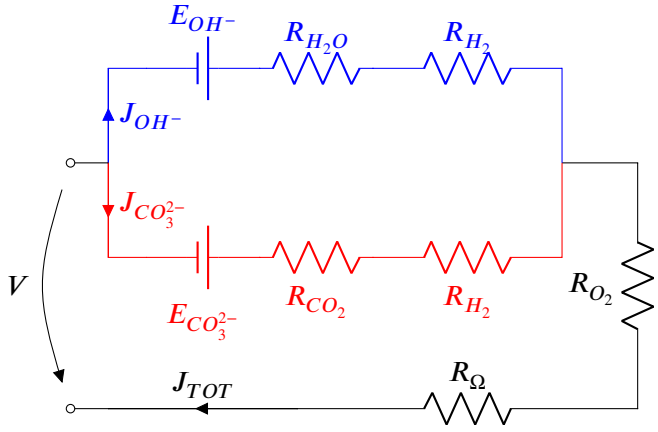

Figure C.5: Circuit representing an MCFC working with dual-anion mechanism, Model 4.B.

Thus, the resistances of each path are described by the following equations:

$$R_{External} = R_\Omega + R_{O_2} \tag{Eq. C.28}$$

$$R_{CO_3^{2-}} = R_{CO_2,CO_3^{2-}} + R_{H_2,CO_3^{2-}} \quad \text{(Eq. C.29)}$$

$$R_{OH^-} = R_{H_2O,OH^-} + R_{H_2,OH^-} \quad \text{(Eq. C.30)}$$

$$R_{O_2} = P_5\ T, e^{\frac{P_6}{T}}\ p^{0.5}\ y_{O_2}^{-0.5}\ y_{CO_2} \quad \text{(Eq. C.31)}$$

Both Models 4.A and B were discarded as from the experimental data it was finally clear that the resistance of both H_2 and O_2 has barely no influence to determine the followed path.

C.6. Model 4.C

Finally, I assumed both H_2 and O_2 related resistances outside the two anion paths. The circuit describing the system is presented in Figure C.6.

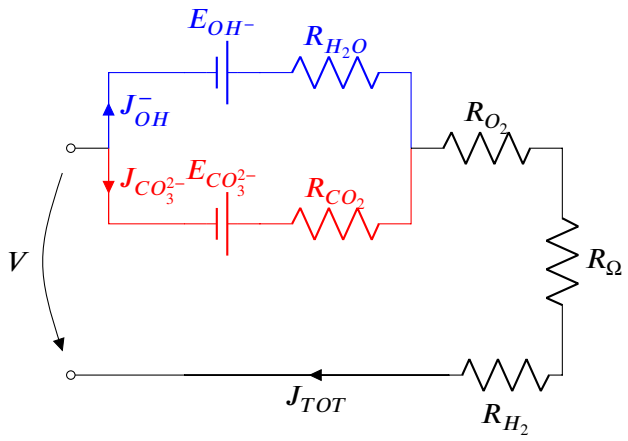

Figure C.6: Circuit representing an MCFC working with dual-anion mechanism, Model 4.C.

The paths resistances are expressible as:

$$R_{External} = R_\Omega + R_{O_2} + R_{H_2} \quad \text{(Eq. C.32)}$$

$$R_{CO_3^{2-}} = R_{CO_2,CO_3^{2-}} \quad \text{(Eq. C.33)}$$

$$R_{OH^-} = R_{H_2O,OH^-} \quad \text{(Eq. C.34)}$$

Then, according to how O_2 and H_2O polarization resistances were considered, I could distinguish between three sub-models.

C.6.1. Model 4.C: base

First O_2 was expressed as function of the sole CO_2 as:

$$R_{O_2} = P_5 \, e^{\frac{P_6}{T}} \, p^{0.5} \, y_{O_2}^{-0.5} \, y_{CO_2} \qquad \text{(Eq. C.35)}$$

C.6.2. Model 4.B: with non-linear O_2

Then, as different experimental data collected even at very low concentration of O_2 (es. 2%) became available, I decided to test the non-linear expression also for O_2 to verify whether it could improve the model. In the non linear form, R_{O_2} becomes:

$$R_{O_2} = -\frac{P_{O_2,1} \, T}{J_{TOT}} \ln\left(1 - \frac{J_{TOT}}{P_{O_2,2} e^{\frac{P_{O_2,3}}{T}} p_{CO_2}^{0.5} p_{H_2O}^{0.5} p_{O_2}^{-0.5}}\right) \qquad \text{(Eq. C.36)}$$

C.6.3. Model 4.C: with R_{H_2O} as function of CO_2

The resistance of water and CO_2 were always written not considering possible effects of one gas on the other due to the carbonate-hydroxide equilibrium.

I tried to implement this aspect in the R_{H_2O}, considering the ratio between H_2O and CO_2 partial pressure as:

$$R_{H_2O} = -\frac{P_{H_2O,1} \, T}{J_{OH^-}} \ln\left(1 - \frac{J_{OH^-}}{P_{H_O,2} \, e^{\frac{P_{H_2O,4}}{T}} \frac{p_{H_2O}}{p_{CO_2}}}\right) \qquad \text{(Eq. C.37)}$$

Although all these options were interesting, I decided to follow the one described in Chapter 3 as it showed more consistency with the experimental data.

D
Appendix: Experimental Data

This appendix group the main inlet and outlet information about the experimental data provided by EMRE and used for the study of the dual-anion mechanism, the model development and to test the quality of the simulations.

ID	Target performance			Total	Cathode molar fraction				Total	Anode molar fraction				Inlet T	Experimental Results			
	U_{H_2}	U_{CO_2}	J	cathode flow	N_2	O_2	CO_2	H_2O	anode flow	CO_2	H_2	H_2O	N_2		Voltage	R_Ω	U_{CO_2}	$t_{CO_3^{2-}}$
	%	%	$mA\,cm^{-2}$	$Nm^3\,h^{-1}$	–				$Nm^3\,h^{-1}$	–				K	mV	$m\Omega$	%	–
1	30%	O/C	O/C	0.20	0.65	0.17	0.08	0.10	0.05	0.18	0.72	0.10	0.00	923	1031			
2	30%	60%	90	0.20	0.65	0.17	0.08	0.10	0.05	0.18	0.72	0.10	0.00	923	867		57.95%	0.9649
3	30%	70%	105	0.20	0.65	0.17	0.08	0.10	0.05	0.18	0.72	0.10	0.00	923	841		66.74%	0.9525
4	30%	80%	120	0.20	0.65	0.17	0.08	0.10	0.06	0.18	0.72	0.10	0.00	923	814		73.53%	0.9183
5	30%	90%	135	0.20	0.65	0.17	0.08	0.10	0.07	0.18	0.72	0.10	0.00	923	776		81.00%	0.8992
6	30%	60%	90	0.41	0.76	0.10	0.04	0.10	0.05	0.18	0.72	0.10	0.00	923	799		54.11%	0.9010
7	30%	70%	105	0.41	0.76	0.10	0.04	0.10	0.05	0.18	0.72	0.10	0.00	923	764		60.74%	0.8669
8	30%	80%	120	0.41	0.76	0.10	0.04	0.10	0.06	0.18	0.72	0.10	0.00	923	729		66.43%	0.8297
9	30%	90%	135	0.41	0.76	0.10	0.04	0.10	0.07	0.18	0.72	0.10	0.00	923	695		69.46%	0.7711
10	30%	100%	150	0.41	0.76	0.10	0.04	0.10	0.08	0.18	0.72	0.10	0.00	923	666		71.88%	0.7182
11	30%	105%	157.5	0.41	0.76	0.10	0.04	0.10	0.08	0.18	0.72	0.10	0.00	923	653		72.17%	0.6867
12	30%	110%	165	0.41	0.76	0.10	0.04	0.10	0.08	0.18	0.72	0.10	0.00	923	638		71.77%	0.6518
13	30%	76%	60	0.21	0.76	0.10	0.04	0.10	0.03	0.05	0.86	0.10	0.00	923	864		66.68%	0.8765
14	30%	76%	120	0.43	0.76	0.10	0.04	0.10	0.05	0.04	0.86	0.10	0.00	923	776		62.80%	0.8255
15	30%	76%	60	0.21	0.76	0.10	0.04	0.10	0.02	0.01	0.89	0.10	0.00	923	871		66.17%	0.8699
16	30%	76%	120	0.43	0.76	0.10	0.04	0.10	0.05	0.01	0.89	0.10	0.00	923	784		63.04%	0.8287
17	30%	76%	60	0.21	0.76	0.10	0.04	0.10	0.03	0.09	0.81	0.10	0.00	923	852		67.01%	0.8808
18	30%	76%	120	0.43	0.76	0.10	0.04	0.10	0.05	0.09	0.81	0.10	0.00	923	756		63.09%	0.8294
19	30%	60%	90	0.41	0.76	0.10	0.04	0.10	0.05	0.18	0.72	0.10	0.00	923	798		54.64%	0.9098
20	30%	70%	90	0.35	0.76	0.10	0.04	0.10	0.05	0.18	0.72	0.10	0.00	923	789		61.42%	0.8792
21	30%	80%	90	0.30	0.76	0.10	0.04	0.10	0.05	0.18	0.72	0.10	0.00	923	780		68.44%	0.8557
22	30%	90%	90	0.27	0.76	0.10	0.04	0.10	0.05	0.18	0.72	0.10	0.00	923	767		75.54%	0.8386
23	30%	100%	90	0.24	0.76	0.10	0.04	0.10	0.05	0.18	0.72	0.10	0.00	923	759		80.06%	0.7998
24	30%	110%	90	0.22	0.76	0.10	0.04	0.10	0.05	0.18	0.72	0.10	0.00	923	749		84.36%	0.7689
25	30%	120%	90	0.20	0.76	0.10	0.04	0.10	0.05	0.18	0.72	0.10	0.00	923	741		88.02%	0.7354
26	30%	130%	90	0.19	0.76	0.10	0.04	0.10	0.05	0.18	0.72	0.10	0.00	923	730		91.22%	0.7035
27	30%	140%	90	0.17	0.76	0.10	0.04	0.10	0.05	0.18	0.72	0.10	0.00	923	722		93.72%	0.6680
28	30%	150%	90	0.16	0.76	0.10	0.04	0.10	0.05	0.18	0.72	0.10	0.00	923	714		95.61%	0.6368
29	30%	70%	120	0.46	0.76	0.10	0.04	0.10	0.06	0.18	0.72	0.10	0.00	923	740	1.22	59.24%	0.8463
30	30%	90%	120	0.36	0.76	0.10	0.04	0.10	0.06	0.18	0.72	0.10	0.00	923	720	1.21	70.97%	0.7899
31	30%	110%	120	0.29	0.76	0.10	0.04	0.10	0.06	0.18	0.72	0.10	0.00	923	700	1.20	81.78%	0.7418
32	30%	130%	120	0.25	0.76	0.10	0.04	0.10	0.06	0.18	0.72	0.10	0.00	923	681	1.20	87.88%	0.6777
33	30%	150%	120	0.22	0.76	0.10	0.04	0.10	0.06	0.18	0.72	0.10	0.00	923	667	1.20	92.41%	0.6155
34	30%	70%	150	0.58	0.76	0.10	0.04	0.10	0.08	0.18	0.72	0.10	0.00	923	690		57.34%	0.8201
35	30%	90%	150	0.45	0.76	0.10	0.04	0.10	0.08	0.18	0.72	0.10	0.00	923	666		67.06%	0.7452
36	30%	110%	150	0.37	0.76	0.10	0.04	0.10	0.08	0.18	0.72	0.10	0.00	923	654		76.34%	0.6931
37	30%	130%	150	0.31	0.76	0.10	0.04	0.10	0.08	0.18	0.72	0.10	0.00	923	644		82.39%	0.6325
38	30%	150%	150	0.27	0.76	0.10	0.04	0.10	0.08	0.18	0.72	0.10	0.00	923	627		87.84%	0.5851

	Target performance			Total	Cathode molar fraction				Total	Anode molar fraction				Inlet T	Experimental Results			
ID	U_{H_2}	U_{CO_2}	J	cathode flow	N_2	O_2	CO_2	H_2O	anode flow	CO_2	H_2	H_2O	N_2		Voltage	R_Ω	U_{CO_2}	$t_{CO_3^{2-}}$
	%	%	$mA\,cm^{-2}$	$Nm^3\,h^{-1}$	–				$Nm^3\,h^{-1}$	–				K	mV	$m\Omega$	%	–
39	30%	76%	90	0.32	0.76	0.10	0.04	0.10	0.05	0.18	0.72	0.10	0.00	923	783		65.75%	0.8644
40	30%	76%	90	0.32	0.78	0.08	0.04	0.10	0.05	0.18	0.72	0.10	0.00	923	775		64.73%	0.8509
41	30%	76%	90	0.32	0.80	0.06	0.04	0.10	0.05	0.18	0.72	0.10	0.00	923	765		66.49%	0.8741
42	30%	76%	90	0.32	0.82	0.04	0.04	0.10	0.05	0.18	0.72	0.10	0.00	923	749		65.68%	0.8634
43	30%	76%	90	0.32	0.84	0.02	0.04	0.10	0.05	0.18	0.72	0.10	0.00	923	648		67.66%	0.8894
44	85%	70%	60	0.23	0.76	0.10	0.04	0.10	0.01	0.18	0.72	0.10	0.00	923	723		60.02%	0.8574
45	85%	90%	60	0.18	0.76	0.10	0.04	0.10	0.01	0.18	0.72	0.10	0.00	923	706		71.66%	0.7976
46	85%	110%	60	0.15	0.76	0.10	0.04	0.10	0.01	0.18	0.72	0.10	0.00	923	692		81.89%	0.7464
47	85%	130%	60	0.13	0.76	0.10	0.04	0.10	0.01	0.18	0.72	0.10	0.00	923	679		90.13%	0.6951
48	85%	150%	60	0.11	0.76	0.10	0.04	0.10	0.01	0.18	0.72	0.10	0.00	923	660		94.36%	0.6285
49	85%	70%	90	0.35	0.76	0.10	0.04	0.10	0.02	0.18	0.72	0.10	0.00	923	703		59.44%	0.8508
50	85%	90%	90	0.27	0.76	0.10	0.04	0.10	0.02	0.18	0.72	0.10	0.00	923	686		72.31%	0.8027
51	85%	110%	90	0.22	0.76	0.10	0.04	0.10	0.02	0.18	0.72	0.10	0.00	923	666		82.25%	0.7496
52	85%	130%	90	0.19	0.76	0.10	0.04	0.10	0.02	0.18	0.72	0.10	0.00	923	646		89.28%	0.6886
53	85%	150%	90	0.16	0.76	0.10	0.04	0.10	0.02	0.18	0.72	0.10	0.00	923	630		94.01%	0.6261
54	85%	70%	120	0.46	0.76	0.10	0.04	0.10	0.02	0.18	0.72	0.10	0.00	923	661		56.95%	0.8136
55	85%	90%	120	0.36	0.76	0.10	0.04	0.10	0.02	0.18	0.72	0.10	0.00	923	642		69.14%	0.7695
56	85%	110%	120	0.29	0.76	0.10	0.04	0.10	0.02	0.18	0.72	0.10	0.00	923	623		78.59%	0.7128
57	85%	130%	120	0.25	0.76	0.10	0.04	0.10	0.02	0.18	0.72	0.10	0.00	923	607		85.73%	0.6611
58	85%	150%	120	0.22	0.76	0.10	0.04	0.10	0.02	0.18	0.72	0.10	0.00	923	594		90.48%	0.6027
59	30%	70%	90	0.23	0.74	0.10	0.06	0.10	0.05	0.18	0.72	0.10	0.00	923	826		64.12%	0.9178
60	30%	80%	90	0.20	0.74	0.10	0.06	0.10	0.05	0.18	0.72	0.10	0.00	923	816		71.58%	0.8949
61	30%	90%	90	0.18	0.74	0.10	0.06	0.10	0.05	0.18	0.72	0.10	0.00	923	805		79.15%	0.8786
62	30%	100%	90	0.16	0.74	0.10	0.06	0.10	0.05	0.18	0.72	0.10	0.00	923	791		85.27%	0.8519
63	30%	110%	90	0.15	0.74	0.10	0.06	0.10	0.05	0.18	0.72	0.10	0.00	923	777		90.14%	0.8215
64	30%	120%	90	0.13	0.74	0.10	0.06	0.10	0.05	0.18	0.72	0.10	0.00	923	762		94.15%	0.7866
65	30%	130%	90	0.13	0.74	0.10	0.06	0.10	0.05	0.18	0.72	0.10	0.00	923	745		96.63%	0.7453
66	30%	70%	150	0.39	0.74	0.10	0.06	0.10	0.08	0.18	0.72	0.10	0.00	923	739		61.60%	0.8811
67	30%	90%	150	0.30	0.74	0.10	0.06	0.10	0.08	0.18	0.72	0.10	0.00	923	715		74.24%	0.8250
68	30%	110%	150	0.25	0.74	0.10	0.06	0.10	0.08	0.18	0.72	0.10	0.00	923	680		83.84%	0.7612
69	30%	130%	150	0.21	0.74	0.10	0.06	0.10	0.08	0.18	0.72	0.10	0.00	923	667		90.37%	0.6938
70	30%	150%	150	0.18	0.74	0.10	0.06	0.10	0.08	0.18	0.72	0.10	0.00	923	649		94.85%	0.6317
71	30%	110%	90	0.22	0.68	0.18	0.04	0.10	0.05	0.18	0.72	0.10	0.00	923	773		83.53%	0.7613
72	30%	110%	90	0.22	0.70	0.16	0.04	0.10	0.05	0.18	0.72	0.10	0.00	923	767		84.06%	0.7662
73	30%	110%	90	0.22	0.72	0.14	0.04	0.10	0.05	0.18	0.72	0.10	0.00	923	763		83.52%	0.7613
74	30%	110%	90	0.22	0.74	0.12	0.04	0.10	0.05	0.18	0.72	0.10	0.00	923	760		83.58%	0.7618
75	30%	110%	90	0.22	0.76	0.10	0.04	0.10	0.05	0.18	0.72	0.10	0.00	923	755		84.08%	0.7663
76	30%	110%	90	0.22	0.78	0.08	0.04	0.10	0.05	0.18	0.72	0.10	0.00	923	747		84.21%	0.7675

ID	Target performance			Total	Cathode molar fraction				Total	Anode molar fraction				Inlet T	Experimental Results			
	U_{H_2}	U_{CO_2}	J	cathode flow	N_2	O_2	CO_2	H_2O	anode flow	CO_2	H_2	H_2O	N_2		Voltage	R_Ω	U_{CO_2}	$t_{CO_3^{2-}}$
	%	%	$mA\,cm^{-2}$	$Nm^3\,h^{-1}$	–				$Nm^3\,h^{-1}$	–				K	mV	$m\Omega$	%	–
77	30%	110%	90	0.22	0.80	0.06	0.04	0.10	0.05	0.18	0.72	0.10	0.00	923	736		84.30%	0.7684
78	30%	110%	90	0.22	0.82	0.04	0.04	0.10	0.05	0.18	0.72	0.10	0.00	923	713		84.48%	0.7700
79	30%	110%	90	0.22	0.83	0.03	0.04	0.10	0.05	0.18	0.72	0.10	0.00	923	680		84.48%	0.7700
80	30%	110%	90	0.22	0.84	0.02	0.04	0.10	0.05	0.18	0.72	0.10	0.00	923	242		94.88%	0.9265
81	30%	70%	90	0.38	0.77	0.09	0.04	0.10	0.05	0.18	0.72	0.10	0.00	923	771		65.06%	0.9313
82	30%	90%	90	0.29	0.77	0.09	0.04	0.10	0.05	0.18	0.72	0.10	0.00	923	741		79.19%	0.8791
83	30%	110%	90	0.24	0.77	0.09	0.04	0.10	0.05	0.18	0.72	0.10	0.00	923	707		89.33%	0.8142
84	30%	130%	90	0.20	0.77	0.09	0.04	0.10	0.05	0.18	0.72	0.10	0.00	923	657		94.93%	0.7321
85	30%	150%	90	0.17	0.77	0.09	0.04	0.10	0.05	0.18	0.72	0.10	0.00	923	612		97.97%	0.6525
86	30%	50%	90	0.97	0.78	0.10	0.02	0.10	0.05	0.18	0.72	0.10	0.00	923	742		40.33%	0.8059
87	30%	70%	90	0.70	0.78	0.10	0.02	0.10	0.05	0.18	0.72	0.10	0.00	923	729		51.91%	0.7431
88	30%	90%	90	0.54	0.78	0.10	0.02	0.10	0.05	0.18	0.72	0.10	0.00	923	718		62.10%	0.6893
89	30%	110%	90	0.44	0.78	0.10	0.02	0.10	0.05	0.18	0.72	0.10	0.00	923	708		69.59%	0.6343
90	30%	130%	90	0.37	0.78	0.10	0.02	0.10	0.05	0.18	0.72	0.10	0.00	923	697		76.74%	0.5918
91	30%	150%	90	0.32	0.78	0.10	0.02	0.10	0.05	0.18	0.72	0.10	0.00	923	686		82.79%	0.5515
92	0%	0%	0	0.34	0.64	0.10	0.16	0.10	0.09	0.20	0.70	0.10	0.00	923	1043		0.81%	0.0000
93	0%	0%	0	0.34	0.68	0.10	0.12	0.10	0.09	0.20	0.70	0.10	0.00	923	1032		0.90%	0.0000
94	0%	0%	0	0.34	0.72	0.10	0.08	0.10	0.09	0.20	0.70	0.10	0.00	923	1016		0.58%	0.0000
95	0%	0%	0	0.34	0.74	0.10	0.06	0.10	0.09	0.20	0.70	0.10	0.00	923	1006		1.18%	0.0000
96	0%	0%	0	0.34	0.76	0.10	0.04	0.10	0.09	0.20	0.70	0.10	0.00	923	990		0.59%	0.0000
97	0%	0%	0	0.34	0.78	0.10	0.02	0.10	0.09	0.20	0.70	0.10	0.00	923	963		-1.14%	0.0000
98	0%	0%	0	0.34	0.79	0.10	0.01	0.10	0.09	0.20	0.70	0.10	0.00	923	939		-8.54%	0.0000
99	0%	0%	0	0.34	0.80	0.10	0.005	0.10	0.09	0.20	0.70	0.10	0.00	923	922		-25.66%	0.0000
100	0%	0%	0	0.38	0.67	0.09	0.14	0.10	0.09	0.20	0.70	0.10	0.00	923	1041		0.68%	-
101	0%	0%	0	0.38	0.70	0.09	0.11	0.10	0.09	0.20	0.70	0.10	0.00	923	1030		1.09%	-
102	0%	0%	0	0.38	0.74	0.09	0.07	0.10	0.09	0.20	0.70	0.10	0.00	923	1014		1.44%	-
103	0%	0%	0	0.38	0.76	0.09	0.05	0.10	0.09	0.20	0.70	0.10	0.00	923	1004		2.32%	-
104	0%	0%	0	0.38	0.77	0.09	0.04	0.10	0.09	0.20	0.70	0.10	0.00	923	985		3.21%	-
105	0%	0%	0	0.38	0.79	0.09	0.02	0.10	0.09	0.20	0.70	0.10	0.00	923	957		5.09%	-
106	0%	0%	0	0.38	0.80	0.09	0.01	0.10	0.09	0.20	0.70	0.10	0.00	923	927		8.47%	-
107	0%	0%	0	0.38	0.81	0.09	0.005	0.10	0.09	0.20	0.70	0.10	0.00	923	901		11.70%	-
108	30%	70%	90	0.35	0.76	0.10	0.04	0.10	0.05	0.18	0.72	0.10	0.00	923	776		61.53%	0.8807
109	30%	90%	90	0.27	0.76	0.10	0.04	0.10	0.05	0.18	0.72	0.10	0.00	923	753		75.22%	0.8350
110	30%	110%	90	0.22	0.76	0.10	0.04	0.10	0.05	0.18	0.72	0.10	0.00	923	734		84.92%	0.7740
111	30%	130%	90	0.19	0.76	0.10	0.04	0.10	0.05	0.18	0.72	0.10	0.00	923	714		91.90%	0.7087
112	30%	150%	90	0.16	0.76	0.10	0.04	0.10	0.05	0.18	0.72	0.10	0.00	923	693		96.29%	0.6413
113	85%	70%	90	0.35	0.76	0.10	0.04	0.10	0.02	0.18	0.72	0.10	0.00	923	692		58.85%	0.8424
114	85%	90%	90	0.27	0.76	0.10	0.04	0.10	0.02	0.18	0.72	0.10	0.00	923	673		70.91%	0.7871

ID	Target performance			Total	Cathode molar fraction				Total	Anode molar fraction				Inlet T	Experimental Results			
	U_{H_2}	U_{CO_2}	J	cathode flow	N_2	O_2	CO_2	H_2O	anode flow	CO_2	H_2	H_2O	N_2		Voltage	R_Ω	U_{CO_2}	$t_{CO_3^{2-}}$
	%	%	$mA\,cm^{-2}$	$Nm^3\,h^{-1}$	–				$Nm^3\,h^{-1}$	–				K	mV	$m\Omega$	%	–
115	85%	110%	90	0.22	0.76	0.10	0.04	0.10	0.02	0.18	0.72	0.10	0.00	923	654		80.95%	0.7378
116	85%	130%	90	0.19	0.76	0.10	0.04	0.10	0.02	0.18	0.72	0.10	0.00	923	637		87.63%	0.6758
117	85%	150%	90	0.16	0.76	0.10	0.04	0.10	0.02	0.18	0.72	0.10	0.00	923	618		92.73%	0.6176
118	30%	70%	120	0.31	0.74	0.10	0.06	0.10	0.06	0.18	0.72	0.10	0.00	923	767		62.91%	0.8987
119	30%	90%	120	0.24	0.74	0.10	0.06	0.10	0.06	0.18	0.72	0.10	0.00	923	740		76.80%	0.8548
120	30%	110%	120	0.20	0.74	0.10	0.06	0.10	0.06	0.18	0.72	0.10	0.00	923	712		86.48%	0.7844
121	30%	130%	120	0.17	0.74	0.10	0.06	0.10	0.06	0.18	0.72	0.10	0.00	923	688		93.22%	0.7189
122	30%	150%	120	0.14	0.74	0.10	0.06	0.10	0.06	0.18	0.72	0.10	0.00	923	664		96.99%	0.6460
123	30%	70%	120	0.46	0.76	0.10	0.04	0.10	0.06	0.18	0.72	0.10	0.00	923	723		57.31%	0.8186
124	30%	90%	120	0.36	0.76	0.10	0.04	0.10	0.06	0.18	0.72	0.10	0.00	923	703		68.49%	0.7623
125	30%	110%	120	0.29	0.76	0.10	0.04	0.10	0.06	0.18	0.72	0.10	0.00	923	685		77.70%	0.7048
126	30%	130%	120	0.25	0.76	0.10	0.04	0.10	0.06	0.18	0.72	0.10	0.00	923	666		84.53%	0.6519
127	30%	150%	120	0.22	0.76	0.10	0.04	0.10	0.06	0.18	0.72	0.10	0.00	923	658		89.85%	0.5984
128	75%	75%	160	0.13	0.62	0.11	0.17	0.10	0.03	0.18	0.72	0.10	0.00	923	776		75.58%	0.9834
129	75%	75%	160	0.13	0.62	0.11	0.17	0.10	0.03	0.18	0.72	0.10	0.00	923	777	1.09	73.61%	0.9825
130	30%	90%	90	0.26	0.76	0.10	0.04	0.10	0.04	0.18	0.72	0.10	0.00	923	786	1.00	74.86%	0.8301
131	30%	110%	90	0.22	0.76	0.10	0.04	0.10	0.04	0.18	0.72	0.10	0.00	923	763	1.04	85.31%	0.7731
132	30%	130%	90	0.18	0.76	0.10	0.04	0.10	0.04	0.18	0.72	0.10	0.00	923	741	1.03	92.33%	0.7101
133	30%	90%	120	0.35	0.76	0.10	0.04	0.10	0.06	0.18	0.72	0.10	0.00	923	740		71.67%	0.7948
134	30%	110%	120	0.29	0.76	0.10	0.04	0.10	0.06	0.18	0.72	0.10	0.00	923	718		81.01%	0.7353
135	30%	130%	120	0.24	0.76	0.10	0.04	0.10	0.06	0.18	0.72	0.10	0.00	923	698		87.88%	0.6758
136	75%	75%	160	0.13	0.62	0.11	0.17	0.10	0.03	0.18	0.72	0.10	0.00	923	778	1.02	-	-
137	30%	70%	120	0.45	0.76	0.10	0.04	0.10	0.06	0.18	0.72	0.10	0.00	923	761	1.00	59.60%	0.8501
138	30%	70%	120	0.45	0.76	0.10	0.04	0.10	0.07	0.18	0.61	0.09	0.12	923	754	1.01	59.96%	0.8552
139	30%	70%	120	0.45	0.76	0.10	0.04	0.10	0.08	0.19	0.51	0.08	0.23	923	749	1.02	58.11%	0.8289
140	30%	70%	120	0.45	0.76	0.10	0.04	0.10	0.10	0.19	0.41	0.07	0.34	923	740	1.03	60.01%	0.8560
141	30%	70%	120	0.45	0.76	0.10	0.04	0.10	0.13	0.19	0.31	0.06	0.44	923	729	1.03	59.61%	0.8502
142	75%	75%	160	0.13	0.62	0.11	0.17	0.10	0.03	0.18	0.72	0.10	0.00	923	777	1.04	-	-
143	30%	130%	120	0.24	0.76	0.10	0.04	0.10	0.06	0.18	0.72	0.10	0.00	923	698		87.17%	0.6704
144	30%	130%	120	0.24	0.76	0.10	0.04	0.10	0.07	0.18	0.61	0.09	0.12	923	691		87.14%	0.6702
145	30%	130%	120	0.24	0.76	0.10	0.04	0.10	0.08	0.19	0.51	0.08	0.23	923	689		87.89%	0.6759
146	30%	130%	120	0.24	0.76	0.10	0.04	0.10	0.10	0.19	0.41	0.07	0.33	923	678		87.51%	0.6730
147	30%	130%	120	0.24	0.76	0.10	0.04	0.10	0.13	0.19	0.31	0.06	0.44	923	665		87.39%	0.6721
148	75%	75%	160	0.13	0.62	0.11	0.17	0.10	0.03	0.18	0.72	0.10	0.00	923	779		-	-
149	30%	70%	90	0.34	0.76	0.10	0.04	0.10	0.04	0.18	0.72	0.10	0.00	923	806		61.81%	0.8844
150	30%	70%	90	0.34	0.76	0.10	0.04	0.10	0.05	0.18	0.60	0.09	0.12	923	801		61.99%	0.8869
151	30%	70%	90	0.34	0.76	0.10	0.04	0.10	0.06	0.19	0.51	0.08	0.23	923	796		61.73%	0.8832
152	30%	70%	90	0.34	0.76	0.10	0.04	0.10	0.08	0.19	0.41	0.07	0.33	923	791		62.09%	0.8883

ID	Target performance			Total	Cathode molar fraction				Total	Anode molar fraction				Inlet T	Experimental Results			
	U_{H_2}	U_{CO_2}	J	cathode flow	N_2	O_2	CO_2	H_2O	anode flow	CO_2	H_2	H_2O	N_2		Voltage	R_Ω	U_{CO_2}	$t_{CO_3^{2-}}$
	%	%	$mA\,cm^{-2}$	$N\,m^3\,h^{-1}$	–				$N\,m^3\,h^{-1}$	–				K	mV	$m\Omega$	%	–
153	30%	70%	90	0.34	0.76	0.10	0.04	0.10	0.10	0.19	0.31	0.06	0.44	923	781		62.05%	0.8878
154	75%	75%	160	0.13	0.62	0.11	0.17	0.10	0.03	0.18	0.72	0.10	0.00	923	779		-	-
155	30%	130%	90	0.18	0.76	0.10	0.04	0.10	0.04	0.18	0.72	0.10	0.00	923	741		92.27%	0.7096
156	30%	130%	90	0.18	0.76	0.10	0.04	0.10	0.05	0.18	0.60	0.09	0.12	923	735		92.28%	0.7097
157	30%	130%	90	0.18	0.76	0.10	0.04	0.10	0.06	0.19	0.51	0.08	0.23	923	728		92.29%	0.7097
158	30%	130%	90	0.18	0.76	0.10	0.04	0.10	0.08	0.19	0.41	0.07	0.33	923	720		92.23%	0.7093
159	30%	130%	90	0.18	0.76	0.10	0.04	0.10	0.10	0.19	0.31	0.06	0.44	923	709		92.24%	0.7094
160	30%	70%	90	0.34	0.76	0.10	0.04	0.10	0.04	0.18	0.72	0.10	0.00	923	806		61.81%	0.8844
161	30%	90%	90	0.26	0.76	0.10	0.04	0.10	0.04	0.18	0.72	0.10	0.00	923	786	1.00	74.86%	0.8301
162	30%	110%	90	0.22	0.76	0.10	0.04	0.10	0.04	0.18	0.72	0.10	0.00	923	763	1.04	85.31%	0.7731
163	30%	130%	90	0.18	0.76	0.10	0.04	0.10	0.04	0.18	0.72	0.10	0.00	923	741	1.03	92.33%	0.7101
164	75%	75%	160	0.13	0.68	0.11	0.17	0.03	0.03	0.18	0.72	0.10	0.00	923	771	1.03	-	-
165	30%	70%	90	0.34	0.83	0.10	0.04	0.03	0.04	0.18	0.72	0.10	0.00	923	789		64.36%	0.9209
166	30%	90%	90	0.26	0.83	0.10	0.04	0.03	0.04	0.18	0.72	0.10	0.00	923	758		79.06%	0.8767
167	30%	110%	90	0.22	0.83	0.10	0.04	0.03	0.04	0.18	0.72	0.10	0.00	923	720		88.95%	0.8061
168	30%	130%	90	0.18	0.83	0.10	0.04	0.03	0.04	0.18	0.72	0.10	0.00	923	680		94.50%	0.7268
169	30%	70%	120	0.45	0.76	0.10	0.04	0.10	0.06	0.18	0.72	0.10	0.00	923	761	1.00	59.60%	0.8501
170	30%	90%	120	0.35	0.76	0.10	0.04	0.10	0.06	0.18	0.72	0.10	0.00	923	740		71.67%	0.7948
171	30%	110%	120	0.29	0.76	0.10	0.04	0.10	0.06	0.18	0.72	0.10	0.00	923	718		81.01%	0.7353
172	30%	130%	120	0.24	0.76	0.10	0.04	0.10	0.06	0.18	0.72	0.10	0.00	923	698		87.88%	0.6758
173	75%	75%	160	0.13	0.68	0.11	0.17	0.03	0.03	0.18	0.72	0.10	0.00	923	772		-	-
174	30%	70%	120	0.45	0.83	0.10	0.04	0.03	0.06	0.18	0.72	0.10	0.00	923	730		62.19%	0.8870
175	30%	90%	120	0.35	0.83	0.10	0.04	0.03	0.06	0.18	0.72	0.10	0.00	923	694		74.21%	0.8229
176	30%	110%	120	0.29	0.83	0.10	0.04	0.03	0.06	0.18	0.72	0.10	0.00	923	658		83.16%	0.7548
177	75%	75%	160	0.13	0.52	0.11	0.17	0.20	0.03	0.18	0.72	0.10	0.00	923	787	1.21	-	-
178	30%	70%	90	0.34	0.66	0.10	0.04	0.20	0.04	0.18	0.72	0.10	0.00	923	818		59.72%	0.8544
179	30%	90%	90	0.26	0.66	0.10	0.04	0.20	0.04	0.18	0.72	0.10	0.00	923	801		73.04%	0.8100
180	30%	110%	90	0.22	0.66	0.10	0.04	0.20	0.04	0.18	0.72	0.10	0.00	923	783		83.13%	0.7533
181	30%	130%	90	0.18	0.66	0.10	0.04	0.20	0.04	0.18	0.72	0.10	0.00	923	767		90.26%	0.6941
182	75%	75%	160	0.13	0.52	0.11	0.17	0.20	0.03	0.18	0.72	0.10	0.00	923	788	1.10	-	-
183	30%	70%	120	0.45	0.66	0.10	0.04	0.20	0.06	0.18	0.72	0.10	0.00	923	781		58.14%	0.8293
184	30%	90%	120	0.35	0.66	0.10	0.04	0.20	0.06	0.18	0.72	0.10	0.00	923	762		69.92%	0.7753
185	30%	110%	120	0.29	0.66	0.10	0.04	0.20	0.06	0.18	0.72	0.10	0.00	923	745		78.94%	0.7166
186	30%	130%	120	0.24	0.66	0.10	0.04	0.20	0.06	0.18	0.72	0.10	0.00	923	731		86.17%	0.6627
187	75%	75%	160	0.14	0.63	0.11	0.17	0.10	0.03	0.18	0.72	0.10	0.00	923	770		-	-
188	30%	70%	90	0.34	0.80	0.10	0.04	0.06	0.04	0.18	0.72	0.10	0.00	923	796		62.68%	0.8969
189	30%	90%	90	0.26	0.80	0.10	0.04	0.06	0.04	0.18	0.72	0.10	0.00	923	770		76.74%	0.8510
190	30%	110%	90	0.22	0.80	0.10	0.04	0.06	0.04	0.18	0.72	0.10	0.00	923	745		87.13%	0.7896

ID	Target performance			Total	Cathode molar fraction				Total	Anode molar fraction				Inlet T	Experimental Results			
	U_{H_2}	U_{CO_2}	J	cathode flow	N_2	O_2	CO_2	H_2O	anode flow	CO_2	H_2	H_2O	N_2		Voltage	R_Ω	U_{CO_2}	$t_{CO_3^{2-}}$
	%	%	$mA\,cm^{-2}$	$Nm^3\,h^{-1}$	–				$Nm^3\,h^{-1}$	–				K	mV	$m\Omega$	%	–
191	30%	130%	90	0.18	0.80	0.10	0.04	0.06	0.04	0.18	0.72	0.10	0.00	923	718		93.54%	0.7194
192	30%	70%	120	0.45	0.80	0.10	0.04	0.06	0.06	0.18	0.72	0.10	0.00	923	746		60.72%	0.8660
193	30%	90%	120	0.35	0.80	0.10	0.04	0.06	0.06	0.18	0.72	0.10	0.00	923	719		72.86%	0.8079
194	30%	110%	120	0.29	0.80	0.10	0.04	0.06	0.06	0.18	0.72	0.10	0.00	923	693		81.84%	0.7428
195	75%	75%	160	0.13	0.62	0.11	0.17	0.10	0.03	0.18	0.72	0.10	0.00	923	777		-	-
196	30%	70%	90	0.34	0.70	0.16	0.04	0.10	0.04	0.18	0.72	0.10	0.00	923	817		61.67%	0.8824
197	30%	70%	90	0.34	0.74	0.12	0.04	0.10	0.04	0.18	0.72	0.10	0.00	923	810		61.65%	0.8821
198	30%	70%	90	0.34	0.76	0.10	0.04	0.10	0.04	0.18	0.72	0.10	0.00	923	803		62.07%	0.8881
199	30%	70%	90	0.34	0.78	0.08	0.04	0.10	0.04	0.18	0.72	0.10	0.00	923	796		62.00%	0.8870
200	30%	70%	90	0.34	0.82	0.04	0.04	0.10	0.04	0.18	0.72	0.10	0.00	923	771		61.92%	0.8860
201	30%	130%	90	0.18	0.70	0.16	0.04	0.10	0.04	0.18	0.72	0.10	0.00	923	754		92.24%	0.7094
202	30%	130%	90	0.18	0.74	0.12	0.04	0.10	0.04	0.18	0.72	0.10	0.00	923	743		92.03%	0.7078
203	30%	130%	90	0.18	0.76	0.10	0.04	0.10	0.04	0.18	0.72	0.10	0.00	923	738		92.54%	0.7117
204	30%	130%	90	0.18	0.78	0.08	0.04	0.10	0.04	0.18	0.72	0.10	0.00	923	729		92.45%	0.7110
205	30%	130%	90	0.18	0.82	0.04	0.04	0.10	0.04	0.18	0.72	0.10	0.00	923	693		93.04%	0.7155
206	30%	70%	120	0.45	0.70	0.16	0.04	0.10	0.06	0.18	0.72	0.10	0.00	923	768		58.94%	0.8406
207	30%	70%	120	0.45	0.74	0.12	0.04	0.10	0.06	0.18	0.72	0.10	0.00	923	760		59.25%	0.8451
208	30%	70%	120	0.45	0.76	0.10	0.04	0.10	0.06	0.18	0.72	0.10	0.00	923	754		58.94%	0.8407
209	30%	70%	120	0.45	0.78	0.08	0.04	0.10	0.06	0.18	0.72	0.10	0.00	923	751		59.50%	0.8487
210	30%	70%	120	0.45	0.82	0.04	0.04	0.10	0.06	0.18	0.72	0.10	0.00	923	722		59.43%	0.8477
211	75%	75%	160	0.13	0.62	0.11	0.17	0.10	0.03	0.18	0.72	0.10	0.00	923	778	1.04	-	-
212	30%	130%	120	0.24	0.70	0.16	0.04	0.10	0.06	0.18	0.72	0.10	0.00	923	718		87.76%	0.6750
213	30%	130%	120	0.24	0.74	0.12	0.04	0.10	0.06	0.18	0.72	0.10	0.00	923	706		87.75%	0.6748
214	30%	130%	120	0.24	0.76	0.10	0.04	0.10	0.06	0.18	0.72	0.10	0.00	923	697		87.41%	0.6723
215	30%	130%	120	0.24	0.78	0.08	0.04	0.10	0.06	0.18	0.72	0.10	0.00	923	687		87.48%	0.6728
216	30%	130%	120	0.24	0.82	0.04	0.04	0.10	0.06	0.18	0.72	0.10	0.00	923	642		87.82%	0.6754
217	75%	75%	160	0.13	0.62	0.11	0.17	0.10	0.03	0.16	0.74	0.10	0.00	923	772		-	-
218	75%	75%	160	0.13	0.62	0.11	0.17	0.10	0.03	0.18	0.72	0.10	0.00	923	774	1.02	73.71%	0.9838
219	30%	90%	90	0.26	0.76	0.10	0.04	0.10	0.04	0.18	0.72	0.10	0.00	923	782	1	74.32%	0.8241
220	30%	110%	90	0.22	0.76	0.10	0.04	0.10	0.04	0.18	0.72	0.10	0.00	923	759	1	84.09%	0.7620
221	30%	130%	90	0.18	0.76	0.10	0.04	0.10	0.04	0.18	0.72	0.10	0.00	923	739	0.99	90.72%	0.6977
222	30%	90%	120	0.35	0.76	0.10	0.04	0.10	0.06	0.18	0.72	0.10	0.00	923	731	1	69.99%	0.7761
223	30%	110%	120	0.29	0.76	0.10	0.04	0.10	0.06	0.18	0.72	0.10	0.00	923	712	1	78.72%	0.7145
224	30%	130%	120	0.24	0.76	0.10	0.04	0.10	0.06	0.18	0.72	0.10	0.00	923	696	1	85.40%	0.6568
225	30%	90%	150	0.44	0.76	0.10	0.04	0.10	0.07	0.18	0.72	0.10	0.00	923	693	0.96	65.70%	0.7309
226	30%	110%	150	0.36	0.76	0.10	0.04	0.10	0.07	0.18	0.72	0.10	0.00	923	676	0.96	73.90%	0.6714
227	30%	130%	150	0.30	0.76	0.10	0.04	0.10	0.07	0.18	0.72	0.10	0.00	923	662	0.96	80.89%	0.6221
228	75%	75%	160	0.13	0.62	0.11	0.17	0.10	0.03	0.18	0.72	0.10	0.00	923	776	1.03	-	-

ID	Target performance			Total	Cathode molar fraction				Total	Anode molar fraction				Inlet T	Experimental Results			
	U_{H_2}	U_{CO_2}	J	cathode flow	N_2	O_2	CO_2	H_2O	anode flow	CO_2	H_2	H_2O	N_2		Voltage	R_Ω	U_{CO_2}	$t_{CO_3^{2-}}$
	%	%	$mA\,cm^{-2}$	$Nm^3\,h^{-1}$	–				$Nm^3\,h^{-1}$	–				K	mV	$m\Omega$	%	–
229	30%	70%	90	0.68	0.86	0.02	0.02	0.10	0.04	0.18	0.72	0.10	0.00	923	687	0.96	51.98%	0.7438
230	30%	90%	90	0.53	0.86	0.02	0.02	0.10	0.04	0.18	0.72	0.10	0.00	923	666	0.95	63.40%	0.7030
231	30%	110%	90	0.43	0.86	0.02	0.02	0.10	0.04	0.18	0.72	0.10	0.00	923	647	0.95	72.78%	0.6595
232	75%	75%	160	0.13	0.62	0.11	0.17	0.10	0.03	0.18	0.72	0.10	0.00	923	777	1.03	-	-
233	75%	75%	160	0.13	0.62	0.11	0.17	0.10	0.03	0.18	0.72	0.10	0.00	923	777	1.01	-	-
234	30%	70%	90	0.68	0.82	0.06	0.02	0.10	0.04	0.18	0.72	0.10	0.00	923	733	0.95	51.07%	0.7307
235	30%	90%	90	0.53	0.82	0.06	0.02	0.10	0.04	0.18	0.72	0.10	0.00	923	719	0.93	62.73%	0.6956
236	30%	110%	90	0.43	0.82	0.06	0.02	0.10	0.04	0.18	0.72	0.10	0.00	923	706	0.95	70.37%	0.6376
237	30%	130%	90	0.37	0.82	0.06	0.02	0.10	0.04	0.18	0.72	0.10	0.00	923	695	0.94	77.60%	0.5968
238	75%	75%	160	0.13	0.62	0.11	0.17	0.10	0.03	0.18	0.72	0.10	0.00	923	778	1	-	-
239	30%	70%	90	0.68	0.78	0.10	0.02	0.10	0.04	0.18	0.72	0.10	0.00	923	749	0.96	51.85%	0.7418
240	30%	90%	90	0.53	0.78	0.10	0.02	0.10	0.04	0.18	0.72	0.10	0.00	923	738	0.95	62.17%	0.6894
241	30%	110%	90	0.43	0.78	0.10	0.02	0.10	0.04	0.18	0.72	0.10	0.00	923	723	0.95	70.31%	0.6372
242	30%	130%	90	0.36	0.78	0.10	0.02	0.10	0.04	0.18	0.72	0.10	0.00	923	712	0.92	77.53%	0.5963
243	75%	75%	160	0.13	0.62	0.11	0.17	0.10	0.03	0.18	0.72	0.10	0.00	923	779	1	-	-
244	30%	70%	90	0.68	0.73	0.15	0.02	0.10	0.04	0.18	0.72	0.10	0.00	923	763	0.96	51.05%	0.7305
245	30%	90%	90	0.53	0.73	0.15	0.02	0.10	0.04	0.18	0.72	0.10	0.00	923	750	0.96	61.61%	0.6832
246	30%	110%	90	0.43	0.73	0.15	0.02	0.10	0.04	0.18	0.72	0.10	0.00	923	738	0.96	70.48%	0.6387
247	30%	130%	90	0.37	0.73	0.15	0.02	0.10	0.04	0.18	0.72	0.10	0.00	923	727	0.96	76.96%	0.5919
248	75%	75%	160	0.13	0.68	0.11	0.17	0.03	0.03	0.18	0.72	0.10	0.00	923	780	1	-	-
249	30%	70%	90	0.68	0.80	0.15	0.02	0.03	0.04	0.18	0.72	0.10	0.00	923	730	0.95	55.03%	0.7874
250	30%	90%	90	0.53	0.80	0.15	0.02	0.03	0.04	0.18	0.72	0.10	0.00	923	706	0.95	65.12%	0.7222
251	30%	110%	90	0.43	0.80	0.15	0.02	0.03	0.04	0.18	0.72	0.10	0.00	923	688	0.97	73.56%	0.6666
252	30%	130%	90	0.37	0.80	0.15	0.02	0.03	0.04	0.18	0.72	0.10	0.00	923	665	1	79.23%	0.6093
253	75%	75%	160	0.13	0.68	0.11	0.17	0.03	0.03	0.18	0.72	0.10	0.00	923	770	1.04	-	-
254	30%	70%	90	0.68	0.80	0.15	0.02	0.03	0.04	0.18	0.72	0.10	0.00	923	716	1.01	-	-
255	30%	90%	90	0.53	0.80	0.15	0.02	0.03	0.04	0.18	0.72	0.10	0.00	923	687	1.04	-	-
256	75%	75%	160	0.13	0.52	0.11	0.17	0.20	0.03	0.18	0.72	0.10	0.00	923	783	1	-	-
257	30%	70%	90	0.68	0.63	0.15	0.02	0.20	0.04	0.18	0.72	0.10	0.00	923	786	0.96	49.41%	0.7069
258	30%	90%	90	0.53	0.63	0.15	0.02	0.20	0.04	0.18	0.72	0.10	0.00	923	774	0.97	59.41%	0.6588
259	30%	110%	90	0.43	0.63	0.15	0.02	0.20	0.04	0.18	0.72	0.10	0.00	923	762	0.95	67.91%	0.6154
260	30%	130%	90	0.37	0.63	0.15	0.02	0.20	0.04	0.18	0.72	0.10	0.00	923	753	0.96	74.39%	0.5721
261	75%	75%	160	0.13	0.62	0.11	0.17	0.10	0.03	0.18	0.72	0.10	0.00	923	780	1	-	-
262	30%	70%	90	0.68	0.83	0.15	0.02	0.00	0.04	0.18	0.72	0.10	0.00	923	641	0.92	59.99%	0.8584
263	75%	75%	160	0.13	0.62	0.11	0.17	0.10	0.03	0.18	0.72	0.10	0.00	923	777	0.98	-	-
264	30%	70%	90	0.68	0.86	0.02	0.02	0.10	0.04	0.18	0.72	0.10	0.00	923	752	0.96	60.06%	0.8593
265	30%	90%	90	0.53	0.86	0.02	0.02	0.10	0.04	0.18	0.72	0.10	0.00	923	732	0.96	73.80%	0.8183
266	30%	110%	90	0.43	0.86	0.02	0.02	0.10	0.04	0.18	0.72	0.10	0.00	923	711	0.96	83.99%	0.7611

ID	Target performance			Total	Cathode molar fraction				Total	Anode molar fraction				Inlet T	Experimental Results			
	U_{H_2}	U_{CO_2}	J	cathode flow	N_2	O_2	CO_2	H_2O	anode flow	CO_2	H_2	H_2O	N_2		Voltage	R_Ω	U_{CO_2}	$t_{CO_3^{2-}}$
	%	%	$mA\,cm^{-2}$	$Nm^3\,h^{-1}$	–				$Nm^3\,h^{-1}$	–				K	mV	$m\Omega$	%	–
267	75%	75%	160	0.13	0.62	0.11	0.17	0.10	0.03	0.18	0.72	0.10	0.00	923	774	0.98	-	-
268	30%	70%	90	0.68	0.73	0.15	0.02	0.10	0.04	0.18	0.72	0.10	0.00	923	801	0.99	58.60%	0.8384
269	30%	90%	90	0.53	0.73	0.15	0.02	0.10	0.04	0.18	0.72	0.10	0.00	923	783	0.98	71.14%	0.7889
270	30%	110%	90	0.43	0.73	0.15	0.02	0.10	0.04	0.18	0.72	0.10	0.00	923	766	0.96	81.31%	0.7368
271	30%	130%	90	0.37	0.73	0.15	0.02	0.10	0.04	0.18	0.72	0.10	0.00	923	750	0.96	88.24%	0.6786
272	30%	70%	90	0.68	0.83	0.15	0.02	0.00	0.04	0.18	0.72	0.10	0.00	923	737	1	68.63%	0.9820
273	30%	90%	90	0.53	0.83	0.15	0.02	0.00	0.04	0.18	0.72	0.10	0.00	923	606	1.14	82.12%	0.9106
274	75%	75%	160	0.13	0.68	0.11	0.17	0.03	0.03	0.18	0.72	0.10	0.00	923	770	1.04	-	-
275	30%	70%	90	0.68	0.80	0.15	0.02	0.03	0.04	0.18	0.72	0.10	0.00	923	783	1.02	62.54%	0.8949
276	30%	90%	90	0.53	0.80	0.15	0.02	0.03	0.04	0.18	0.72	0.10	0.00	923	756	1.01	76.32%	0.8463
277	30%	110%	90	0.43	0.80	0.15	0.02	0.03	0.04	0.18	0.72	0.10	0.00	923	729	1.01	85.34%	0.7733
278	30%	130%	90	0.37	0.80	0.15	0.02	0.03	0.04	0.18	0.72	0.10	0.00	923	702	1.02	91.67%	0.7050

Experimental data collected using cathode CC having 35% open area at a constant inlet temperature of 923 K for a cell working in cross-flow.

ID	Target performance			Total	Cathode molar fraction				Total	Anode molar fraction				Inlet T	Experimental Results			
	U_{H_2}	U_{CO_2}	J	cathode flow	N_2	O_2	CO_2	H_2O	anode flow	CO_2	H_2	H_2O	N_2		Voltage	R_Ω	U_{CO_2}	$t_{CO_3^{2-}}$
	%	%	$mA\,cm^{-2}$	$Nm^3\,h^{-1}$	–				$Nm^3\,h^{-1}$	–				K	mV	$m\Omega$	%	–
279	75%	75%	160	0.13	0.62	0.11	0.17	0.10	0.03	0.18	0.72	0.10	0.00	923	774	1.09	74.34%	0.9969
280	30%	70%	120	0.46	0.76	0.10	0.04	0.10	0.06	0.18	0.72	0.10	0.00	923	752		58.26%	0.8204
281	30%	90%	120	0.36	0.76	0.10	0.04	0.10	0.06	0.18	0.72	0.10	0.00	923	733		69.29%	0.7751
282	30%	110%	120	0.29	0.76	0.10	0.04	0.10	0.06	0.18	0.72	0.10	0.00	923	711		78.27%	0.7135
283	30%	130%	120	0.25	0.76	0.10	0.04	0.10	0.06	0.18	0.72	0.10	0.00	923	697		84.30%	0.6496
284	75%	75%	160	0.13	0.62	0.11	0.17	0.10	0.03	0.18	0.72	0.10	0.00	873	755	1.24/1.28	74.60%	1.0005
285	30%	70%	120	0.46	0.76	0.10	0.04	0.10	0.06	0.18	0.72	0.10	0.00	873	727		58.44%	0.8268
286	30%	90%	120	0.36	0.76	0.10	0.04	0.10	0.06	0.18	0.72	0.10	0.00	873	707		69.59%	0.7785
287	30%	110%	120	0.29	0.76	0.10	0.04	0.10	0.06	0.18	0.72	0.10	0.00	873	687		77.94%	0.7105
288	30%	130%	120	0.25	0.76	0.10	0.04	0.10	0.06	0.18	0.72	0.10	0.00	873	669		83.17%	0.6447
289	75%	75%	160	0.13	0.62	0.11	0.17	0.10	0.03	0.18	0.72	0.10	0.00	898	769	1.06/1.11	74.41%	0.9980
290	75%	75%	160	0.13	0.62	0.11	0.17	0.10	0.03	0.18	0.72	0.10	0.00	898	769	1.06/1.11	-	-
291	30%	70%	90	0.35	0.76	0.10	0.04	0.10	0.04	0.18	0.72	0.10	0.00	898	796		61.97%	0.8800
292	30%	90%	90	0.27	0.76	0.10	0.04	0.10	0.04	0.18	0.72	0.10	0.00	898	773		74.32%	0.8292
293	30%	110%	90	0.22	0.76	0.10	0.04	0.10	0.04	0.18	0.72	0.10	0.00	898	751		84.13%	0.7707
294	30%	130%	90	0.19	0.76	0.10	0.04	0.10	0.04	0.18	0.72	0.10	0.00	898	731		90.69%	0.7030
295	75%	75%	160	0.13	0.62	0.11	0.17	0.10	0.03	0.18	0.72	0.10	0.00	898	768		73.12%	0.9805
296	30%	70%	120	0.46	0.76	0.10	0.04	0.10	0.06	0.18	0.72	0.10	0.00	898	744		57.88%	0.8207
297	30%	90%	120	0.36	0.76	0.10	0.04	0.10	0.06	0.18	0.72	0.10	0.00	898	720		69.14%	0.7734
298	30%	110%	120	0.29	0.76	0.10	0.04	0.10	0.06	0.18	0.72	0.10	0.00	898	699		77.70%	0.7084
299	30%	130%	120	0.25	0.76	0.10	0.04	0.10	0.06	0.18	0.72	0.10	0.00	898	684		84.35%	0.6539
300	75%	75%	160	0.13	0.62	0.11	0.17	0.10	0.03	0.18	0.72	0.10	0.00	923	774	1.02/1.07	73.73%	0.9888
301	30%	70%	120	0.46	0.76	0.10	0.04	0.10	0.06	0.18	0.72	0.10	0.00	923	750		57.43%	0.8245
302	30%	90%	120	0.36	0.76	0.10	0.04	0.10	0.06	0.18	0.72	0.10	0.00	923	732		68.62%	0.7676
303	30%	110%	120	0.29	0.76	0.10	0.04	0.10	0.06	0.18	0.72	0.10	0.00	923	711		77.41%	0.7057
304	30%	130%	120	0.25	0.76	0.10	0.04	0.10	0.06	0.18	0.72	0.10	0.00	923	698		84.04%	0.6514
305	75%	75%	160	0.13	0.62	0.11	0.17	0.10	0.03	0.18	0.72	0.10	0.00	948	774	0.91/0.95	72.71%	0.9751
306	30%	70%	90	0.35	0.76	0.10	0.04	0.10	0.04	0.18	0.72	0.10	0.00	948	801		60.00%	0.8562
307	30%	90%	90	0.27	0.76	0.10	0.04	0.10	0.04	0.18	0.72	0.10	0.00	948	782		72.39%	0.8077
308	30%	110%	90	0.22	0.76	0.10	0.04	0.10	0.04	0.18	0.72	0.10	0.00	948	765	0.91/	81.96%	0.7508
309	30%	130%	90	0.19	0.76	0.10	0.04	0.10	0.04	0.18	0.72	0.10	0.00	948	750		89.22%	0.6916
310	75%	75%	160	0.13	0.62	0.11	0.17	0.10	0.03	0.18	0.72	0.10	0.00	948	774	0.90/0.94	-	-
311	30%	70%	120	0.46	0.76	0.10	0.04	0.10	0.06	0.18	0.72	0.10	0.00	948	762		56.87%	0.8094
312	30%	90%	120	0.36	0.76	0.10	0.04	0.10	0.06	0.18	0.72	0.10	0.00	948	740		68.75%	0.7690
313	30%	110%	120	0.29	0.76	0.10	0.04	0.10	0.06	0.18	0.72	0.10	0.00	948	723		77.46%	0.7061
314	30%	130%	120	0.25	0.76	0.10	0.04	0.10	0.06	0.18	0.72	0.10	0.00	948	708		84.36%	0.6539
315	75%	75%	160	0.13	0.62	0.11	0.17	0.10	0.03	0.18	0.72	0.10	0.00	923	772	1.00/1.03	73.77%	0.9893
316	75%	75%	160	0.13	0.62	0.11	0.17	0.10	0.03	0.18	0.72	0.10	0.00	848	723	1.32/1.36	74.74%	1.0023

ID	Target performance			Total	Cathode molar fraction				Total	Anode molar fraction				Inlet T	Experimental Results			
	U_{H_2}	U_{CO_2}	J	cathode flow	N_2	O_2	CO_2	H_2O	anode flow	CO_2	H_2	H_2O	N_2		Voltage	R_Ω	U_{CO_2}	$t_{CO_3^{2-}}$
	%	%	$mA\,cm^{-2}$	$N\,m^3\,h^{-1}$	–				$N\,m^3\,h^{-1}$	–				K	mV	$m\Omega$	%	–
317	30%	70%	120	0.46	0.76	0.10	0.04	0.10	0.06	0.18	0.72	0.10	0.00	848	705		56.96%	0.8178
318	30%	90%	120	0.36	0.76	0.10	0.04	0.10	0.06	0.18	0.72	0.10	0.00	848	684		68.57%	0.7671
319	30%	110%	120	0.29	0.76	0.10	0.04	0.10	0.06	0.18	0.72	0.10	0.00	848	667		75.14%	0.6851
320	30%	130%	120	0.25	0.76	0.10	0.04	0.10	0.06	0.18	0.72	0.10	0.00	848	650		80.99%	0.6278
321	75%	75%	160	0.13	0.62	0.11	0.17	0.10	0.03	0.18	0.72	0.10	0.00	923	774	0.95/0.99	73.64%	0.9876
322	75%	75%	160	0.13	0.62	0.11	0.17	0.10	0.03	0.18	0.72	0.10	0.00	923	772		-	-
323	30%	90%	90	0.16	0.73	0.10	0.07	0.10	0.04	0.18	0.72	0.10	0.00	923	811	0.95/0.99	80.79%	0.8981
324	30%	110%	90	0.13	0.73	0.10	0.07	0.10	0.04	0.18	0.72	0.10	0.00	923	783		91.57%	0.8293
325	30%	130%	90	0.11	0.73	0.10	0.07	0.10	0.04	0.18	0.72	0.10	0.00	923	751		94.15%	0.7196
326	30%	90%	90	0.16	0.73	0.10	0.07	0.10	0.04	0.18	0.72	0.10	0.00	923	840	0.95/0.99	85.52%	0.9451
327	30%	110%	90	0.13	0.73	0.10	0.07	0.10	0.04	0.18	0.72	0.10	0.00	923	803	0.96/1.00	92.02%	0.8327
328	30%	130%	90	0.11	0.73	0.10	0.07	0.10	0.04	0.18	0.72	0.10	0.00	923	764		96.54%	0.7368
329	75%	75%	160	0.13	0.62	0.11	0.17	0.10	0.03	0.18	0.72	0.10	0.00	923	772		-	-
330	30%	90%	90	0.27	0.76	0.10	0.04	0.10	0.04	0.18	0.72	0.10	0.00	923	776		73.75%	0.8191
331	30%	110%	90	0.22	0.76	0.10	0.04	0.10	0.04	0.18	0.72	0.10	0.00	923	757		83.52%	0.7576
332	30%	130%	90	0.18	0.76	0.10	0.04	0.10	0.04	0.18	0.72	0.10	0.00	923	741		90.59%	0.6925
333	30%	90%	90	0.27	0.76	0.10	0.04	0.10	0.04	0.18	0.72	0.10	0.00	923	813		81.11%	0.8957
334	30%	110%	90	0.22	0.76	0.10	0.04	0.10	0.04	0.18	0.72	0.10	0.00	923	788		92.14%	0.8334
335	30%	130%	90	0.18	0.76	0.10	0.04	0.10	0.04	0.18	0.72	0.10	0.00	923	760		97.77%	0.7463
336	75%	75%	160	0.13	0.62	0.11	0.17	0.10	0.03	0.18	0.72	0.10	0.00	923	771		-	-
337	30%	90%	90	0.53	0.78	0.10	0.02	0.10	0.04	0.18	0.72	0.10	0.00	923	741		60.67%	0.6777
338	30%	110%	90	0.43	0.78	0.10	0.02	0.10	0.04	0.18	0.72	0.10	0.00	923	729		69.08%	0.6317
339	30%	130%	90	0.37	0.78	0.10	0.02	0.10	0.04	0.18	0.72	0.10	0.00	923	719		76.02%	0.5838
340	75%	75%	160	0.13	0.62	0.11	0.17	0.10	0.03	0.18	0.72	0.10	0.00	923	769		-	-
341	30%	90%	90	0.53	0.78	0.10	0.02	0.10	0.04	0.18	0.72	0.10	0.00	923	770		71.55%	0.7858
342	30%	110%	90	0.43	0.78	0.10	0.02	0.10	0.04	0.18	0.72	0.10	0.00	923	752		80.77%	0.7293
343	30%	130%	90	0.37	0.78	0.10	0.02	0.10	0.04	0.18	0.72	0.10	0.00	923	739		88.06%	0.6729
344	75%	75%	160	0.13	0.62	0.11	0.17	0.10	0.03	0.18	0.72	0.10	0.00	923	766		-	-

Experimental data collected using cathode CC having 35% open area at different inlet temperatures for a cell working in cross flow. The data with the N_2 composition colored in purple had He instead.

ID	Target Performance			Cathode flow	Cathode molar fractions				Anode flow	Anode molar fractions				Inlet T	Experimental Results			
	U_{H_2}	U_{CO_2}	J	TOT	N_2	O_2	CO_2	H_2O	TOT	CO_2	H_2	H_2O	N_2		Voltage	R_Ω	U_{CO_2}	$t_{CO_3^{-2}}$
	%	%	$mA\,cm^{-1}$	$Nm^3\,h^{-1}$	-				$Nm^3\,h^{-1}$	-				K	mV	$m\Omega$	%	-
345	75%	75%	160	0.13	0.62	0.11	0.17	0.10	0.03	0.18	0.72	0.10	0.00	923	784	1.54	74.84%	0.9989
346	30%	70%	90	0.34	0.76	0.10	0.04	0.10	0.04	0.18	0.72	0.10	0.00	923	839		66.28%	0.9483
347	30%	80%	90	0.30	0.76	0.10	0.04	0.10	0.04	0.18	0.72	0.10	0.00	923	829		74.80%	0.9365
348	30%	90%	90	0.26	0.76	0.10	0.04	0.10	0.04	0.18	0.72	0.10	0.00	923	819		82.78%	0.9179
349	30%	100%	90	0.24	0.76	0.10	0.04	0.10	0.04	0.18	0.72	0.10	0.00	923	807		89.46%	0.8960
350	30%	110%	90	0.22	0.76	0.10	0.04	0.10	0.04	0.18	0.72	0.10	0.00	923	790		94.60%	0.8572
351	30%	120%	90	0.20	0.76	0.10	0.04	0.10	0.04	0.18	0.72	0.10	0.00	923	772		97.56%	0.8143
352	75%	75%	160	0.13	0.62	0.11	0.17	0.10	0.03	0.18	0.72	0.10	0.00	923	787		-	-
353	30%	70%	120	0.45	0.76	0.10	0.04	0.10	0.06	0.18	0.72	0.10	0.00	923	811		66.68%	0.9511
354	30%	80%	120	0.40	0.76	0.10	0.04	0.10	0.06	0.18	0.72	0.10	0.00	923	801		74.44%	0.9320
355	30%	90%	120	0.35	0.76	0.10	0.04	0.10	0.06	0.18	0.72	0.10	0.00	923	787		82.52%	0.9151
356	30%	100%	120	0.32	0.76	0.10	0.04	0.10	0.06	0.18	0.72	0.10	0.00	923	772		88.73%	0.8887
357	30%	110%	120	0.29	0.76	0.10	0.04	0.10	0.06	0.18	0.72	0.10	0.00	923	754		93.78%	0.8512
358	30%	120%	120	0.26	0.76	0.10	0.04	0.10	0.06	0.18	0.72	0.10	0.00	923	733		96.82%	0.8052
359	75%	75%	160	0.13	0.68	0.11	0.17	0.03	0.03	0.18	0.72	0.10	0.00	923	781		-	-
360	30%	80%	120	0.40	0.83	0.10	0.04	0.03	0.06	0.18	0.72	0.10	0.00	923	790		76.38%	0.9563
361	30%	90%	120	0.35	0.83	0.10	0.04	0.03	0.06	0.18	0.72	0.10	0.00	923	772		84.59%	0.9380
362	30%	100%	120	0.32	0.83	0.10	0.04	0.03	0.06	0.18	0.72	0.10	0.00	923	752		90.98%	0.9112
363	30%	110%	120	0.29	0.83	0.10	0.04	0.03	0.06	0.18	0.72	0.10	0.00	923	727		95.47%	0.8665
364	30%	120%	120	0.26	0.83	0.10	0.04	0.03	0.06	0.18	0.72	0.10	0.00	923	703		97.94%	0.8146
365	75%	75%	160	0.13	0.65	0.11	0.17	0.06	0.03	0.18	0.72	0.10	0.00	923	782		-	-
366	30%	80%	120	0.40	0.80	0.10	0.04	0.06	0.06	0.18	0.72	0.10	0.00	923	792		75.55%	0.9459
367	30%	90%	120	0.35	0.80	0.10	0.04	0.06	0.06	0.18	0.72	0.10	0.00	923	779		83.26%	0.9233
368	30%	100%	120	0.32	0.80	0.10	0.04	0.06	0.06	0.18	0.72	0.10	0.00	923	761		89.65%	0.8980
369	30%	110%	120	0.29	0.80	0.10	0.04	0.06	0.06	0.18	0.72	0.10	0.00	923	738		94.33%	0.8562
370	30%	120%	120	0.26	0.80	0.10	0.04	0.06	0.06	0.18	0.72	0.10	0.00	923	715		97.32%	0.8094
371	75%	75%	160	0.13	0.52	0.11	0.17	0.20	0.03	0.18	0.72	0.10	0.00	923	796		-	-
372	30%	80%	120	0.40	0.66	0.10	0.04	0.20	0.06	0.18	0.72	0.10	0.00	923	812		72.52%	0.9079
373	30%	90%	120	0.35	0.66	0.10	0.04	0.20	0.06	0.18	0.72	0.10	0.00	923	800		80.27%	0.8901
374	30%	100%	120	0.32	0.66	0.10	0.04	0.20	0.06	0.18	0.72	0.10	0.00	923	790		86.17%	0.8630
375	30%	110%	120	0.29	0.66	0.10	0.04	0.20	0.06	0.18	0.72	0.10	0.00	923	773		91.69%	0.8322
376	30%	120%	120	0.26	0.66	0.10	0.04	0.20	0.06	0.18	0.72	0.10	0.00	923	761		94.97%	0.7898
377	75%	75%	160	0.13	0.62	0.11	0.17	0.10	0.03	0.18	0.72	0.10	0.00	923	788	1.20	-	-
378	30%	80%	150	0.49	0.76	0.10	0.04	0.10	0.07	0.18	0.72	0.10	0.00	923	768		73.71%	0.9201
379	30%	90%	150	0.44	0.76	0.10	0.04	0.10	0.07	0.18	0.72	0.10	0.00	923	754		81.09%	0.9022
380	30%	100%	150	0.40	0.76	0.10	0.04	0.10	0.07	0.18	0.72	0.10	0.00	923	734		86.85%	0.8699
381	30%	110%	150	0.36	0.76	0.10	0.04	0.10	0.07	0.18	0.72	0.10	0.00	923	717		91.52%	0.8316

ID	Target Performance			Cathode flow	Cathode molar fractions				Anode flow	Anode molar fractions				Inlet T	Experimental Results			
	U_{H_2}	U_{CO_2}	J	TOT	N_2	O_2	CO_2	H_2O	TOT	CO_2	H_2	H_2O	N_2		Voltage	R_Ω	U_{CO_2}	$t_{CO_3^{-2}}$
	%	%	$mA\,cm^{-1}$	$Nm^3\,h^{-1}$	-				$Nm^3\,h^{-1}$	-				K	mV	$m\Omega$	%	-
382	30%	120%	150	0.33	0.76	0.10	0.04	0.10	0.07	0.18	0.72	0.10	0.00	923	701		94.50%	0.7876
383	75%	75%	160	0.13	0.62	0.11	0.17	0.10	0.03	0.18	0.72	0.10	0.00	923	790	1.20	-	-
384	30%	80%	180	0.59	0.76	0.10	0.04	0.10	0.09	0.18	0.72	0.10	0.00	923	730		72.66%	0.9075
385	30%	90%	180	0.53	0.76	0.10	0.04	0.10	0.09	0.18	0.72	0.10	0.00	923	719		79.16%	0.8801
386	30%	100%	180	0.47	0.76	0.10	0.04	0.10	0.09	0.18	0.72	0.10	0.00	923	700		84.46%	0.8434
387	30%	110%	180	0.43	0.76	0.10	0.04	0.10	0.09	0.18	0.72	0.10	0.00	923	684		89.09%	0.8100
388	30%	90%	90	0.27	0.76	0.10	0.04	0.10	0.05	0.72	0.18	0.10	0.00	923	818	1.20	89.77%	0.9953
389	30%	110%	90	0.22	0.76	0.10	0.04	0.10	0.05	0.72	0.18	0.10	0.00	923	790	1.21	96.59%	0.8728
390	30%	130%	90	0.19	0.76	0.10	0.04	0.10	0.05	0.72	0.18	0.10	0.00	923	762	1.59	98.87%	0.7807
391	30%	90%	120	0.37	0.76	0.10	0.04	0.10	0.06	0.72	0.18	0.10	0.00	923	795	1.20	86.85%	0.9808
392	30%	110%	120	0.30	0.76	0.10	0.04	0.10	0.06	0.72	0.18	0.10	0.00	923	768	1.14	94.59%	0.8975
393	30%	130%	120	0.26	0.76	0.10	0.04	0.10	0.06	0.72	0.18	0.10	0.00	923	730	1.16	98.51%	0.7911
394	30%	70%	90	0.34	0.76	0.10	0.04	0.10	0.05	0.72	0.18	0.10	0.00	923	840		67.88%	
395	30%	90%	90	0.27	0.76	0.10	0.04	0.10	0.05	0.72	0.18	0.10	0.00	923	817		86.86%	
396	30%	110%	90	0.22	0.76	0.10	0.04	0.10	0.05	0.72	0.18	0.10	0.00	923	782		96.10%	
397	30%	130%	90	0.18	0.76	0.10	0.04	0.10	0.05	0.72	0.18	0.10	0.00	923	747		97.74%	
398	30%	90%	120	0.36	0.76	0.10	0.04	0.10	0.06	0.72	0.18	0.10	0.00	923	783		86.49%	
399	30%	110%	120	0.29	0.76	0.10	0.04	0.10	0.06	0.72	0.18	0.10	0.00	923	747		96.30%	
400	30%	130%	120	0.25	0.76	0.10	0.04	0.10	0.06	0.72	0.18	0.10	0.00	923	719		98.81%	
401	30%	90%	150	0.44	0.76	0.10	0.04	0.10	0.08	0.72	0.18	0.10	0.00	923	750		84.74%	
402	30%	110%	150	0.36	0.76	0.10	0.04	0.10	0.08	0.72	0.18	0.10	0.00	923	718		94.39%	
403	30%	90%	90	0.10	0.76	0.10	0.04	0.10	0.05	0.18	0.72	0.10	0.00	923	827	1.27	78.35%	0.3365
404	30%	110%	90	0.22	0.76	0.10	0.04	0.10	0.05	0.18	0.72	0.10	0.00	923	797	1.34	91.23%	0.8072
405	30%	130%	90	0.18	0.76	0.10	0.04	0.10	0.05	0.18	0.72	0.10	0.00	923	775	1.30	97.55%	0.7380
406	30%	90%	120	0.36	0.76	0.10	0.04	0.10	0.06	0.18	0.72	0.10	0.00	923	791	1.33	81.90%	0.8975
407	30%	110%	120	0.30	0.76	0.10	0.04	0.10	0.06	0.18	0.72	0.10	0.00	923	766	1.31	90.46%	0.8138
408	30%	130%	120	0.24	0.76	0.10	0.04	0.10	0.06	0.18	0.72	0.10	0.00	923	747	1.24	97.99%	0.7401
409	30%	90%	120	0.36	0.76	0.10	0.04	0.10	0.06	0.18	0.72	0.10	0.00	923	792	1.29	75.52%	0.8414
410	30%	110%	120	0.29	0.76	0.10	0.04	0.10	0.06	0.18	0.72	0.10	0.00	923	762	1.27	89.51%	0.7883
411	30%	130%	120	0.24	0.76	0.10	0.04	0.10	0.06	0.18	0.72	0.10	0.00	923	732	1.20	97.23%	0.7291
412	30%	90%	150	0.44	0.76	0.10	0.04	0.10	0.08	0.18	0.72	0.10	0.00	923	761	1.27	76.09%	0.8354
413	30%	110%	150	0.36	0.76	0.10	0.04	0.10	0.08	0.18	0.72	0.10	0.00	923	734	1.24	88.20%	0.7863
414	30%	130%	150	0.31	0.76	0.10	0.04	0.10	0.08	0.18	0.72	0.10	0.00	923	716	1.24	93.54%	0.7169
415	30%	90%	120	0.38	0.77	0.09	0.04	0.10	0.06	0.18	0.72	0.10	0.00	923	813	1.35	77.98%	0.8895
416	30%	110%	120	0.31	0.77	0.09	0.04	0.10	0.06	0.18	0.72	0.10	0.00	923	790	1.25	90.78%	0.8448
417	30%	130%	120	0.26	0.77	0.09	0.04	0.10	0.06	0.18	0.72	0.10	0.00	923	764	1.24	96.93%	0.7600
418	30%	90%	120	0.36	0.76	0.10	0.04	0.10	0.06	0.18	0.72	0.10	0.00	923	796	1497.00	77.10%	0.8581

ID	Target Performance			Cathode flow	Cathode molar fractions				Anode flow	Anode molar fractions				Inlet T	Experimental Results			
	U_{H_2}	U_{CO_2}	J	TOT	N_2	O_2	CO_2	H_2O	TOT	CO_2	H_2	H_2O	N_2		Voltage	R_Ω	U_{CO_2}	$t_{CO_3^{-2}}$
	%	%	$mA\,cm^{-1}$	$Nm^3\,h^{-1}$	-				$Nm^3\,h^{-1}$	-				K	mV	$m\Omega$	%	-
419	30%	110%	120	0.29	0.76	0.10	0.04	0.10	0.06	0.18	0.72	0.10	0.00	923	768	1.41	89.52%	0.8120
420	30%	130%	120	0.25	0.76	0.10	0.04	0.10	0.06	0.18	0.72	0.10	0.00	923	745	1.37	95.94%	0.7399
421	30%	90%	150	0.45	0.76	0.10	0.04	0.10	0.08	0.18	0.72	0.10	0.00	923	763	1.44	77.59%	0.8622
422	30%	110%	150	0.36	0.76	0.10	0.04	0.10	0.08	0.18	0.72	0.10	0.00	923	736	1.36	87.33%	0.7929
423	30%	130%	150	0.31	0.76	0.10	0.04	0.10	0.08	0.18	0.72	0.10	0.00	923	713	1.37	94.90%	0.7286
424	30%	90%	120	0.38	0.77	0.10	0.04	0.10	0.06	0.18	0.72	0.10	0.00	923	817	1.51	77.01%	0.8699
425	30%	110%	120	0.31	0.77	0.09	0.04	0.10	0.06	0.18	0.72	0.10	0.00	923	793	1.43	91.19%	0.8409
426	30%	130%	120	0.26	0.77	0.09	0.04	0.10	0.06	0.18	0.72	0.10	0.00	923	764	1.37	97.79%	0.7645
427	65%	70%	140	0.24	0.74	0.07	0.09	0.10	0.03	0.18	0.72	0.10	0.00	923	777	1.39	65.58%	0.9360
428	65%	90%	140	0.19	0.74	0.07	0.09	0.10	0.03	0.18	0.72	0.10	0.00	923	752	1.40	83.37%	0.9269
429	65%	110%	140	0.15	0.74	0.07	0.09	0.10	0.03	0.18	0.72	0.10	0.00	923	716	1.30	95.64%	0.8693
430	65%	130%	140	0.13	0.74	0.07	0.09	0.10	0.03	0.18	0.72	0.10	0.00	923	663	1.23	99.40%	0.7654
431	30%	70%	140	0.36	0.74	0.10	0.06	0.10	0.07	0.18	0.72	0.10	0.00	923	827	1.36	64.48%	0.9203
432	30%	90%	140	0.28	0.74	0.10	0.06	0.10	0.07	0.18	0.72	0.10	0.00	923	806	1.32	82.00%	0.9116
433	30%	110%	140	0.23	0.74	0.10	0.06	0.10	0.07	0.18	0.72	0.10	0.00	923	769	1.30	94.88%	0.8624
434	30%	130%	140	0.20	0.74	0.10	0.06	0.10	0.07	0.18	0.72	0.10	0.00	923	728	1.26	99.20%	0.7638
435	65%	70%	140	0.36	0.74	0.10	0.06	0.10	0.03	0.18	0.72	0.10	0.00	923	779	1.33	65.43%	0.9339
436	65%	90%	140	0.28	0.74	0.10	0.06	0.10	0.03	0.18	0.72	0.10	0.00	923	759	1.32	81.62%	0.9074
437	65%	110%	140	0.23	0.74	0.10	0.06	0.10	0.03	0.18	0.72	0.10	0.00	923	728	1.28	93.63%	0.8510
438	65%	130%	140	0.20	0.74	0.10	0.06	0.10	0.03	0.18	0.72	0.10	0.00	923	691	1.26	98.54%	0.7587
439	65%	70%	140	0.27	0.74	0.08	0.08	0.10	0.03	0.17	0.73	0.10	0.00	923	784	1.37	66.64%	0.9511
440	65%	90%	140	0.21	0.74	0.08	0.08	0.10	0.03	0.17	0.73	0.10	0.00	923	764	1.35	83.38%	0.9270
441	65%	110%	140	0.17	0.74	0.08	0.08	0.10	0.03	0.17	0.73	0.10	0.00	923	727	1.35	95.31%	0.8663
442	65%	130%	140	0.15	0.74	0.08	0.08	0.10	0.03	0.17	0.73	0.10	0.00	923	679	1.22	99.19%	0.7637
443	65%	75%	140	0.32	0.73	0.10	0.06	0.10	0.03	0.17	0.73	0.10	0.00	923	776	1.37	70.44%	0.9392
444	65%	75%	140	0.23	0.74	0.07	0.09	0.10	0.03	0.17	0.73	0.10	0.00	923	773	1.36	71.90%	0.9587
445	65%	70%	140	0.27	0.80	0.08	0.08	0.04	0.03	0.19	0.77	0.10	0.00	923	779	1.33	66.83%	0.9538
446	65%	90%	140	0.21	0.80	0.08	0.08	0.04	0.03	0.19	0.77	0.10	0.00	923	753	1.39	85.22%	0.9474
447	65%	110%	140	0.17	0.80	0.08	0.08	0.04	0.03	0.19	0.77	0.10	0.00	923	699	1.28	97.40%	0.8853
448	65%	70%	140	0.17	0.72	0.11	0.13	0.04	0.03	0.19	0.77	0.10	0.00	923	807	1.38	67.55%	0.9641
449	65%	70%	90	0.11	0.72	0.11	0.13	0.04	0.02	0.19	0.77	0.11	0.00	923	839	1.38	68.06%	0.9703
450	30%	90%	120	0.36	0.76	0.10	0.04	0.10	0.06	0.18	0.72	0.10	0.00	923	804	1.31	78.94%	0.8740
451	30%	110%	120	0.29	0.76	0.10	0.04	0.10	0.06	0.18	0.72	0.10	0.00	923	768	1.35	92.12%	0.8226
452	30%	130%	120	0.25	0.76	0.10	0.04	0.10	0.06	0.18	0.72	0.10	0.00	923	743	1.00	96.69%	0.7397
453	30%	90%	150	0.46	0.76	0.10	0.04	0.10	0.08	0.18	0.72	0.10	0.00	923	781	1.27	79.88%	0.8955
454	30%	110%	150	0.37	0.76	0.10	0.04	0.10	0.08	0.18	0.72	0.10	0.00	923	748	1.11	90.32%	0.8121
455	30%	130%	150	0.31	0.76	0.10	0.04	0.10	0.08	0.18	0.72	0.10	0.00	923	716	1.33	96.00%	0.7371

ID	Target Performance			Cathode flow	Cathode molar fractions				Anode flow	Anode molar fractions				Inlet T	Experimental Results			
	U_{H_2}	U_{CO_2}	J	TOT	N_2	O_2	CO_2	H_2O	TOT	CO_2	H_2	H_2O	N_2		Voltage	R_Ω	U_{CO_2}	$t_{CO_3^{-2}}$
	%	%	$mA\,cm^{-1}$	$Nm^3\,h^{-1}$	-				$Nm^3\,h^{-1}$	-				K	mV	$m\Omega$	%	-
456	30%	90%	120	0.38	0.76	0.10	0.04	0.10	0.06	0.18	0.72	0.10	0.00	923	803	1.16	75.85%	0.8770
457	30%	110%	120	0.31	0.76	0.10	0.04	0.10	0.06	0.18	0.72	0.10	0.00	923	770	1.19	96.54%	0.9132
458	30%	130%	120	0.26	0.76	0.10	0.04	0.10	0.06	0.18	0.72	0.10	0.00	923	742	1.26	98.93%	0.7882
459	30%	90%	120	0.37	0.76	0.10	0.04	0.10	0.03	0.18	0.72	0.10	0.00	923	756	0.96	78.51%	0.8790
460	30%	110%	120	0.29	0.76	0.10	0.04	0.10	0.03	0.18	0.72	0.10	0.00	923	738	1.35	88.60%	0.8037
461	30%	130%	120	0.25	0.76	0.10	0.04	0.10	0.03	0.18	0.72	0.10	0.00	923	707	1.37	96.31%	0.7327
462	30%	90%	150	0.45	0.76	0.10	0.04	0.10	0.03	0.18	0.72	0.10	0.00	923	732	1.24	78.47%	0.8676
463	30%	110%	150	0.37	0.76	0.10	0.04	0.10	0.03	0.18	0.72	0.10	0.00	923	703	1.29	89.71%	0.8052
464	30%	130%	150	0.31	0.76	0.10	0.04	0.10	0.03	0.18	0.72	0.10	0.00	923	679	1.28	94.76%	0.7229
465	30%	90%	120	0.36	0.76	0.10	0.04	0.10	0.06	0.18	0.72	0.10	0.00	923	785	1.24	80.38%	0.8983
466	30%	110%	120	0.29	0.76	0.10	0.04	0.10	0.06	0.18	0.72	0.10	0.00	923	757	1.22	92.74%	0.8205
467	30%	130%	120	0.25	0.76	0.10	0.04	0.10	0.06	0.18	0.72	0.10	0.00	923	738	1.17	97.59%	0.7515
468	30%	90%	150	0.45	0.76	0.10	0.04	0.10	0.08	0.18	0.72	0.10	0.00	923	760	1.20	82.41%	0.9100
469	30%	110%	150	0.36	0.76	0.10	0.04	0.10	0.08	0.18	0.72	0.10	0.00	923	731	1.16	93.34%	0.8253
470	30%	130%	150	0.31	0.76	0.10	0.04	0.10	0.08	0.18	0.72	0.10	0.00	923	711	1.02	98.02%	0.7450
471	30%	90%	120	0.36	0.76	0.10	0.04	0.10	0.06	0.18	0.72	0.10	0.00	923	780	1.13	82.22%	0.9111
472	30%	110%	120	0.29	0.76	0.10	0.04	0.10	0.06	0.18	0.72	0.10	0.00	923	757	1.24	94.20%	0.8351
473	30%	130%	120	0.25	0.76	0.10	0.04	0.10	0.06	0.18	0.72	0.10	0.00	923	743	1.18	98.25%	0.7575
474	30%	90%	150	0.45	0.76	0.10	0.04	0.10	0.08	0.18	0.72	0.10	0.00	923	762	1.23	83.80%	0.9164
475	30%	110%	150	0.36	0.76	0.10	0.04	0.10	0.08	0.18	0.72	0.10	0.00	923	736	1.16	94.05%	0.8310
476	30%	130%	150	0.31	0.76	0.10	0.04	0.10	0.08	0.18	0.72	0.10	0.00	923	716	1.14	98.51%	0.7489
477	65%	70%	140	0.27	0.74	0.08	0.08	0.10	0.03	0.18	0.72	0.10	0.00	923	772	1.35	66.51%	0.9514
478	65%	90%	140	0.21	0.74	0.08	0.08	0.10	0.03	0.18	0.72	0.10	0.00	923	751	1.31	86.55%	0.9515
479	65%	70%	150	0.50	0.75	0.11	0.04	0.10	0.03	0.18	0.72	0.10	0.00	923	738	1.31	73.65%	1.0180
480	65%	90%	150	0.40	0.74	0.11	0.05	0.10	0.03	0.18	0.72	0.10	0.00	923	725	1.30	83.24%	0.9152
481	65%	110%	150	0.32	0.74	0.11	0.04	0.10	0.03	0.18	0.72	0.10	0.00	923	701	1.24	94.47%	0.8458

Experimental data collected using cathode CC having 90% open area using a cell in cross-flow configuration. The data with the N_2 composition colored in purple had He instead.

ID	Target performance			Total	Cathode molar fraction				Total	Anode molar fraction				Inlet T	Experimental Results			
	U_{H_2}	U_{CO_2}	J	cathode flow	N_2	O_2	CO_2	H_2O	anode flow	CO_2	H_2	H_2O	N_2		Voltage	R_Ω	U_{CO_2}	$t_{CO_3^{2-}}$
	%	%	$mA\,cm^{-2}$	$Nm^3\,h^{-1}$	–				$Nm^3\,h^{-1}$	–				K	mV	$m\Omega$	%	–
482	30%	90%	120	0.35	0.76	0.10	0.04	0.10	0.06	0.18	0.72	0.10	0.00	873	771	1.68	79.29%	0.8671
483	30%	110%	120	0.29	0.76	0.10	0.04	0.10	0.06	0.18	0.72	0.10	0.00	873	738	1.65	90.38%	0.8058
484	30%	130%	120	0.24	0.76	0.10	0.04	0.10	0.06	0.18	0.72	0.10	0.00	873	716	1.63	96.45%	0.7334
485	30%	90%	150	0.44	0.76	0.10	0.04	0.10	0.08	0.18	0.72	0.10	0.00	873	730	1.66	76.31%	0.8342
486	30%	110%	150	0.36	0.76	0.10	0.04	0.10	0.08	0.18	0.72	0.10	0.00	873	705	1.62	87.83%	0.7863
487	30%	130%	150	0.30	0.76	0.10	0.04	0.10	0.08	0.18	0.72	0.10	0.00	873	682	1.57	93.97%	0.7085
488	30%	90%	120	0.36	0.76	0.10	0.04	0.10	0.06	0.18	0.72	0.10	0.00	873	769	1.00	83.43%	0.9227
489	30%	110%	120	0.29	0.76	0.10	0.04	0.10	0.06	0.18	0.72	0.10	0.00	873	733	1.57	93.21%	0.8465
490	30%	130%	120	0.25	0.76	0.10	0.04	0.10	0.06	0.18	0.72	0.10	0.00	873	698	1.33	97.58%	0.7393
491	30%	90%	150	0.44	0.76	0.10	0.04	0.10	0.08	0.18	0.72	0.10	0.00	873	724	1.71	82.30%	0.8946
492	30%	110%	150	0.36	0.76	0.10	0.04	0.10	0.08	0.18	0.72	0.10	0.00	873	695	1.65	90.90%	0.8186
493	30%	130%	150	0.31	0.76	0.10	0.04	0.10	0.08	0.18	0.72	0.10	0.00	873	669	1.61	95.28%	0.7305

Experimental data collected using cathode CC having 90% open area using a cell in cross-flow configuration with inlet temperature of 873 K. The data with the N_2 composition colored in purple had He instead.

ID	Target performance			Total	Cathode molar fraction				Total	Anode molar fraction				Inlet T	Experimental Results			
	U_{H_2}	U_{CO_2}	J	cathode flow	N_2	O_2	CO_2	H_2O	anode flow	CO_2	H_2	H_2O	N_2		Voltage	R_Ω	U_{CO_2}	$t_{CO_3^{2-}}$
	%	%	$mA\,cm^{-2}$	$Nm^3\,h^{-1}$	–				$Nm^3\,h^{-1}$	–				K	mV	$m\Omega$	%	–
SCREEN 1																		
494	30%	90%	120	0.36	0.76	0.10	0.04	0.10	0.06	0.18	0.72	0.10	0.00	923	787	1.13	78.08%	0.862413
495	30%	110%	120	0.30	0.76	0.10	0.04	0.10	0.06	0.18	0.72	0.10	0.00	923	762	1.13	87.73%	0.78516
496	30%	130%	120	0.25	0.76	0.10	0.04	0.10	0.06	0.18	0.72	0.10	0.00	923	738	1.09	94.70%	0.720264
497	30%	90%	150	0.45	0.76	0.10	0.04	0.10	0.08	0.18	0.72	0.10	0.00	923	754	1.13	75.64%	0.834198
498	30%	110%	150	0.37	0.76	0.10	0.04	0.10	0.08	0.18	0.72	0.10	0.00	923	735	1.13	83.75%	0.752323
499	30%	130%	150	0.31	0.76	0.10	0.04	0.10	0.08	0.18	0.72	0.10	0.00	923	707	1.09	92.68%	0.693958
500	30%	90%	120	0.38	0.77	0.09	0.04	0.10	0.06	0.18	0.72	0.10	0.00	923	815	1.14	79.74%	0.905562
501	30%	110%	120	0.31	0.77	0.09	0.04	0.10	0.06	0.18	0.72	0.10	0.00	923	791	1.14	91.37%	0.836753
502	30%	130%	120	0.26	0.77	0.09	0.04	0.10	0.06	0.18	0.72	0.10	0.00	923	761	1.10	97.29%	0.750228
SCREEN 2																		
503	30%	90%	120	0.36	0.76	0.10	0.04	0.10	0.06	0.18	0.72	0.10	0.00	923	792	1.16	78.20%	0.861619
504	30%	110%	120	0.29	0.76	0.10	0.04	0.10	0.06	0.18	0.72	0.10		923	766	1.18	90.29%	0.803259
505	30%	130%	120	0.25	0.76	0.10	0.04	0.10	0.06	0.18	0.72	0.10	0.00	923	738	1.14	95.96%	0.721189
506	30%	90%	150	0.45	0.76	0.10	0.04	0.10	0.08	0.18	0.72	0.10	0.00	923	763	1.21	76.62%	0.842505
507	30%	110%	150	0.37	0.76	0.10	0.04	0.10	0.08	0.18	0.72	0.10	0.00	923	736	1.21	87.38%	0.779677
508	30%	130%	150	0.31	0.76	0.10	0.04	0.10	0.08	0.18	0.72	0.10	0.00	923	712	1.16	94.34%	0.710103
509	30%	90%	120	0.38	0.77	0.09	0.04	0.10	0.06	0.18	0.72	0.10	0.00	923	821	1.21	78.04%	0.854684
510	30%	110%	120	0.31	0.77	0.09	0.04	0.10	0.06	0.18	0.72	0.10	0.00	923	795	1.23	90.88%	0.814446
511	30%	130%	120	0.26	0.77	0.09	0.04	0.10	0.06	0.18	0.72	0.10	0.00	923	762	1.16	97.31%	0.7486

Experimental data collected using cathode CC having 70% open area and two different screen feature with a cell working in cross-flow configuration. The data with the N_2 composition colored in purple had He instead.

ID	Target performance			Total	Cathode molar fraction				Total	Anode molar fraction				Inlet T	Experimental Results			
	U_{H_2}	U_{CO_2}	J	cathode flow	N_2	O_2	CO_2	H_2O	anode flow	CO_2	H_2	H_2O	N_2		Voltage	R_Ω	U_{CO_2}	$t_{CO_3^{2-}}$
	%	%	$mA\,cm^{-2}$	$Nm^3\,h^{-1}$	–				$Nm^3\,h^{-1}$	–				K	mV	$m\Omega$	%	–
512	75%	75%	160	0.13	0.62	0.11	0.17	0.10	0.03	0.18	0.72	0.10	0.00	923	770	1.2	-	-
513	30%	70%	120	0.45	0.76	0.10	0.04	0.10	0.06	0.18	0.72	0.10	0.00	923	803	1.18	29.85%	0.9542
514	30%	90%	120	0.35	0.76	0.10	0.04	0.10	0.06	0.18	0.72	0.10	0.00	923	775	1.18	29.46%	0.9072
515	30%	110%	120	0.29	0.76	0.10	0.04	0.10	0.06	0.18	0.72	0.10	0.00	923	740	1.14	28.67%	0.8442
516	30%	130%	120	0.24	0.76	0.10	0.04	0.10	0.06	0.18	0.72	0.10	0.00	923	709	1.06	27.31%	0.7600
517	75%	75%	160	0.13	0.62	0.11	0.17	0.10	0.03	0.18	0.72	0.10	0.00	923		1.16	-	-
518	30%	70%	150	0.56	0.76	0.10	0.04	0.10	0.07	0.18	0.72	0.10	0.00	923	790	1.14	29.99%	0.9631
519	30%	90%	150	0.44	0.76	0.10	0.04	0.10	0.07	0.18	0.72	0.10	0.00	923	762	1.12	29.39%	0.9218
520	30%	110%	150	0.36	0.76	0.10	0.04	0.10	0.07	0.18	0.72	0.10	0.00	923	724	1.11	28.22%	0.8490
521	30%	130%	150	0.30	0.76	0.10	0.04	0.10	0.07	0.18	0.72	0.10	0.00	923	690	1.02	26.83%	0.7607
522	75%	75%	160	0.13	0.62	0.11	0.17	0.10	0.03	0.18	0.72	0.10	0.00	923	777	1.2	-	-
523	65%	70%	120	0.45	0.76	0.10	0.04	0.10	0.03	0.18	0.72	0.10	0.00	923	761	1.13	69.22%	0.9557
524	65%	90%	120	0.35	0.76	0.10	0.04	0.10	0.03	0.18	0.72	0.10	0.00	923	735	1.13	68.37%	0.9227
525	65%	110%	120	0.29	0.76	0.10	0.04	0.10	0.03	0.18	0.72	0.10	0.00	923	705	1.12	67.33%	0.8612
526	65%	130%	120	0.24	0.76	0.10	0.04	0.10	0.03	0.18	0.72	0.10	0.00	923	662	1.1	65.37%	0.7607
527	75%	75%	160	0.13	0.62	0.11	0.17	0.10	0.03	0.18	0.72	0.10	0.00	923	773	1.1	-	-
528	65%	70%	150	0.56	0.76	0.10	0.04	0.10	0.03	0.18	0.72	0.10	0.00	923	744	1.13	66.12%	0.9286
529	65%	90%	150	0.44	0.76	0.10	0.04	0.10	0.03	0.18	0.72	0.10	0.00	923	719	1.06	65.84%	0.8922
530	65%	110%	150	0.36	0.76	0.10	0.04	0.10	0.03	0.18	0.72	0.10	0.00	923	685	1.03	64.10%	0.8592
531	30%	70%	120	0.45	0.76	0.10	0.04	0.10	0.06	0.18	0.72	0.10	0.00	923	815	1.09	29.79%	0.9638
532	30%	90%	120	0.35	0.76	0.10	0.04	0.10	0.06	0.18	0.72	0.10	0.00	923	793	1.07	29.51%	0.9212
533	30%	110%	120	0.29	0.76	0.10	0.04	0.10	0.06	0.18	0.72	0.10	0.00	923	757	1.04	28.69%	0.8694
534	30%	130%	120	0.24	0.76	0.10	0.04	0.10	0.06	0.18	0.72	0.10	0.00	923	713	0.98	26.67%	0.7634
535	75%	75%	160	0.13	0.62	0.11	0.17	0.10	0.03	0.18	0.72	0.10	0.00	923	776	1.1	-	-
536	30%	70%	150	0.56	0.76	0.10	0.04	0.10	0.07	0.18	0.72	0.10	0.00	923	790	1.09	29.91%	0.9525
537	30%	90%	150	0.44	0.76	0.10	0.04	0.10	0.07	0.18	0.72	0.10	0.00	923	768	1.06	29.84%	0.9146
538	30%	110%	150	0.36	0.76	0.10	0.04	0.10	0.07	0.18	0.72	0.10	0.00	923	734	1.04	28.54%	0.8691
539	30%	130%	150	0.30	0.76	0.10	0.04	0.10	0.07	0.18	0.72	0.10	0.00	923	691	1	27.05%	0.7644
540	75%	75%	160	0.13	0.62	0.11	0.17	0.10	0.03	0.18	0.72	0.10	0.00	923	771	1.15	-	-
541	30%	70%	120	0.45	0.76	0.10	0.04	0.10	0.06	0.18	0.72	0.10	0.00	923	814	1.1	29.82%	0.9577
542	30%	90%	120	0.35	0.76	0.10	0.04	0.10	0.06	0.18	0.72	0.10	0.00	923	792	1.1	29.84%	0.9294
543	30%	110%	120	0.29	0.76	0.10	0.04	0.10	0.06	0.18	0.72	0.10	0.00	923	757	1.05	29.03%	0.8714
544	30%	130%	120	0.24	0.76	0.10	0.04	0.10	0.06	0.18	0.72	0.10	0.00	923	713	1.02	27.60%	0.7627
545	75%	75%	160	0.13	0.62	0.11	0.17	0.10	0.03	0.18	0.72	0.10	0.00	923	773	1.15	-	-
546	30%	70%	120	0.23	0.72	0.10	0.08	0.10	0.06	0.18	0.72	0.10	0.00	923	840	1.2	30.31%	0.9914
547	30%	90%	120	0.18	0.72	0.10	0.08	0.10	0.06	0.18	0.72	0.10	0.00	923	817	1.2	30.25%	0.9716
548	30%	110%	120	0.14	0.72	0.10	0.08	0.10	0.06	0.18	0.72	0.10	0.00	923	758	1.1	29.02%	0.8962
549	75%	75%	160	0.13	0.62	0.11	0.17	0.10	0.03	0.18	0.72	0.10	0.00	923	769	1.3	-	-

ID	Target performance			Total	Cathode molar fraction				Total	Anode molar fraction				Inlet T	Experimental Results			
	U_{H_2}	U_{CO_2}	J	cathode flow	N_2	O_2	CO_2	H_2O	anode flow	CO_2	H_2	H_2O	N_2		Voltage	R_Ω	U_{CO_2}	$t_{CO_3^{2-}}$
	%	%	$mA\,cm^{-2}$	$Nm^3\,h^{-1}$	–				$Nm^3\,h^{-1}$	–				K	mV	$m\Omega$	%	–
550	65%	70%	120	0.23	0.72	0.10	0.08	0.10	0.03	0.18	0.72	0.10	0.00	923	789	1.25	65.98%	0.9777
551	65%	90%	120	0.18	0.72	0.10	0.08	0.10	0.03	0.18	0.72	0.10	0.00	923	761	1.2	66.67%	0.9605
552	65%	110%	120	0.14	0.72	0.10	0.08	0.10	0.03	0.18	0.72	0.10	0.00	923	699	1.13	64.91%	0.8937
553	75%	75%	160	0.13	0.62	0.11	0.17	0.10	0.03	0.18	0.72	0.10	0.00	923	771	1.24	-	-
554	30%	70%	120	0.10	0.62	0.10	0.18	0.10	0.06	0.18	0.72	0.10	0.00	923	862	1.25	30.91%	1.0084
555	30%	90%	120	0.08	0.62	0.10	0.18	0.10	0.06	0.18	0.72	0.10	0.00	923	829	1.25	30.54%	0.9900
556	30%	110%	120	0.07	0.62	0.10	0.18	0.10	0.06	0.18	0.72	0.10	0.00	923	784	1.2	30.42%	0.9722
557	75%	75%	160	0.13	0.62	0.11	0.17	0.10	0.03	0.18	0.72	0.10	0.00	923	769	1.19	-	-
558	65%	70%	120	0.10	0.62	0.10	0.18	0.10	0.03	0.18	0.72	0.10	0.00	923	808	1.19	66.54%	1.0098
559	65%	90%	120	0.08	0.62	0.10	0.18	0.10	0.03	0.18	0.72	0.10	0.00	923	772	1.19	67.17%	0.9936
560	65%	100%	120	0.07	0.62	0.10	0.18	0.10	0.03	0.18	0.72	0.10	0.00	923	719	1.14	66.09%	0.9739
561	75%	75%	160	0.13	0.62	0.11	0.17	0.10	0.03	0.18	0.72	0.10	0.00	923	768	1.15	-	-
562	65%	75%	140	0.25	0.74	0.08	0.08	0.10	0.03	0.18	0.72	0.10	0.00	923	757	1.1	65.48%	0.9752
563	75%	75%	140	0.25	0.74	0.08	0.08	0.10	0.03	0.18	0.72	0.10	0.00	923	740	1.1	76.32%	0.9803
564	90%	75%	140	0.25	0.74	0.08	0.08	0.10	0.02	0.18	0.72	0.10	0.00	923	702	1.2	93.57%	0.9745
565	75%	75%	160	0.13	0.62	0.11	0.17	0.10	0.03	0.18	0.72	0.10	0.00	923	765	1.15	-	-
566	65%	90%	120	0.31	0.74	0.11	0.05	0.10	0.03	0.18	0.72	0.10	0.00	923	745	1	65.62%	0.9379
567	75%	90%	120	0.31	0.74	0.11	0.05	0.10	0.02	0.18	0.72	0.10	0.00	923	726	1	77.19%	0.9232
568	90%	90%	120	0.31	0.74	0.11	0.05	0.10	0.02	0.18	0.72	0.10	0.00	923	694	1.05	92.93%	0.9231
568	65%	75%	140	0.25	0.74	0.08	0.08	0.10	0.02	0.15	0.61	0.08	0.15	923	762	1.18	64.06%	0.9829
569	75%	75%	140	0.25	0.74	0.08	0.08	0.10	0.02	0.15	0.61	0.08	0.15	923	734	1.18	80.15%	0.9851
570	90%	75%	140	0.25	0.74	0.08	0.08	0.10	0.01	0.15	0.61	0.08	0.15	923	690	1.18	96.16%	0.9779
571	30%	90%	120	0.36	0.76	0.10	0.04	0.10	0.06	0.18	0.72	0.10	0.00	923	757	1.224	85.60%	0.9402
572	30%	110%	120	0.29	0.76	0.10	0.04	0.10	0.06	0.18	0.72	0.10	0.00	923	730	1.142	94.79%	0.8604
573	30%	130%	120	0.24	0.76	0.10	0.04	0.10	0.06	0.18	0.72	0.10	0.00	923	702	1.063	98.59%	0.7416
574	30%	90%	150	0.45	0.76	0.10	0.04	0.10	0.08	0.18	0.72	0.10	0.00	923	736	1.186	83.55%	0.9210
575	30%	70%	150	0.37	0.76	0.10	0.04	0.10	0.08	0.18	0.72	0.10	0.00	923	703	1.115	94.46%	0.8479
576	30%	90%	150	0.31	0.76	0.10	0.04	0.10	0.08	0.18	0.72	0.10	0.00	923	681	1.071	98.42%	0.7493
577	65%	70%	140	0.27	0.74	0.08	0.08	0.10	0.03	0.18	0.72	0.10	0.00	923	759	1.284	66.83%	0.9472
578	65%	90%	140	0.21	0.74	0.08	0.08	0.10	0.03	0.18	0.72	0.10	0.00	923	732	1.225	85.49%	0.9435
579	65%	70%	150	0.50	0.75	0.11	0.05	0.10	0.03	0.18	0.72	0.10	0.00	923	710	1.183	73.98%	1.0296
580	65%	90%	150	0.40	0.74	0.11	0.05	0.10	0.03	0.18	0.72	0.10	0.00	923	687	1.138	86.31%	0.9565
581	65%	110%	150	0.32	0.74	0.11	0.05	0.10	0.03	0.18	0.72	0.10	0.00	923	650	1.142	95.41%	0.8661

Experimental data collected using cathode CC having 90% open area with a cell working in co-flow configuration.

ID	Target performance			Total	Cathode molar fraction				Total	Anode molar fraction				Inlet T	Experimental Results			
	U_{H_2}	U_{CO_2}	J	cathode flow	N_2	O_2	CO_2	H_2O	anode flow	CO_2	H_2	H_2O	N_2		Voltage	R_Ω	U_{CO_2}	$t_{CO_3^{2-}}$
	%	%	$mA\,cm^{-2}$	$Nm^3\,h^{-1}$	–				$Nm^3\,h^{-1}$	–				K	mV	$m\Omega$	%	–
582	75%	75%	160	0.13	0.62	0.11	0.17	0.10	0.03	0.18	0.72	0.10	0.00	923	790	1.26	74.70%	0.9970
583	30%	70%	120	0.45	0.76	0.10	0.04	0.10	0.06	0.18	0.72	0.10	0.00	923	817	1.25	67.16%	0.9579
584	30%	90%	120	0.35	0.76	0.10	0.04	0.10	0.06	0.18	0.72	0.10	0.00	923	800	1.24	84.49%	0.9369
585	30%	110%	120	0.29	0.76	0.10	0.04	0.10	0.06	0.18	0.72	0.10	0.00	923	775	1.2	96.66%	0.8774
586	30%	130%	120	0.24	0.76	0.10	0.04	0.10	0.06	0.18	0.72	0.10	0.00	923	737	1.13	99.77%	0.7673
587	75%	75%	160	0.13	0.62	0.11	0.17	0.10	0.03	0.18	0.72	0.10	0.00	923	789	1.26	-	-
588	30%	70%	150	0.56	0.76	0.10	0.04	0.10	0.07	0.18	0.72	0.10	0.00	923	789	1.21	67.73%	0.9667
589	30%	90%	150	0.44	0.76	0.10	0.04	0.10	0.07	0.18	0.72	0.10	0.00	923	770	1.21	83.31%	0.9268
590	30%	110%	150	0.36	0.76	0.10	0.04	0.10	0.07	0.18	0.72	0.10	0.00	923	740	1.17	95.86%	0.8709
591	30%	130%	150	0.30	0.76	0.10	0.04	0.10	0.07	0.18	0.72	0.10	0.00	923	704	1.12	99.61%	0.7660
592	75%	75%	160	0.13	0.62	0.11	0.17	0.10	0.03	0.18	0.72	0.10	0.00	923	793	1.16	-	-
593	65%	70%	120	0.45	0.76	0.10	0.04	0.10	0.03	0.18	0.72	0.10	0.00	923	768	1.14	67.35%	0.9607
594	65%	90%	120	0.35	0.76	0.10	0.04	0.10	0.03	0.18	0.72	0.10	0.00	923	755	1.14	83.29%	0.9236
595	65%	110%	120	0.29	0.76	0.10	0.04	0.10	0.03	0.18	0.72	0.10	0.00	923	733	1.1	95.83%	0.8698
596	65%	130%	120	0.24	0.76	0.10	0.04	0.10	0.03	0.18	0.72	0.10	0.00	923	704	1.09	99.43%	0.7647
597	75%	75%	160	0.13	0.62	0.11	0.17	0.10	0.03	0.18	0.72	0.10	0.00	923	792	1.16	-	-
598	65%	70%	150	0.56	0.76	0.10	0.04	0.10	0.03	0.18	0.72	0.10	0.00	923	741	1.14	66.86%	0.9543
599	65%	90%	150	0.44	0.76	0.10	0.04	0.10	0.03	0.18	0.72	0.10	0.00	923	725	1.14	82.23%	0.9147
600	65%	110%	150	0.36	0.76	0.10	0.04	0.10	0.03	0.18	0.72	0.10	0.00	923	702	1.12	94.90%	0.8622
601	65%	130%	150	0.30	0.76	0.10	0.04	0.10	0.03	0.18	0.72	0.10	0.00	923	673	1.06	99.22%	0.7631
602	75%	75%	160	0.13	0.62	0.11	0.17	0.10	0.03	0.18	0.72	0.10	0.00	923	785	1.17	-	-
603	75%	75%	160	0.13	0.62	0.11	0.17	0.10	0.03	0.18	0.72	0.10	0.00	898	774	1.37	-	-
604	30%	70%	120	0.45	0.76	0.10	0.04	0.10	0.06	0.18	0.72	0.10	0.00	898	808	1.4	67.49%	0.9626
605	30%	90%	120	0.35	0.76	0.10	0.04	0.10	0.06	0.18	0.72	0.10	0.00	898	791	1.39	84.15%	0.9331
606	30%	110%	120	0.29	0.76	0.10	0.04	0.10	0.06	0.18	0.72	0.10	0.00	898	761	1.34	96.85%	0.8791
607	30%	130%	120	0.24	0.76	0.10	0.04	0.10	0.06	0.18	0.72	0.10	0.00	898	719	1.25	99.80%	0.7675
608	75%	75%	160	0.13	0.62	0.11	0.17	0.10	0.03	0.18	0.72	0.10	0.00	873	750	1.64	-	-
609	30%	70%	120	0.45	0.76	0.10	0.04	0.10	0.06	0.18	0.72	0.10	0.00	873	798	1.65	67.10%	0.9571
610	30%	90%	120	0.35	0.76	0.10	0.04	0.10	0.06	0.18	0.72	0.10	0.00	873	779	1.64	84.75%	0.9398
611	30%	110%	120	0.29	0.76	0.10	0.04	0.10	0.06	0.18	0.72	0.10	0.00	873	744	1.6	97.45%	0.8845
612	30%	130%	120	0.24	0.76	0.10	0.04	0.10	0.06	0.18	0.72	0.10	0.00	873	700	1.5	99.90%	0.7683
613	65%	70%	120	0.45	0.76	0.10	0.04	0.10	0.03	0.18	0.72	0.10	0.00	873	756	1.63	67.50%	0.9628
614	65%	90%	120	0.35	0.76	0.10	0.04	0.10	0.03	0.18	0.72	0.10	0.00	873	737	1.6	84.54%	0.9374
615	65%	110%	120	0.29	0.76	0.10	0.04	0.10	0.03	0.18	0.72	0.10	0.00	873	711	1.59	96.68%	0.8776
616	75%	75%	160	0.13	0.62	0.11	0.17	0.10	0.03	0.18	0.72	0.10	0.00	873	749	1.54	-	-
617	65%	70%	140	0.27	0.74	0.08	0.08	0.10	0.03	0.18	0.72	0.10	0.00	873	749	1.59	69.12%	0.9881
618	65%	90%	140	0.21	0.74	0.08	0.08	0.10	0.03	0.18	0.72	0.10	0.00	873	732	1.56	87.15%	0.9687
619	65%	110%	140	0.17	0.74	0.08	0.08	0.10	0.03	0.18	0.72	0.10	0.00	873	694	1.49	99.37%	0.9026

ID	Target performance			Total	Cathode molar fraction				Total	Anode molar fraction				Inlet T	Experimental Results			
	U_{H_2}	U_{CO_2}	J	cathode flow	N_2	O_2	CO_2	H_2O	anode flow	CO_2	H_2	H_2O	N_2		Voltage	R_Ω	U_{CO_2}	$t_{CO_3^{2-}}$
	%	%	$mA\,cm^{-2}$	$N m^3\,h^{-1}$	–				$N m^3\,h^{-1}$	–				K	mV	$m\Omega$	%	–
620	75%	75%	160	0.13	0.62	0.11	0.17	0.10	0.03	0.18	0.72	0.10	0.00	848	684	2	-	-
621	30%	70%	120	0.45	0.76	0.10	0.04	0.10	0.06	0.18	0.72	0.10	0.00	848	774	1.93	68.51%	0.9773
622	30%	90%	120	0.35	0.76	0.10	0.04	0.10	0.06	0.18	0.72	0.10	0.00	848	756	1.91	85.33%	0.9462
623	30%	110%	120	0.29	0.76	0.10	0.04	0.10	0.06	0.18	0.72	0.10	0.00	848	717	1.9	97.67%	0.8865
624	75%	75%	160	0.13	0.62	0.11	0.17	0.10	0.03	0.18	0.72	0.10	0.00	923	787	1.2	-	-
625	30%	70%	120	0.45	0.76	0.10	0.04	0.10	0.06	0.18	0.72	0.10	0.00	923	818	1.18	67.26%	0.9593
626	30%	90%	120	0.35	0.76	0.10	0.04	0.10	0.06	0.18	0.72	0.10	0.00	923	802	1.18	84.12%	0.9328
627	30%	110%	120	0.29	0.76	0.10	0.04	0.10	0.06	0.18	0.72	0.10	0.00	923	776	1.16	96.59%	0.8768
628	30%	130%	120	0.24	0.76	0.10	0.04	0.10	0.06	0.18	0.72	0.10	0.00	923	735	1.1	99.69%	0.7667
629	75%	75%	160	0.13	0.62	0.11	0.17	0.10	0.03	0.18	0.72	0.10	0.00	948	793	1.03	-	-
630	30%	70%	120	0.45	0.76	0.10	0.04	0.10	0.06	0.18	0.72	0.10	0.00	948	819	1.01	66.68%	0.9511
631	30%	90%	120	0.35	0.76	0.10	0.04	0.10	0.06	0.18	0.72	0.10	0.00	948	805	1.02	83.46%	0.9255
632	30%	110%	120	0.29	0.76	0.10	0.04	0.10	0.06	0.18	0.72	0.10	0.00	948	782	1.01	95.85%	0.8700
633	30%	130%	120	0.24	0.76	0.10	0.04	0.10	0.06	0.18	0.72	0.10	0.00	948	748	0.96	99.51%	0.7653
634	75%	75%	160	0.13	0.62	0.11	0.17	0.10	0.03	0.18	0.72	0.10	0.00	923	782	1.22	-	-
635	65%	90%	120	0.35	0.76	0.10	0.04	0.10	0.03	0.18	0.72	0.10	0.00	923	751	1.19	83.13%	0.9219
636	75%	90%	120	0.35	0.76	0.10	0.04	0.10	0.02	0.18	0.72	0.10	0.00	923	735	1.2	82.55%	0.9154
637	85%	90%	120	0.35	0.76	0.10	0.04	0.10	0.02	0.18	0.72	0.10	0.00	923	713	1.18	82.55%	0.9154
638	95%	90%	120	0.35	0.76	0.10	0.04	0.10	0.02	0.18	0.72	0.10	0.00	923	675	1.16	80.06%	0.8878
639	0%	0%	0	0.23	0.62	0.10	0.18	0.10	0.22	0.18	0.72	0.10	0.00	923	1058		2.05%	1.0000
640	0%	0%	0	0.22	0.79	0.10	0.01	0.10	0.22	0.18	0.72	0.10	0.00	923	934		-30.54%	1.0000
641	0%	0%	0	0.22	0.79	0.10	0.01	0.10	0.18	0.01	0.89	0.10	0.00	923	1092		19.63%	1.0000
642	0%	0%	0	0.22	0.79	0.10	0.01	0.10	0.18	0.01	0.89	0.10	0.00	923	1098		50.09%	1.0000
643	0%	0%	0	0.22	0.79	0.10	0.01	0.10	0.22	0.18	0.72	0.10	0.00	923	933		-14.78%	1.0000
644	0%	0%	0	0.22	0.79	0.10	0.01	0.10	0.22	0.18	0.72	0.10	0.00	923	934		-22.60%	1.0000
645	0%	0%	0	0.23	0.72	0.10	0.18	0.00	0.22	0.18	0.72	0.10	0.00	923	1085		1.84%	1.0000
646	0%	0%	0	0.23	0.89	0.10	0.01	0.00	0.22	0.18	0.72	0.10	0.00	923	943		18.81%	1.0000
647	0%	0%	0	0.23	0.89	0.10	0.01	0.00	0.18	0.01	0.89	0.10	0.00	923	1261		77.35%	1.0000
648	30%	90%	120	0.70	0.78	0.10	0.02	0.10	0.06	0.18	0.72	0.10	0.00	923	754	1.19	77.39%	1.0000
649	30%	110%	120	0.58	0.78	0.10	0.02	0.10	0.06	0.18	0.72	0.10	0.00	923	736	1.13	89.83%	1.0000
650	30%	130%	120	0.49	0.78	0.10	0.02	0.10	0.06	0.18	0.72	0.10	0.00	923	716	1.08	96.97%	1.0000
651	30%	90%	150	0.45	0.76	0.10	0.04	0.10	0.08	0.18	0.72	0.10	0.00	923	747	1.503	84.46%	0.9283
652	30%	110%	150	0.37	0.76	0.10	0.04	0.10	0.08	0.18	0.72	0.10	0.00	923	726	1.4	94.54%	0.8619
653	30%	130%	150	0.30	0.76	0.10	0.04	0.10	0.08	0.18	0.72	0.10	0.00	923	706	1.388	98.78%	0.7396
654	65%	70%	140	0.27	0.74	0.08	0.08	0.10	0.03	0.18	0.72	0.10	0.00	923	780	1.505	68.34%	0.9471
655	65%	90%	140	0.21	0.74	0.08	0.08	0.10	0.03	0.18	0.72	0.10	0.00	923	764	1.518	86.75%	0.9414
656	65%	70%	150	0.50	0.75	0.11	0.05	0.10	0.03	0.18	0.72	0.10	0.00	923	749	1.414	72.12%	1.0217
657	65%	90%	150	0.40	0.74	0.11	0.05	0.10	0.03	0.18	0.72	0.10	0.00	923	735	1.481	84.98%	0.9385

ID	Target performance			Total	Cathode molar fraction				Total	Anode molar fraction				Inlet T	Experimental Results			
	U_{H_2}	U_{CO_2}	J	cathode flow	N_2	O_2	CO_2	H_2O	anode flow	CO_2	H_2	H_2O	N_2		Voltage	R_Ω	U_{CO_2}	$t_{CO_3^{2-}}$
	%	%	$mA\,cm^{-2}$	$Nm^3\,h^{-1}$	–				$Nm^3\,h^{-1}$	–				K	mV	$m\Omega$	%	–
658	65%	110%	150	0.32	0.74	0.11	0.05	0.10	0.03	0.18	0.72	0.10	0.00	923	711	1.437	95.72%	0.8641
659	30%	90%	150	0.45	0.76	0.10	0.04	0.10	0.08	0.18	0.72	0.10	0.00	923	759	1.506	86.73%	0.9593
660	30%	110%	150	0.37	0.76	0.10	0.04	0.10	0.08	0.18	0.72	0.10	0.00	923	729	1.29	95.78%	0.8636
661	30%	130%	150	0.31	0.76	0.10	0.04	0.10	0.08	0.18	0.72	0.10	0.00	923	706	1.371	98.97%	0.7556

Experimental data collected using cathode CC having 90% open area with a cell working in counter-flow configuration.

Bibliography

[1] C.Y. Yuh and J.R. Selman. Polarization of the Molten Carbonate Fuel Cell Anode and Cathode. *Journal of The Electrochemical Society*, 131(9):2062, 1984. doi: 10.1149/1.2116020.

[2] S.G. Hong and J.R. Selman. A Stochastic Structure Model for Liquid-Electrolyte Fuel CellElectrodes, with Special Application to MCFCs: I. Electrode Structure Generation and Characterization. *Journal of The Electrochemical Society*, 151(5):A739, 2004. doi: 10.1149/1.1695381.

[3] E. Arato, E. Audasso, L. Barelli, B. Bosio, and G. Discepoli. Kinetic modelling of molten carbonate fuel cells: Effects of cathode water and electrode materials. *Journal of Power Sources*, 330:18 – 27, 2016. doi: 10.1016/j.jpowsour.2016.08.123.

[4] E. Audasso, B. Bosio, and S. Nam. Extension of an effective MCFC kinetic model to a wider range of operating conditions. *International Journal of Hydrogen Energy*, 41(12):5571 – 5581, 2016. doi: 10.1016/j.ijhydene.2015.10.152.

[5] F.R. Bianchi, B. Bosio, A. Baldinelli, and L. Barelli. Optimization of a Reference Kinetic Model for Solid Oxide Fuel Cells. *Catalysts*, 10:104, 2020. doi: 10.3390/catal10010104.

[6] NETL. Seventh Edition Fuel Cell Handbook. Technical report, National Energy Technology Laboratory, Pittsburgh, PA, and Morgantown, WV (US), 2004.

[7] P. Breeze. Chapter 1 - An Introduction to Fuel Cells. In P. Breeze, editor, *Fuel Cells*, pages 1 – 10. Academic Press, 2017. ISBN 978-0-08-101039-6. doi: 10.1016/B978-0-08-101039-6.00001-7.

[8] C.G. Lee. Overpotential Behavior of Carbon Monoxide Fuel in a Molten Carbonate Fuel Cell. *Fuel Cells*, 12(4):550–556, 2012. doi: 10.1002/fuce.201100149.

[9] N. Di Giulio, B. Bosio, V. Cigolotti, and S.W. Nam. Experimental and theoretical analysis of H_2S effects on MCFCs. *International Journal of Hydrogen Energy*, 37(24):19329 – 19336, 2012. doi: 10.1016/j.ijhydene.2012.03.086.

[10] I. Rexed, C. Lagergren, and G. Lindbergh. Effect of sulfur contaminants on MCFC performance. *International Journal of Hydrogen Energy*, 39(23):12242 – 12250, 2014. doi: 10.1016/j.ijhydene.2014.03.068.

[11] K. Hemmes and J. R. Selman. *O_2-reduction at high temperature: MCFC*. John Wiley and Sons, Ltd, 2010. ISBN 9780470974001. doi: 10.1002/9780470974001.f205044.

[12] Lu S.H. and J. R. Selman. Electrode kinetics of oxygen reduction on gold in molten carbonate. *Journal of Electroanalytical Chemistry*, 333(1):257 – 271, 1992. doi: 10.1016/0022-0728(92)80395-K. An international journal devoted to all aspects of electrode kinetics, interfacial structure, properties of electrolytes, colloid and biological electrochemistry.

[13] L. Chen, X. Cheng, C. Lin, and C. Huang. In-situ Raman spectroscopic studies on the oxide species in molten Li/K_2CO_3. *Electrochimica Acta*, 47(9):1475 – 1480, 2002. doi: 10.1016/S0013-4686(01)00872-6.

[14] L.L. Zhang, X.Y. Huang, C.Y. Qin, Kyle Brinkman, Y.H. Gong, S.W. Wanga, and K. Huang. First spectroscopic identification of pyrocarbonate for high CO_2 flux membranes containing highly interconnected three dimensional ionic channels. *Physical Chemistry Chemical Physics*, 15:13147–13152, 2013. doi: 10.1039/C3CP52362D.

[15] L.J. Chen, C.J. Lin, J. Zuo, L.C. Song, and C.H. Huang. First Spectroscopic Observation of Peroxocarbonate/ Peroxodicarbonate in Molten Carbonate. *The Journal of Physical Chemistry B*, 108 (23):7553–7556, jun 2004. ISSN 1520-6106. doi: 10.1021/jp035749l. URL 10.1021/jp035749l.

[16] M. Cassir, B. Malinowska, W. Peelen, K. Hemmes, and J.H.W. de Wit. Identification and electrochemical characterization of in situ produced and added reduced oxygen species in molten Li_2CO_3 + K_2CO_3. *Journal of Electroanalytical Chemistry*, 433(1):195 – 205, 1997. doi: 10.1016/S0022-0728(97)00292-1.

[17] R.W. Reeve and A.C.C. Tseung. Factors affecting the dissolution and reduction of oxygen in molten carbonate electrolytes. part 1: Effect of temperature and alkali carbonate mixture. *Journal of Electroanalytical Chemistry*, 403(1):69 – 83, 1996. doi: 10.1016/0022-0728(95)04190-7.

[18] N. Di Giulio, E. Audasso, B. Bosio, J. Han, and S.J. McPhail. Experimental influence of operating variables on the performances of MCFCs under SO_2 poisoning. *International Journal of Hydrogen Energy*, 40(19):6430 – 6439, 2015. doi: 10.1016/j.ijhydene.2015.03.041.

[19] N. Di Giulio, B. Bosio, J. Han, and S.J. McPhail. Experimental analysis of SO_2 effects on Molten Carbonate Fuel Cells. *International Journal of Hydrogen Energy*, 39(23):12300 – 12308, 2014. doi: 10.1016/j.ijhydene.2014.04.120.

[20] M. Kawase, Y. Mugikura, T. Watanabe, Y. Hiraga, and T. Ujihara. Effects of NH_3 and NO_X on the performance of MCFCs. *Journal of Power Sources*, 104(2):265 – 271, 2002. ISSN 0378-7753. doi: 10.1016/S0378-7753(01)00949-1.

[21] S. McPhail, L. Leto, M. Della Pietra, V. Cigolotti, and A. Moreno. International Status of Molten Carbonate Fuel Cells Technology - 2015. Technical report, ENEA, 2015. URL https://www.enea.it/en/publications/abstract/Molten-Carbonate-Fuel-Cells-2015.

[22] A. Moreno, S. McPhail., and R. Bove. International Status of Molten Carbonate Fuel Cell (MCFC) Technology - 2008. Technical report, ENEA, 2008. URL https://www.energyagency.at/fileadmin/dam/pdf/projekte/gebaeude/afc-molten-carbonate.pdf.

[23] R. Ortiz Cebolla, J. Davies, and E. Weidner. Global deployment of large capacity stationary fuel cells. Technical report, European Commission, 2019.

[24] E4tech. The Fuel Cell Industry Review 2019. Technical report, E4tech, 2019. URL www.FuelCellIndustryReview.com.

[25] T. Tronstad, H. Høgmoen Åstrand, G. Petra Haugom, and L. Langfeldt. Study on the use of fuel cells in shipping. Technical report, EMSA, European Maritime Safety Agency, 2017. URL http://www.emsa.europa.eu/emsa-homepage/2-news-a-press-centre/news/2921-emsa-study-on-the-use-of-fuel-cells-in-shipping.html.

[26] J. Han, J.F. Charpentier, and T. Tang. State of the art of fuel cells for ship applications. Technical report, 2012.

[27] FCE and ExxonMobil expand agreement for carbon capture tech. *Fuel Cells Bulletin*, 2019(12):7, 2019. ISSN 1464-2859. doi: 10.1016/S1464-2859(19)30511-5.

[28] L. Hu, G. Lindbergh, and C. Lagergren. Operating the nickel electrode with hydrogen-lean gases in the molten carbonate electrolysis cell (MCEC). *International Journal of Hydrogen Energy*, 41 (41):18692 – 18698, 2016. doi: 10.1016/j.ijhydene.2016.06.037.

[29] J.P. Perez-Trujillo, F. Elizalde-Blancas, M. Della Pietra, and S. McPhail. A numerical and experimental comparison of a single reversible molten carbonate cell operating in fuel cell mode and electrolysis mode. *Applied Energy*, 226:1037 – 1055, 2018. doi: 10.1016/j.apenergy.2018.05.121.

[30] H. Meskine, V. Albin, M. Cassir, A. Ringuedé, and V. Lair. Electrochemical investigations on CO_2 reduction mechanism in molten carbonates in view of H_2O/CO_2 co-electrolysis. *International Journal of Hydrogen Energy*, 2020. doi: 10.1016/j.ijhydene.2020.07.008.

[31] L. Barelli, G. Bidini, G. Cinti, and J. Milewski. High temperature electrolysis using Molten Carbonate Electrolyzer. *International Journal of Hydrogen Energy*, 2020. doi: doi.org/10.1016/j.ijhydene.2020.07.220.

[32] L.G. Austin, M. Ariet, R.D. Walker, G.B. Wood, and R.H. Comyn. Simple-Pore and Thin-Film Models of Porous Gas Diffusion Electrodes. *Industrial & Engineering Chemistry Fundamentals*, 4(3):321–327, aug 1965. doi: 10.1021/i160015a015.

[33] G. Wilemski. Simple Porous Electrode Models for Molten Carbonate Fuel Cells. *Journal of The Electrochemical Society*, 130(1):117, 1983. doi: 10.1149/1.2119635.

[34] S. Srinivasan and H.D. Hurwitz. Theory of a thin film model of porous gas-diffusion electrodes. *Electrochimica Acta*, 12(5):495 – 512, 1967. doi: 10.1016/0013-4686(67)80019-7.

[35] T. L. Wolf and G. Wilemski. Molten Carbonate Fuel Cell Performance Model. *Journal of The Electrochemical Society*, 130(1):48, 1983. doi: 10.1149/1.2119681.

[36] J.R. Selman C.Y. Yuh. The Polarization of Molten Carbonate Fuel Cell Electrodes. *Journal of The Electrochemical Society*, 138(12):3649, 1991. doi: 10.1149/1.2085474.

[37] H.R. Kunz, L.J. Bregoli, and S.T. Szymanski. A Homogeneous/Agglomerate Model for Molten Carbonate Fuel Cell Cathodes. *Journal of The Electrochemical Society*, 131(12):2815, 1984. doi: 10.1149/1.2115415.

[38] H. R. Kunz and L.A. Murphy. The Effect of Oxidant Composition on the Performance of Molten Carbonate Fuel Cells. *Journal of The Electrochemical Society*, 135(5):1124, 1988. doi: 10.1149/1.2095891.

[39] E. Fontes, C. Lagergren, and D. Simonsson. Mathematical modelling of the MCFC cathode. *Electrochimica Acta*, 38(18):2669 – 2682, 1993. doi: 10.1016/0013-4686(93)85085-D.

[40] N. Subramanian, B. S. Haran, R. E. White, and B. N. Popov. Full Cell Mathematical Model of a MCFC. *Journal of The Electrochemical Society*, 150(10):A1360, 2003. doi: 10.1149/1.1604786.

[41] V. Sampath, A.F. Sammells, and J.R. Selman. A Performance and Current Distribution Model for Scaled-Up Molten Carbonate Fuel Cells. *Journal of The Electrochemical Society*, 127(1):79, 1980. doi: 10.1149/1.2129643.

[42] Y. Mugikura, T. Abe, T. Watanabe, and Y. Izaki. Analysis of Performance of Molten Carbonate Fuel Cell II. Development of a Performance Correlation Equation, 溶融炭酸塩型燃料電池の性能評価II。性能相関式の開発. *Denki Kagaku oyobi Kogyo Butsuri Kagaku*, 60(2):124–130, 1992. doi: 10.5796/electrochemistry.60.124.

[43] Y. Mugikura, K. Shimazu, T. Watanabe, Y. Izaki, T. Abe, H. Urushibata, H. Maeda, K. Sato, and T. Murahashi. Analysis of Performance of Molten Carbonate Fuel Cell I. Pressurized Test of Single Cell, 溶融炭酸塩型燃料電池の性能評価I. 小型単セルによる加圧性能の分析. *Denki Kagaku oyobi Kogyo Butsuri Kagaku*, 60(2):117–123, 1992. doi: 10.5796/electrochemistry.60.117.

[44] H. Morita, Y. Mugikura, Y. Izaki, T. Watanabe, and T. Abe. Analysis of Performance of Molten Carbonate Fuel Cell IV. Performance Formulation Based on Cathode Reaction Mechanisms,溶融炭酸塩型燃料電池の性能評価IV. カソード反応論に基づく性能表示式の高精度化. *Denki Kagaku oyobi Kogyo Butsuri Kagaku*, 63(11):1053–1060, 1995. doi: 10.5796/kogyobutsurikagaku.63.1053.

[45] H. Morita, Y. Mugikura, Y. Izaki, T. Watanabe, and T. Abe. Analysis of Performance of Molten Carbonate Fuel Cell V. Formulation of Anode Reaction Resistance, 溶融炭酸塩型燃料電池の性能評価V. アノード反応抵抗表示式の導出. *Denki Kagaku oyobi Kogyo Butsuri Kagaku*, 65 (9):740–746, 1997. doi: 10.5796/kogyobutsurikagaku.65.740.

[46] H. Morita, M. Komoda, Y. Mugikura, Y. Izaki, T. Watanabe, Y. Masuda, and T. Matsuyama. Performance analysis of molten carbonate fuel cell using a Li/Na electrolyte. *Journal of Power Sources*, 112(2):509 – 518, 2002. doi: 10.1016/S0378-7753(02)00468-8.

[47] T. Nishina, S. Ohuchi, K. Yamada, and I. Uchida. Water effect on oxygen reduction in molten (Li+K)CO_3 eutectic. *Journal of Electroanalytical Chemistry*, 408(1):181 – 187, 1996. doi: 10.1016/0022-0728(96)04514-7.

[48] J. Milewski, G. Discepoli, and U. Desideri. Modeling the performance of MCFC for various fuel and oxidant compositions. *International Journal of Hydrogen Energy*, 39(22):11713 – 11721, 2014. doi: 10.1016/j.ijhydene.2014.05.151.

[49] S.F. Au, N. Woudstra, K. Hemmes, and I. Uchida. Verification of a simple numerical fuel cell model in a flowsheeting program by performance testing of a 110 cm^2 molten carbonate fuel cell. *Energy Conversion and Management*, 44(14):2297 – 2307, 2003. doi: 10.1016/S0196-8904(02)00253-4.

[50] J. Brouwer, F. Jabbari, E. Martins Leal, and T. Orr. Analysis of a molten carbonate fuel cell: Numerical modeling and experimental validation. *Journal of Power Sources*, 158(1):213 – 224, 2006. doi: 10.1016/j.jpowsour.2005.07.093.

[51] P. Heidebrecht and K. Sundmacher. Molten carbonate fuel cell (mcfc) with internal reforming: model-based analysis of cell dynamics. *Chemical Engineering Science*, 58(3):1029 – 1036, 2003. doi: 10.1016/S0009-2509(02)00644-9.

[52] W. He and Q. Chen. Three-dimensional simulation of a molten carbonate fuel cell stack using computational fluid dynamics technique. *Journal of Power Sources*, 55(1):25 – 32, 1995. doi: 10.1016/0378-7753(94)02164-X.

[53] W He and Q Chen. Three-dimensional simulation of a molten carbonate fuel cell stack under transient conditions. *Journal of Power Sources*, 73(2):182 – 192, 1998. doi: 10.1016/S0378-7753(97)02800-0.

[54] F. Yoshiba, T. Abe, and T. Watanabe. Numerical analysis of molten carbonate fuel cell stack performance: diagnosis of internal conditions using cell voltage profiles. *Journal of Power Sources*, 87(1):21 – 27, 2000. doi: 10.1016/S0378-7753(99)00352-3.

[55] S.Y. Lee, D.H. Kim, H.C. Lim, and G.Y. Chung. Mathematical modeling of a molten carbonate fuel cell (mcfc) stack. *International Journal of Hydrogen Energy*, 35(23):13096 – 13103, 2010. doi: 10.1016/j.ijhydene.2010.04.070. Asian Hydrogen Energy Conference 2009.

[56] A. Szczęśniak, J. Milewski, L. Szabłowski, W. Bujalski, and O. Dybiński. Dynamic model of a molten carbonate fuel cell 1 kW stack. *Energy*, 200:117442, 2020. doi: 10.1016/j.energy.2020.117442.

[57] F. Yang, X.J. Zhu, and G.Y. Cao. Nonlinear fuzzy modeling of a MCFC stack by an identification method. *Journal of Power Sources*, 166(2):354 – 361, 2007. doi: 10.1016/j.jpowsour.2007.01.062.

[58] C. Shen, G.Y. Cao, X.J. Zhu, and X.J. Sun. Nonlinear modeling and adaptive fuzzy control of MCFC stack. *Journal of Process Control*, 12(8):831 – 839, 2002. doi: 10.1016/S0959-1524(02)00013-6.

[59] C. Shen, G.Y. Cao, and X.J. Zhu. Nonlinear modeling of MCFC stack based on RBF neural networks identification. *Simulation Modelling Practice and Theory*, 10(1):109 – 119, 2002. doi: 10.1016/S1569-190X(02)00064-3.

[60] R. Carapellucci, R. Saia, and L. Giordano. Study of Gas-steam Combined Cycle Power Plants Integrated with MCFC for Carbon Dioxide Capture. *Energy Procedia*, 45:1155 – 1164, 2014. doi: 10.1016/j.egypro.2014.01.121. ATI 2013 - 68th Conference of the Italian Thermal Machines Engineering Association.

[61] S. Campanari, P. Chiesa, G. Manzolini, and S. Bedogni. Economic analysis of CO_2 capture from natural gas combined cycles using Molten Carbonate Fuel Cells. *Applied Energy*, 130:562 – 573, 2014. doi: 10.1016/j.apenergy.2014.04.011.

[62] S. Campanari, P. Chiesa, G. Manzolini, A. Giannotti, F. Federici, P. Bedont, and F. Parodi. Application of MCFCs for active CO_2 capture within natural gas combined cycles. *Energy Procedia*, 4:1235 – 1242, 2011. doi: 10.1016/j.egypro.2011.01.179. 10th International Conference on Greenhouse Gas Control Technologies.

[63] L. Mastropasqua, M. Spinelli, A. Paganoni, and S. Campanari. Preliminary design of a MW-class demo system for CO_2 capture with MCFC in a university campus cogeneration plant. *Energy Procedia*, 126:453 – 460, 2017. doi: 10.1016/j.egypro.2017.08.213. ATI 2017 - 72nd Conference of the Italian Thermal Machines Engineering Association.

[64] U. Desideri, S. Proietti, P. Sdringola, G. Cinti, and F. Curbis. MCFC-based CO_2 capture system for small scale CHP plants. *International Journal of Hydrogen Energy*, 37(24):19295 – 19303, 2012. doi: 10.1016/j.ijhydene.2012.05.048. 2011 International Workshop on Molten Carbonates & Related Topics.

[65] S. Campanari. Carbon dioxide separation from high temperature fuel cell power plants. *Journal of Power Sources*, 112(1):273 – 289, 2002. doi: 10.1016/S0378-7753(02)00395-6.

[66] G. Discepoli, J. Milewski, and U. Desideri. Off-design operation of coal power plant integrated with natural gas fueled molten carbonate fuel cell as CO_2 reducer. *International Journal of Hydrogen Energy*, 41(8):4773 – 4783, 2016. doi: 10.1016/j.ijhydene.2016.01.065.

[67] R. Carapellucci, D. Di Battista, and R. Cipollone. The retrofitting of a coal-fired subcritical steam power plant for carbon dioxide capture: A comparison between MCFC-based active systems and conventional MEA. *Energy Conversion and Management*, 194:124 – 139, 2019. doi: 10.1016/j.enconman.2019.04.077.

[68] V. Spallina, M. C. Romano, S. Campanari, and G. Lozza. Application of MCFC in Coal Gasification Plants for High Efficiency CO_2 Capture. *Journal of Engineering for Gas Turbines and Power*, 134(1), 10 2011. doi: 10.1115/1.4004128. 011701.

[69] L.Q. Duan, S.Y. Sun, L. Yue, W.J. Qu, and Y.P. Yang. Study on a new IGCC (Integrated Gasification Combined Cycle) system with co2 capture by integrating MCFC (Molten Carbonate Fuel Cell). *Energy*, 87:490 – 503, 2015. doi: 10.1016/j.energy.2015.05.011.

[70] L.Q. Duan, J.N. Zhu, l. Yue, and Y.P. Yang. Study on a gas-steam combined cycle system with CO_2 capture by integrating molten carbonate fuel cell. *Energy*, 74:417 – 427, 2014. doi: 10.1016/j.energy.2014.07.006.

[71] R. Hill, S. Scott, D. Butler, S.P. Sit, D. Burt, R. Narayanan, T. Cole, C. Li, V. Lightbown, and Z. J. Zhou. Application of molten carbonate fuel cell for CO_2 capture in thermal in situ oil sands facilities. *International Journal of Greenhouse Gas Control*, 41:276 – 284, 2015. doi: 10.1016/j.ijggc.2015.07.024.

[72] M. Spinelli, M.C. Romano, S. Consonni, S. Campanari, M. Marchi, and G. Cinti. Application of Molten Carbonate Fuel Cells in Cement Plants for CO_2 Capture and Clean Power Generation. *Energy Procedia*, 63:6517 – 6526, 2014. doi: 10.1016/j.egypro.2014.11.687. 12th International Conference on Greenhouse Gas Control Technologies, GHGT-12.

[73] L. Mastropasqua, L. Pierangelo, M. Spinelli, M.C. Romano, S. Campanari, and S. Consonni. Molten Carbonate Fuel Cells retrofits for CO_2 capture and enhanced energy production in the steel industry. *International Journal of Greenhouse Gas Control*, 88:195 – 208, 2019. doi: 10.1016/j.ijggc.2019.05.033.

[74] R. Chacartegui, B. Monje, D. Sánchez, J.A. Becerra, and S. Campanari. Molten carbonate fuel cell: Towards negative emissions in wastewater treatment CHP plants. *International Journal of Greenhouse Gas Control*, 19:453 – 461, 2013. ISSN 1750-5836. doi: 10.1016/j.ijggc.2013.10.007.

[75] J.D. Slater, T. Chronopoulos, R.S. Panesar, F.D. Fitzgerald, and M. Garcia. Review and techno-economic assessment of fuel cell technologies with CO_2 capture. *International Journal of Greenhouse Gas Control*, 91:102818, 2019. doi: 10.1016/j.ijggc.2019.102818.

[76] P. Greppi, B. Bosio, and E. Arato. Membranes and Molten Carbonate Fuel Cells to Capture CO_2 and Increase Energy Production in Natural Gas Power Plants. *Industrial and Engineering Chemistry Research*, 52:8755–8764, 2013. doi: 10.1021/ie302725a.

[77] M. Minutillo, A. Perna, and E. Jannelli. SOFC and MCFC system level modeling for hybrid plants performance prediction. *International Journal of Hydrogen Energy*, 39(36):21688 – 21699, 2014. doi: 10.1016/j.ijhydene.2014.09.082.

[78] B. Conti, B. Bosio, S. McPhail, F. Santoni, D. Pumiglia, and E. Arato. A 2-D model for Intermediate Temperature Solid Oxide Fuel Cells Preliminarily Validated on Local Values. *Catalysts*, 9: 36, 2019. doi: 10.3390/catal9010036.

[79] F.R. Bianchi, R. Spotorno, P. Piccardo, and B. Bosio. Solid Oxide Fuel Cell Performance Analysis through Local Modelling. *Catalysts*, 10:519, 2020. doi: 10.3390/catal10050519.

[80] A. Araoz. Aspen custom modeler overview.

[81] E. Audasso, P. Campbell, M. Della Pietra, M.C. Ferrari, B. Bosio, and E. Arato. Molten carbonate fuel cells in integrated systems for the exploitation of poor fuels and the segregation of CO_2. *Bulgarian Chemical Communications*, 50:99–107, 2018. URL https://www.scopus.com/inward/record.uri?eid=2-s2.0-85060040347{&}partnerID=40{&}md5=e6e1c26b442c8fb37c590209ac35e786.

[82] R. Cooper, D. Bove, E. Audasso, M.C. Ferrari, and B. Bosio. A feasibility assessment of a retrofit Molten Carbonate Fuel Cell coal-fired plant for flue gas CO_2 segregation. *International Journal of Hydrogen Energy*, 2020. doi: DOI.

[83] C.C. Dean, J. Blamey, N.H. Florin, M.J. Al-Jeboori, and P.S. Fennell. The calcium looping cycle for CO_2 capture from power generation, cement manufacture and hydrogen production. *Chemical Engineering Research and Design*, 89(6):836 – 855, 2011. doi: 10.1016/j.cherd.2010.10.013.

[84] A. Perejón, L.M. Romeo, Y. Lara, P. Lisbona, A. Martínez, and J.M. Valverde. The Calcium-Looping technology for CO_2 capture: On the important roles of energy integration and sorbent behavior. *Applied Energy*, 162:787 – 807, 2016. doi: 10.1016/j.apenergy.2015.10.121.

[85] A. Calabrò, P. Deiana, P. Fiorini, G. Girardi, and S. Stendardo. Possible optimal configurations for the ZECOMIX high efficiency zero emission hydrogen and power plant. *Energy*, 33(6):952 – 962, 2008. doi: 10.1016/j.energy.2008.01.004. PRES 2006. 9th Conference of Process Integration, Modelling and Optimisation for Energy Saving and Pollution Reduction - PRES 2006.

[86] E. Lasseuguette, M. Carta, S. Brandani, and M.C. Ferrari. Effect of humidity and flue gas impurities on CO_2 permeation of a polymer of intrinsic microporosity for post-combustion capture. *International Journal of Greenhouse Gas Control*, 50:93 – 99, 2016. doi: 10.1016/j.ijggc.2016.04.023.

[87] D.M. Turi, M. Ho, M.C. Ferrari, P. Chiesa, D.E. Wiley, and M.C. Romano. CO_2 capture from natural gas combined cycles by CO_2 selective membranes. *International Journal of Greenhouse Gas Control*, 61:168 – 183, 2017. doi: 10.1016/j.ijggc.2017.03.022.

[88] T.C. Merkel, H.Q. Lin, X.T. Wei, and R. Baker. Power plant post-combustion carbon dioxide capture: An opportunity for membranes. *Journal of Membrane Science*, 359(1):126 – 139, 2010. doi: 10.1016/j.memsci.2009.10.041. Membranes and CO2 Separation.

[89] Aspen Technology Inc. *Getting Started Modelling Processes with Solids*, 2013. URL http://profsite.um.ac.ir/~fanaei/_private/Solids8_4.pdf.

[90] E. Audasso, S. Nam, E. Arato, and B. Bosio. Preliminary model and validation of molten carbonate fuel cell kinetics under sulphur poisoning. *Journal of Power Sources*, 352:216 – 225, 2017. doi: 10.1016/j.jpowsour.2017.03.091.

[91] T. Watanabe, Y. Izaki, Y. Mugikura, H. Morita, M. Yoshikawa, M. Kawase, F. Yoshiba, and K. Asano. Applicability of molten carbonate fuel cells to various fuels. *Journal of Power Sources*, 160(2):868 – 871, 2006. doi: 10.1016/j.jpowsour.2006.06.058. Special issue including selected papers presented at the International Workshop on Molten Carbonate Fuel Cells and Related Science and Technology 2005 together with regular papers.

[92] Y.X. Sun, E. Zwolińska, and A.G. Chmielewski. Abatement technologies for high concentrations of NO_X and SO_2 removal from exhaust gases: A review. *Critical Reviews in Environmental Science and Technology*, 46(2):119–142, 2016. doi: 10.1080/10643389.2015.1063334.

[93] J. Kaminski. Technologies and costs of SO_2-emissions reduction for the energy sector. *Applied Energy*, 75(3):165 – 172, 2003. doi: 10.1016/S0306-2619(03)00029-1. Energex 2002 - Environmental Control and Waste Recycling - Topic V.

[94] G. Xu, Y. Yang, N. Wang, X. Yuan, J. Li, and X. Song. Analysis on Energy Consumption and Optimal Operation of FGD System in Power Plant. In *2010 Asia-Pacific Power and Energy Engineering Conference*, pages 1–4, 2010.

[95] M. Songolzadeh, M. Soleimani, M. Takht Ravanchi, and R. Songolzadeh. Carbon Dioxide Separation From Flue Gases: A Technological, Review Emphasizing Reduction in Greenhouse Gas Emissions. *The Scientific World Journal*, 1, 2014. doi: 10.1155/2014/828131.

[96] G. Xu, L. Li, Y.P. Yang, L.H. Tian, T. Liu, and K. Zhang. A novel CO_2 cryogenic liquefaction and separation system. *Energy*, 42(1):522 – 529, 2012. doi: 10.1016/j.energy.2012.02.048. 8th World Energy System Conference, WESC 2010.

[97] M.J. Tuinier, M. van Sint Annaland, and J.A.M. Kuipers. A novel process for cryogenic CO_2 capture using dynamically operated packed beds—an experimental and numerical study. *International Journal of Greenhouse Gas Control*, 5(4):694 – 701, 2011. doi: 10.1016/j.ijggc.2010.11.011.

[98] S. McPhail, A. Aarva, H. Devianto, R. Bove, and A. Moreno. SOFC and MCFC: Commonalities and opportunities for integrated research. *International Journal of Hydrogen Energy*, 36(16):10337 – 10345, 2011. doi: 10.1016/j.ijhydene.2010.09.071. European Fuel Cell 2009.

[99] A. F. Massardo and B. Bosio. Assessment of Molten Carbonate Fuel Cell Models and Integration With Gas and Steam Cycles . *Journal of Engineering for Gas Turbines and Power*, 124(1):103–109, 02 2001. doi: 10.1115/1.1398551.

[100] Y.P. Yang and R.R. Zhai. MEA-based CO_2 Capture Technology and Its Application in Power Plants. In Jatin Nathwani and Artie Ng, editors, *Paths to Sustainable Energy*, chapter 24. IntechOpen, Rijeka, 2010. doi: 10.5772/13012.

[101] E. Audasso, B. Bosio, D. Bove, E. Arato, T. Barckholtz, G. Kiss, J. Rosen, H. Elsen, R. Blanco Gutierrez, L. Han, T. Geary, C. Willman, A. Hilmi, C.Y. Yuh, and H. Ghezel-Ayagh. New, Dual-Anion Mechanism for Molten Carbonate Fuel Cells Working as Carbon Capture Devices. *Journal of The Electrochemical Society*, 167(8):084504, apr 2020. doi: 10.1149/1945-7111/ab8979.

[102] K. Sugiura, K. Takei, K. Tanimoto, and Y. Miyazaki. The carbon dioxide concentrator by using MCFC. *Journal of Power Sources*, 118(1):218 – 227, 2003. doi: 10.1016/S0378-7753(03)00084-3. Scientific Advances in Fuel Cell Systems.

[103] N. Busson, S. Palous, J. Millet, and R. Buvet. Propriétés chimiques et électrochimiques de l'eau dans les carbonates alcalins fondus. *Electrochimica Acta*, 12(12):1609 – 1629, 1967. doi: 10.1016/0013-4686(67)80076-8.

[104] G.J. Janz. Molten carbonate electrolytes as acid-base solvent systems. *Journal of Chemical Education*, 44(10):581, 1967. doi: 10.1021/ed044p581.

[105] J. Rosen, T. Geary, A. Hilmi, R. Blanco-Gutierrez, C.Y. Yuh, C.S. Pereira, Han L, R.A. Johnson, C.A. Willman, H. Ghezel-Ayagh, and T.A. Barckholtz. Molten Carbonate Fuel Cell Performance for CO_2 Capture from Natural Gas Combined Cycle Flue Gas. *Journal of The Electrochemical Society*, 167(6):064505, mar 2020. doi: 10.1149/1945-7111/ab7a9f.

[106] L. Xing, J.M. Hao, X.F. Li, Y. Zhang, Z.G. Hu, and Y.F. Gao. Polarization modeling and performance optimization of a molten sodium hydroxide direct carbon fuel cell (mhdcfc). *Journal of Power Sources*, 363:428 – 441, 2017. doi: 10.1016/j.jpowsour.2017.07.113.

[107] B. Bosio, P. Costamagna, and F. Parodi. Modeling and experimentation of molten carbonate fuel cell reactors in a scale-up process. *Chemical Engineering Science*, 54(13):2907 – 2916, 1999. doi: 10.1016/S0009-2509(98)00414-X.

[108] B. Bosio, N. Di Giulio, S.W. Nam, and A. Moreno. An effective semi-empiric model for MCFC kinetics: Theoretical development and experimental parameters identification. *International Journal of Hydrogen Energy*, 39(23):12273 – 12284, 2014. doi: 10.1016/j.ijhydene.2014.04.119.

[109] H. Morita, Y. Mugikura, Y. Izaki, T. Watanabe, and T. Abe. Model of Cathode Reaction Resistance in Molten Carbonate Fuel Cells. *Journal of The Electrochemical Society*, 145(5):1511–1517, dec 2019. doi: 10.1149/1.1838512.

[110] W: Xing, T. Peters, M.L. Fontaine, A. Evans, P.P. Henriksen, T. Norby, and R. Bredesen. Steam-promoted CO_2 flux in dual-phase CO_2 separation membranes. *Journal of Membrane Science*, 482:115 – 119, 2015. ISSN 0376-7388. doi: 10.1016/j.memsci.2015.02.029.

[111] A. Evans, W. Xing, and T. Norby. Electromotive force (emf) determination of transport numbers for native and foreign ions in molten alkali metal carbonates. *Journal of The Electrochemical Society*, 162(10):F1135–F1143, 2015. doi: 10.1149/2.0121510jes.

[112] C. Xia, Y. Li, Ye.Tian, Q.H. Liu, Y.C. Zhao, L.J. Jia, and Y.D. Li. A high performance composite ionic conducting electrolyte for intermediate temperature fuel cell and evidence for ternary ionic conduction. *Journal of Power Sources*, 188(1):156 – 162, 2009. doi: 10.1016/j.jpowsour.2008.11.068.

[113] E. Audasso, B. Bosio, D. Bove, E. Arato, T. Barckholtz, G. Kiss, J. Rosen, H. Elsen, R. Blanco Gutierrez, L. Han, T. Geary, C. Willman, A. Hilmi, C. Y. Yuh, and H. Ghezel-Ayagh. The Effects of Gas Diffusion in Molten Carbonate Fuel Cells Working as Carbon Capture Devices. *Journal of The Electrochemical Society*, 167(11):114515, jul 2020. doi: 10.1149/1945-7111/aba8b6.

[114] D. Bove, E. Audasso, T. Barckholtz, G. Kiss, J. Rosen, and B. Bosio. Process analysis of molten carbonate fuel cells in carbon capture applications. *International Journal of Hydrogen Energy*, 2020. doi: 10.1016/j.ijhydene.2020.08.020.

[115] *Fuel Cells in the Waste-to-Energy Chain : Distributed Generation Through Non-Conventional Fuels and Fuel Cells*. Springer, 2012.

[116] B. Bosio, P. Costamagna, F. Parodi, and B. Passalacqua. Industrial experience on the development of the molten carbonate fuel cell technology. *Journal of Power Sources*, 74(2):175 – 187, 1998. doi: 10.1016/S0378-7753(98)00052-4.

[117] G. Accardo, D. Frattini, A. Moreno, S.P. Yoon, J.H. Han, and S.W. Nam. Influence of nano zirconia on nial anodes for molten carbonate fuel cell: Characterization, cell tests and post-analysis. *Journal of Power Sources*, 338:74 – 81, 2017. doi: 10.1016/j.jpowsour.2016.11.029.

[118] B. Bosio, T. Barckholtz, P.H. Kalamaras, G. Kiss, J. Rosen, D. Bove, and E. Audasso. Experimental and modelling investigation of CO_3^{2-} and OH^- equilibrium effects on Molten Carbonate Fuel Cell performance in carbon Capture applications. *Frontiers in Energy Research*, submitted.

[119] M. Mizuhata, T. Ohta, and s. Deki. Polarized Raman Spectra of Molten Carbonates Influenced by the Surface Acidity of the Coexisting Inorganic Powder. *Electrochemistry*, 77(8):721–724, 2009. doi: 10.5796/electrochemistry.77.721.

[120] I D Zakir'yanova, E V Nikolaeva, A L Bove, and B D Antonov. Electrical Conductivity and Raman Spectra of Disperse Systems α-Al_2O_3–Li_2CO_3–Na_2CO_3–K_2CO_3–NaCl Melt. *Russian Metallurgy (Metally)*, 2018(2):181–185, 2018. doi: 10.1134/S0036029518020246.

[121] I.D. Zakiriyanova, V.A Khokhlov, and V.A. Kochedykov. Raman spectra and microdynamics of the hydroxide-ion in molten NaOH and NaCl-NaOH mixtures. *Journal of Molecular Liquids*, 83 (1):153 – 162, 1999. doi: 10.1016/S0167-7322(99)00082-3.

[122] K. Hemmes and M. Cassir. A Theoretical Study of the Carbon/Carbonate/Hydroxide (Electro-) Chemical System in a Direct Carbon Fuel Cell. *Journal of Fuel Cell Science and Technology*, 8 (5), 06 2011. doi: 10.1115/1.4003750. 051005.

[123] S. Frangini and A. Masi. Molten carbonates for advanced and sustainable energy applications: Part i. revisiting molten carbonate properties from a sustainable viewpoint. *International Journal of Hydrogen Energy*, 41(41):18739 – 18746, 2016. doi: 10.1016/j.ijhydene.2015.12.073.

[124] G. J. Janz and R. P. T. Tomkins. Molten salts: Volume 5, part 2. additional single and multi-component salt systems. electrical conductance, density, viscosity and surface tension data. *Journal of Physical and Chemical Reference Data*, 12(3):591–815, 1983. doi: 10.1063/1.555693.

[125] S.B. Beale. Calculation procedure for mass transfer in fuel cells. *Journal of Power Sources*, 128 (2):185 – 192, 2004. doi: doi.org/10.1016/j.jpowsour.2003.09.053.

[126] Bianchi, F. and Baldinelli, A. and Barelli, L. and Cinti, G. and Audasso, E. and Bosio, B. Multiscale Modeling for Reversible Solid Oxide Cell Operation. *Energies*, 13(19):1–16, 2020. doi: 10.3390/en13195058.

[127] L. Spiridigliozzi, G. Accardo, E. Audasso, B. Bosio, S.P. Yoon, and G. Dell'Agli. Synthesis of easily sinterable ceramic electrolytes based on bi-doped 8ysz for it-sofc applications. *AIMS Materials Science*, 6(4):610–620, 2019. doi: 10.3934/matersci.2019.4.610.

[128] E. Audasso, Y. Kim, J. Cha, V. Cigolotti, H. Jeong, Y.S. Jo, Y. Kim, S.H. Choi, S.P. Yoon, S.W. Nam, and H. Sohn. In situ exsolution of rh nanoparticles on a perovskite oxide surface: Efficient rh catalysts for dry reforming. *Korean Journal of Chemical Engineering*, 37(8):1401–1410, 2020. doi: 10.1007/s11814-020-0592-4.

[129] E. Audasso, F.R. Bianchi, and B. Bosio. 2D Simulation for CH_4 Internal Reforming-SOFCs: An Approach to Study Performance Degradation and Optimization. *Energies*, 13:4116, 2020. doi: 10.3390/en13164116.

[130] G. Dispenza, F. Sergi, G. Napoli, V. Antonucci, and L. Andaloro. Evaluation of hydrogen production cost in different real case studies. *Journal of Energy Storage*, 24:100757, 2019. doi: 10.1016/j.est.2019.100757.

[131] M. Saidi. Performance assessment and evaluation of catalytic membrane reactor for pure hydrogen production via steam reforming of methanol. *International Journal of Hydrogen Energy*, 42(25): 16170 – 16185, 2017. doi: 10.1016/j.ijhydene.2017.05.130.

[132] A. Capa, R. García, D. Chen, F. Rubiera, C. Pevida, and M.V. Gil. On the effect of biogas composition on the H_2 production by sorption enhanced steam reforming (sesr). *Renewable Energy*, 160:575 – 583, 2020. doi: 10.1016/j.renene.2020.06.122.

[133] X.Y. Zhou, H. Huang, and H.T. Liu. Study of partial oxidation reforming of methane to syngas over self-sustained electrochemical promotion catalyst. *International Journal of Hydrogen Energy*, 38 (15):6391 – 6396, 2013. doi: 10.1016/j.ijhydene.2013.03.047.

[134] L.C. Cao, I.K.M. Yu, X.N. Xiong, D.C.W. Tsang, S.C. Zhang, J.H. Clark, C.W. Hu, Y.H. Ng, J. Shang, and Y.S. Ok. Biorenewable hydrogen production through biomass gasification: A review and future prospects. *Environmental Research*, 186:109547, 2020. doi: 10.1016/j.envres.2020.109547.

[135] L. Mastropasqua, I. Pecenati, A. Giostri, and S. Campanari. Solar hydrogen production: Techno-economic analysis of a parabolic dish-supported high-temperature electrolysis system. *Applied Energy*, 261:114392, 2020. doi: 10.1016/j.apenergy.2019.114392.

[136] K. Ahmed and K. Foger. Kinetics of internal steam reforming of methane on Ni/YSZ-based anodes for solid oxide fuel cells. *Catalysis Today*, 63(2):479 – 487, 2000. doi: 10.1016/S0920-5861(00)00494-6.

[137] X.J. Luo and K.F. Fong. Development of 2d dynamic model for hydrogen-fed and methane-fed solid oxide fuel cells. *Journal of Power Sources*, 328:91 – 104, 2016. doi: 10.1016/j.jpowsour.2016.08.005.

[138] S.H. Sohn, S.M. Baek, J.H. Nam, and C.J. Kim. Two-dimensional micro/macroscale model for intermediate-temperature solid oxide fuel cells considering the direct internal reforming of methane. *International Journal of Hydrogen Energy*, 41(12):5582 – 5597, 2016. doi: 10.1016/j.ijhydene.2016.01.161.

[139] L.K. Chiang, H.C. Liu, Y.H. Shiu, C.H. Lee, and R.Y. Lee. Thermal stress and thermo-electrochemical analysis of a planar anode-supported solid oxide fuel cell: Effects of anode porosity. *Journal of Power Sources*, 195(7):1895 – 1904, 2010. doi: 10.1016/j.jpowsour.2009.10.011.

[140] F. Greco, H. Lund Frandsen, A. Nakajo, M.F. Madsen, and J. Van herle. Modelling the impact of creep on the probability of failure of a solid oxide fuel cell stack. *Journal of the European Ceramic Society*, 34(11):2695 – 2704, 2014. doi: 10.1016/j.jeurceramsoc.2013.12.055. Modelling and Simulation meet Innovation in Ceramics Technology.

[141] D. Mogensen, J.D. Grunwaldt, P.V. Hendriksen, K. Dam-Johansen, and J.U. Nielsen. Internal steam reforming in solid oxide fuel cells: Status and opportunities of kinetic studies and their impact on modelling. *Journal of Power Sources*, 196(1):25 – 38, 2011. doi: 10.1016/j.jpowsour.2010.06.091.

[142] P. Aguiar, C.S. Adjiman, and N.P. Brandon. Anode-supported intermediate temperature direct internal reforming solid oxide fuel cell. i: model-based steady-state performance. *Journal of Power Sources*, 138(1):120 – 136, 2004. doi: 10.1016/j.jpowsour.2004.06.040.

[143] D. Papurello and A. Lanzini. SOFC single cells fed by biogas: Experimental tests with trace contaminants. *Waste Management*, 72:306 – 312, 2018. doi: 10.1016/j.wasman.2017.11.030.

[144] H. Madi, A. Lanzini, S. Diethelm, D. Papurello, J. Van herle, M. Lualdi, J. Gutzon Larsen, and M. Santarelli. Solid oxide fuel cell anode degradation by the effect of siloxanes. *Journal of Power Sources*, 279:460 – 471, 2015. doi: 10.1016/j.jpowsour.2015.01.053. 9th International Conference on Lead-Acid Batteries – LABAT 2014.

[145] H.S. Lee, H.M. Lee, J.Y. Park, and H.T. Lim. Degradation behavior of ni-ysz anode-supported solid oxide fuel cell (SOFC) as a function of H_2S concentration. *International Journal of Hydrogen Energy*, 43(49):22511 – 22518, 2018. doi: 10.1016/j.ijhydene.2018.09.189.

[146] V. Vorontsov, J.L. Luo, A.R. Sanger, and K.T. Chuang. Synthesis and characterization of new ternary transition metal sulfide anodes for H_2S-powered solid oxide fuel cell. *Journal of Power Sources*, 183(1):76 – 83, 2008. doi: 10.1016/j.jpowsour.2008.04.055.

[147] J. Badur, M. Lemański, T. Kowalczyk, P. Ziółkowski, and S. Kornet. Zero-dimensional robust model of an SOFC with internal reforming for hybrid energy cycles. *Energy*, 158(C):128–138, 2018. doi: 10.1016/j.energy.2018.05.

[148] Q.L. Hou, H.B. Zhao, and X.Y. Yang. Thermodynamic performance study of the integrated MR-SOFC-CCHP system. *Energy*, 150:434 – 450, 2018. doi: 10.1016/j.energy.2018.02.105.

[149] V. Menon, A. Banerjee, J. Dailly, and O. Deutschmann. Numerical analysis of mass and heat transport in proton-conducting SOFCs with direct internal reforming. *Applied Energy*, 149:161 – 175, 2015. doi: 10.1016/j.apenergy.2015.03.037.

[150] M. Andersson, J.L. Yuan, and B. Sundén. SOFC modeling considering hydrogen and carbon monoxide as electrochemical reactants. *Journal of Power Sources*, 232:42 – 54, 2013. doi: 10.1016/j.jpowsour.2012.12.122.

[151] M. Chalusiak, M. Wrobel, M. Mozdzierz, K. Berent, J.S. Szmyd, S. Kimijima, and G. Brus. A numerical analysis of unsteady transport phenomena in a Direct Internal Reforming Solid Oxide Fuel Cell. *International Journal of Heat and Mass Transfer*, 131:1032 – 1051, 2019. doi: 10.1016/j.ijheatmasstransfer.2018.11.113.

[152] J. Li, G.Y. Cao, X.J. Zhu, and H.Y. Tu. Two-dimensional dynamic simulation of a direct internal reforming solid oxide fuel cell. *Journal of Power Sources*, 171(2):585 – 600, 2007. doi: 10.1016/j.jpowsour.2007.07.029.

[153] T.X. Ho, P. Kosinski, A.C. Hoffmann, and A. Vik. Transport, chemical and electrochemical processes in a planar solid oxide fuel cell: Detailed three-dimensional modeling. *Journal of Power Sources*, 195(19):6764 – 6773, 2010. doi: 10.1016/j.jpowsour.2010.03.090.

[154] K. Nikooyeh, A.A. Jeje, and J.M. Hill. 3d modeling of anode-supported planar SOFC with internal reforming of methane. *Journal of Power Sources*, 171(2):601 – 609, 2007. doi: 10.1016/j.jpowsour.2007.07.003.

[155] A. Lanzini, P. Leone, M. Pieroni, M. Santarelli, D. Beretta, and S. Ginocchio. Experimental Investigations and Modeling of Direct Internal Reforming of Biogases in Tubular Solid Oxide Fuel Cells. *Fuel Cells*, 11(5):697–710, 2011. doi: 10.1002/fuce.201000173.

[156] B. Stoeckl, V. Subotić, D. Reichholf, H. Schroettner, and C. Hochenauer. Extensive analysis of large planar SOFC: Operation with humidified methane and carbon monoxide to examine carbon deposition based degradation. *Electrochimica Acta*, 256:325 – 336, 2017. doi: 10.1016/j.electacta.2017.09.026.

[157] Q.P. Fang, L. Blum, P. Batfalsky, N.H. Menzler, U. Packbier, and D. Stolten. Durability test and degradation behavior of a 2.5 kW SOFC stack with internal reforming of LNG. *International Journal of Hydrogen Energy*, 38(36):16344 – 16353, 2013. doi: 10.1016/j.ijhydene.2013.09.140.

[158] V. Subotić, C. Schluckner, B. Stoeckl, M. Preininger, V. Lawlor, S. Pofahl, H. Schroettner, and C. Hochenauer. Towards practicable methods for carbon removal from Ni-YSZ anodes and restoring the performance of commercial-sized ASC-SOFCs after carbon deposition induced degradation. *Energy Conversion and Management*, 178:343 – 354, 2018. doi: 10.1016/j.enconman.2018.10.022.

[159] J.M. Klein, Y. Bultel, M. Pons, and P. Ozil. Modeling of a Solid Oxide Fuel Cell Fueled by Methane: Analysis of Carbon Deposition. *Journal of Fuel Cell Science and Technology*, 4(4):425–434, 05 2006. doi: 10.1115/1.2759504.

[160] M. Yan, M. Zeng, Chen Q, Y, and Q.W. Wang. Numerical study on carbon deposition of SOFC with unsteady state variation of porosity. *Applied Energy*, 97:754 – 762, 2012. doi: 10.1016/j.apenergy.2012.02.055. Energy Solutions for a Sustainable World - Proceedings of the Third International Conference on Applied Energy, May 16-18, 2011 - Perugia, Italy.

[161] D. Sánchez, R. Chacartegui, A. Muñoz, and T. Sánchez. On the effect of methane internal reforming modelling in solid oxide fuel cells. *International Journal of Hydrogen Energy*, 33(7):1834 – 1844, 2008. doi: 10.1016/j.ijhydene.2008.01.024.

[162] *Perry's Chemical engineers' handbook*. Sixth edition / prepared by a staff of specialists under the editorial direction of late editor Robert H. Perry ; editor, Don W. Green ; assistant editor, James O. Maloney. New York : McGraw-Hill, [1984] ©1984. URL https://search.library.wisc.edu/catalog/999552107102121.

[163] J.G. Xu and G.F. Froment. Methane steam reforming, methanation and water-gas shift: I. intrinsic kinetics. *AIChE Journal*, 35(1):88–96, 1989. doi: 10.1002/aic.690350109.

[164] H. Timmermann, W. Sawady, R. Reimert, and E. Ivers-Tiffée. Kinetics of (reversible) internal reforming of methane in solid oxide fuel cells under stationary and apu conditions. *Journal of Power Sources*, 195(1):214 – 222, 2010. doi: 10.1016/j.jpowsour.2009.07.019.

[165] P. Kazempoor and R.J. Braun. Model validation and performance analysis of regenerative solid oxide cells for energy storage applications: Reversible operation. *International Journal of Hydrogen Energy*, 39(11):5955 – 5971, 2014. doi: 10.1016/j.ijhydene.2014.01.186.

[166] F.P. Nagel, T.J. Schildhauer, D.M.A. Biollaz, and S. Stucki. Charge, mass and heat transfer interactions in solid oxide fuel cells operated with different fuel gases—A sensitivity analysis. *Journal of Power Sources*, 184(1):129 – 142, 2008. doi: 10.1016/j.jpowsour.2008.05.044.

[167] L. van Biert, K. Visser, and P.V. Aravind. Intrinsic methane steam reforming kinetics on nickel-ceria solid oxide fuel cell anodes. *Journal of Power Sources*, 443:227261, 2019. doi: 10.1016/j.jpowsour.2019.227261.

[168] *THE YELLOW PAGES OF SOFC TECHNOLOGY International Status of SOFC deployment 2017*. VTT Technical Research Centre of Finland Ltd, P.O. Box 1000, 02044 VTT, Finland, 2017.

[169] T. Chen, W.G. Wang, H.M., T.S. Li, and C. Xu. Evaluation of carbon deposition behavior on the nickel/yttrium-stabilized zirconia anode-supported fuel cell fueled with simulated syngas. *Journal of Power Sources*, 196(5):2461 – 2468, 2011. doi: https://doi.org/10.1016/j.jpowsour.2010.11.095.

[170] K. Ahmed and K. Föger. Analysis of equilibrium and kinetic models of internal reforming on solid oxide fuel cell anodes: Effect on voltage, current and temperature distribution. *Journal of Power Sources*, 343:83 – 93, 2017. doi: https://doi.org/10.1016/j.jpowsour.2017.01.039.

[171] C.Y. Jiang, Y.C. Gu, W.B. Guan, J.H. Zheng, M. Ni, and Z. Zhong. 3d thermo-electro-chemo-mechanical coupled modeling of solid oxide fuel cell with double-sided cathodes. *International Journal of Hydrogen Energy*, 45(1):904 – 915, 2020. doi: https://doi.org/10.1016/j.ijhydene.2019.10.139.

[172] D. Naegu, G. Tsekouras, D.N. Miller, H. Ménard and J.T.S. Irvine. In situ growth of nanoparticles through control of non-stoichiometry. *Nature Chemistry*, 5:916–923, 2013. doi: 10.1038/nchem.1773.

[173] Tong Wei, Lichao Jia, Haoyu Zheng, Bo Chi, Jian Pu, and Jian Li. $LaMnO_3$-based perovskite with in-situ exsolved Ni nanoparticles: a highly active, performance stable and coking resistant catalyst for CO_2 dry reforming of CH_4. *Applied Catalysis A: General*, 564:199 – 207, 2018. doi: 10.1016/j.apcata.2018.07.031.

[174] D. Neagu, T. S. Oh, D. N. Miller, S. M. Bukhari, S. R. Gamble, R. J. Gorte, J. M. Vohs, and J. T.S. Irvine. Nano-socketed nickel particles with enhanced coking resistance grown in situ by redox exsolution. *Nature Communications*, 6, 2015. doi: 10.1038/ncomms9120.

[175] R. Palcheva, U. Olsbye, M. Palcut, P. Rauwel, G. Tyuliev, N. Velinov, and H.H. Fjellvåg. Rh promoted $La_{0.75}Sr_{0.25}(Fe_{0.8}Co_{0.2})_{1-x}Ga_xO_{3-\delta}$ perovskite catalysts: Characterization and catalytic performance for methane partial oxidation to synthesis gas. *Applied Surface Science*, 357:45 – 54, 2015. doi: 10.1016/j.apsusc.2015.08.237.

[176] S.M. Park, Y.G. Kim, H.S. Han, Y.S. Chung, W.E. Yoon, J.I. Choi, and W.B. Kim. In situ exsolved Co nanoparticles on Ruddlesden-Popper material as highly active catalyst for CO_2 electrolysis to CO. *Applied Catalysis B: Environmental*, 248:147 – 156, 2019. doi: 10.1016/j.apcatb.2019.02.013.

[177] Despoina Papargyriou, David Noel Miller, and John Thomas Sirr Irvine. Exsolution of fe–ni alloy nanoparticles from (la,sr)(cr,fe,ni)O_3 perovskites as potential oxygen transport membrane catalysts for methane reforming. *Journal of Materials Chemistry A*, 7:15812–15822, 2019. doi: 10.1039/C9TA03711J.

[178] D. Zubenko, S. Singh, and B.A. Rosen. Exsolution of re-alloy catalysts with enhanced stability for methane dry reforming. *Applied Catalysis B: Environmental*, 209:711 – 719, 2017. doi: 10.1016/j.apcatb.2017.03.047.

[179] Y.J. Chai, Y. Fu, H. Feng, W.B. Kong, C.K. Yuan, B.R. Pan, J. Zhang, and Y.H. Sun. A Nickel-Based Perovskite Catalyst with a Bimodal Size Distribution of Nickel Particles for Dry Reforming of Methane. *ChemCatChem*, 10(9):2078–2086, 2018. doi: 10.1002/cctc.201701483.

[180] J.H. Oh, B.W. Kwon, J.W. Cho, C.H. Lee, M.K. Kim, S.H. Choi, S.P. Yoon, J.H. Han, S.W. Nam, J.Y. Kim, S.S. Jang, K.B. Lee, and H.C. Ham. Importance of Exsolution in Transition-Metal (Co, Rh, and Ir)-Doped $LaCrO_3$ Perovskite Catalysts for Boosting Dry Reforming of CH_4 Using CO_2 for Hydrogen Production. *Industrial & Engineering Chemistry Research*, 58(16):6385–6393, 2019. doi: 10.1021/acs.iecr.8b05337.

[181] E.I. Papaioannou, D. Neagu, W.K.W. Ramli, J.T.S. Irvine, and I.S. Metcalfe. Sulfur-Tolerant, Exsolved Fe–Ni Alloy Nanoparticles for CO Oxidation. *Topics in Catalysis*, 62(17):1149–1156, 2019. ISSN 1572-9028. doi: 10.1007/s11244-018-1053-8.

[182] B.W. Kwon, J.H. Oh, G.S. Kim, S.P. Yoon, J.H. Han, S.W. Nam, and H.C. Ham. The novel perovskite-type ni-doped $Sr_{0.92}Y_{0.08}TiO_3$ catalyst as a reforming biogas (CH_4+CO_2) for H_2 production. *Applied Energy*, 227:213 – 219, 2018. doi: 10.1016/j.apenergy.2017.07.105.

[183] G.S. Kim, B.Y. Lee, H.C. Ham, J.H. Han, S.W. Nam, J.H. Moon, and S.P. Yoon. Highly active and stable $Sr_{0.92}Y_{0.08}Ti_{1-x}Ru_xO_{3-\delta}$ in dry reforming for hydrogen production. *International Journal of Hydrogen Energy*, 44(1):202 – 212, 2019. doi: doi.org/10.1016/j.ijhydene.2018.03.116. State of the Art Materials for Hydrogen Energy.

[184] G.S. Kim, B.Y. Lee, G. Accardo, H.C. Ham, J.H. Moon, and S.P. Yoon. Improved catalytic activity under internal reforming solid oxide fuel cell over new rhodium-doped perovskite catalyst. *Journal of Power Sources*, 423:305 – 315, 2019. doi: 10.1016/j.jpowsour.2019.03.082.

[185] D.A.J.M. Ligthart, R.A. van Santen, and E.J.M. Hensen. Influence of particle size on the activity and stability in steam methane reforming of supported rh nanoparticles. *Journal of Catalysis*, 280 (2):206 – 220, 2011. doi: 10.1016/j.jcat.2011.03.015.

[186] Z.L. Zhang, V.A. Tsipouriari, A.M. Efstathiou, and X.E. Verykios. Reforming of Methane with Carbon Dioxide to Synthesis Gas over Supported Rhodium Catalysts: I. Effects of Support and Metal Crystallite Size on Reaction Activity and Deactivation Characteristics. *Journal of Catalysis*, 158(1):51 – 63, 1996. doi: doi.org/10.1006/jcat.1996.0005.

[187] H.J. Borg, L.C.A. Van Den Oetelaar, and J.W. Niemantsverdriet. Preparation of a rhodium catalyst from rhodium trichloride on a flat, conducting alumina support studied with static secondary ion mass spectrometry and monochromatic X-ray photoelectron spectroscopy. *Catalysis Letters*, 17: 81–95, 1993. doi: 10.1007/BF00763930.

[188] D. F. Fairbanks and C. R. Wilke. Diffusion coefficients in multicomponent gas mixtures. *Industrial & Engineering Chemistry*, 42(3):471–475, 1950. doi: 10.1021/ie50483a022.

[189] John J. Byrne, D. Maguire, and John K. A. Clarke. Gas-phase interdiffusion coefficients for some polar organic compounds. *The Journal of Physical Chemistry*, 71(9):3051–3052, 1967. doi: 10.1021/j100868a044.

[190] C. R. Wilke and C. Y. Lee. Estimation of diffusion coefficients for gases and vapors. *Industrial & Engineering Chemistry*, 47(6):1253–1257, 1955. doi: 10.1021/ie50546a056.

[191] E. N. Fuller and J. C. Giddings. A Comparison of Methods for Predicting Gaseous Diffusion Coefficients. *Journal of Chromatographic Science*, 3(7):222–227, 07 1965. doi: 10.1093/chromsci/3.7.222.

[192] Edward N. Fuller, Paul D. Schettler, and J. Calvin. Giddings. New method for prediction of binary gas-phase diffusion coefficients. *Industrial & Engineering Chemistry*, 58(5):18–27, 1966. doi: 10.1021/ie50677a007.